Diss. ETH No. 24068

Discontinuous Finite Element Methods for Eddy Current Simulation

A dissertation submitted to
ETH Zürich

for the degree of
Doctor of Sciences

presented by
RAFFAEL CASAGRANDE
MSc ETH CSE, ETH Zürich
born March 12, 1988
citizen of
Lucerne LU, Switzerland

accepted on the recommendation of
Prof. Dr. Ralf Hiptmair, ETH Zürich, examiner
Prof. Dr.-Ing. Stefan Kurz, Technische Universität Darmstadt, co-examiner
Dr. Jörg Ostrowski, ABB Corporate Research, co-examiner

2017

Abstract

This thesis is concerned with the simulation of 3D electromagnetic fields in the magneto-quasi-static limit with an emphasis on two applications: Firstly, we consider the case of *rigid bodies moving at non-relativistic speed* in time domain, and secondly, we investigate the *resolution of thin electromagnetic boundary/skin layers* on coarse meshes in frequency domain.

In both cases the presented approach is based on a vector potential formulation and requires the coupling of discontinuous basis functions across mesh element boundaries. This is accomplished with the Symmetric Weighted Interior Penalty (SWIP), respectively Non-symmetric Weighted Interior Penalty (NWIP) discretization of the **curl curl** operator. A numerical experiment shows that for *arbitrary-non-conforming meshes* the non-zero eigenvalues of the SWIP discretization are not well-separated from the kernel, i.e. spectral pollution occurs and the Galerkin matrix can become very ill-conditioned. We circumvent this problem by shifting the spectrum slightly, that is we introduce an artificial, but small conductivity in insulators. Thereby we also take care of the non-trivial kernel of the discrete SWIP/NWIP **curl curl** operator.

The SWIP/NWIP methods support very general classes of (possibly) discontinuous approximation spaces. In fact, we prove a best approximation result w.r.t. the SWIP/NWIP energy norm under the mild assumption that the traces of all basis functions and the traces of their derivatives are square integrable. In particular, non-polynomial, exponential-type basis functions are supported. For edge-functions of the first kind we show that one order of convergence in h is lost at arbitrary-non-conforming mesh interfaces; most notably, *first-order edge functions fail to converge*. This issue can be resolved by increasing the polynomial degree locally at non-conforming mesh interfaces.

Moving, rigid bodies are handled by splitting the computational domain into subdomains such that we can use a Lagrangian description of the eddy current model in each subdomain. This means that we mesh every subdomain separately and treat the non-conforming interfaces with the SWIP method. However, in order to couple the electromagnetic fields across an interface, they must be expressed w.r.t. the *same (moving) frame of reference* on both sides; that is the electromagnetic fields must be Galilei transformed on one side of the interface. We show that in the absence of *sliding contacts* one can get rid of this additional transformation locally at the sliding interfaces which simplifies the coupling transmission conditions considerably.

Boundary layers are treated by enriching the standard edge element approximation space with modulated exponential-type basis functions and coupling them with the NWIP method. Numerical experiments show that on a coarse mesh this method is a *viable competitive alternative to the low-order finite element method, respectively Impedance Boundary Conditions (IBC)*, and it outperforms these two alternatives for boundary layers of moderate size. Unfortunately, all three methods resolve the boundary layers poorly in edges/corners of the conductor due to the intrinsic 2D/3D nature of the boundary layer and the *singular behavior* of the exact solution. For moderate skin-depths the most dominant singularities stem from the discontinuity of the conductivity but for the skin-depth $\to 0$ the singularities of the limit problem (perfect electric conductor) become stronger and eventually dominate the former. For 2D problems we propose to enrich the approximation space additionally with both types of singularities to improve its approximation properties in corners. Numerical experiments conducted on a model problem show that this method *suffers from severe numerical instabilities*.

Zusammenfassung

Diese Arbeit behandelt die Simulation von 3D elektromagnetischen Feldern in der magneto-quasi-statischen Näherung. Der Fokus liegt auf zwei Anwendungen: Einerseits untersucht die Arbeit im Zeitbereich den Fall von Starrkörpern, die sich mit nichtrelativistischer Geschwindigkeit bewegen. Zum anderen untersuchen wir die numerische Auflösung von dünnen elektromagnetischen Grenzschichten auf groben Gittern im Frequenzbereich.

In beiden Fällen basiert der Ansatz auf einer Vektorpotentialformulierung und erfordert die Kopplung von unstetigen Basisfunktionen über Gitterelementgrenzen hinweg. Dies wird durch eine Symmetric Weighted Interior Penalty (SWIP) respektive eine Nonsymmetric Weighted Interior Penalty (NWIP)-Diskretisierung des **curl curl** Operators erreicht. Ein numerisches Experiment zeigt, dass die nicht-null Eigenwerte und der Kern der SWIP Diskretisierung auf beliebig-nicht-konformen Gittern nicht eindeutig voneinander getrennt sind, d.h. unechte Eigenwerte werden beobachtet und die Galerkinmatrix kann sehr schlecht konditioniert sein. Wir umgehen dieses Problem, indem wir das Spektrum ein wenig verschieben: wir führen eine künstliche, aber niedrige Leitfähigkeit im Nichtleiter ein. Dadurch erledigt sich auch das Problem vom nicht-trivialen Nullraum des diskreten SWIP/NWIP **curl curl** Operators.

Das SWIP/NWIP-Verfahren unterstützt sehr allgemeine (möglicherweise) unstetige Approximationsräume: Unter der Voraussetzung, dass die Spur der Basisfunktionen quadratisch-integrierbar ist, können wir den Fehler der Methode bezüglich der SWIP/NWIP-Energienorm bis auf eine Konstante durch den besten Approximationsfehler abschätzen. Vor allem lässt sich die Theorie auf nicht-polynomielle, exponentielle Basisfunktionen anwenden. Wir zeigen, dass an nicht-konformen Gitterschnittstellen eine Konvergenzordnung in h verloren geht, falls man Nédélec-Basisfunktionen der ersten Art verwendet. *Insbesondere führen Nédélec-Funktionen der ersten Ordnung zu keiner Konvergenz.* Dieses Problem kann gelöst werden, indem man an den nicht-konformen Gitterschnittstellen lokal den Polynomgrad erhöht.

Bewegte Starrkörper behandeln wir, indem wir das Rechengebiet in Teilgebiete zerlegen und das Wirbelstromproblem in jedem Teilgebiet in Lagrangeschen Variablen ausdrücken. Das Gitter auf einem Teilgebiet kann dabei unabhängig vom Gitter auf anderen Teilgebieten gewählt werden, da die (nicht-konformen) Gitterschnittstellen mithilfe des SWIP-Verfahrens behandelt werden. Beim Formulieren der Kopplungsbedingungen muss man allerdings beachten, dass die elektromagnetischen Felder auf beiden Seiten

im gleichen (bewegten) Bezugssystem ausgedrückt werden müssen, d.h. die elektromagnetischen Felder müssen auf einer Seite mithilfe der Galileitransformation umgerechnet werden. Wir zeigen, dass diese Extratransformation lokal an der Schnittstelle zwischen den Teilgebieten umgangen werden kann, falls keine schleifenden Kontakte existieren. Dadurch vereinfachen sich die Kopplungsbedingungen erheblich.

Grenzschichten werden aufgelöst, indem der Standard-Nédélec-Approximationsraum mit modulierten, exponentiellen Basisfunktionen angereichert wird und das resultierende System mit dem NWIP Verfahren gelöst wird. Numerische Experimente zeigen, dass diese Methode auf groben Gittern eine *konkurrenzfähige Alternative zur Low-Order-Finite-Elemente-Methode, respektive zu Impedanzrandbedingungen (IBC) darstellt.* Insbesondere löst unser Verfahren Grenzschichten mit moderater Eindringtiefe erheblich besser auf. Aufgrund des intrinsischen 2D/3D Charakters der Grenzschicht, und dem singulären Verhalten der exakten Lösung in Ecken/Kanten des Leiters, wird die Grenzschicht an diesen Orten von allen drei Verfahren nicht zufriedenstellend aufgelöst. Bei moderaten Eindringtiefen ist das singuläre Verhalten auf die Diskontinuität der elektrischen Leitfähigkeit zurückzuführen, aber bei kleiner werdenden Eindringtiefen werden die Singularitäten des Limitproblems (perfekter elektrischer Leiter) stärker und dominieren schlussendlich. Für 2D-Probleme, schlagen wir deshalb vor, den Approximationsraum zusätzlich mit den beiden Singularitätstypen anzureichern, um die Approximationseigenschaften in den Ecken des Leiters zu verbessern. Numerische Experimente an einem simplen Modellproblem zeigen, dass diese Methode leider ernsthafte, numerische Stabilitätsprobleme hat.

Acknowledgments

First of all, I would like to thank my supervisors Prof. Ralf Hiptmair and Jörg Ostrowski for giving me the opportunity to pursue this PhD but also for guiding and supporting me during my studies. I'm particularly grateful that I had the freedom to try some of my own ideas, even if they were not of immediate use to ABB, and I'm also very thankful that both of you supported me in my quest for the optimal software design.

I also want to express my deepest gratitude towards my colleague Christoph Winkelmann. You really helped me to focus on my research during all these years by taking care of many ABB related matters. At the same time, we had a lot of very stimulating discussions which were only possible because you took the time to contemplate the issue. Thank you. HyDi as well as my research profited enormously from these discussions and I think we proved that sometimes $1 + 1 \gg 2$.

Also, I would like to thank Prof. Stefan Kurz for the few, but very fruitful discussions which provided me valuable, alternative points of view.

I'm very grateful to Christoph Winkelmann, Prof. Stefan Kurz, Prof. Ralf Hiptmair and Jörg Ostrowski for carefully reviewing this thesis and providing constructive remarks.

I also want to take the chance to thank all the members of SAM and of the ABB research group in Baden-Dättwil for the enjoyable, inspiring atmosphere. In particular, I want to mention Robert, Lars, Andreas, Denis, Jakob, Ryan, Deep, Roger, Prashanth and Daniele and the early lunch group from the ABB research center, Christoph Reutlinger, Irena and Jonas.

Finally, I want to mention the unconditional support of Julia and my family for which I'm greatly thankful.

One ounce of motivation
is worth a pound of persuasion.

DR. JIM BOHN

Contents

Introduction

Nowadays computers (or smartphones) can be found in nearly every household and they serve a plethora of purposes that range from sophisticated analysis tools to pure entertainment (of humans). The subject of this thesis belongs more to the first category but we will see that it can also be entertaining in its own right. In fact, long before Computers became a consumer product in the 1970's, people (mostly scientists) were already using computers to perform tedious calculations: The first computer was essentially a very large pocket-calculator that was orders of magnitudes slower than a human. But since then these machines have evolved into very sophisticated computing platforms and Moore's law dictates that their performance doubles every two years, something that natural evolution just cannot do.

Fortunately, raw computing power is not everything and micro-processors are still very dependent on humans: they must be told what to do. In fact, since the advent of computers, human researchers have advanced numerical algorithms from simple techniques to very refined methods. This thesis continues this effort in the hope that it allows engineers to better understand/design their products and in the hope that scientists can build on it and improve the described algorithms/software.

Setting. This thesis is part of a larger collaboration between ABB corporate research and ETH Zürich entitled "High resolution simulation tool for power devices" that is partially funded by the Commission for Technology and Innovation (CTI). Its primary purpose is the development of a tool for the simulation of electromagnetic fields that arise during the formation of electric arcs in circuit breakers, as well as the alternating current loss distribution in power devices. This tool is called HyDi and has been developed by the author and Christoph Winkelmann such that it

i) can handle *hybrid 3D meshes*,

ii) can deal with non-matching, sliding meshes,

iii) can resolve very thin skin-layers in conductors,

iv) is well-documented, and

v) can be easily adapted to future requirements.

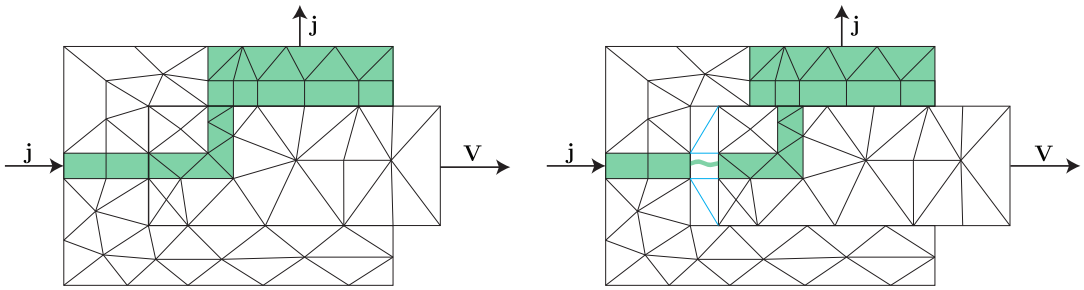

(a) $t = 0$ (b) $t > 0$

Figure 0.1: Schematic view of a simple circuit breaker. The green shading depicts the path of the electric current $\boldsymbol{j}$ while the black lines represent the underlying, moving meshes. The blue mesh is different for every time $t > 0$.

Requirements i) and ii) are important for simulating electric arcs in circuit breakers [113]. In fact, one must solve a Magnetohydrodynamic (MHD) problem to describe the fluid/plasma as well as the electromagnetic fields. In practice this means that HyDi is coupled to a Computational Fluid Dynamics (CFD) solver that is based on the Finite Volume Method (FVM). For reasons of efficiency HyDi and the CFD solver both operate on the same mesh, but since boundary layers are usually resolved using highly anisotropic hexahedral/prismatic elements in the FVM, HyDi must also support hybrid meshes.

In order to motivate requirement ii) consider the very basic circuit breaker shown in Figure 0.1 that consists of two components: the plug is the component that is moving to the right with velocity $\boldsymbol{V}$ whereas the tulip remains fixed. The corresponding meshes are initially ($t = 0$) conforming (i.e. there are no hanging nodes) but they become non-conforming for $t > 0$. The classical Finite Element Method (FEM) is not able to deal with such meshes so that we resort to using the Symmetric Weighted Interior Penalty (SWIP) method locally at the sliding interfaces (Chapter 4). We would like to point out that sliding meshes are also useful in many other applications such as the simulation of rotating machines (e.g. electric motors/generators) or more general magnetic actuators.

Electromagnetic boundary/skin layers (requirement iii)) are usually encountered when the simulation involves high frequencies, high magnetic permeabilities and/or high electric conductivities. This is for example the case for transformers, circuit breakers and processes such as induction hardening [112]. The major problem is mostly that the size of the boundary layer can be orders of magnitude smaller than the characteristic size of the system. Generating a mesh that can resolve such a boundary layer requires a lot of skills and experience, and usually also time. Often it is also prohibitively expensive to carry out the simulation on such a mesh due to the sheer number of unknowns so that it is desirable to not refine the mesh at all. HyDi uses an enriched approximation space to resolve boundary layers at sub-grid-scale (see Chapter 5).

Remark 0.0.1 (Heat conduction and boundary layers)**.** *The main motivation for resolving*

the skin-effect in conductors is the quantification of the Ohmic losses, i.e. one is interested in the temperature distribution inside the conductor which is for example essential to determine if the oil in a transformer can catch fire. However, as it turns out it is not always necessary to resolve the boundary layer accurately to get an accurate temperature distribution: The Wiedemann-Franz law states that the electric conductivity is directly proportional to the thermal conductivity (and the temperature), i.e. good electric conductors possess usually a high thermal conductivity so that the heat generated by the Ohmic losses in the skin-layer is conducted very fast into the interior. In technical applications, the relevant time- and length-scales often permit to consider this process as nearly instantaneous. This means that the temperature distribution is extremely smeared out and is not very sensitive to the local distribution of the Ohmic losses, i.e. it then suffices to determine the global *Ohmic losses accurately without necessarily resolving the actual boundary layer. One notable exception where this argument is not applicable, is inductive hardening: Here the idea is exactly to heat/cool only parts of the workpiece and hence the boundary layers must be resolved.*

Requirements iv) and v) may seem obvious at first but they cannot be taken for granted. In particular, scientific codes often lack a comprehensive documentation, and extensibility is often not even considered. Although this is often blamed on the limited amount of time and resources in a typical research project, the author feels that this should not be an excuse: especially in bigger projects where multiple people are involved good documentation and software design pay off sooner or later. Christoph Winkelmann and the author have gone to great lengths to make sure that HyDi fulfills requirements iv) and v) and we hope that others can benefit from it; we certainly have.

Scope of this work. This document describes the main algorithmic and mathematical contributions of the author to the above-mentioned research project. In particular, it describes the implementation of requirements ii) and iii) in great detail and analyzes them from a theoretical point of view. Numerical experiments underline the developed theory and provide further insights.

Although the author invested a substantial effort into the implementation of requirements i), iv) and v) we will only touch on these topics in this document. We refer the reader to the comprehensive, separate documentation of HyDi that explains these points in more detail.

Overview. We briefly introduce Maxwell's equations in Chapter 1 so that we can derive and motivate the governing equations of the magneto-quasi-static limit (eddy current) and of the static limit. For clearer presentation and better understanding this first chapter omits most mathematical details.

Chapter 2 will make these mathematical details more explicit and introduce the mathematical tools that are needed to state the equations of Chapter 1 in a variational

setting. Following this rather dry exposition we apply these tools to the electro- and magnetostatic problems as well as the time-harmonic eddy current problem to derive the corresponding variational formulations. We also prove estimates for the regularization error that stem from the artificially introduced conductivity in insulators.

Chapter 3 is devoted to the numerical solution of the generic, 3D **curl curl** Boundary Value Problem (BVP) using the Discontinuous Galerkin (DG) method. Both the eddy current problem as well as the magnetostatic problem are instances of this generic **curl curl** problem. The main result of this chapter is a best approximation theorem that applies to very general, discrete approximation spaces defined on arbitrarily-non-conforming meshes for both the Symmetric Weighted Interior Penalty (SWIP) and the Non-symmetric Weighted Interior Penalty (NWIP) method. Moreover, we show that one order of convergence in h is lost when edge functions of the first kind are used. A recurring theme of this chapter is also the relationship between FEM and DG and how to apply DG only in some parts of the domain.

The following two chapters apply the mathematical framework developed in Chapters 2 and 3: Chapter 4 deals with problems defined on arbitrary-non-conforming meshes and contains a thorough numerical study of the magnetostatic problem posed on two hemispheres that can be rotated against each other. We show numerically that the SWIP discretization of the **curl curl** operator yields spurious eigenvalues and that first order edge functions of the first kind generally fail to converge. The second part of Chapter 4 deals with the eddy current problem in time-domain in the presence of moving, rigid bodies. Here, we first study how the eddy current problem looks in any moving frame of reference and we state the Galilei-transformation rules for the electromagnetic fields. Using this we derive a Lagrangian description of the eddy current problem and we show that in the absence of sliding contacts, we can get rid of the Galilei-transformation in a neighborhood of the sliding interfaces. Finally, we present a simple Euler time stepping method, prove its convergence and illustrate the theory on two numerical examples.

Chapter 5 considers the time-harmonic eddy current problem and focuses on the resolution of boundary layers on coarse meshes using the NWIP method. Throughout the chapter, the general idea is to enrich the approximation space with suitable basis functions: We first present a very simple method where the standard edge element approximation space is enriched with exponential-type boundary layer functions. Thereby we can resolve boundary layers at subgrid-scale on flat surfaces but in corners/edges of the conductor the method fails due to the intrinsic 2D/3D behavior of the boundary layer and the singular behavior of the exact solution. In order to study the problem more easily, we switch to a simple 2D model problem and propose to enrich the approximation space additionally with singular functions and to refine the mesh locally to resolve the boundary layer.

The final Chapter 6 briefly covers requirement v) that we have introduced above: We present software design aspects of HyDi and how we ensure maintainability and extensibility of the codebase. Moreover, we give a comprehensive list of HyDi's current features

and describe a numerically robust algorithm to merge two conforming grids into one, possibly non-conforming grid, cf. Figure 0.1.

1 Fundamentals of Electromagnetics

1.1 Maxwell's Equations

In 1873 Maxwell published "A Treatise on Electricity and Magnetism" [95] and introduced his celebrated system of equations. Until today Maxwell's equations remain one of the corner stones of classical electrodynamics; On a macroscopic level, they can explain virtually all phenomena related to electromagnetism.

In this thesis, we will forgo the derivation of Maxwell's equations from experimental observations since this is explained in great detail in many excellent textbooks, see for example Jackson [80]. Instead we will directly consider the so called macroscopic version of Maxwell's equations where the fields $\boldsymbol{D}$ and $\boldsymbol{H}$) are used to model the behavior of different materials on a microscopic level (see Section 1.1.3).

In this chapter, we will deliberately keep the amount of mathematical machinery down to a minimum and focus on the physical ideas instead. In particular, we will assume that all functions/variables are sufficiently smooth.

1.1.1 Field Variables

We will consider the comprehensive 3D vector calculus formulation of Maxwell's equations which is based on four space-time dependent vector-fields:

- The magnetic induction $\boldsymbol{B}$ (in $\mathrm{V\,s\,m^{-2}}$)
- The (electric) displacement field $\boldsymbol{D}$ (in $\mathrm{A\,s\,m^{-2}}$)
- The electric field $\boldsymbol{E}$ (in $\mathrm{V\,m^{-1}}$)
- The magnetic field $\boldsymbol{H}$ (in $\mathrm{A\,m^{-1}}$)

These fields are generated by (external) sources:

- The scalar valued, free charge density ρ (in $\mathrm{C\,m^{-3}}$)
- The current density $\boldsymbol{j}$ (in $\mathrm{A\,m^{-2}}$)

Here the corresponding SI-units are meter (m), second (s), Volt (V), Ampere (A) and Coulomb (C).

1.1.2 Differential and Integral Formulations

Maxwell's equations can be compactly written in the form of a system of first order Partial Differential Equations (PDE):

$$\begin{cases} \mathbf{curl}\, \boldsymbol{E} + \dfrac{\partial \boldsymbol{B}}{\partial t} = 0, & \text{(1.1a)} \\ \mathbf{curl}\, \boldsymbol{H} - \dfrac{\partial \boldsymbol{D}}{\partial t} = \boldsymbol{j}, & \text{(1.1b)} \\ \operatorname{div} \boldsymbol{D} = \rho, & \text{(1.1c)} \\ \operatorname{div} \boldsymbol{B} = 0. & \text{(1.1d)} \end{cases}$$

The electromagnetic fields $\boldsymbol{E}$, $\boldsymbol{B}$, $\boldsymbol{H}$, and $\boldsymbol{D}$ are the unknowns of the system whereas $\boldsymbol{j}$ and ρ are either given externally and/or can be calculated from the other fields by means of *constitutive relations*, see Section 1.1.3.

The system of differential equations (1.1) is easily recast as integral equations by virtue of Stokes' and Gauss' theorem:

$$\int_{\partial\Sigma} \boldsymbol{E} \cdot \boldsymbol{t}\, \mathrm{d}\ell + \frac{\partial}{\partial t} \int_{\Sigma} \boldsymbol{B} \cdot \boldsymbol{n}\, \mathrm{d}S = 0, \tag{1.2a}$$

$$\int_{\partial\Sigma} \boldsymbol{H} \cdot \boldsymbol{t}\, \mathrm{d}\ell - \frac{\partial}{\partial t} \int_{\Sigma} \boldsymbol{D} \cdot \boldsymbol{n}\, \mathrm{d}S = \int_{\Sigma} \boldsymbol{j} \cdot \boldsymbol{n}\, \mathrm{d}S, \tag{1.2b}$$

$$\int_{\partial\Omega} \boldsymbol{D} \cdot \boldsymbol{n}\, \mathrm{d}S = \int_{\Omega} \rho\, \mathrm{d}V, \tag{1.2c}$$

$$\int_{\partial\Omega} \boldsymbol{B} \cdot \boldsymbol{n}\, \mathrm{d}S = 0. \tag{1.2d}$$

Here Ω is any compact subset of $\mathbb{R}^3$ with piecewise smooth boundary $\partial\Omega$, and Σ is a 2D, compact, orientable, smooth manifold embedded in $\mathbb{R}^3$ with boundary $\partial\Sigma$. Moreover, $\boldsymbol{n}$ denotes the unit normal to the surfaces $\partial\Omega$ and $\partial\Sigma$, $\boldsymbol{t}$ the unit tangent to the curve $\partial\Sigma$, and $\mathrm{d}\ell$, $\mathrm{d}S$, $\mathrm{d}V$ denote the line-, surface-, and volume-element, respectively.

Equations (1.1a), (1.2a) describe *Faraday's law of induction*: A change in the magnetic flux through the surface Σ enclosed by the loop $\partial\Sigma$ induces an electric field $\boldsymbol{E}$ along $\partial\Sigma$. Equations (1.1b), (1.2b) are the *(extended) Ampère's law* which states that a magnetic field is created by an electric current $\boldsymbol{j}$ and/or the *displacement current* $\frac{\partial}{\partial t}\int_{\Sigma} \boldsymbol{D} \cdot \boldsymbol{n}\, \mathrm{d}S$. Note that the displacement current is not an electric current in the traditional sense, i.e. it does not transport charges but still it generates a magnetic field $\boldsymbol{H}$.

Gauss' law (1.1c), (1.2c) describes how electric charges give rise to the electric displacement field $\boldsymbol{D}$ and follows in the static case from Coulomb's law. Finally, the *magnetic Gauss' law* (1.1d) (or (1.2d) in integral form) asserts that there are no magnetic monopoles.

Remark 1.1.1. *Maxwell's equations are compatible with* special relativity *[59]. That is, they take the same form in all inertial frames of reference if time and space, as well as the electromagnetic fields, undergo a Lorentz transformation [80].*

Charge conservation By taking the divergence of Ampère's law (1.1b) and adding the time derivative of Gauss' law (1.1c) we arrive at the continuity equation

$$\frac{\partial \rho}{\partial t} + \operatorname{div} \boldsymbol{j} = 0. \tag{1.3}$$

It expresses the fundamental principle of charge conservation: Electric charges can be neither destroyed nor created.

1.1.3 Constitutive Relations for Linear Materials

Maxwell's equations (1.1) must be complemented with additional relations that establish an explicit dependence between $\boldsymbol{E}$, $\boldsymbol{D}$, $\boldsymbol{j}$, $\boldsymbol{B}$ and $\boldsymbol{H}$. For the empty space (vacuum) these relations are rather simple:

$$\boldsymbol{D} = \epsilon_0 \boldsymbol{E}, \qquad \boldsymbol{B} = \mu_0 \boldsymbol{H}, \qquad \boldsymbol{j} = 0, \tag{1.4}$$

with the two fundamental constants [101]

$$\text{Vacuum permittivity } \epsilon_0 \approx 8.854\,187\,817 \times 10^{-12}\,\mathrm{A\,s\,V^{-1}\,m^{-1}}, \tag{1.5}$$

$$\text{Vacuum permeability } \mu_0 := 4\pi \times 10^{-7}\,\mathrm{V\,s\,A^{-1}\,m^{-1}}. \tag{1.6}$$

By substituting the relations (1.4) into Maxwell's equations (1.1) one obtains the *microscopic Maxwell's equations* which hold universally in all materials on a microscopic scale, i.e. the individual electrons/nuclei must be resolved. Through a careful, spatial averaging [80, Chapter 6.6] of the electromagnetic fields one can derive the *macroscopic Maxwell's equations* which hold on much larger length- and time-scales. In particular, one obtains (neglecting higher order terms) the following *constitutive relations* for the macroscopic (i.e. spatially averaged) electromagnetic fields:

$$\boldsymbol{D} = \epsilon_0 \boldsymbol{E} + \boldsymbol{P}. \qquad \boldsymbol{B} = \mu_0 (\boldsymbol{H} + \boldsymbol{M}). \tag{1.7}$$

Here $\boldsymbol{P}$ is the macroscopic polarization of the bound charges and $\boldsymbol{M}$ is the macroscopic magnetization. Both $\boldsymbol{P}$ and $\boldsymbol{M}$ depend on the underlying material.

For *isotropic linear materials*, we have $\boldsymbol{P} = \epsilon_0 \chi_e \boldsymbol{E}$ and $\boldsymbol{M} = \chi_m \boldsymbol{H}$ with χ_e and χ_m being the electric and magnetic susceptibility, respectively [80, Chapter 4.3]. Consequently, we can rewrite the constitutive relations (1.7) as

$$\boldsymbol{D} = \underbrace{\epsilon_0 \epsilon_r}_{:=\epsilon} \boldsymbol{E}, \qquad \boldsymbol{B} = \underbrace{\mu_0 \mu_r}_{:=\mu} \boldsymbol{H}, \tag{1.8}$$

with $\epsilon_r = (1+\chi_e)$, $\mu_r = (1+\chi_m)$ being the relative permittivity and relative permeability of the material, respectively. The coefficients ϵ and μ are termed permittivity and permeability and can in principle be uniformly positive, space-time dependent functions. For simplicity, we will assume in the rest of this chapter that they are smooth functions in $\mathbb{R}^3$.

Generalized Ohm's law So far, the system of equations (1.1), (1.3) and (1.8) is still underdetermined because there are 18 scalar unknowns but only 15 scalar equations. The missing piece is a generalized version of Ohm's law:

$$\boldsymbol{j} = \sigma(\boldsymbol{E} + \boldsymbol{V} \times \boldsymbol{B}) + \boldsymbol{j}^i. \tag{1.9}$$

Here $\sigma \geq 0$ is the electric conductivity with SI-units $[\sigma] = \mathrm{A\,V^{-1}\,m^{-1}}$. It describes the "mobility" and density of the charge carriers (e.g. electrons). The term $\boldsymbol{E} + \boldsymbol{V} \times \boldsymbol{B}$ describes how the Lorentz forces act upon the charge carriers, with $\boldsymbol{V} : (\boldsymbol{x}, t) \to \mathbb{R}^3$ being the velocity of the underlying material w.r.t. the laboratory frame of reference. We will mostly assume that $\boldsymbol{V} \equiv 0$ except in Section 4.2 where we consider the eddy current problem in a moving frame of reference. Finally, $\boldsymbol{j}^i$ is the externally *impressed* current datum that excites the system.

Remark 1.1.2. *In practice, most materials show the linear behavior of* (1.8)/(1.9) *only for small field strengths and low frequencies (or not at all). In particular the relation between* $\boldsymbol{B}$ *and* $\boldsymbol{H}$ *can be much more complex: For ferromagnetic materials, such as iron, the relationship between* $\boldsymbol{M}$ *and* $\boldsymbol{B}$ *is not only highly non-linear but even depends on the state of the system at previous times (hysteresis). There is a vast number of models that describe this more complex behavior. Interestingly most non-linear relationships without hysteresis can be recast into the form* (1.8)/(1.9) *but with* μ, ϵ, σ *being functions of* $\boldsymbol{B}$ *and* $\boldsymbol{E}$*, respectively.*

Remark 1.1.3. *The simple constitutive relations* (1.8) *and* (1.9) *can be generalized to anisotropic materials by choosing* ϵ, μ, σ *tensor valued.*

Remark 1.1.4. *The constitutive relations are all derived under the assumption that the underlying material is at rest, respectively that the velocity* $\boldsymbol{V}$ *is much smaller than the speed of light and so in particular they do not hold in the same way in a moving frame of reference, cf. Remark 1.1.1, [127, Chapter 7].*

Remark 1.1.5 (Physical units)**.** *To simplify the presentation, we will omit the physical units of all variables in the rest of this thesis which corresponds to nondimensionalization, cf. [91, Section 6.2.3].*

1.2 Quasi-Static Approximation, Eddy Currents

The so-called *eddy current problem* [80, Chapter 5.18] [141] [5] is obtained by dropping the displacement current $\frac{\partial \boldsymbol{D}}{\partial t}$ from Ampère's law (1.1b) and neglecting Gauss' law (1.1c):

$$\begin{cases} \mathbf{curl}\, \boldsymbol{E} + \dfrac{\partial \boldsymbol{B}}{\partial t} = 0, & \text{(1.10a)} \\ \mathbf{curl}\, \boldsymbol{H} = \boldsymbol{j}, & \text{(1.10b)} \\ \operatorname{div} \boldsymbol{B} = 0, & \text{(1.10c)} \end{cases}$$

with the constitutive relations for linear materials being,

$$\boldsymbol{B} = \mu \boldsymbol{H}, \qquad \boldsymbol{j} = \sigma(\boldsymbol{E} + \boldsymbol{V} \times \boldsymbol{B}) + \boldsymbol{j}^i. \tag{1.11}$$

We will see in Sections 2.6 and 4.2 that the eddy current problem (1.10), (1.11) has generally infinitely many solutions $(\boldsymbol{B}, \boldsymbol{E})$. However, all these solutions share the same magnetic induction $\boldsymbol{B}$ and inside conductors ($\sigma > 0$) the electric fields also agree for all of them. It is only inside insulators where the electric field $\boldsymbol{E}$ differs from one solution to the other, i.e. *the electric field $\boldsymbol{E}$ is not well-defined inside insulators.* From all these solutions, it is possible to select one solution that fulfills also the electric Gauss' law (1.1c) inside the insulator for a prescribed ρ, cf. Theorem 2.6.4 for the time-harmonic case. However, inside conductors the free charge density ρ cannot be prescribed. Instead ρ must be calculated in a post-processing step from the solution of the eddy current problem using Gauss' law (1.1c).

Physically, this can be interpreted as follows: the free charges rearrange instantaneously such that $\operatorname{div}(\epsilon \boldsymbol{E}) = \rho$ and $\operatorname{div}(\boldsymbol{j}) = 0$ hold for all times (see below). However, this implies that the continuity Equation (1.3) may be violated by the solution of the eddy current problem (1.10) [88]. In fact, from Ampére's law (1.10b) we have $\operatorname{div} \boldsymbol{j} = 0$. On the other hand, we have $\rho = \operatorname{div}(\frac{\epsilon}{\sigma}\boldsymbol{j}) = \mathbf{grad}(\frac{\epsilon}{\sigma}) \cdot \boldsymbol{j}$. In general, $\frac{\epsilon}{\sigma}$ is not a constant and $\frac{\partial \boldsymbol{j}}{\partial t} \neq 0$, hence $\frac{\partial \rho}{\partial t} \neq 0$. This is in contradiction with the continuity equation (1.3).

In other words: The eddy current problem (1.10) is not compatible with the continuity Equation (1.3). The current density $\boldsymbol{j}$ of the eddy current problem (1.10) cannot explain changes in the free charge density and we cannot interpret $\boldsymbol{j}$ in terms of charge transport [88].

Justification for the Eddy Current Problem Simply put the eddy current problem is a valid approximation of the full Maxwell's equations if the displacement current $\frac{\partial \boldsymbol{D}}{\partial t}$ is small compared to $\mathbf{curl}\, \boldsymbol{H}$ and $\boldsymbol{j}$ (cf. [35]). This is of course *not* the case if the considered problem/apparatus relies on physical phenomena related to the displacement current, such as the propagation of electro-magnetic waves or capacitive effects.

Note that Faraday's law of induction and Ampère's law (without the displacement current) are still included in the eddy current problem. In particular devices such as transformers and processes such as induction hardening are well described by the eddy current problem.

One can make this precise [131, 56, 141, 76, 91] and note that by dropping the displacement current from Maxwell's equations (1.1b) one converts the hyperbolic system of PDE's into a parabolic system of PDE's. In some sense this corresponds to dropping the finite speed of propagation $c = 1/\sqrt{\mu\epsilon}$ and treating the fields as if they propagated instantaneously. Or in other, equivalent words: It is assumed that the system is small compared to the electromagnetic wavelength associated with the dominant time-scale δt of the system: If d is the characteristic length of the system and $\lambda = c\,\delta t$ is the smallest wavelength, then the eddy current approximation is valid if

$$d \ll \lambda = \frac{\delta t}{\sqrt{\mu\epsilon}}.$$

A more careful analysis by Dirks [56] shows that inside conductors it is additionally required that the electric relaxation time τ is much smaller than δt:

$$\tau := \frac{\epsilon}{\sigma} \ll \delta t.$$

Remark 1.2.1. *Instead of dropping the displacement current $\frac{\partial \boldsymbol{D}}{\partial t}$ from Maxwell's equations one can also drop the magnetic inductance $\frac{\partial \boldsymbol{B}}{\partial t}$ from Maxwell's equations [56, 88]. This is usually called the electro-quasi-static approximation which is for example used in the modeling of microelectronic devices [56, 146]. It resembles very much the eddy current problem* (1.10) *but the roles of $\boldsymbol{E}$ and $\boldsymbol{H}$, respectively $\boldsymbol{B}$ and $\boldsymbol{D}$ are switched and the constitutive relations are different.*

1.2.1 Time-Harmonic Regime

Let us assume that the constitutive relations (1.8) and Ohm's law (1.9) hold with ϵ, μ, σ being functions of the space variables only. It is then easy to check that if the excitation $\boldsymbol{j}^i$ is time-harmonic with angular frequency $\omega \geq 0$,

$$\boldsymbol{j}^i(\boldsymbol{x}, t) = \operatorname{Re}\left(\hat{\boldsymbol{j}}^i(\boldsymbol{x}) e^{i\omega t}\right),$$

then all the electromagnetic fields will also be time-harmonic after initial relaxation:

$$\begin{aligned}
\boldsymbol{D}(\boldsymbol{x}, t) &= \operatorname{Re}\left(\hat{\boldsymbol{D}}(\boldsymbol{x}) e^{i\omega t}\right), & \boldsymbol{E}(\boldsymbol{x}, t) &= \operatorname{Re}\left(\hat{\boldsymbol{E}}(\boldsymbol{x}) e^{i\omega t}\right), \\
\boldsymbol{B}(\boldsymbol{x}, t) &= \operatorname{Re}\left(\hat{\boldsymbol{B}}(\boldsymbol{x}) e^{i\omega t}\right), & \boldsymbol{H}(\boldsymbol{x}, t) &= \operatorname{Re}\left(\hat{\boldsymbol{H}}(\boldsymbol{x}) e^{i\omega t}\right), \\
\boldsymbol{j}(\boldsymbol{x}, t) &= \operatorname{Re}\left(\hat{\boldsymbol{j}}(\boldsymbol{x}) e^{i\omega t}\right).
\end{aligned}$$

Here $\hat{\boldsymbol{D}}$, $\hat{\boldsymbol{E}}$, $\hat{\boldsymbol{B}}$, $\hat{\boldsymbol{H}}$, $\hat{\boldsymbol{j}}$, $\hat{\boldsymbol{j}}^{\boldsymbol{i}}$ are all complex valued vector fields in $\mathbb{R}^3$ that solve the *time-harmonic eddy current equations*:

$$\begin{cases}
\operatorname{\mathbf{curl}} \hat{\boldsymbol{E}} + i\omega \hat{\boldsymbol{B}} = 0, & \text{(1.12a)} \\
\operatorname{\mathbf{curl}} \hat{\boldsymbol{H}} = \hat{\boldsymbol{j}}, & \text{(1.12b)} \\
\operatorname{div} \hat{\boldsymbol{B}} = 0. & \text{(1.12c)}
\end{cases}$$

In this thesis, we will always assume that the velocity $\boldsymbol{V} = 0$ for time-harmonic settings. Therefore the constitutive laws simplify to

$$\hat{\boldsymbol{B}} = \mu \hat{\boldsymbol{H}}, \qquad \hat{\boldsymbol{j}} = \sigma \hat{\boldsymbol{E}} + \hat{\boldsymbol{j}}^i.$$

1.3 Electro- and Magnetostatics

If we assume that the electric as well the magnetic field do not vary in time (or if the rate of change is negligible in Equations (1.1a), (1.1b), (1.3)) the time derivatives drop out of Maxwell's equations. The equations then decouple into three systems of first order PDE's that can be solved one after the other.

The Stationary Electric Current Problem for linear materials [1] is obtained from the continuity Equation (1.3) and Faraday's law by dropping the time derivative,

$$\begin{cases} \mathbf{curl}\, \boldsymbol{E} = 0, & \text{(1.13a)} \\ \operatorname{div} \boldsymbol{j} = 0, & \text{(1.13b)} \\ \boldsymbol{j} = \sigma \boldsymbol{E} + \boldsymbol{j}^i. & \text{(1.13c)} \end{cases}$$

We remark that this problem determines the electric field $\boldsymbol{E}$ only inside conductors ($\sigma > 0$). By using the electric Gauss' law (1.1c) we can determine the density of free space charges ρ inside the conductor from the solution of (1.13). This ρ can then in turn be used as the right-hand side of the electrostatic problem (1.14) to calculate the electric field $\boldsymbol{E}$ in all of $\mathbb{R}^3$. Moreover, the total current density $\boldsymbol{j}$ can be used as the right-hand side of the magnetostatic problem (1.15).

Remark 1.3.1 (Stationary Currents). *In principal, stationary currents cannot exist in a static setting because any electric current will decay exponentially to zero with relaxation time $\tau = \epsilon/\sigma$ [91, Section 4.2]. But in practice, one often has the situation where an external device (e.g. a battery) exerts a non-electrostatic force, called the electromotive force, that drives a stationary electric current. This force is modeled by the impressed current density $\boldsymbol{j}^i$.*

The Electrostatic Problem for linear materials is obtained from Faraday's law (1.1a) and Gauss' law (1.1c) by dropping the time derivative,

$$\begin{cases} \mathbf{curl}\, \boldsymbol{E} = 0, & \text{(1.14a)} \\ \operatorname{div} \boldsymbol{D} = \rho, & \text{(1.14b)} \\ \boldsymbol{D} = \epsilon \boldsymbol{E}. & \text{(1.14c)} \end{cases}$$

[1] Clearly, the constitutive law (1.13c) can be modified to account for non-linear and/or non-isotropic materials, cf. Remark 1.1.2.

In comparison to the stationary electric current problem (1.13), the electrostatic problem (1.14) determines the electric field $\boldsymbol{E}$ inside conductors *and insulators* for a given ρ. However, to be consistent with the stationary electric current problem, the free charge density ρ inside conductors must be derived from the solution of problem (1.13) using Gauss' law $\rho = \operatorname{div}(\epsilon \boldsymbol{E})$. Physically this corresponds to the free charges distributing themselves such that $\operatorname{div} \boldsymbol{j} = 0$, cf. [91, Section 2.6].

The Magnetostatic Problem for linear materials is obtained from Ampère's law (1.1b) and the magnetic Gauss' law (1.1d):

$$\begin{cases} \mathbf{curl}\, \boldsymbol{H} = \boldsymbol{j}, & \text{(1.15a)} \\ \operatorname{div} \boldsymbol{B} = 0, & \text{(1.15b)} \\ \boldsymbol{B} = \mu \boldsymbol{H}. & \text{(1.15c)} \end{cases}$$

Taking the divergence of (1.15a) we obtain the continuity equation

$$\operatorname{div} \boldsymbol{j} = 0, \tag{1.16}$$

which is a *compatibility condition* for the external current density $\boldsymbol{j}$. We note that the solution of the stationary electric current problem (1.13) fulfills this compatibility condition and is thus a viable right-hand side for (1.15a).

2 Variational Framework

In the previous chapter, we have seen many systems of Partial Differential Equations (PDE) which we always manipulated under the assumption that the involved functions/fields are smooth enough, but we have tactically omitted the question of solvability; In order to investigate the existence and uniqueness of a solution we need to supplement the PDEs with boundary conditions and define the space(s) in which the solution is sought.

This chapter will first very briefly summarize classical results on Sobolev spaces and the theory of PDEs: Section 2.1 presents the lemma of Lax-Milgram for abstract Hilbert spaces. The following Section 2.2 gives examples of such Hilbert spaces, namely it introduces commonly used Sobolev spaces for domains with Lipschitz boundary. Finally, Section 2.3 sheds some light on the connection between some of these spaces. The next three sections apply the well-known results of the previous Sections to the electrostatic/stationary electric current problem (Section 2.4), the magnetostatic problem (Section 2.5) and the time-harmonic eddy current problem (Section 2.6).

2.1 Abstract Solution Theory

We start our discussion with the abstract concept of *well-posedness* (in the sense of Hadamard):

Definition 2.1.1 (Well-posedness, Hadamard [73]). *A boundary value problem is said to be well-posed if,*

i) A solution to the problem exists.

ii) The solution is unique.

iii) The solution depends continuously on the input data.

Definition 2.1.2 (Sesquilinear Form). *Let H be a Hilbert space. We say that $a : H \times H \to \mathbb{C}$ is a sesquilinear form if a is linear in the first argument and conjugate-linear in the second argument:*

$$a(u_1 + u_2, v) = a(u_1, v) + a(u_2, v), \qquad a(\lambda u, v) = \lambda a(u, v),$$
$$a(u, v_1 + v_2) = a(u, v_1) + a(u, v_2), \qquad a(u, \lambda v) = \overline{\lambda} a(u, v).$$

for all $u, u_1, u_2, v, v_1, v_2 \in H$ *and* $\lambda \in \mathbb{C}$. *Moreover,* a *is said to be bounded/coercive if there are positive real constants* c *and* α *such that*

$$|a(u,v)| \leq c \|u\|_H \|v\|_H \qquad \textit{(Boundedness)}, \tag{2.1}$$

$$|a(u,u)| \geq \alpha \|u\|_H^2 \qquad \textit{(Coercivity)}, \tag{2.2}$$

for all $u, v \in H$.

Lemma 2.1.3 (Lax-Milgram, [104, Lemma 3.1]). *Let* H *be a Hilbert space and* $a(u,v)$ *be a bounded, coercive sesquilinear form in* $H \times H$. *Then for every linear form* $\ell \in H'$ *the problem*

$$\textit{Find } u \in H \textit{ such that } a(v,u) = \ell(v) \textit{ for all } v \in H. \tag{2.3}$$

has a unique solution u *and we have the estimate* $\|u\|_H \leq 1/\alpha \|\ell\|_{H'}$. *Here* α *is the constant from* (2.2).

If the bilinear form a is in addition real valued and symmetric, problem 2.3 can be interpreted as a (energy) minimization problem, cf. [31], [117].

2.2 Function Spaces

2.2.1 Assumptions on the Domain Ω

We begin our discussion with the domain Ω on which we pose our Boundary Value Problem (BVP). Throughout this thesis, we denote by Ω a domain, that is, an open, bounded subset of $\mathbb{R}^d$ with $d = 2, 3$.

The following definition is from Girault and Raviart [69, Definition 1.1]:

Definition 2.2.1 (Lipschitz Domain). *Let* Ω *be a bounded, open subset of* $\mathbb{R}^d$. *We say that its boundary* $\partial\Omega$ *is Lipschitz continuous if for every* $\boldsymbol{x} \in \partial\Omega$ *there exists a neighborhood* $\mathcal{O}$ *of* $\boldsymbol{x}$ *in* $\mathbb{R}^d$ *and new orthogonal coordinates* $\boldsymbol{y} = (\boldsymbol{y}', y_d)$ *where* $\boldsymbol{y}' = (y_1, \ldots, y_{d-1})^T$, *such that:*

i) $\mathcal{O}$ *is a hypercube in the new coordinates:*

$$\mathcal{O} = \{\, \boldsymbol{y} | -a_j < y_j < a_j,\ 1 \leq j \leq d \} \,.$$

ii) There exists a Lipschitz-continuous function ϕ *defined on*

$$\mathcal{O}' = \left\{ \boldsymbol{y}' \middle| -a_j < y_j < a_j,\ 1 \leq j \leq d-1 \right\}$$

with $|\phi(\boldsymbol{y}')| \leq a_d/2$ *for all* $\boldsymbol{y}' \in \mathcal{O}'$ *such that:*

$$\Omega \cap \mathcal{O} = \left\{ \boldsymbol{y} \middle| y_d < \phi\left(\boldsymbol{y}'\right) \right\},$$
$$\partial\Omega \cap \mathcal{O} = \left\{ \boldsymbol{y} \middle| y_d = \phi\left(\boldsymbol{y}'\right) \right\}.$$

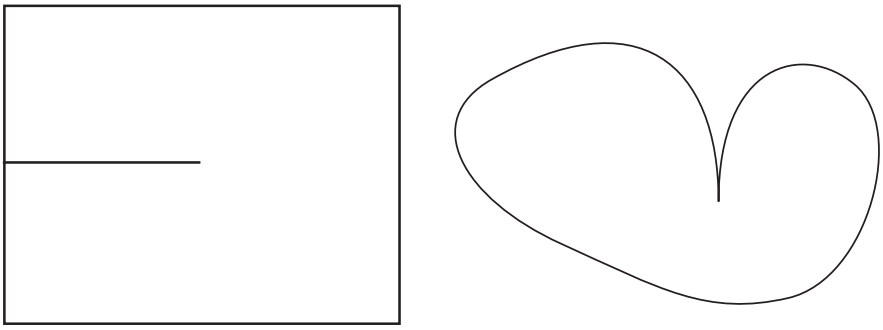

(a) Domain with a slit

(b) Domain with a cusp

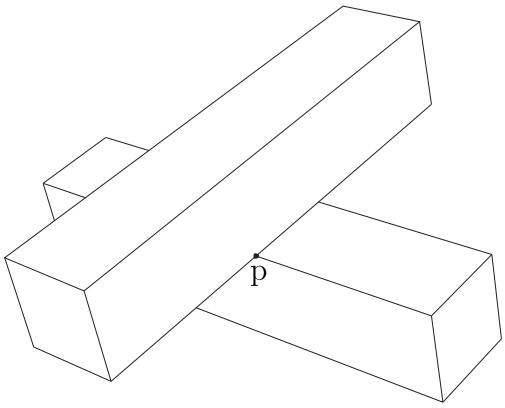

(c) Simple polyhedral domain that is not Lipschitz: One cannot construct an orthogonal coordinate system at point p such that $\mathcal{O} \cap \Omega$ is locally the graph of a function.

Figure 2.1: Three domains that do not posses a Lipschitz boundary.

Essentially this definition states that a Lipschitz domain Ω is locally defined by the graph of a *Lipschitz* function. Polygons (2D) and polyhedrons (3D) are usually Lipschitz but there are a few notable exceptions [96]:

i) The domain Ω cannot be on two sides of boundary, i.e. domains with a slit are not allowed (see Figure 2.1a).

ii) Domains with cusps are not allowed since the function ϕ would not be Lipschitz anymore.

iii) Some less trivial cases in 3D such as the one shown in Figure 2.1c where one cannot represent $\partial\Omega$ as the graph of a function in a neighborhood of the point p.

One important property of Lipschitz domains Ω is that the normal $\boldsymbol{n}$ exists almost everywhere on $\partial\Omega$, i.e. $\boldsymbol{n} \in L^\infty(\partial\Omega)^d$ see [104, Chapter 2, Lemma 4.2], [36].

2.2.2 Standard Sobolev Spaces

Let us start by defining some standard spaces of functions on a domain $\Omega \subset \mathbb{R}^d$ (with the standard norms):

$C^k(\Omega; X)$	The set of k-times continuously differentiable functions with values in X;
$C^{0,1}(\Omega; X)$	The set of Lipschitz continuous functions on Ω;
$C_0^k(\Omega; X)$	The set of k-times continuously differentiable functions with compact support on Ω;
$C^k(\overline{\Omega}; X)$	Set of functions that are k-times continuously differentiable up to the boundary $\partial\Omega$, or equivalently: The restriction of $C_0^k(\mathbb{R}^d)$ to Ω.

$L^p(\Omega; X) \coloneqq \left\{ f : \Omega \to \mathbb{C} |\ f \text{ measurable, } \int_\Omega |f|^p \,\mathrm{d}V < \infty \right\}$;
$L^\infty(\Omega; X) \coloneqq \{ f : \Omega \to \mathbb{C} |\ f \text{ measurable, } \inf \{ C \geq 0 |\ f(x) \leq C \text{ a.e. } \} < \infty \}$

Here X is usually the field of complex numbers $\mathbb{C}$ but can also be the field of real numbers $\mathbb{R}$. Moreover, $k \in \mathbb{N}$ and $1 \leq p < \infty$. If there is no ambiguity we will simplify the notation and drop the space X, i.e. we write $C^k(\Omega)$, $L^p(\Omega)$, etc.

Definition 2.2.2 (Sobolev Space). *Let $\boldsymbol{\alpha} \in \mathbb{N}^d$ be a multi-index with norm $\|\boldsymbol{\alpha}\|_{\ell^1} \coloneqq \sum_{i=1}^d |\alpha_i|$. Furthermore let $s \in \mathbb{N}$ and $1 \leq p \leq \infty$. Then the Sobolev space $W^{s,p}(\Omega)$ on an open set $\Omega \subseteq \mathbb{R}^d$ is defined by*

$$W^{s,p}(\Omega) \coloneqq \{ f \in L^p(\Omega) |\ \mathrm{D}^{\boldsymbol{\alpha}} f \in L^p(\Omega),\ \|\boldsymbol{\alpha}\|_{\ell^1} \leq s \},$$

which we equip with the (semi-)norm

$$\|f\|_{W^{s,p}} \coloneqq \left(\sum_{\|\boldsymbol{\alpha}\|_{\ell^1} \leq s} \|\mathrm{D}^{\boldsymbol{\alpha}} f\|_{L^p}^p \right)^{1/p}, \qquad |f|_{W^{s,p}} \coloneqq \left(\sum_{\|\boldsymbol{\alpha}\|_{\ell^1} = s} \|\mathrm{D}^{\boldsymbol{\alpha}} f\|_{L^p}^p \right)^{1/p}.$$

Furthermore, we define the Hilbert Space *[99]*

$$H^s(\Omega) \coloneqq W^{s,2}(\Omega),$$

which we equip with the inner product

$$(f, g)_{H^s} \coloneqq \sum_{\|\boldsymbol{\alpha}\|_{\ell^1} \leq s} (\mathrm{D}^{\boldsymbol{\alpha}} f, \mathrm{D}^{\boldsymbol{\alpha}} g)_{L^2}.$$

Note that in all expressions above the differential $\mathrm{D}^{\boldsymbol{\alpha}} f$ must be interpreted as a distributional derivative, see [62, Chapter 5] or [96, Chapter 3].

For the definition of the trace spaces we will also need Sobolev spaces with non-integer smoothness coefficient s. We present here the definition due to Slobodeckiĭ, which is however equivalent to the Bessel-Potential definition for Lipschitz domains [96, Theorem 3.18].

Definition 2.2.3 (Sobolev Spaces with non-integer s, [104]). *Let $\Omega \subseteq \mathbb{R}^d$, $1 \leq p < \infty$, $s \geq 0$ be* non-integer*. Then the space $W^{s,p}(\Omega)$ is the subspace of $W^{\lfloor s \rfloor,p}(\Omega)$ such that for $\|\boldsymbol{\alpha}\|_{\ell^1} = \lfloor s \rfloor$*

$$\int_\Omega \int_\Omega \frac{|\mathrm{D}^{\boldsymbol{\alpha}} f(\boldsymbol{x}) - \mathrm{D}^{\boldsymbol{\alpha}} f(\boldsymbol{y})|^p}{|\boldsymbol{x} - \boldsymbol{y}|^{d+p(s-\lfloor s \rfloor)}} \,\mathrm{d}\boldsymbol{x}\,\mathrm{d}\boldsymbol{y} < \infty.$$

Here $\lfloor s \rfloor$ is the biggest integer $\leq s$. The corresponding norm for $W^{s,p}(\Omega)$ is defined as

$$\|f\|_{W^{s,p}} \coloneqq \left(\|f\|^p_{W^{\lfloor s \rfloor,p}} + \sum_{\|\boldsymbol{\alpha}\|_{\ell^1} = \lfloor s \rfloor} \int_\Omega \int_\Omega \frac{|\mathrm{D}^{\boldsymbol{\alpha}} f(\boldsymbol{x}) - \mathrm{D}^{\boldsymbol{\alpha}} f(\boldsymbol{y})|^p}{|\boldsymbol{x} - \boldsymbol{y}|^{d+p(s-\lfloor s \rfloor)}} \,\mathrm{d}\boldsymbol{x}\,\mathrm{d}\boldsymbol{y} \right)^{1/p}.$$

The following gives a characterization of the functions in $W^{s,p}$ in terms of smooth functions:

Theorem 2.2.4 (Global approximation by smooth functions [71, Theorem 1.4.2.1]). *Let $\Omega \subset \mathbb{R}^d$ be a bounded Lipschitz domain, $1 \leq p < \infty$, $s \geq 0$ then $W^{s,p}(\Omega)$ is the closure of $\left\{ f \in C^\infty(\overline{\Omega}) \middle| \ \|f\|_{W^{s,p}} < \infty \right\}$ w.r.t. the norm $\|\cdot\|_{W^{s,p}}$.*

This theorem implies that every $f \in W^{s,p}(\Omega)$ can be approximated by a sequence $\{f_i\}_{i \geq 1} \subset C^\infty(\overline{\Omega})$ such that $f_i \to f$ w.r.t. to the $\|\cdot\|_{W^{s,p}}$ norm. Note that $C_0^\infty(\Omega)$ is generally *not* dense in $W^{s,p}(\Omega)$. This motivates the introduction of the Sobolev space $W_0^{s,p}(\Omega)$.

Definition 2.2.5. *Let $s \geq 0$, $1 \leq p \leq \infty$.*

$$W_0^{s,p}(\Omega) \coloneqq \textit{closure of } C_0^\infty(\Omega) \textit{ in the } W^{s,p}(\Omega) \textit{ norm.}$$

For a fixed p the Sobolev Spaces form a continuous scale of spaces which are embedded in each other:

Lemma 2.2.6 (Sobolev Scale, [104, Chapter 2, Lemma 5.4]). *Let Ω be a bounded Lipschitz domain, and let $p \geq 1$, $s \geq 0$, $0 \leq t < s$. Then $W^{s,p}(\Omega) \hookrightarrow W^{t,p}(\Omega)$.*

Theorem 2.2.7 (Extension Theorem,[71, Theorem 1.4.3.1], [54, Theorem 5.4]). *Let Ω be bounded, Lipschitz and $0 < s \leq 1$, $1 < p < \infty$. There exists a continuous, linear operator $E_s : W^{s,p}(\Omega)$ into $W^{s,p}(\mathbb{R}^d)$ such that*

$$E_s u|_\Omega = u.$$

This theorem holds also for $s \in \mathbb{N}$.

Lemma 2.2.8 ([71, Theorem 1.4.2.4], [96, Section 3]). *Let Ω be a bounded, Lipschitz domain $\Omega \in \mathbb{R}^d$. Then $C_0^\infty(\Omega)$ is dense in $W^{s,p}(\Omega)$ for $0 < s \leq 1/p$.*

In other words: for $0 < s \leq 1/p$ we have $W^{s,p}(\Omega) = W_0^{s,p}(\Omega)$.

2.2.3 Dual Spaces

Definition 2.2.9 ([71, Definition 1.3.2.3]). *For $s < 0$ we denote by $W^{s,p}(\Omega)$ the dual space of $W_0^{-s,q}(\Omega)$ where q is the Hölder conjugate of p, i.e. $1/p + 1/q = 1$.*

In particular, we have $H^{-s}(\Omega) = (H_0^s(\Omega))'$ for $s \geq 0$.

Remark 2.2.10. *Some authors [96] prefer to define $W^{-s,q}(\Omega)$, $s > 0$, to be the dual of the space $\tilde{W}^{s,p}(\Omega) \coloneqq \{f \in W^{s,p}(\Omega) |\ \tilde{f} \in W^{s,p}(\mathbb{R}^d)\}$ where $\tilde{f}$ is the extension of f by zero to $\mathbb{R}^d$. For Lipschitz domains and for $s \notin \{\frac{1}{2}, \frac{3}{2}, \frac{5}{2}, \ldots\}$ the two definitions coincide [96, Theorem 3.33], cf. also our discussion of the space $H_{00}^{1/2}$ below.*

Remark 2.2.11 (Gelfand Triple and Pivot Space). *Considering Theorem 2.2.4 it is clear that the Hilbert spaces $H_0^s(\Omega)$, $L^2(\Omega)$ and $H^{-s}(\Omega)$, $s > 0$, can be densely embedded in each other:*

$$\begin{aligned} \iota_1 :&\quad H_0^s(\Omega) \to L^2(\Omega), &\quad f &\mapsto f, \\ \iota_2 :&\quad L^2(\Omega) \to H^{-s}(\Omega), &\quad f &\mapsto (f, \cdot)_{L^2(\Omega)}. \end{aligned}$$

In other words, we have the Gelfand triple *$H_0^s(\Omega) \subset L^2(\Omega) \simeq L^2(\Omega)' \subset H^{-s}(\Omega)$. By this we mean that with any $f \in H_0^s(\Omega)$ we will naturally associate $\iota_2\iota_1 f \in H^{-s}(\Omega)$ which is defined by the L^2 scalar product. Thus, L^2 is called the* Pivot Space *of the Gelfand triple.*

Alternatively, one could also use the Riesz representation theorem to show that $H_0^s(\Omega)$ is isometrically (anti-)isomorphic to $H^{-s}(\Omega)$ and use this to associate with $f \in H_0^1(\Omega)$ a $f' \in H^{-1}(\Omega)$. We will however not make use of this connection in this work. See also Remark 3 in Chapter 5 of [31] for an instructive example.

Trace Mapping

Let Ω be bounded, Lipschitz so that we can define the trace-map $\gamma_D : C^{0,1}(\Omega) \to C^{0,1}(\partial\Omega)$ by:

$$\gamma_D(f) \coloneqq f|_{\partial\Omega} \tag{2.4}$$

In light of Theorem 2.2.4, a natural question is whether the trace-map γ_D can be extended to Sobolev spaces. The following theorem states the precise condition for such a statement to hold.

Theorem 2.2.12 (Trace theorem for $W^{s,p}$, [102, Theorem 3.9]). *Let Ω be a bounded domain with Lipschitz boundary and let $1/p < s \leq 1$. Then the mapping γ_D defined on $C^\infty(\overline{\Omega})$ by (2.4) has a unique continuous extension as a linear operator, still denoted by γ_D, from $W^{s,p}(\Omega)$ onto $W^{s-1/p,p}(\partial\Omega)$.*

A simple consequence of the above theorem and the open mapping theorem is

Corollary 2.2.13. *Under the assumptions of Theorem 2.2.12 there exists a constant C such that for all $g \in W^{s-1/p,p}(\partial\Omega)$ there exists a* lifting *$\tilde{g} \in W^{s,p}(\Omega)$ with*

$$\gamma_D(\tilde{g}) = g, \qquad \|\tilde{g}\|_{W^{s,p}(\Omega)} \leq C \|g\|_{W^{1-1/s,p}(\partial\Omega)}.$$

Finally, we can characterize $W_0^{s,p}(\Omega)$ as follows:

Theorem 2.2.14 ([71, Theorem 1.5.1.6])**.** *Let $\Omega \subset \mathbb{R}^d$ be a bounded, Lipschitz domain and let $1/p < s \leq 1$. Then we have $W_0^{s,p}(\Omega) = \operatorname{Ker} \gamma_D = \{f \in W^{s,p}(\Omega) | \gamma_D(f) = 0\}$.*

For the case $s = 1$ Theorem 2.2.12 takes the slightly stronger form

Theorem 2.2.15 ([30, Theorem 1.6.6])**.** *Let Ω be a bounded domain with Lipschitz boundary and let $1 \leq p \leq \infty$. Then there is a constant C such that*

$$\|f\|_{L^p(\partial\Omega)} \leq C \|f\|_{L^p(\Omega)}^{1-1/p} \|f\|_{W^{1,p}(\Omega)}^{1/p} \quad \forall f \in W^{1,p}(\Omega).$$

The space $H_{00}^{1/2}(\Omega)$

Since $H_0^1(\Omega)$ is the closure of $C_0^\infty(\Omega)$ w.r.t. $\|\cdot\|_{H^1(\Omega)}$, it is clear that the extension of a function $f \in H_0^1(\Omega)$ by zero to all of $\mathbb{R}^d$, $\tilde{f}$, lies in $H^1(\mathbb{R}^d)$ (cf. Lemma 3.2.6). More generally, Grisvard [71, Corollary 1.4.4.5] shows that the extension of $f \in H_0^s(\Omega)$ by zero to $\mathbb{R}^d$ belongs to $H^s(\mathbb{R}^d)$ if $0 < s < 1$ and $s \neq 1/2$, see also [96, Theorem 3.33]. I.e. the case $s = 1/2$ is a very special corner case which motivates the introduction of the following space:

Definition 2.2.16. *Let $\Omega \subset \mathbb{R}^d$ be a domain with Lipschitz boundary. The space $H_{00}^{1/2}(\Omega)$ contains all functions that can be extended by zero to a function in $H^{1/2}(\mathbb{R}^d)$:*

$$H_{00}^{1/2}(\Omega) \coloneqq \left\{ f \in H^{1/2}(\Omega) |\ \tilde{f} \in H^{1/2}(\mathbb{R}^d) \right\},$$

where $\tilde{f}$ is the extension of f by zero to $\mathbb{R}^d$. The corresponding norm is [71, Corollary 1.4.4.10, Definition 1.3.2.5]

$$\|f\|_{H_{00}^{1/2}(\Omega)}^2 \coloneqq \|f\|_{H^{1/2}(\Omega)}^2 + \int_\Omega \frac{|f(\boldsymbol{x})|^2}{\operatorname{dist}(\boldsymbol{x}; \partial\Omega)} \,\mathrm{d}\boldsymbol{x},$$

where $\operatorname{dist}(\boldsymbol{x}; \partial\Omega)$ is the distance of $\boldsymbol{x}$ to $\partial\Omega$.

See also the books of Lions and Magenes [94, Theorem 11.7] and Tartar [144, Chapter 33] for further insights.

Remark 2.2.17. *In the definition of the Sobolev spaces we have always assumed that Ω is an open set in $\mathbb{R}^d$, so that strictly speaking the space $W^{s-1/p,p}(\partial\Omega)$ is undefined. One can however extend the notion of Sobolev spaces to manifolds in $\mathbb{R}^d$. More precisely, let $\Gamma \subseteq \partial\Omega$ be an open subset of the Lipschitz boundary of a bounded domain Ω. If Γ has itself Lipschitz boundary or if $\partial\Gamma = \emptyset$, then the properties of Sobolev spaces for bounded domains $\Omega \subset \mathbb{R}^d$ with Lipschitz boundary carry over to the Sobolev spaces $H^s(\Gamma)$ and $H_0^s(\Gamma)$ for $|s| \leq 1$. In particular, we have $H_{00}^{1/2}(\partial\Omega) = H^{1/2}(\partial\Omega) = H_0^{1/2}(\partial\Omega)$ since $\partial\Omega$ doesn't have a boundary. This topic is discussed in more detail in [69, Definition 1.4], [96, Chapter 3], [71, Section 1.3.3].*

2.2.4 Sobolev Spaces for Vector Fields

So far, we have only considered the Sobolev spaces $W^{s,p}$ and variants of it. If $p = 2$ and $s = 1$ the space $W^{s,p}(\Omega)$ is the natural domain of definition of the weak gradient operator **grad**. In this section, we will look at Sobolev spaces of vector fields that are the natural domain of definition for the differential operators div and **curl**. Later on, they will help us to extend the well-known Poincaré lemma (see e.g. [52, Part A: Lemma 3]) and the Hodge/Helmholtz decomposition to Sobolev spaces. Most of the material in this section stems from the book by Girault and Raviart [69] which offers a comprehensive introduction into the subject. See also [52], [92].

Sobolev Spaces related to the Divergence Operator

We begin by defining the weak divergence operator:

Definition 2.2.18 (Weak Divergence)**.** *Let $\boldsymbol{A} \in L^2(\Omega)^d$, $d = 2, 3$. We call $g = \operatorname{div} \boldsymbol{A} \in L^2(\Omega)$ the weak divergence (if it exists) of the vector field $\boldsymbol{A}$ if*

$$\int_\Omega g\varphi \,\mathrm{d}V = -\int_\Omega \boldsymbol{A} \cdot \mathbf{grad}\, \varphi \,\mathrm{d}V \qquad \text{for all } \varphi \in C_0^\infty(\Omega).$$

Note that the weak divergence is always unique, if it exists (see [62]). We can now define the natural domain of the operator div for any domain $\Omega \subset \mathbb{R}^d$:

$$\begin{aligned} \boldsymbol{H}(\operatorname{div};\Omega) &\coloneqq \left\{ \boldsymbol{A} \in L^2(\Omega)^d \,\middle|\, \operatorname{div} \boldsymbol{A} \in L^2(\Omega) \right\}, \\ \boldsymbol{H}_0(\operatorname{div};\Omega) &\coloneqq \text{ closure of } C_0^\infty(\Omega)^d \text{ in } \|\cdot\|_{\boldsymbol{H}(\operatorname{div};\Omega)}, \end{aligned}$$

with the norm

$$\|\boldsymbol{A}\|_{\boldsymbol{H}(\operatorname{div};\Omega)} \coloneqq \left(\|\boldsymbol{A}\|_{L^2(\Omega)^d}^2 + \|\operatorname{div} \boldsymbol{A}\|_{L^2(\Omega)}^2 \right)^{1/2}.$$

As with $W^{s,p}(\Omega)$, there is a corresponding density result for $\boldsymbol{H}(\operatorname{div};\Omega)$:

Theorem 2.2.19 (Global approximation by smooth functions [69, Theorem 2.4]). *Let $\Omega \subset \mathbb{R}^d$ have a Lipschitz boundary. The space $C^\infty(\overline{\Omega})^d$ is dense in $\boldsymbol{H}(\mathrm{div};\Omega)$.*

Let us now introduce the natural trace operator

$$\gamma_N(\boldsymbol{A}) \coloneqq \boldsymbol{n} \cdot \boldsymbol{A}|_{\partial\Omega}\,, \tag{2.5}$$

where $\boldsymbol{n}$ is the outer unit normal of the surface $\partial\Omega$. The following is the analogue of the trace theorem 2.2.12 for $\boldsymbol{H}(\mathrm{div};\Omega)$:

Theorem 2.2.20 (Trace theorem for $\boldsymbol{H}(\mathrm{div};\Omega)$, [69, Theorem 2.5, Corollary 2.8]). *Let $\Omega \subset \mathbb{R}^d$ be a bounded domain with Lipschitz boundary. The trace operator γ_N defined on $C^\infty(\overline{\Omega})^d$ by (2.5) can be extended by continuity to a linear and continuous mapping, still denoted by γ_N, from $\boldsymbol{H}(\mathrm{div};\Omega)$ onto $H^{-1/2}(\partial\Omega)$.*

Corollary 2.2.21 (Green's first formula, [69, (2.17)]). *Let Ω be a bounded domain in $\mathbb{R}^d$ with Lipschitz boundary. Then for all $\boldsymbol{v} \in \boldsymbol{H}(\mathrm{div};\Omega)$ and all $\varphi \in H^1(\Omega)$:*

$$\int_\Omega \boldsymbol{v} \cdot \mathbf{grad}\,\varphi \,\mathrm{d}V + \int_\Omega \varphi \,\mathrm{div}\,\boldsymbol{v}\,\mathrm{d}V = \langle \gamma_D(\varphi), \gamma_N(\boldsymbol{v})\rangle_{N,\partial\Omega}\,, \tag{2.6}$$

with the duality product $\langle a,b\rangle_{N,\partial\Omega} \coloneqq \langle a,b\rangle_{H^{1/2}(\partial\Omega),H^{-1/2}(\partial\Omega)}$.

As before we can characterize the space $\boldsymbol{H}_0(\mathrm{div};\Omega)$ by its trace:

Theorem 2.2.22 ([69, Theorem 2.6]). *Let $\Omega \subset \mathbb{R}^d$ be bounded, Lipschitz. We have $\boldsymbol{H}_0(\mathrm{div};\Omega) = \mathrm{Ker}(\gamma_N) = \{\boldsymbol{A} \in \boldsymbol{H}(\mathrm{div};\Omega) | \gamma_N(\boldsymbol{A}) = 0\}$.*

Sobolev Spaces related to the Curl Operator

The weak **curl** operator is defined similarly to the weak div operator:

Definition 2.2.23 (Weak vector valued Curl). *Let $\boldsymbol{A} \in L^2(\Omega)^3$. We call $\boldsymbol{g} = \mathbf{curl}\,\boldsymbol{A} \in L^2(\Omega)^3$ the weak curl (if it exists) of the vector field $\boldsymbol{A}$ if*

$$\int_\Omega \boldsymbol{g} \cdot \boldsymbol{A}'\,\mathrm{d}V = \int_\Omega \boldsymbol{A} \cdot \mathbf{curl}\,\boldsymbol{A}'\,\mathrm{d}V \qquad \text{for all } \boldsymbol{A}' \in C_0^\infty(\Omega)^3.$$

The associated Sobolev spaces on a domain $\Omega \subset \mathbb{R}^3$ are:

$$\begin{aligned}\boldsymbol{H}(\mathbf{curl};\Omega) &\coloneqq \left\{\boldsymbol{A} \in L^2(\Omega)^3 \,\middle|\, \mathbf{curl}\,\boldsymbol{A} \in L^2(\Omega)^3\right\},\\ \boldsymbol{H}_0(\mathbf{curl};\Omega) &\coloneqq \text{ closure of } C_0^\infty(\Omega)^3 \text{ in } \|\cdot\|_{\boldsymbol{H}(\mathbf{curl};\Omega)}\,,\end{aligned}$$

with the (semi-)norm

$$\begin{aligned}\|\boldsymbol{A}\|_{\boldsymbol{H}(\mathbf{curl};\Omega)} &\coloneqq \left(\|\boldsymbol{A}\|^2_{L^2(\Omega)^3} + \|\mathbf{curl}\,\boldsymbol{A}\|^2_{L^2(\Omega)^3}\right)^{1/2},\\ |\boldsymbol{A}|_{\boldsymbol{H}(\mathbf{curl};\Omega)} &\coloneqq \|\mathbf{curl}\,\boldsymbol{A}\|_{L^2(\Omega)^3}\,.\end{aligned}$$

In order to define the curl in $2D$, we first define the $2D$ *cross product*:

Definition 2.2.24 (2D cross product). *The 2D cross product is defined in terms of the 3D cross product: A scalar $u \in \mathbb{C}$ is interpreted as $(0,0,u)^T \in \mathbb{C}^3$ while a vector $\boldsymbol{u} \in \mathbb{C}^2$ is interpreted as $(u_1,u_2,0)^T \in \mathbb{C}^3$. One then computes the 3D cross products between the two 3D vectors and restricts the result back to the 2D setting by the same rules:*

i) If $\boldsymbol{u},\boldsymbol{v} \in \mathbb{C}^2$ then $\boldsymbol{u} \times \boldsymbol{v} \coloneqq u_1 v_2 - u_2 v_1 \in \mathbb{C}$.

ii) If $u \in \mathbb{C}$, $\boldsymbol{v} \in \mathbb{C}^2$ then $u \times \boldsymbol{v} \coloneqq (-uv_2, uv_1)^T \in \mathbb{C}^2$.

iii) If $\boldsymbol{u} \in \mathbb{C}^2$, $v \in \mathbb{C}$ then $\boldsymbol{u} \times v \coloneqq -v \times \boldsymbol{u} \in \mathbb{C}^2$.

Using the notation of the 2D cross product we define the $2D$ *scalar-* and *vector valued* curl as follows [1]:

$$\operatorname{curl} \boldsymbol{A} \coloneqq \boldsymbol{\nabla} \times \boldsymbol{A} = \frac{\partial A_y}{\partial x} - \frac{\partial A_x}{\partial y}, \qquad \mathbf{curl}\, f = \boldsymbol{\nabla} \times f = \begin{pmatrix} \frac{\partial f}{\partial y}, & -\frac{\partial f}{\partial x} \end{pmatrix}^T.$$

The weak version of the scalar- and vector valued 2D curl operators is defined analogously to the 3D case. It will suffice to consider only the Sobolev space for the scalar valued curl,

$$\boldsymbol{H}(\operatorname{curl};\Omega) \coloneqq \left\{ \boldsymbol{A} \in L^2(\Omega)^2 \middle| \operatorname{curl} \boldsymbol{A} \in L^2(\Omega) \right\}.$$

The corresponding (semi-)norms and the space $\boldsymbol{H}_0(\operatorname{curl};\Omega)$ are defined similarly to the 3D case. Note that we will sometimes denote $\boldsymbol{H}(\operatorname{curl};\Omega)$, $\boldsymbol{H}_0(\operatorname{curl};\Omega)$ by $\boldsymbol{H}(\mathbf{curl};\Omega)$ and $\boldsymbol{H}_0(\mathbf{curl};\Omega)$, respectively, in statements that hold for $d = 2, 3$.

Theorem 2.2.25 (Global approximation by smooth functions, [69, Theorem 2.10]). *Let $\Omega \subset \mathbb{R}^d$, be Lipschitz (not necessarily bounded). Then $C^\infty(\overline{\Omega})^d$ is dense in $H(\mathbf{curl};\Omega)$.*

In the following we will characterize the trace space of the 3D $\boldsymbol{H}(\mathbf{curl};\Omega)$ space (i.e. $\Omega \subset \mathbb{R}^3$). Consider the two trace operators

$$\gamma_\tau(\boldsymbol{A}) \coloneqq \boldsymbol{n} \times \boldsymbol{A}|_{\partial\Omega},$$
$$\gamma_\pi(\boldsymbol{A}) \coloneqq (\boldsymbol{n} \times \boldsymbol{A}) \times \boldsymbol{n}|_{\partial\Omega},$$

where $\boldsymbol{n}$ is the outer unit normal of the surface $\partial\Omega$. For smooth enough $\boldsymbol{A}$ and Ω, $\gamma_\pi(\boldsymbol{A})$ is essentially the tangential component of $\boldsymbol{A}$ on the surface $\partial\Omega$: $(\boldsymbol{n}\times\boldsymbol{A})\times\boldsymbol{n} = \boldsymbol{A} - (\boldsymbol{n}\cdot\boldsymbol{A})\boldsymbol{n}$. Similarly, $\gamma_\tau(\boldsymbol{A})$ is $\gamma_\pi(\boldsymbol{A})$ rotated by 90° around $\boldsymbol{n}$: $\boldsymbol{n} \times \boldsymbol{A} = \boldsymbol{n} \times (\boldsymbol{A} - \boldsymbol{n}(\boldsymbol{n} \cdot \boldsymbol{A}))$.

Theorem 2.2.26 (Trace theorem for $\boldsymbol{H}(\mathbf{curl};\Omega)$, [36, Theorem 4.1]). *Let $\Omega \subset \mathbb{R}^3$, be a bounded domain with Lipschitz boundary. The operators γ_τ, γ_π defined on $C^\infty(\overline{\Omega})^3$ can be extended by continuity to linear, continuous, surjective mappings*

$$\gamma_\tau : \boldsymbol{H}(\mathbf{curl};\Omega) \to \boldsymbol{H}^{-1/2}(\operatorname{div}_{\partial\Omega};\partial\Omega), \text{ and}$$
$$\gamma_\pi : \boldsymbol{H}(\mathbf{curl};\Omega) \to \boldsymbol{H}^{-1/2}(\mathbf{curl}_{\partial\Omega};\partial\Omega).$$

[1] For flat surfaces they agree with the general scalar and vectorial surface curl operators from differential geometry [106, Section 2.5.6].

We will not define in detail the range spaces of γ_τ and γ_π because this is very involved for Lipschitz domains (a much easier characterization is possible if Ω convex or of class $C^{1,1}$ [3]). Instead we refer the interested reader to the paper of Buffa et al. [36] for the precise definition. The important point is that $H^{-1/2}(\mathrm{div}_{\partial\Omega};\partial\Omega)$, $\boldsymbol{H}^{-1/2}(\mathbf{curl}_{\partial\Omega};\partial\Omega)$ are continuously embedded in $\boldsymbol{H}^{-1/2}(\partial\Omega)^3$ and that they intrinsically characterize the range spaces of γ_τ, γ_π, respectively, on any set $\partial\Omega$.

Corollary 2.2.27 (Green's second formula, [36, Equation (35)]). *Let $\Omega \subset \mathbb{R}^3$ be bounded with Lipschitz boundary. Then the following Green's formula holds:*

$$(\mathbf{curl}\,\boldsymbol{A}, \boldsymbol{\phi})_{L^2(\Omega)^3} = \langle \gamma_\tau(\boldsymbol{A}), \gamma_\pi(\boldsymbol{\phi})\rangle_{\tau,\partial\Omega} + (\boldsymbol{A}, \mathbf{curl}\,\boldsymbol{\phi})_{L^2(\Omega)^3} \tag{2.7}$$

for all $\boldsymbol{A}, \boldsymbol{\phi} \in \boldsymbol{H}(\mathbf{curl};\Omega)$. The duality product $\langle\cdot,\cdot\rangle_{\tau,\partial\Omega}$ is defined as in [36, Equation (36)] and is an extension of the L^2 inner product.

We remark that for $\boldsymbol{\phi} \in H^1(\Omega)^3$ the duality product

$$\langle \gamma_\tau(\boldsymbol{A}), \gamma_\pi(\boldsymbol{\phi})\rangle_{\tau,\partial\Omega} = \langle \gamma_\tau(\boldsymbol{A}), \gamma_D(\boldsymbol{\phi})\rangle_{H^{-1/2}(\partial\Omega)^3, H^{1/2}(\partial\Omega)^3},$$

where $\gamma_D(\boldsymbol{\phi})$ is the standard trace operator γ_D applied to each component of $\boldsymbol{\phi}$ [69].

Green's second formula also allows us to characterize the space $\boldsymbol{H}(\mathbf{curl};\Omega)$ by tangential continuity:

Proposition 2.2.28 (Characterization of $\boldsymbol{H}(\mathbf{curl};\Omega)$). *Let $\Omega \subset \mathbb{R}^3$ be an open subset with Lipschitz boundary that is split into two non-empty, disjoint open subsets $\overline{\Omega} = \overline{\Omega_1 \cup \Omega_2}$. Furthermore, assume that $\Gamma = \partial\Omega_1 \cap \partial\Omega_2$ has Lipschitz boundary (cf. Remark 2.2.17). Then a function $\boldsymbol{A} \in L^2(\Omega)^3$ with $\boldsymbol{A}|_{\Omega_i} \in \boldsymbol{H}(\mathbf{curl};\Omega_i)$, $i = 1, 2$, belongs to $\boldsymbol{H}(\mathbf{curl};\Omega)$ if and only if*

$$\gamma_\tau\left(\boldsymbol{A}|_{\Omega_1}\right)\big|_\Gamma = -\,\gamma_\tau\left(\boldsymbol{A}|_{\Omega_2}\right)\big|_\Gamma \qquad \text{in } (H_{00}^{1/2}(\Gamma)')^3. \tag{2.8}$$

Here the restriction of $\gamma_\tau(\boldsymbol{A}|_{\Omega_i})$ to Γ is defined by $\langle \gamma_\tau(\boldsymbol{A}|_{\Omega_i})|_\Gamma, \varphi\rangle_{(H_{00}^{1/2}(\Gamma)')^3, H_{00}^{1/2}(\Gamma)^3} := \langle \gamma_\tau(\boldsymbol{A}|_{\Omega_i}), \tilde{\varphi}\rangle_{H^{-1/2}(\partial\Omega_i)^3, H^{1/2}(\partial\Omega_i)^3}$, where $\tilde{\varphi}$ is the extension of φ by zero to $\partial\Omega_i$, $i = 1, 2$.

Proof. Let $\boldsymbol{\varphi} \in C_0^\infty(\Omega)^3$ and use Green's second formula (2.7) to get

$$\begin{aligned}
\int_\Omega \boldsymbol{A}\cdot\mathbf{curl}\,\boldsymbol{\varphi} &= \int_{\Omega_1} \boldsymbol{A}\cdot\mathbf{curl}\,\boldsymbol{\varphi} + \int_{\Omega_2} \boldsymbol{A}\cdot\mathbf{curl}\,\boldsymbol{\varphi},\\
&= \int_{\Omega_1} \mathbf{curl}\,\boldsymbol{A}\cdot\boldsymbol{\varphi} - \langle \gamma_\tau(\boldsymbol{A}|_{\Omega_1}), \gamma_\pi(\boldsymbol{\varphi}|_{\Omega_1})\rangle_{H^{-1/2}(\partial\Omega_1)^3, H^{1/2}(\partial\Omega_1)^3}\\
&\quad + \int_{\Omega_2} \mathbf{curl}\,\boldsymbol{A}\cdot\boldsymbol{\varphi} - \langle \gamma_\tau(\boldsymbol{A}|_{\Omega_2}), \gamma_\pi(\boldsymbol{\varphi}|_{\Omega_2})\rangle_{H^{-1/2}(\partial\Omega_2)^3, H^{1/2}(\partial\Omega_2)^3},\\
&= \int_{\Omega_1} \mathbf{curl}\,\boldsymbol{A}\cdot\boldsymbol{\varphi} - \langle \gamma_\tau(\boldsymbol{A}|_{\Omega_1})|_\Gamma\,,\, \gamma_\pi(\boldsymbol{\varphi}|_{\Omega_1})|_\Gamma\rangle_{(H_{00}^{1/2}(\Gamma)')^3, H_{00}^{1/2}(\Gamma)^3}
\end{aligned}$$

$$+\int_{\Omega_2} \mathbf{curl}\, \boldsymbol{A}\cdot\boldsymbol{\varphi} - \langle \gamma_\tau(\boldsymbol{A}|_{\Omega_2})|_\Gamma\,,\, \gamma_\pi(\boldsymbol{\varphi}|_{\Omega_2})|_\Gamma\rangle_{(H_{00}^{1/2}(\Gamma)')^3, H_{00}^{1/2}(\Gamma)^3}\,. \quad (2.9)$$

In the last step, we have used that $\gamma_\pi(\boldsymbol{\varphi}|_{\Omega_i})|_\Gamma \in H_{00}^{1/2}(\Gamma)$ for $i = 1, 2$. Now if (2.8) holds then (2.9) is just the definition of the weak curl operator and we have $\mathbf{curl}\, \boldsymbol{A} \in L^2(\Omega)^3$. Conversely, if $\boldsymbol{A} \in \boldsymbol{H}(\mathbf{curl}; \Omega)$ the right-hand side of (2.9) must be equal to $\int_\Omega \mathbf{curl}\, \boldsymbol{A}\cdot\boldsymbol{\varphi}$ and hence (2.8) follows. □

Theorem 2.2.29 ([69, Theorem 2.12]). *Let $\Omega \subset \mathbb{R}^d$ be bounded, Lipschitz. We have $\boldsymbol{H}_0(\mathbf{curl}; \Omega) = \mathrm{Ker}(\gamma_\tau) = \{\boldsymbol{A} \in H(\mathbf{curl}; \Omega) |\ \gamma_\tau(\boldsymbol{A}) = 0\}$.*

Remark 2.2.30. *In some parts of this work we will write the dual products formally as integrals:*

$$\langle \gamma_D(\varphi), \gamma_N(\boldsymbol{v})\rangle_{N,\partial\Omega} = \int_{\partial\Omega} \varphi \boldsymbol{n}\cdot\boldsymbol{v},$$
$$\langle \gamma_\tau(\boldsymbol{A}), \gamma_\pi(\boldsymbol{\phi})\rangle_{\tau,\partial\Omega} = \int_{\partial\Omega} (\boldsymbol{n}\times\boldsymbol{A})\cdot\boldsymbol{\phi},$$

they should however always be interpreted as dual products.

2.3 Connection between H^1, $\boldsymbol{H}(\mathbf{curl})$, $\boldsymbol{H}(\mathrm{div})$

In the previous section, we have introduced a zoo of Sobolev spaces related to the operators **grad**, **curl** and div. As it turns out there is an intimate connection in between these spaces that we want to make more explicit in this section.

2.3.1 De Rahm Diagram

An easy way to understand the relation between the different spaces is to consider the *de Rahm diagram* :

$$\mathbb{C} \xrightarrow{\iota} H^1(\Omega) \xrightarrow{\mathbf{grad}} \boldsymbol{H}(\mathbf{curl}; \Omega) \xrightarrow{\mathbf{curl}} \boldsymbol{H}(\mathrm{div}; \Omega) \xrightarrow{\mathrm{div}} L^2(\Omega) \xrightarrow{0} \{0\} \quad (2.10)$$

$$\{0\} \xrightarrow{\iota} H_0^1(\Omega) \xrightarrow{\mathbf{grad}} \boldsymbol{H}_0(\mathbf{curl}; \Omega) \xrightarrow{\mathbf{curl}} \boldsymbol{H}_0(\mathrm{div}; \Omega) \xrightarrow{\mathrm{div}} L^2(\Omega) \xrightarrow{\int_\Omega} \mathbb{C} \quad (2.11)$$

Here ι is the identity map, 0 denotes the zero map and $\int_\Omega : L^2(\Omega) \to \mathbb{C}, f \mapsto \int_\Omega f\,\mathrm{d}V$ denotes the averaging operator. Moreover, if $\Omega \subset \mathbb{R}^3$ is a bounded, contractible domain with Lipschitz boundary we have that (2.10), (2.11) form an *exact sequence. That means that the range of each operator coincides with the kernel of the following operator*, cf. [74, Theorem 3.1], [27], [60], [156].

We will not prove this powerful statement in its full generality because it is not needed for the rest of the thesis. Instead we will present selected results that are special cases of the above exact sequence.

Remark 2.3.1. *In 2D one has the shorter exact sequences*

$$\mathbb{C} \xrightarrow{\iota} H^1(\Omega) \xrightarrow{\mathbf{grad}} \boldsymbol{H}(\mathrm{curl};\Omega) \xrightarrow{\mathrm{curl}} L^2(\Omega) \xrightarrow{0} \{0\},$$
$$\mathbb{C} \xrightarrow{\iota} H^1(\Omega) \xrightarrow{\mathbf{curl}} \boldsymbol{H}(\mathrm{div};\Omega) \xrightarrow{\mathrm{div}} L^2(\Omega) \xrightarrow{0} \{0\},$$

respectively.

Looking at the exact sequence (2.10) we see that the kernel of the curl operator can be characterized by gradient fields:

Theorem 2.3.2 ([69, Theorem 2.9])**.** *Let $\Omega \subset \mathbb{R}^d$ be a bounded, simply-connected domain with Lipschitz boundary, $d = 2, 3$. A function $\boldsymbol{A}$ of $L^2(\Omega)^d$ satisfies*

$$\mathbf{curl}\, \boldsymbol{A} = 0 \text{ in } \Omega$$

iff there exists a function $\varphi \in H^1(\Omega)$ which is unique up to a constant, such that

$$\boldsymbol{A} = \mathbf{grad}\, \varphi.$$

Similarly, we can characterize the kernel of the div operator, cf. (2.11):

Theorem 2.3.3. *Let $\Omega \subset \mathbb{R}^d$, $d = 2, 3$, be a bounded, Lipschitz, simply-connected domain with connected boundary and let $\boldsymbol{A} \in \boldsymbol{H}_0(\mathrm{div};\Omega)$ be such that $\mathrm{div}\, \boldsymbol{A} = 0$.*

i) If $d = 2$ there exists a stream function $\phi \in H^1_0(\Omega)$, unique up to a constant, such that $\boldsymbol{A} = \mathbf{curl}\, \phi$.

ii) If $d = 3$ there exists a unique stream function $\boldsymbol{\phi} \in \boldsymbol{H}_0(\mathbf{curl};\Omega)$ such that $\boldsymbol{A} = \mathbf{curl}\, \boldsymbol{\phi}$ and $\mathrm{div}\, \boldsymbol{\phi} = 0$.

This theorem is proven for $d = 2$ in [69, Corollary 3.1] and for $d = 3$ it is a special case of [69, Theorem 3.6].

Corollary 2.3.4. *In addition to the assumptions of Theorem 2.3.3 assume $d = 3$ and let $\kappa \in L^\infty(\Omega)$ be a uniformly positive coefficient function, i.e. $0 < \kappa_{min} < \kappa < \kappa_{max} < \infty$ almost everywhere. Then there exists a unique stream function $\boldsymbol{\psi} \in \boldsymbol{H}_0(\mathbf{curl};\Omega)$ such that $\boldsymbol{A} = \mathbf{curl}\, \boldsymbol{\psi}$ and $\mathrm{div}(\kappa\boldsymbol{\psi}) = 0$.*

Proof. Let $\boldsymbol{\phi}$ be the vector potential from Theorem 2.3.3. We seek a function $\tilde{\boldsymbol{\phi}} \in \boldsymbol{H}_0(\mathbf{curl};\Omega)$ such that

$$\begin{cases} \mathbf{curl}\, \tilde{\boldsymbol{\phi}} = 0 & \text{in } L^2(\Omega)^3, \quad (2.12a) \\ \mathrm{div}(\kappa\tilde{\boldsymbol{\phi}}) = -\mathrm{div}(\kappa\boldsymbol{\phi}) & \text{in } (\boldsymbol{H}(\mathrm{div};\Omega))'. \quad (2.12b) \end{cases}$$

We can then choose $\psi = \tilde{\boldsymbol{\phi}} + \boldsymbol{\phi}$ in Corollary 2.3.4.

It remains to show that the BVP (2.12) has a unique solution $\tilde{\boldsymbol{\phi}}$: From Theorem 2.3.2 and (2.12a) we can deduce that $\tilde{\boldsymbol{\phi}} = \mathbf{grad}\,\varphi$ with $\varphi \in H^1(\Omega)$. Moreover, since $\gamma_\tau(\mathbf{grad}\,\varphi) = \gamma_\tau(\tilde{\boldsymbol{\phi}}) = 0$, φ cannot not change along $\partial\Omega$, cf. [102, Proof of Corollary 3.51]. Since $\partial\Omega$ is connected and φ is unique up to a constant there must exist a φ with $\gamma_D(\varphi) = 0$. Therefore (2.12) is equivalent to the following variational problem:

$$\begin{cases} \text{Find } \varphi \in H_0^1(\Omega) \text{ subject to} \\ \quad \displaystyle\int_\Omega \kappa\,\mathbf{grad}\,\varphi \cdot \mathbf{grad}\,\varphi'\,\mathrm{d}V = \int_\Omega \kappa\boldsymbol{\phi} \cdot \mathbf{grad}\,\varphi'\,\mathrm{d}V \qquad \text{for all } \varphi' \in H_0^1(\Omega). \end{cases} \tag{2.13}$$

Using the lemma of Lax-Milgram 2.1.3 it is easy to check that this BVP has one and only one solution φ which proves the assertion. □

Remark 2.3.5. *Corollary 2.3.4 still holds if κ is zero in a subset of Ω but the vector potential $\boldsymbol{\psi}$ is no longer unique. To see this split $\overline{\Omega} = \overline{\Omega_0 \sqcup \Omega_\kappa}$ [2] such that $\kappa = 0$ in Ω_0 and note that the same proof applies with one change: The variational formulation (2.13) does not have a unique solution anymore since it is a Poisson equation posed on Ω_κ with mixed, homogeneous Neumann / Dirichlet boundary conditions, cf. Section 2.4.*

A consequence of the projection theorem for Hilbert spaces is the Helmholtz/Hodge type decomposition, see [52, Chapter IX, §1, Proposition 1], [92, Section 8.2]:

Theorem 2.3.6 (Helmholtz/Hodge decomposition of $L^2(\Omega)^d$)**.** *Let $\Omega \subset \mathbb{R}^d$, $d = 2, 3$, be a connected, bounded domain with Lipschitz boundary. Furthermore, let $\kappa \in L^\infty(\Omega)$ be uniformly positive, i.e. $0 < \kappa_{min} \leq \kappa \leq \kappa_{max} < \infty$ almost everywhere. Then we have the orthogonal decompositions*

$$L^2(\Omega)^d = \mathbf{grad}\,H^1(\Omega) \oplus_\kappa \left\{\kappa^{-1}\boldsymbol{f} \middle| \boldsymbol{f} \in \boldsymbol{H}_0(\mathrm{div};\Omega), \mathrm{div}\,\boldsymbol{f} = 0\right\}, \tag{2.14}$$

$$= \mathbf{grad}\,H_0^1(\Omega) \oplus_\kappa \left\{\kappa^{-1}\boldsymbol{f} \middle| \boldsymbol{f} \in \boldsymbol{H}(\mathrm{div};\Omega), \mathrm{div}\,\boldsymbol{f} = 0\right\}. \tag{2.15}$$

Here $\oplus_\kappa$ denotes the orthogonal sum w.r.t. the inner product $(f,g)_{L^2_\kappa(\Omega)} \coloneqq (\kappa f, g)_{L^2(\Omega)}$.

Note that Theorem 2.3.3 can be used to characterize the spaces on the right of (2.15).

2.3.2 Friedrich's Inequalities

The exact sequences (2.10) and (2.11) also imply the existence of so-called Friedrich constants. For example, (2.11) shows that the **grad** operator, defined on $H_0^1(\Omega)$, has an empty kernel and that its range coincides with the kernel of the **curl** operator, i.e. the gradient operator has closed range and thus the **grad** has a bounded inverse, i.e. $\|f\|_{H^1(\Omega)} < C\,\|\mathbf{grad}\,f\|_{L^2(\Omega)^3}$. The following is a more general result of the same principle:

[2] The square cup $\sqcup$ denotes a union of disjoint sets: $Z = X \sqcup Y \Leftrightarrow (Z = X \cup Y) \wedge (X \cap Y = \emptyset)$

Theorem 2.3.7 (Friedrich's inequality for $H^1(\Omega)$, [104, Chapter 1, Theorem 1.9]). *Let $\Omega \subset \mathbb{R}^d$, $d = 2, 3$, be a bounded, connected domain with Lipschitz boundary and let $\Gamma \subseteq \partial\Omega$, $\mathrm{meas}(\Gamma) \neq 0$. Then for all $u \in H^1(\Omega)$ we have*

$$\|u\|_{H^1(\Omega)} \leq C_F \left(\|u\|^2_{L^2(\Gamma)} + |u|^2_{H^1(\Omega)} \right)^{1/2} \tag{2.16}$$

Here the Friedrich constant C_F *depends only on the domain Ω.*

And similarly, for the space $\boldsymbol{H}(\mathbf{curl}; \Omega)$:

Theorem 2.3.8 (Friedrich's inequality for $\boldsymbol{H}(\mathbf{curl})$). *Let $\Omega \subset \mathbb{R}^3$, be a bounded Lipschitz domain and let $\kappa \in L^\infty(\Omega)$ be uniformly positive, i.e. $0 < \kappa_{min} \leq \kappa \leq \kappa_{max} < \infty$. Furthermore, denote by Γ_i, $i \geq 0$, the connected components of $\partial\Omega$. Then for all vector fields $\boldsymbol{A} \in \boldsymbol{H}_0(\mathbf{curl}; \Omega)$ with $\mathrm{div}(\kappa \boldsymbol{A}) \in L^2(\Omega)^3$ we have*

$$\left\| \sqrt{\kappa} \boldsymbol{A} \right\|_{L^2(\Omega)^3} \leq C_{F,\mathbf{curl}} \left(\|\mathbf{curl}\, \boldsymbol{A}\|_{L^2(\Omega)^3} + \|\mathrm{div}(\kappa \boldsymbol{A})\|_{L^2(\Omega)^3} + \sum_{i \geq 1} \left| \langle \gamma_N(\kappa \boldsymbol{A}), 1 \rangle_{N, \Gamma_i} \right| \right). \tag{2.17}$$

with $C_{F,\mathbf{curl}}$ independent of $\boldsymbol{A}$.

The proof of this theorem is usually done by contradiction (see e.g. [102, Corollary 3.51]) and relies on the compact embedding $\boldsymbol{H}_0(\mathbf{curl}; \Omega) \cap \kappa^{-1} \boldsymbol{H}(\mathrm{div}; \Omega) \hookrightarrow L^2(\Omega)^3$, cf. [149], [81], [92] [114] [102, Corollary 3.51]. More recently Pauly [114] has given explicit bounds on the Friedrich's constant:

Theorem 2.3.9 ([114, Theorem 6]). *In addition to the assumptions of Theorem 2.3.8, assume that $\Omega \subset \mathbb{R}^3$ is convex and $\mathrm{div}(\kappa \boldsymbol{A}) = 0$. Then $C_{F,\mathbf{curl}} \leq \sqrt{\kappa_{max}} c_p$ with $c_p \leq \mathrm{diam}(\Omega)/\pi$ being the Poincaré constant (see [114]).*

2.4 Electrostatics, Poisson's Equation

In this section, we will derive the boundary value problem(s) corresponding to the (real valued) electrostatic problem (1.14) and the stationary electric current problem (1.13) from Chapter 1. For the rest of this thesis we will make the following crucial assumption about the material parameters:

Assumption 2.4.1. *The electric permittivity ϵ, the magnetic permeability μ and the conductance σ all lie in $L^\infty(\Omega; \mathbb{R})$ and are uniformly positive and real valued. The conductance σ can be exactly zero. In particular constants exist such that*

$$\begin{aligned} 0 < \epsilon_{min} \leq \epsilon \leq \epsilon_{max} < \infty, \\ 0 < \mu_{min} \leq \mu \leq \mu_{max} < \infty, \\ 0 < \sigma_{min} \leq \sigma \leq \sigma_{max} < \infty \text{ or } \sigma = 0, \end{aligned}$$

almost everywhere.

We start from the observation that both the electrostatic problem, as well as the stationary electric current problem, require $\mathbf{curl}\, \boldsymbol{E} = 0$. Let us assume that $\boldsymbol{E} \in L^2(\Omega;\mathbb{R})^d$, i.e. that the electric field energy $\|\sqrt{\epsilon}\boldsymbol{E}\|^2_{L^2(\Omega)}$ is finite. Assuming that the problem is posed on a simply connected domain Ω, Theorem 2.3.2 implies that

$$\boldsymbol{E} = \mathbf{grad}\, \varphi \text{ with the } \textit{electrostatic potential } \ \varphi \in H^1(\Omega). \tag{2.18}$$

Substituting (2.18) into (1.14b), (1.13b), respectively, gives

$$\operatorname{div}(\epsilon\, \mathbf{grad}\, \varphi) = 0, \qquad\qquad \operatorname{div}(\sigma\, \mathbf{grad}\, \varphi) = 0.$$

Obviously the electrostatic and the stationary electric current problem are very similar in nature; They are both instances of the more general Poisson boundary value problem:

$$\begin{cases} \text{Find } \varphi \in H^1(\Omega) \text{ subject to} & \\ \qquad -\operatorname{div}(\kappa\, \mathbf{grad}\, \varphi) = f & \text{in } L^2(\Omega), \qquad (2.19a)\\ \qquad\qquad \varphi = g_D & \text{on } H^{1/2}(\Gamma_D), \Gamma_D \subset \partial\Omega, \qquad (2.19b)\\ \qquad \kappa\, \mathbf{grad}\, \varphi \cdot \boldsymbol{n} = g_N & \text{on } H^{1/2}_{00}(\Gamma_N)', \Gamma_N \coloneqq \partial\Omega \setminus \overline{\Gamma_D}. \qquad (2.19c) \end{cases}$$

The stationary electric current problem (1.13) amounts to choosing $\kappa = \sigma$, $f \equiv 0$ and thus the *Neumann boundary condition* (2.19c) prescribes the normal component of the electric current density $\sigma\boldsymbol{E} \cdot \boldsymbol{n}$ through Γ_N. Similarly, the electrostatic problem is equivalent to the Poisson problem (2.19) if $\kappa = \epsilon$ and $f = -\rho$. In this case the *Neumann boundary condition* fixes the normal component of the displacement field $\boldsymbol{D}$. Finally, the *Dirichlet boundary condition* (2.19b) prescribes the value of the electric potential φ on Γ_D.

Since $\varphi \in H^1(\Omega)$, the natural space for g_D is $H^{1/2}(\Gamma_D)$. We must assume that the boundary of Γ_D is smooth enough (cf. Remark 2.2.17) such that g_D can be extended to a function in $H^{1/2}(\partial\Omega)$ by Theorem 2.2.7. Using 2.2.13 we can then lift this extension to all of Ω. I.e. we need the following property:

Property 2.4.2 (Lifting). *There is a domain specific constant $\tilde{C}_\Omega$ such that for every $g_D \in H^{1/2}(\Gamma_D)$ there is a lifting $\tilde{g}_D \in H^1(\Omega)$ with $\|\tilde{g}\|_{H^1(\Omega)} \leq \tilde{C}_\Omega \|g\|_{H^{1/2}(\Gamma_D)}$ and $\gamma_D(\tilde{g}_D)|_{\Gamma_D} = g_D$.*

Using the lifting $\tilde{g}_D$ we can enforce the Dirichlet boundary conditions in a *strong sense*, that is we incorporate them into the affine trial space

$$H^1_{0,\Gamma_D}(\Omega) + \{\tilde{g}_D\}.$$

Here the "+" is a Minkowski sum of the lifting $\tilde{g}_D$ and the test space

$$H^1_{0,\Gamma_D}(\Omega) \coloneqq \left\{ \varphi \in H^1(\Omega) \middle|\ \gamma_D(\varphi)|_{\Gamma_D} = 0 \right\}.$$

Note that if the test function $\varphi' \in H^1_{0,\Gamma_D}(\Omega)$ then $\gamma_D(\varphi') \in H^{1/2}_{00}(\Gamma_N)$. We can therefore interpret the Neumann boundary condition with $g_N \in H^{1/2}_{00}(\Gamma_N)'$.

Finally let us assume that $f \in L^2(\Omega)$ so that $\kappa \operatorname{\mathbf{grad}} \varphi \in \boldsymbol{H}(\operatorname{div};\Omega)$. We can then multiply (2.19a) by a test function $\varphi' \in H^1_{0,\Gamma_D}(\Omega)$ and use Green's formula (2.6) to get the variational formulation of (2.19):

Find $\varphi \in (H^1_{0,\Gamma_D}(\Omega) + \{\tilde{g}_D\})$ subject to

$$\int_\Omega \kappa \operatorname{\mathbf{grad}} \varphi \cdot \operatorname{\mathbf{grad}} \varphi' \,\mathrm{d}V = \int_\Omega f\varphi' \,\mathrm{d}V + \left\langle \gamma_D(\varphi'), g_N \right\rangle_{H^{1/2}_{00}(\Gamma_N), H^{1/2}_{00}(\Gamma_N)'} \quad \forall \varphi' \in H^1_{0,\Gamma_D}(\Omega). \tag{2.20}$$

Proposition 2.4.3. *Let Ω be a bounded, Lipschitz domain with boundary $\partial\Omega = \overline{\Gamma_D \sqcup \Gamma_N}$ that has property 2.4.2. Moreover, let $f \in L^2(\Omega)$, $g_N \in H^{1/2}_{00}(\Gamma_N)'$, and $g_D \in H^{1/2}(\Gamma_D)$ be given. Then the variational formulation* (2.20) *is equivalent to the BVP* (2.19)*: If φ is a solution of* (2.19) *then it is also a solution of* (2.20) *and vice versa.*

Proof. We have already shown (2.19) $\Rightarrow$ (2.20) and it remains to show the reverse statement (2.20) $\Rightarrow$ (2.19).

1. Let $\varphi' \in C^\infty_0(\Omega)$, then (2.20) gives $\int_\Omega \kappa \operatorname{\mathbf{grad}} \varphi \cdot \operatorname{\mathbf{grad}} \varphi' \,\mathrm{d}V = \int_\Omega f\varphi' \,\mathrm{d}V$, but this is exactly the definition of the weak div operator so that $-\operatorname{div}(\kappa \operatorname{\mathbf{grad}} \varphi) = f \in L^2(\Omega)$.
2. (2.19b) is clearly satisified.
3. (2.19c) is obtained by applying Green's formula (2.2.21) to (2.20).

□

Theorem 2.4.4. *In addition to the assumptions of Proposition 2.4.3 assume that Ω is connected and $\operatorname{meas}_{\mathbb{R}^{d-1}}(\Gamma_D) > 0$. Then the Poisson problem* (2.19) *(respectively* (2.20)*) is well-posed in the sense of Hadamard (Definition 2.1.1) and we have the estimate*

$$\|\varphi\|_{H^1(\Omega)} \leq \frac{1}{\kappa_{min} C_F} \left(\|f\|_{L^2(\Omega)} + C \|g_N\|_{H^{1/2}_{00}(\Gamma_N)'} + \tilde{C}_\Omega \kappa_{max} \|g_D\|_{H^{1/2}(\Gamma_D)} \right).$$

The constants C_F, C and $\tilde{C}_\Omega$ depend only on the domain Ω.

Proof. Note that the bilinear form $a(\varphi, \varphi') \coloneqq \int_\Omega \kappa \operatorname{\mathbf{grad}} \varphi \cdot \operatorname{\mathbf{grad}} \varphi' \,\mathrm{d}V$ is coercive on the space $H^1_{0,\Gamma_D}(\Omega)$: $a(\varphi,\varphi) \geq \kappa_{\min} |\varphi|^2_{H^1(\Omega)} \geq C_F \kappa_{\min} \|\varphi\|^2_{H^1(\Omega)}$ where we have used the Friedrichs inequality 2.3.7 in the last step.

Moreover, a is clearly bounded: $a(\varphi,\varphi') \leq \kappa_{\max} \|\varphi\|_{H^1} \|\varphi'\|_{H^1}$. We can therefore apply the Lax-Milgram Lemma 2.1.3 with

$$\ell(\varphi') = \left(f, \varphi'\right)_{L^2(\Omega)} + \left\langle g_N, \gamma_D(\varphi') \right\rangle + \left(\kappa \operatorname{\mathbf{grad}} \tilde{g}_D, \operatorname{\mathbf{grad}} \varphi'\right)_{L^2(\Omega)}$$

and get

$$\begin{aligned}\|\varphi\|_{H^1(\Omega)} &\leq \frac{1}{\kappa_{\min} C_F} \sup_{\substack{\varphi' \in H^1_{0,g_D}(\Omega), \\ \varphi' \neq 0}} \frac{\ell(\varphi')}{\|\varphi'\|_{H^1}}, \\ &\leq \frac{1}{\kappa_{\min} C_F} \left(\|f\|_{L^2(\Omega)} + C \|g_N\|_{H^{1/2}_{00}(\Gamma_N)'} + \kappa_{\max} \|\tilde{g}_D\|_{H^1(\Omega)} \right).\end{aligned}$$

In the last step, we have used the Cauchy-Schwarz inequality, the continuity of the duality pairing $\langle \cdot, \cdot \rangle_{H^{1/2}_{00}(\Gamma_N)', H^{1/2}_{00}(\Gamma_N)}$ and the continuity of the trace operator γ_D (see Theorem 2.2.12). Now we use Property 2.4.2 to get the desired result. □

Remark 2.4.5. *If* $\operatorname{meas}(\Gamma_D) = 0$*, it can be shown that the solution* φ *of problem* (2.19) *is unique up to a constant if the compatibility condition*

$$\langle g_N, 1 \rangle_{N, \partial\Omega} + \int_\Omega f \, \mathrm{d}V = 0$$

is fulfilled (cf. (2.20)*). In this case the proof is slightly different, see for example [69, Section 1.4].*

Bibliographical Remarks The solution theory for the Poisson problem is classical, see for example [69]. The case of mixed Dirichlet/Neumann boundary conditions, as we have discussed it here, is much more delicate [144] and is covered in more generality in [63, 134].

2.5 Magnetostatics

In this section, we derive the BVP corresponding to the (real valued) 3D magnetostatic problem (1.15) and show that it is well-posed.

Let $\Omega \subset \mathbb{R}^3$ be a bounded, simply-connected domain with connected, Lipschitz boundary. We will assume that $\boldsymbol{B} \cdot \boldsymbol{n} = \gamma_N(\boldsymbol{B}) = 0$ on $\partial\Omega$ which reflects the decay of the magnetic field far away from the sources.

The magnetic Gauss' law (1.15b) and Theorem 2.3.3 imply the existence of a real valued vector potential $\boldsymbol{A} \in \boldsymbol{H}_0(\mathbf{curl}; \Omega)$ such that $\boldsymbol{B} = \mathbf{curl}\, \boldsymbol{A}$. Using Ampère's law and the relation $\boldsymbol{B} = \mu \boldsymbol{H}$ we arrive at the *ungauged vector potential formulation* of the magnetostatic problem:

$$\begin{cases} \text{Find } \boldsymbol{A} \in \boldsymbol{H}_0(\mathbf{curl}; \Omega) \text{ subject to} \\ \qquad \mathbf{curl}\left(\mu^{-1} \mathbf{curl}\, \boldsymbol{A}\right) = \boldsymbol{j}. \end{cases} \tag{2.21}$$

Note that the $\mathbf{curl} - \mathbf{curl}$ operator has an infinite-dimensional kernel that is spanned by $\mathbf{grad}\, H^1_0(\Omega)$, cf. exact sequence (2.11). Therefore, the above ungauged problem is

clearly ill-posed on the space $\boldsymbol{H}_0(\mathbf{curl};\Omega)$ because the solution $\boldsymbol{A}$ is only unique up to gradient fields. This is somewhat expected since only the **curl** of $\boldsymbol{A}$ has a physical interpretation, but not $\boldsymbol{A}$ itself. We also remark that the Friedrich's inequality (2.17) implies that the non-zero eigenvalues of the $\mathbf{curl}-\mathbf{curl}$ operator are well separated from 0. Hence it is possible to show that problem (2.21) is well-posed on the quotient space $\boldsymbol{H}_0(\mathbf{curl};\Omega)/\,\mathbf{grad}\, H_0^1(\Omega)$ if the right-hand side $\boldsymbol{j}$ fulfills the compatibility condition $\operatorname{div}\boldsymbol{j}=0$. Also, observe that the boundary condition $\gamma_\tau(\boldsymbol{A})=0$ implies automatically $\gamma_N(\mathbf{curl}\,\boldsymbol{A})=\gamma_N(\boldsymbol{B})=0$ (cf. exact sequence property (2.11)).

For the numerical solution of problem (2.21) it is often desirable to have a unique solution $\boldsymbol{A}$: If, again, we start from the magnetic Gauss' law (1.15b), but use Corollary 2.3.4 we get the existence of a *unique* vector potential $\boldsymbol{A}\in\boldsymbol{H}_0(\mathbf{curl};\Omega)$ satisfying

$$\begin{aligned}\boldsymbol{B}&=\mathbf{curl}\,\boldsymbol{A},\\ \operatorname{div}(\mu^{-1}\boldsymbol{A})&=0.\end{aligned}\tag{2.22}$$

This leads to the so-called *Coulomb gauged vector potential formulation* of the magnetostatic problem (1.15):

$$\begin{cases}\text{Find } \boldsymbol{A}\in V:=\left\{\boldsymbol{f}\in\boldsymbol{H}_0(\mathbf{curl};\Omega)\,\middle|\,\operatorname{div}(\mu^{-1}\boldsymbol{f})=0\right\}\text{ subject to}\\ \qquad\qquad\mathbf{curl}\left(\mu^{-1}\,\mathbf{curl}\,\boldsymbol{A}\right)=\boldsymbol{j},\qquad\text{in } L^2(\Omega)^3.\end{cases}\tag{2.23}$$

Here we have incorporated the (artificial) *Coulomb* gauge condition (2.22) into the ansatz space V. We will prove the well-posedness of BVP (2.23) in the next section, cf. Theorem 2.5.2.

2.5.1 Regularization

Solving the problem (2.23) on a computer using a finite dimensional subspace $V_h\subset V$ is often complicated because one cannot easily construct a basis of V_h that fulfills the divergence constraint $\operatorname{div}(\mu^{-1}\boldsymbol{A})=0$.

Usually this problem is resolved by seeking the solution $\boldsymbol{A}$ in the larger space $\boldsymbol{H}_0(\mathbf{curl};\Omega)$ (for which suitable discrete approximation spaces exist) and including the divergence constraint as an additional equation. This additional equation must be balanced by an additional unknown, the Lagrange multiplier ϕ, and one arrives at the mixed problem

$$\begin{cases}\text{Find } \boldsymbol{A}\in\boldsymbol{H}_0(\mathbf{curl};\Omega),\ \phi\in H_0^1(\Omega)\text{ subject to}\\ \qquad\mathbf{curl}\left(\mu^{-1}\,\mathbf{curl}\,\boldsymbol{A}\right)+\mu^{-1}\,\mathbf{grad}\,\phi=\boldsymbol{j}\qquad\text{in } L^2(\Omega)^3,\\ \qquad\operatorname{div}\left(\mu^{-1}\boldsymbol{A}\right)=0\qquad\text{in }\Omega.\end{cases}$$

It is easily proven that the above formulation is equivalent to the BVP (2.23). Its solution can be approximated by *mixed* finite element methods where one seeks the discrete solutions in the discrete approximation spaces $V_h\subset\boldsymbol{H}_0(\mathbf{curl};\Omega)$, $U_h\subset H_0^1(\Omega)$.

Unfortunately, the discrete stability of mixed finite element methods will depend on the choice of the pair V_h, U_h and so must be proven separately for the discrete problem. This is in strong contrast to the Poisson problem (2.20) which is *coercive*. The lovely property of coercivity is that it also holds on subspaces[3]; For the Poisson problem (2.20), this means that any subspace $V_h \subset H^1_{0,\Gamma_D}(\Omega)$ will yield a stable discretization scheme.

With the numerical discretization in mind, we present here a *regularized* magnetostatic problem which is *coercive* and analyze the error due to regularization. More precisely, the regularized magnetostatic problem with regularization parameter $\varepsilon > 0$ reads as:

$$\begin{cases} \text{Find } \boldsymbol{A}^\varepsilon \in \boldsymbol{H}_0(\mathbf{curl};\Omega) \text{ subject to} \\ \qquad \mathbf{curl}\left(\mu^{-1}\,\mathbf{curl}\,\boldsymbol{A}^\varepsilon\right) + \varepsilon\mu^{-1}\boldsymbol{A}^\varepsilon = \boldsymbol{j} \qquad \text{in } L^2(\Omega)^3. \end{cases} \tag{2.25}$$

If we take the divergence of (2.25) and use that $\operatorname{div} \boldsymbol{j} = 0$ (charge conservation) we get that every solution $\boldsymbol{A}^\varepsilon$ fulfills the gauge condition (2.22):

$$\operatorname{div}\left(\mu^{-1}\boldsymbol{A}^\varepsilon\right) = 0 \qquad \text{in } \Omega.$$

So, if $\varepsilon > 0$ the BVP (2.25) is equivalent to

$$\begin{cases} \text{Find } \boldsymbol{A}^\varepsilon \in V \text{ subject to} \\ \mathbf{curl}\left(\mu^{-1}\,\mathbf{curl}\,\boldsymbol{A}^\varepsilon\right) + \varepsilon\mu^{-1}\boldsymbol{A}^\varepsilon = \boldsymbol{j} \qquad \text{in } L^2(\Omega)^3. \end{cases} \tag{2.26}$$

Note that this BVP is also equivalent to the plain magnetostatic problem (2.23) for $\varepsilon = 0$.

Lemma 2.5.1. *Let $\Omega \subset \mathbb{R}^3$ be a bounded, simply-connected domain with connected Lipschitz boundary. Furthermore, let $\boldsymbol{j} \in L^2(\Omega)^3$ such that $\operatorname{div}\boldsymbol{j} = 0$ and let $\varepsilon \geq 0$. Then the (regularized) magnetostatic problem (2.26) is equivalent to the variational formulation*

$$\begin{cases} \textit{Find } \boldsymbol{A}^\varepsilon \in V \textit{ such that for all } \boldsymbol{A}' \in V\textit{:} \\ \displaystyle\int_\Omega \mu^{-1}\,\mathbf{curl}\,\boldsymbol{A}^\varepsilon \cdot \mathbf{curl}\,\boldsymbol{A}'\,\mathrm{d}V + \varepsilon\int_\Omega \mu^{-1}\boldsymbol{A}^\varepsilon\cdot\boldsymbol{A}'\,\mathrm{d}V = \int_\Omega \boldsymbol{j}\cdot\boldsymbol{A}'\,\mathrm{d}V. \end{cases} \tag{2.27}$$

Proof. (2.26) $\Rightarrow$ (2.27): First, we note that if $\boldsymbol{A}^\varepsilon$ is a solution of the BVP (2.26) then multiplication with $\boldsymbol{A}' \in V \subset L^2(\Omega)$ and integration by parts (cf. Green's formula (2.7)) shows that $\boldsymbol{A}^\varepsilon$ is also a solution of (2.27).

(2.27) $\Rightarrow$ (2.26): Showing the reverse is a bit more involved since V is a proper subspace of $L^2(\Omega)$. In the following, let $\boldsymbol{A}^\varepsilon$ be a solution of the variational formulation (2.27). By the density of $\boldsymbol{H}_0(\mathbf{curl};\Omega)$ in $L^2(\Omega)^3$ it suffices to show

$$\left(\mathbf{curl}\left(\mu^{-1}\,\mathbf{curl}\,\boldsymbol{A}^\varepsilon\right), \boldsymbol{A}'\right)_{L^2(\Omega)^3} + \varepsilon\left(\mu^{-1}\boldsymbol{A}^\varepsilon, \boldsymbol{A}'\right)_{L^2(\Omega)^3} = \left(\boldsymbol{j}, \boldsymbol{A}'\right)_{L^2(\Omega)^3} \tag{2.28}$$

[3] See Boffi et al. [24, p. 39] for a (humorous) explanation for why everybody wants coercivity and what this has to do with Cinderella.

for all $\boldsymbol{A}' \in \boldsymbol{H}_0(\mathbf{curl};\Omega)$.

Using $\kappa = \mu^{-1}$ in Theorem 2.3.6 we can split $\boldsymbol{A}' = \mathbf{grad}\,\varphi + \boldsymbol{\phi}$ into $\varphi \in H_0^1(\Omega)$, $\boldsymbol{\phi} \in L^2(\Omega)^3$ such that $\operatorname{div}(\mu^{-1}\boldsymbol{\phi}) = 0$. Moreover, since $\mathbf{grad}\,\varphi, \boldsymbol{A}' \in \boldsymbol{H}_0(\mathbf{curl};\Omega)$ we must have $\boldsymbol{\phi} \in \boldsymbol{H}_0(\mathbf{curl};\Omega)$, i.e. $\boldsymbol{\phi} \in V$.

Using Green's second formula (2.7) on the variational formulation (2.27) we see that (2.28) holds for arbitrary $\boldsymbol{A}' = \boldsymbol{\phi} \in V$. Moreover, (2.28) holds for all $\boldsymbol{A}' = \mathbf{grad}\,\varphi$:

$$\begin{aligned}
\left(\mathbf{curl}\left(\mu^{-1}\,\mathbf{curl}\,\boldsymbol{A}^\varepsilon\right), \mathbf{grad}\,\varphi\right)_{L^2(\Omega)^3} &= 0 \qquad && \text{by Green's second formula (2.7),}\\
\left(\mu^{-1}\boldsymbol{A}^\varepsilon, \mathbf{grad}\,\varphi\right)_{L^2(\Omega)^3} &= 0 && \text{since } \operatorname{div}\left(\mu^{-1}\boldsymbol{A}^\varepsilon\right) = 0 \text{ and}\\
\left(\boldsymbol{j}, \mathbf{grad}\,\varphi\right)_{L^2(\Omega)^3} &= 0 && \text{since } \operatorname{div}\boldsymbol{j} = 0.
\end{aligned}$$

Therefore (2.28) holds for all $\boldsymbol{A}' \in \boldsymbol{H}_0(\mathbf{curl};\Omega)$ and thus by density for all $\boldsymbol{A}' \in L^2(\Omega)^3$. □

Theorem 2.5.2. *Under the assumptions of Lemma 2.5.1, the (regularized) magnetostatic problem* (2.26) *is well posed for all* $\varepsilon \geq 0$ *and we have the a-priori estimate*

$$\left\|\mu^{-1/2}\,\mathbf{curl}\,\boldsymbol{A}^\varepsilon\right\|^2_{L^2(\Omega)^3} + \varepsilon\left\|\mu^{-1/2}\boldsymbol{A}^\varepsilon\right\|^2_{L^2(\Omega)^3} \leq \mu_{max} C^2_{F,\mathbf{curl}}\left\|\mu^{1/2}\boldsymbol{j}\right\|^2_{L^2(\Omega)^3}. \tag{2.29}$$

Proof. Thanks to Lemma 2.5.1 we can apply the lemma of Lax-Milgram 2.1.3 to the variational formulation (2.27):

i) The bilinear form $a^\varepsilon(\boldsymbol{A}^\varepsilon, \boldsymbol{A}') \coloneqq \int_\Omega \mu^{-1}\,\mathbf{curl}\,\boldsymbol{A}^\varepsilon \cdot \mathbf{curl}\,\boldsymbol{A}'\,\mathrm{d}V + \varepsilon\int_\Omega \mu^{-1}\boldsymbol{A}^\varepsilon \cdot \boldsymbol{A}'\,\mathrm{d}V$ of the variational formulation (2.27) is coercive with respect to the energy norm $\|\boldsymbol{A}\|^2_{V,\varepsilon} \coloneqq a^\varepsilon(\boldsymbol{A},\boldsymbol{A})$ with coercivity constant $\alpha = 1$.

ii) Using the Cauchy-Schwarz inequality it is clear that a^ε is bounded, $|a^\varepsilon(\boldsymbol{A},\boldsymbol{A}')| < \|\boldsymbol{A}\|_{V,\varepsilon}\,\|\boldsymbol{A}'\|_{V,\varepsilon}$.

iii) Applying the Lemma of Lax-Milgram 2.1.3 we obtain:

$$\begin{aligned}
\|\boldsymbol{A}^\varepsilon\|_{V,\varepsilon} &\leq \sup_{\substack{\boldsymbol{A}'\in V\\ \boldsymbol{A}'\neq 0}} \frac{\int_\Omega \boldsymbol{j}\cdot\boldsymbol{A}'\,\mathrm{d}V}{\|\boldsymbol{A}'\|_{V,\varepsilon}},\\
&\leq \sup_{\substack{\boldsymbol{A}'\in V\\ \boldsymbol{A}'\neq 0}} \frac{\left\|\mu^{1/2}\boldsymbol{j}\right\|_{L^2(\Omega)^3}\left\|\mu^{-1/2}\boldsymbol{A}'\right\|_{L^2(\Omega)^3}}{\left\|\mu^{-1/2}\,\mathbf{curl}\,\boldsymbol{A}'\right\|_{L^2(\Omega)^3}},\\
&\overset{(2.17)}{\leq} \sqrt{\mu_{\max}} C_{F,\mathbf{curl}}\left\|\mu^{1/2}\boldsymbol{j}\right\|_{L^2(\Omega)^3}.
\end{aligned}$$

□

Note that in the estimate (2.29) we lose the control over $\left\|\mu^{-1/2}\boldsymbol{A}^{\varepsilon}\right\|_{L^2(\Omega)^3}$ as $\varepsilon \to 0$ [4] whereas we can estimate the magnitude of $\mathbf{curl}\,\boldsymbol{A}^{\varepsilon}$ independent of ε. This is all that is needed since only the curl of the vector potential $\boldsymbol{A}^{\varepsilon}$ has a physical interpretation.

Corollary 2.5.3. *Under the assumptions of Lemma 2.5.1, we can bound the relative* **curl** regularization *error as follows:*

$$\frac{\left\|\mu^{-1/2}\,\mathbf{curl}\left(\boldsymbol{A}^{\varepsilon}-\boldsymbol{A}^{0}\right)\right\|_{L^2(\Omega)^3}}{\left\|\mu^{-1/2}\,\mathbf{curl}\,\boldsymbol{A}^{0}\right\|_{L^2(\Omega)^3}} \leq \varepsilon\mu_{max}C^2_{F,\mathbf{curl}}.$$

Moreover, if Ω is convex we have $C_{F,\mathbf{curl}} \leq \mu_{min}^{-1/2}\,\mathrm{diam}(\Omega)/\pi$.

Proof. The proof is a generalization of the one of [120, Lemma 2.1], see also [156, Corollary 3.30]. We subtract (2.23) from (2.26) and get:

$$\mathbf{curl}\left(\mu^{-1}\,\mathbf{curl}\left(\boldsymbol{A}^{\varepsilon}-\boldsymbol{A}^{0}\right)\right)+\varepsilon\mu^{-1}\left(\boldsymbol{A}^{\varepsilon}-\boldsymbol{A}^{0}\right)=-\varepsilon\mu^{-1}\boldsymbol{A}^{0}.$$

We can now apply Theorem 2.5.2 to the above problem and get

$$\begin{aligned}\left\|\mu^{-1/2}\,\mathbf{curl}(\boldsymbol{A}^{\varepsilon}-\boldsymbol{A}^{0})\right\|_{L^2(\Omega)^3} &\leq \varepsilon\sqrt{\mu_{\max}}C_{F,\mathbf{curl}}\left\|\mu^{-1/2}\boldsymbol{A}^{0}\right\|_{L^2(\Omega)^3}\\ &\overset{(2.17)}{\leq} \varepsilon\mu_{\max}C^2_{F,\mathbf{curl}}\left\|\mu^{-1/2}\,\mathbf{curl}\,\boldsymbol{A}^{0}\right\|_{L^2(\Omega)^3},\end{aligned}$$

which proves the inequality. The bound of $C_{F,\mathbf{curl}}$ stems from Theorem 2.3.9 □

Bibliographical notes Reitzinger and Schöberl [120] and Zaglmayer [156] both prove that the regularization error $\|\boldsymbol{A}^{\varepsilon}-\boldsymbol{A}\|$ is proportional to ε for the case $\mu \equiv const.$ Our proof of Corollary 2.5.3 is an extension of this result to formulations based on the (improved) regularization term $\varepsilon\mu^{-1}\boldsymbol{A}$. Moreover, we can give an a-priori bound for the regularization error for convex domains thanks to [114], cf. Theorem 2.3.9.

2.6 Time-harmonic Eddy Current Problem

Let $\Omega \subset \mathbb{R}^3$ be a bounded, Lipschitz, simply-connected domain with connected boundary $\partial\Omega$. We decompose Ω into two open Lipschitz subsets, $\Omega_\sigma = \{\boldsymbol{x} \in \Omega | \sigma(\boldsymbol{x}) \geq \sigma_{\min}\}$ (conductor) and $\Omega_0 = \{\boldsymbol{x} \in \Omega | \sigma(\boldsymbol{x}) = 0\}$ (insulator), such that $\overline{\Omega} = \overline{\Omega_0} \sqcup \overline{\Omega_\sigma}$. Furthermore, we denote by $\{\Gamma_i\}_{i\geq 0}$ the connected components of $\partial\Omega_0$ and we assume that there is only one Γ_0 that is also part of the external boundary $\partial\Omega$, i.e. $\Gamma_i \cap \partial\Omega = \emptyset$ for all $i > 0$.

[4] We could of course use Friedrich's inequality (2.17) to "regain" control over $\left\|\mu^{-1/2}\boldsymbol{A}^{\varepsilon}\right\|_{L^2(\Omega)^3}$.

The 3D, time-harmonic eddy current problem for linear materials reads as, cf. (1.12):

$$\begin{cases} \text{Find } \hat{\boldsymbol{E}} \in \boldsymbol{H}_0(\mathbf{curl};\Omega),\ \hat{\boldsymbol{B}} \in \boldsymbol{H}_0(\mathrm{div};\Omega) \text{ subject to} & \\ \qquad \mathbf{curl}\,\hat{\boldsymbol{E}} + i\omega\hat{\boldsymbol{B}} = 0 & \text{in } L^2(\Omega)^3, \quad (2.30a) \\ \qquad \mathbf{curl}\,\mu^{-1}\hat{\boldsymbol{B}} - \sigma\hat{\boldsymbol{E}} = \hat{\boldsymbol{j}}^i & \text{in } L^2(\Omega)^3, \quad (2.30b) \\ \qquad \mathrm{div}\,\hat{\boldsymbol{B}} = 0 & \text{in } \Omega. \quad (2.30c) \end{cases}$$

Note that we have included the boundary condition $\gamma_\tau(\hat{\boldsymbol{E}}) = 0$ which implies $\gamma_N(\hat{\boldsymbol{B}}) = 0$ (by (2.30a)), which in turn reflects the decay of the magnetic induction $\hat{\boldsymbol{B}}$ far away from the sources $\hat{\boldsymbol{j}}^i$, cf. [35, Proposition 3.1].

Remark 2.6.1. *In practice the constraint $\gamma_\tau(\hat{\boldsymbol{E}}) = 0$ is not a big problem but it is in some sense too restrictive if one only wants to enforce $\gamma_N(\hat{\boldsymbol{B}}) = 0$. One could relax the condition by choosing $\hat{\boldsymbol{E}} \in \boldsymbol{H}_0(\mathbf{curl};\Omega) \oplus \mathbf{grad}\, H^1(\Omega)$ which would allow for more general boundary conditions. However, this introduces an additional unknown and complicates the analysis unnecessarily.*

The eddy current problem (2.30) can be reduced to one unknown: let $\boldsymbol{A} = -\frac{1}{i\omega}\hat{\boldsymbol{E}} \in \boldsymbol{H}_0(\mathbf{curl};\Omega)$. Faraday's law (2.30a) then implies $\hat{\boldsymbol{B}} = \mathbf{curl}\,\boldsymbol{A}$ so that the magnetic Gauss law (2.30c) is automatically fulfilled. Finally, we apply Ampère's law (2.30b) to arrive at the *temporally gauged vector potential formulation*

$$\begin{cases} \text{Find } \boldsymbol{A} \in \boldsymbol{H}_0(\mathbf{curl};\Omega) \text{ subject to} & \\ \qquad \mathbf{curl}\left(\mu^{-1}\,\mathbf{curl}\,\boldsymbol{A}\right) + i\omega\sigma\boldsymbol{A} = \hat{\boldsymbol{j}}^i & \text{in } L^2(\Omega)^3. \quad (2.31) \end{cases}$$

Remark 2.6.2 (Temporal Gauge)**.** *In the physics literature, the more general ansatz $\boldsymbol{E} = -i\omega\boldsymbol{A} - \mathbf{grad}\,\varphi$ is often used. Here $\boldsymbol{A}$ is any vector potential such that $\mathbf{curl}\,\boldsymbol{A} = \boldsymbol{B}$, cf. Theorem 2.3.6. In this case $\boldsymbol{A}$ and φ are the components of the relativistic 4-potential [127] and are not uniquely determined by $\boldsymbol{E}$ and $\boldsymbol{B}$. The* temporal gauge *$\varphi = 0$ fixes $\boldsymbol{A}$ uniquely* for a given *$\boldsymbol{E}$. However, the eddy-current problem determines the electric field $\boldsymbol{E}$ only up to gradient fields inside insulators and hence $\boldsymbol{A}$ is also not unique inside insulators, i.e. the eddy current problem* (2.31) *is in some sense still* ungauged*. This contrasts with the full time-harmonic Maxwell's equations, where the choice $\varphi = 0$ determines $\boldsymbol{A}$ uniquely since $\boldsymbol{E}$ is uniquely defined in the whole domain if $\Omega_\sigma \neq \emptyset$, cf. [102, Chapter 4] .*

We could of course restate (2.31) in terms of $\hat{\boldsymbol{E}}$ (the so-called $\boldsymbol{E}$-formulation) but the above formulation has the advantage that it is stable for $\omega \to 0$:

Proposition 2.6.3. *For $\omega > 0$ the formulations* (2.31) *and* (2.30) *are equivalent if we substitute*

$$\hat{\boldsymbol{E}} = i\omega\boldsymbol{A} \qquad\qquad \hat{\boldsymbol{B}} = \mathbf{curl}\,\boldsymbol{A}.$$

Moreover, if $\omega = 0$ the formulation (2.31) *is equivalent to the magnetostatic problem* (2.21).

The imposed current $\hat{\boldsymbol{j}}^i$ is subject to compatibility conditions: First let $\varphi \in C_0^\infty(\Omega_0)$ and multiply (2.31) with $\mathbf{grad}\,\varphi$ to obtain $\left(\hat{\boldsymbol{j}}^i, \mathbf{grad}\,\varphi\right)_{L^2(\Omega_0)^3} = 0$. Since this holds for arbitrary φ we must have

$$\operatorname{div} \hat{\boldsymbol{j}}^i = 0 \qquad \text{in } L^2(\Omega_0). \tag{2.32}$$

The second compatibility condition is less obvious: Let $\varphi_j \in C^\infty(\overline{\Omega_0})$ be such that $\gamma_D(\varphi_j)|_{\Gamma_i} \equiv \delta_{i,j}$. Now multiply (2.31) with $\mathbf{grad}\,\varphi_j$ and use Green's first/second formula (2.6)/(2.7) to get

$$\sum_i \int_{\Gamma_i} (\boldsymbol{n} \times (\mu^{-1}\,\mathbf{curl}\,\boldsymbol{A})) \cdot \mathbf{grad}\,\varphi_j = \sum_i \int_{\Gamma_i} \varphi_j \boldsymbol{n} \cdot \hat{\boldsymbol{j}}^i - \int_{\Omega_0} \varphi_j \operatorname{div} \hat{\boldsymbol{j}}^i.$$

Now note that φ_j is a constant on every Γ_i and thus the term on the left is zero since $\boldsymbol{n} \times \mathbf{grad}\,\varphi_j = 0$. Therefore, the second compatibility condition on $\hat{\boldsymbol{j}}^i$ is

$$\int_{\Gamma_j} \boldsymbol{n} \cdot \hat{\boldsymbol{j}}^i|_{\Omega_0} = 0 \qquad \text{for all } j \geq 1 \tag{2.33}$$

Let us briefly mention the variational formulation of (2.31):

$$\begin{cases} \text{Find } \boldsymbol{A} \in \boldsymbol{H}_0(\mathbf{curl};\Omega) \text{ such that for all } \boldsymbol{A}' \in \boldsymbol{H}_0(\mathbf{curl};\Omega): \\ \displaystyle\int_\Omega \mu^{-1}\,\mathbf{curl}\,\boldsymbol{A} \cdot \overline{\mathbf{curl}\,\boldsymbol{A}'}\,\mathrm{d}V + i\omega \int_{\Omega_\sigma} \sigma \boldsymbol{A} \cdot \overline{\boldsymbol{A}'}\,\mathrm{d}V = \int_\Omega \hat{\boldsymbol{j}}^i \cdot \overline{\boldsymbol{A}'}\,\mathrm{d}V. \end{cases} \tag{2.34}$$

As in the magnetostatic problem the solution $\boldsymbol{A}$ of the above boundary value problem is not unique in Ω_0. But it is possible to prove, cf. [35, Theorem 3.2], [141, Theorem 2.2], [4]:

Theorem 2.6.4. *Let Ω_σ and Ω_0 be bounded domains with Lipschitz continuous boundary and let $\hat{\boldsymbol{j}}^i \in L^2(\Omega)^3$ fulfill the compatibility conditions* (2.32) *and* (2.33)*. Then the BVP* (2.31) *has a unique solution $\boldsymbol{A} \in \boldsymbol{H}_0(\mathbf{curl};\Omega)$, if we impose*

$$\operatorname{div}(\mu^{-1}\boldsymbol{A}) = 0 \qquad \text{in } \Omega_0, \tag{2.35a}$$

$$\int_{\Gamma_j} \boldsymbol{n} \cdot \left(\mu^{-1}\boldsymbol{A}\right)\big|_{\Omega_0} = 0 \qquad \text{for all } j \geq 1. \tag{2.35b}$$

2.6.1 Regularization

As before for the magnetostatic problem, we also consider the *regularized* time-harmonic eddy current problem

$$\begin{cases} \text{Find } \boldsymbol{A}^\varepsilon \in \boldsymbol{H}_0(\mathbf{curl};\Omega) \text{ subject to} \\ \mathbf{curl}\left(\mu^{-1}\,\mathbf{curl}\,\boldsymbol{A}^\varepsilon\right) + i\omega\sigma\boldsymbol{A}^\varepsilon + \varepsilon\mu^{-1}\chi_{\Omega_0}\boldsymbol{A}^\varepsilon = \hat{\boldsymbol{j}}^i \qquad \text{in } L^2(\Omega)^3. \end{cases} \tag{2.36}$$

Here χ_{Ω_0} is the characteristic function that takes the value 1 in Ω_0 and is zero elsewhere. The corresponding weak formulation is obtained by integrating by parts and reads as

$$\begin{cases} \text{Find } \boldsymbol{A}^\varepsilon \in \boldsymbol{H}_0(\mathbf{curl};\Omega) \text{ subject to} \\ \qquad a^\varepsilon(\boldsymbol{A}^\varepsilon, \boldsymbol{A}') = \left(\hat{\boldsymbol{j}}, \boldsymbol{A}'\right)_{L^2(\Omega)^3} \text{for all } \boldsymbol{A}' \in \boldsymbol{H}_0(\mathbf{curl};\Omega) \end{cases} \tag{2.37}$$

with sesquilinear form

$$a^\varepsilon(\boldsymbol{A}^\varepsilon, \boldsymbol{A}') = \int_\Omega \mu^{-1}\,\mathbf{curl}\,\boldsymbol{A}^\varepsilon \cdot \overline{\mathbf{curl}\,\boldsymbol{A}'} + i\omega \int_{\Omega_\sigma} \sigma \boldsymbol{A}^\varepsilon \cdot \overline{\boldsymbol{A}'} + \varepsilon \int_{\Omega_0} \mu^{-1} \boldsymbol{A}^\varepsilon \cdot \overline{\boldsymbol{A}'}. \tag{2.38}$$

Using the Lax-Milgram Lemma 2.1.3 one easily infers that the regularized problem (2.36)/(2.37) is well-posed for all $\varepsilon > 0$.

Theorem 2.6.5. *Let $\hat{\boldsymbol{j}}^i \in L^2(\Omega)^3$ fulfill the compatibility conditions* (2.32), (2.33) *and let $\boldsymbol{A}^\varepsilon \in \boldsymbol{H}_0(\mathbf{curl};\Omega)$ be the solution of* (2.36)*. Moreover, assume that Ω_σ is a non-empty, compact subset of Ω. Then the a-priori estimate*

$$\|\boldsymbol{A}^\varepsilon\|_{\boldsymbol{H}(\mathbf{curl};\Omega)} \leq C \left\|\hat{\boldsymbol{j}}^i\right\|_{L^2(\Omega)^3}$$

holds with C being independent of ε.

Proof. In this proof, C will be any constant independent of ε and we denote by $\Gamma = \partial\Omega_0 \cap \partial\Omega_\sigma$ the interface between the conductor and insulator. Using the lemma of Lax-Milgram it is easily seen that problem (2.36) has a unique solution $\boldsymbol{A}^\varepsilon$. However, the coercivity constant will depend on ε so that we *cannot* deduce the above a-priori estimate. Hence, we want to show that the sesquilinear form a^ε of (2.38) is coercive with coercivity constant independent of ε, i.e.

$$\left| \left\|\mu^{-1/2}\,\mathbf{curl}\,\boldsymbol{A}^\varepsilon\right\|^2_{L^2(\Omega)^3} + i\omega \left\|\sqrt{\sigma}\boldsymbol{A}^\varepsilon\right\|^2_{L^2(\Omega)^3} + \varepsilon \left\|\mu^{-1/2}\boldsymbol{A}^\varepsilon\right\|^2_{L^2(\Omega)^3} \right| \geq C \left\|\boldsymbol{A}^\varepsilon\right\|^2_{\boldsymbol{H}(\mathbf{curl};\Omega)}.$$

Since $||a| + i\,|b|| \geq \frac{1}{\sqrt{2}}(|a| + |b|)$ it suffices to show

$$\left\|\mu^{-1/2}\,\mathbf{curl}\,\boldsymbol{A}^\varepsilon\right\|^2_{L^2(\Omega)^3} + \omega \left\|\sqrt{\sigma}\boldsymbol{A}^\varepsilon\right\|^2_{L^2(\Omega)^3} \geq C \left\|\boldsymbol{A}^\varepsilon\right\|^2_{\boldsymbol{H}(\mathbf{curl};\Omega)}.$$

We first bound $\|\boldsymbol{A}^\varepsilon\|_{L^2(\Omega_0)^3}$ in the energy norm. For this we split $\boldsymbol{A}^\varepsilon = \boldsymbol{A}_\tau + \mathbf{grad}\,\varphi + \boldsymbol{A}^-$, where

i) $\boldsymbol{A}_\tau \in \boldsymbol{H}(\mathbf{curl};\Omega_0)$ is a lifting of $\gamma_\tau(\boldsymbol{A}^\varepsilon) \in \boldsymbol{H}^{-1/2}(\mathrm{div}_{\partial\Omega_0};\partial\Omega_0)$ such that $\|\boldsymbol{A}_\tau\|_{\boldsymbol{H}(\mathbf{curl};\Omega_0)} \leq C\,\|\gamma_\tau(\boldsymbol{A}^\varepsilon)\|_{\boldsymbol{H}^{-1/2}(\mathrm{div}_{\partial\Omega_0};\partial\Omega_0)} = \|\gamma_\tau(\boldsymbol{A}^\varepsilon)|_\Gamma\|_{\boldsymbol{H}^{-1/2}(\mathrm{div}_\Gamma;\Gamma)}$.

ii) $\varphi \in \mathcal{U} := \{\varphi \in H^1(\Omega_0) |\ \varphi = c_i \text{ on } \Gamma_i\ i \geq 1, \varphi = 0 \text{ on } \Gamma_0\}$ is such that

$$\left(\mu^{-1}\,\mathbf{grad}\,\varphi, \mathbf{grad}\,\varphi'\right)_{L^2(\Omega_0)^3} = \left(\mu^{-1}(\boldsymbol{A}^\varepsilon - \boldsymbol{A}_\tau), \mathbf{grad}\,\varphi'\right)_{L^2(\Omega_0)^3} \quad \text{for all } \varphi' \in \mathcal{U}.$$

Note that $\left(\mu^{-1}\boldsymbol{A}^\varepsilon, \mathbf{grad}\,\varphi'\right)_{L^2(\Omega_0)^3} = 0$ since $\operatorname{div}\left(\varepsilon\mu^{-1}\boldsymbol{A}^\varepsilon\right) = 0$ in $L^2(\Omega_0)$ and $\int_{\Gamma_i} \mu^{-1}\boldsymbol{A}^\varepsilon \cdot \boldsymbol{n} = 0$. Using the lemma of Lax-Milgram together with the Friedrich inequality (2.16) we infer that there is indeed a unique solution φ of the above problem. Setting $\varphi' = \varphi$ we get

$$\left\|\mu^{-1/2}\,\mathbf{grad}\,\varphi\right\|^2_{L^2(\Omega_0)^3} \leq \left\|\mu^{-1/2}\boldsymbol{A}_\tau\right\|_{L^2(\Omega_0)^3} \left\|\mu^{-1/2}\,\mathbf{grad}\,\varphi\right\|_{L^2(\Omega_0)^3}.$$

iii) $\boldsymbol{A}^- := \boldsymbol{A}^\varepsilon - \boldsymbol{A}_\tau - \mathbf{grad}\,\varphi$. Since $\mathbf{grad}\,\varphi \in \boldsymbol{H}_0(\mathbf{curl};\Omega_0)$, $\boldsymbol{A}^- \in \boldsymbol{H}_0(\mathbf{curl};\Omega_0)$ and we have

$$\int_{\Omega_0} \mu^{-1}\boldsymbol{A}^- \cdot \mathbf{grad}\,\varphi' = \int_{\Omega_0} \mu^{-1}(\boldsymbol{A}^\varepsilon - \boldsymbol{A}_\tau - \mathbf{grad}\,\varphi) \cdot \mathbf{grad}\,\varphi' = 0 \text{ for all } \varphi' \in \mathcal{U}.$$

Integration by parts shows that $\int_{\Gamma_i} \mu^{-1}\boldsymbol{A}^- \cdot \boldsymbol{n} = 0$ and $\operatorname{div}\mu^{-1}\boldsymbol{A}^- = 0$ in $L^2(\Omega_0)$. Therefore, we can use the Friedrich inequality (2.17) to deduce $\|\boldsymbol{A}^-\|_{L^2(\Omega_0)^3} \leq C\,\|\mathbf{curl}\,\boldsymbol{A}^-\|_{L^2(\Omega_0)^3}$.

Combining all these results we get:

$$\begin{aligned}
\|\boldsymbol{A}^\varepsilon\|_{L^2(\Omega_0)^3} &\leq \|\boldsymbol{A}_\tau\|_{L^2(\Omega_0)^3} + \|\mathbf{grad}\,\varphi\|_{L^2(\Omega_0)^3} + \left\|\boldsymbol{A}^-\right\|_{L^2(\Omega_0)^3} \\
&\leq C(\|\boldsymbol{A}_\tau\|_{L^2(\Omega_0)^3} + \left\|\mathbf{curl}\,\boldsymbol{A}^-\right\|_{L^2(\Omega_0)^3}) \\
&\leq C(\|\boldsymbol{A}_\tau\|_{L^2(\Omega_0)^3} + \|\mathbf{curl}\,\boldsymbol{A}_\tau\|_{L^2(\Omega_0)^3} + \|\mathbf{curl}\,\boldsymbol{A}^\varepsilon\|_{L^2(\Omega_0)^3}) \\
&\leq C(\|\,\gamma_\tau(\boldsymbol{A}^\varepsilon)|_\Gamma\|_{\boldsymbol{H}^{-1/2}(\operatorname{div}_\Gamma;\Gamma)} + \|\mathbf{curl}\,\boldsymbol{A}^\varepsilon\|_{L^2(\Omega_0)^3}).
\end{aligned}$$

Finally, using $\|\,\gamma_\tau(\boldsymbol{A}^\varepsilon)|_\Gamma\|_{\boldsymbol{H}^{-1/2}(\operatorname{div}_\Gamma;\Gamma)} \leq C\,\|\boldsymbol{A}^\varepsilon\|_{\boldsymbol{H}(\mathbf{curl};\Omega_\sigma)}$ we can bound

$$\|\boldsymbol{A}\|_{L^2(\Omega)^3} \leq C\left(\|\mathbf{curl}\,\boldsymbol{A}\|_{L^2(\Omega_0)^3} + \|\boldsymbol{A}\|_{\boldsymbol{H}(\mathbf{curl};\Omega_\sigma)}\right)$$

which shows that $a^\varepsilon(\boldsymbol{A}, \boldsymbol{A}')$ is coercive with a constant independent of ε. □

Remark 2.6.6. *The assumption that Ω_σ is strictly contained in Ω can probably be dropped. In fact, if $\partial\Omega_0$ and $\partial\Omega_\sigma$ are of class $C^{1,1}$ one can use the techniques of [3], [4] to restrict/extend $\gamma_\tau(\boldsymbol{A}^\varepsilon)$ to Γ. Similarly, if Ω_0 and Ω_σ are Lipschitz polyhedrons one can use the techniques of [33]. If one assumes only Lipschitz continuity of the boundary the situation is much more complicated, [36].*

An immediate corollary of the above Theorem 2.6.5 is:

Corollary 2.6.7. *Let $\boldsymbol{A}^0 \in \boldsymbol{H}_0(\mathbf{curl};\Omega)$ be the solution of (2.31) such that (2.35) hold and let $\boldsymbol{A}^\varepsilon$ be the solution of the regularized problem (2.36). Under the assumptions of Theorem 2.6.5, we can then bound the relative regularization error as follows:*

$$\frac{\left\|\boldsymbol{A}^\varepsilon - \boldsymbol{A}^0\right\|_{\boldsymbol{H}(\mathbf{curl};\Omega)}}{\left\|\boldsymbol{A}^0\right\|_{\boldsymbol{H}(\mathbf{curl};\Omega)}} \leq C\varepsilon.$$

Here C is independent of $\hat{\boldsymbol{j}}^i$ and ε.

Remark 2.6.8. *In contrast to Corollary 2.5.3 we cannot give an upper bound for the constant C of Corollary 2.6.7: A careful inspection of the proof of Theorem 2.6.5 reveals that C depends on the Friedrich inequality constant $C_{F,\mathbf{curl}}$ of the insulator Ω_0. Since Ω_0 is usually not convex we cannot apply Theorem 2.3.9.*

Proof. The proof is analogue to the one of Corollary 2.5.3 and is left out for brevity. □

Bibliographical notes The regularized magnetostatic/eddy current problem is also considered by [156], [120], [89], [133] to obtain a coercive, discrete Galerkin matrix. Bachinger et al. [14] present a result like Corollary 2.6.7 but their proof seems to be erroneous: Lemma 30 in [14] claims that $\boldsymbol{A}^\varepsilon$ is divergence free, i.e. $\operatorname{div} \boldsymbol{A}^\varepsilon = 0$ which is clearly wrong if $\operatorname{meas}(\Omega_\sigma) > 0$.

There are also many other ways to deal with the non-uniqueness of the vector potential $\boldsymbol{A}$:

- One can discretize directly the temporally gauged formulation (2.31) and solve the resulting, singular system of equations if the discrete right-hand side $\boldsymbol{j}^i$ lies in the range of the system matrix. In particular, if (2.31) is discretized using Nedelec's edge elements (Section 3.4.3) the latter can be asserted and yields a stable method [141]. The singular system is usually solved by the Conjugate Gradient (CG) or BiCGSTAB method [141, 84], possibly using the regularized magnetostatic/eddy current problem as a preconditioner [17].

- One can impose the constraint $\operatorname{div} \mu^{-1}\boldsymbol{A} = 0$ directly in a mixed formulation [147]. This introduces additional Lagrange multipliers and leads to a discrete saddle-point problem. Moreover, it is not straightforward to prove discrete stability if enriched approximation spaces are used (Chapter 5).

- The constraint $\operatorname{div} \mu^{-1}\boldsymbol{A}$ can also be incorporated directly into the approximation space by means of so-called tree-cotree techniques [6]. According to Sterz [141] the conditioning of the system matrix depends heavily on the construction of the tree. Alternatively, one can just enforce the constraint $\operatorname{div} \boldsymbol{A} = 0$ on the higher-order, interior (bubble) shape functions and use the regularized formulation (2.36) for the remaining shape-functions [156].

- One can "ellipticize" the eddy current/magnetostatic problem by adding an additional **grad** div term to (2.31)/(2.21). However, this requires that $\boldsymbol{A} \in X_N \coloneqq \boldsymbol{H}_0(\mathbf{curl};\Omega) \cap \boldsymbol{H}(\mathrm{div};\Omega)$ and hence the X_N conforming approximation space must be normally and tangentially continuous across interfaces, i.e. the discrete spaces are contained in $H^1(\Omega)^3 \cap \boldsymbol{H}_0(\mathbf{curl};\Omega)$. This may lead to perilous, spurious solutions because $H^1(\Omega)^3 \cap \boldsymbol{H}_0(\mathbf{curl};\Omega)$ can be a *closed* subspace of X_N. This is for example the case if Ω has reentrant corners [48]. So, if $\boldsymbol{A} \notin H^1(\Omega)^3 \cap \boldsymbol{H}_0(\mathbf{curl};\Omega)$ the discrete approximation will not be able to approximate $\boldsymbol{A} \in X_N$. Nevertheless, one observes convergence since $H^1(\Omega)^3 \cap \boldsymbol{H}_0(\mathbf{curl};\Omega)$ is closed, but the discrete solutions convergence to the *wrong solution*. See the dissertation of Schneebeli [132] for a numerical example. This issue has been overcome by Costabel and Dauge [48] by a suitable weighting of the **grad** div term near singularities.

3 Discontinuous Galerkin Method

In the previous chapter, we have introduced the variational formulations of the electro/magneto-static problem and of the time-harmonic eddy current problem. We will now present a way to discretize these equations by means of the Discontinuous Galerkin (DG) method. As we will show DG can be seen as a generalization of the well-known Finite Element Method (FEM) to approximation spaces which are discontinuous across element boundaries. In particular, the discontinuous approximation spaces are not subsets of the Sobolev spaces $H^1(\Omega)$, $\boldsymbol{H}(\mathbf{curl};\Omega)$ anymore, i.e. they are *non-conforming*.

Note that the (regularized) magnetostatic problem (2.27), the (regularized) eddy current problem (2.37) as well as the Poisson equation are all coercive. Thus, if the approximation spaces are conforming, one can just pose the variational formulations presented in the previous chapter on the discrete approximation space to arrive at a (discrete) stable method.

Unfortunately, this does not immediately carry over to *non-conforming* approximation spaces. Instead we must supplement the variational formulations with additional terms to achieve discrete stability.

On the other hand, being able to use discontinuous basis functions gives a lot of flexibility which we will exploit in the following two chapters: In Chapter 4, we will construct polynomial approximation spaces on *non-conforming meshes* and in Chapter 5 we will *enrich* standard polynomial spaces with functions tailored to the problem to improve the approximation properties. In both cases the basis functions are naturally discontinuous and can be easily handled by DG.

Probably the simplest DG-formulation is the so-called Symmetric Interior Penalty (SIP) method introduced by Nitsche [108], see also [8]. Here the continuity is enforced by *penalizing* jumps over the mesh faces. In this work, we consider mostly the SIP method and variants of it, such as the Non-symmetric Interior Penalty (NIP) introduced by Rivière et al. [122], the method by Oden et al. [110] as well as the weighted interior penalty method by Dryja [57].

This chapter sets the theoretical foundation for the following two Chapters 4 and 5: Section 3.1 introduces and characterizes (sequences of) meshes which we will use to discretize the domain Ω. Based on this we introduce "broken" Sobolev spaces on a mesh in Section 3.2 and use them to define the symmetric/non-symmetric interior penalty method for a very general class of approximation spaces in Section 3.3. Sections 3.4

and 3.5 discuss the case of polynomial approximation spaces and present interpolation estimates.

3.1 Meshes

A mesh $\mathcal{T}_h$ of a domain $\Omega \in \mathbb{R}^d$ is a partition of Ω into a finite number of open subsets T_i (the elements of the mesh) such that $\overline{\Omega} = \overline{\bigsqcup_i T_i}$. The mesh-width h is defined as $h \coloneqq \max_{T \in \mathcal{T}_h} h_T$ with $h_T \coloneqq \operatorname{diam}(T)$ being the diameter of element T.

In this work, we will always assume that every mesh element $T \in \mathcal{T}_h$ is the image of a reference element $\hat{T}$ under a smooth, bijective transformation $\Phi_T : \hat{T} \to T$. This mapping is assumed to be non-degenerate: the $\det(\mathrm{D}\Phi_T)$ is strictly positive in $\hat{T}$, but not necessarily on $\partial\hat{T}$ [1]. We classify the types of meshes based on the reference elements $\hat{T}$:

Definition 3.1.1 (Simplicial Mesh). *$\mathcal{T}_h$ is called a* simplicial mesh *if for every element $T \in \mathcal{T}_h$ there is a smooth, bijective transformation Φ_T which maps the unit d-simplex onto the mesh element T.*

So, if $d = 2$ a simplicial mesh can contain only triangular elements whereas in 3D it can contain only tetrahedrons. One can relax this condition and allow also other element types:

Definition 3.1.2 (Hybrid Mesh). *$\mathcal{T}_h$ is called a* hybrid mesh *if*

- *$d = 2$ and every $T \in \mathcal{T}_h$ is the image of either the reference triangle or quadrilateral, or*
- *$d = 3$ and every $T \in \mathcal{T}_h$ is the image of the reference tetrahedron, pyramid, triangular prism or hexahedron (cf. Figure 3.1).*

Clearly every simplicial mesh is a hybrid mesh. Also, note that the notion of a hybrid mesh can be extended to arbitrary dimensions using a recursive definition, cf. [109, Section A.1]. Moreover, the above definition allows for *curved elements*, the contrary of which is an affine mesh:

Definition 3.1.3 (Affine mesh). *A mesh element $T \in \mathcal{T}_h$ is called affine if its mapping $\Phi_T : \hat{T} \to T$ is an affine mapping. An* affine mesh *is a mesh where all elements are affine.*

Note that an affine mesh is also a polyhedral mesh, i.e. the faces of each element are planar.

[1] Namely, for the pyramid, we will use a mapping where $\mathrm{D}\Phi_T$ is multi-valued at the top corner, cf. [18] and Chapter 6.

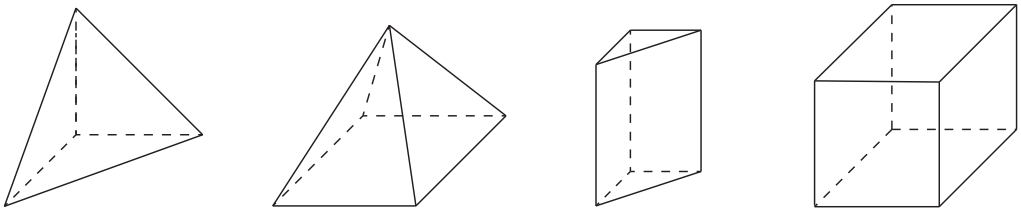

(a) Tetrahedron (b) Pyramid (c) Prism (d) Hexahedron

Figure 3.1: 3D, hybrid reference elements.

Mesh Faces Let T be an element of a hybrid mesh $\mathcal{T}_h$. We define $\mathbb{F}_T$ to be the set of $d-1$ dimensional facets of a mesh element $T \in \mathcal{T}_h$. For example, a hexahedral element has 6 quadrilateral facets whereas a tetrahedral element has 4 triangular facets. The (non-empty) intersection of two facets is called an *inner face* while the (non-empty) intersection of a facet with the boundary $\partial\Omega$ is called a *boundary face*. Note that in a 3D hybrid mesh facets are always a triangle or quadrilateral but the (non-empty) intersection of two (affine) facets is a convex polygon with up to 8 nodes. We define the following sets of faces:

$$
\begin{aligned}
\mathcal{F}_h^b &\coloneqq \text{Set of boundary faces in } \mathcal{T}_h,\\
\mathcal{F}_h^i &\coloneqq \text{Set of inner faces in } \mathcal{T}_h,\\
\mathcal{F}_h &\coloneqq \mathcal{F}_h^b \cup \mathcal{F}_h^i,\\
\mathcal{F}_T &\coloneqq \text{Set of all faces that lie on the boundary of a mesh element } T.
\end{aligned}
$$

Definition 3.1.4 (Conforming mesh)**.** *A hybrid mesh $\mathcal{T}_h$ is said to be* conforming*/matching if every $F \in \mathcal{F}_h^i$ is a facet of exactly two elements in $\mathcal{T}_h$.*

Note that a conforming mesh cannot have *hanging nodes*.

Definition 3.1.5 (k-irregular mesh)**.** *A mesh $\mathcal{T}_h$ is* k-irregular *if*

i) every inner face $F = T_i \cap T_j$ is a facet of at least one of the adjacent elements, i.e. $F \in \mathbb{F}_{T_i}$ or $F \in \mathbb{F}_{T_j}$, and

ii) every facet $\tilde{F} \in \mathbb{F}_T$, $T \in \mathcal{T}_h$ consists of at most $k+1$ faces.

k-irregular meshes usually result from a *hanging node refinement*, cf. Figure 3.2. Also, note that sliding meshes are generally not k-irregular.

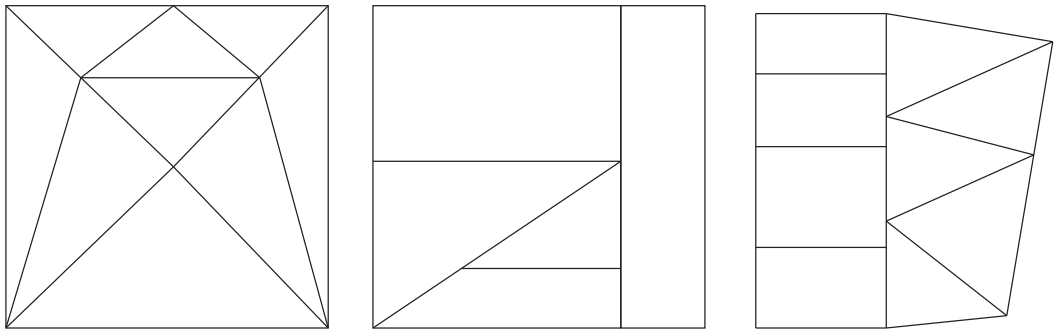

(a) simplicial, affine, conforming mesh (b) hybrid, non-conforming, non-affine 2-irregular mesh (c) hybrid, affine, non-conforming

Figure 3.2: Different types of 2D meshes

Mesh sequences One way to increase the accuracy of the numerical solution is to decrease the mesh-width h, that is we consider a sequence of meshes,

$$\mathcal{T}_{\mathcal{H}} \coloneqq \{\mathcal{T}_h\}_{h\in\mathcal{H}}\,.$$

Here $\mathcal{H}$ is a set of mesh-widths and is a countable subset of $\mathbb{R}^+ \coloneqq \{x \in \mathbb{R} | x > 0\}$ having 0 as the only accumulation point.

In order to derive estimates for the interpolation error on a sequence of meshes we have to make sure that the mesh quality does not deteriorate as $h \to 0$, i.e. the mesh sequence should be *shape regular*.

Definition 3.1.6 (Shape Regular, [42, Property (H1), Section 3.2])**.** *A mesh sequence $\mathcal{T}_{\mathcal{H}}$ is said to be* shape regular *if there exists a constant $\sigma_{\mathcal{H}}$ such that for all $\mathcal{T}_h \in \mathcal{T}_{\mathcal{H}}$, all $T \in \mathcal{T}_h$ we have*

$$\frac{h_T}{\rho_T} \leq \sigma_{\mathcal{H}}.$$

Here $h_T = \operatorname{diam}(T)$ and ρ_T is the diameter of the largest sphere contained in $\overline{T}$.

Note that shape-regularity only measures the mesh element quality and in particular it allows graded meshes: As $h \to 0$ the elements in one part of the domain can become much smaller than the elements in other parts of the domain. For simplicial, 2D meshes shape regularity translates into a condition on the angles of the mesh elements. Indeed, one readily checks that $\frac{h_T}{\rho_T} \geq \frac{1}{\sin\theta_T}$ where θ_T denotes the smallest angle of the triangular element T. In other words, the triangles cannot become too flat as $h \to 0$.

A stricter condition on a mesh sequence is *quasi-uniformity*:

Definition 3.1.7 (Quasi-uniform mesh sequence)**.** *A sequence of meshes, $\mathcal{T}_{\mathcal{H}}$ is* quasi-uniform *if and only if it is shape regular and if there is a constant $C > 0$ such that*

$$\text{for all } h \in \mathcal{H},\ \text{all } T \in \mathcal{T}_h,\ Ch \leq h_T.$$

3.2 Broken Sobolev Spaces

For the discussion of the DG method it will be essential to consider *broken Sobolev spaces* defined on a mesh $\mathcal{T}_h$ of Ω:

$$\begin{aligned} W^{s,p}(\mathcal{T}_h) &\coloneqq \{f \in L^p(\Omega) | \forall T \in \mathcal{T}_h,\, f|_T \in W^{s,p}(T)\}\,, \\ \boldsymbol{H}(\mathbf{curl};\mathcal{T}_h) &\coloneqq \left\{\boldsymbol{A} \in L^2(\Omega)^3 \middle| \forall T \in \mathcal{T}_h,\, \boldsymbol{A}|_T \in \boldsymbol{H}(\mathbf{curl};T)\right\}, \\ \boldsymbol{H}(\mathrm{curl};\mathcal{T}_h) &\coloneqq \left\{\boldsymbol{A} \in L^2(\Omega)^2 \middle| \forall T \in \mathcal{T}_h,\, \boldsymbol{A}|_T \in \boldsymbol{H}(\mathrm{curl};T)\right\}, \\ \boldsymbol{H}(\mathrm{div};\mathcal{T}_h) &\coloneqq \left\{\boldsymbol{A} \in L^2(\Omega)^d \middle|\, \forall T \in \mathcal{T}_h,\, \boldsymbol{A}|_T \in \boldsymbol{H}(\mathrm{div};T)\right\}. \end{aligned}$$

As before we set $H^s(\mathcal{T}_h) \coloneqq W^{s,2}(\mathcal{T}_h)$. These spaces are broken in the sense that their elements belong only locally on each mesh element to $W^{s,p}$, respectively $\boldsymbol{H}(\mathbf{curl})$, $\boldsymbol{H}(\mathrm{div})$. This motivates the introduction of the broken differential operators:

Definition 3.2.1 (Broken gradient, [55, Definition 1.21])**.** *The* broken gradient*,* $\mathbf{grad}_h : W^{1,p}(\mathcal{T}_h) \to L^p(\Omega)^d$*, is defined such that,*

$$\forall f \in W^{1,p}(\mathcal{T}_h), \forall T \in \mathcal{T}_h : \qquad (\mathbf{grad}_h f)|_T \coloneqq \mathbf{grad}\,(f|_T)\,.$$

Definition 3.2.2 (Broken curl)**.** *The* broken curl*,* $\mathbf{curl}_h : \boldsymbol{H}(\mathbf{curl};\mathcal{T}_h) \to L^2(\Omega)^3$*, is defined such that,*

$$\forall \boldsymbol{A} \in \boldsymbol{H}(\mathbf{curl};\mathcal{T}_h), \forall T \in \mathcal{T}_h : \qquad (\mathbf{curl}_h \boldsymbol{A})|_T \coloneqq \mathbf{curl}\,(\boldsymbol{A}|_T)\,.$$

Note that if there is no ambiguity, we will usually drop the subscript h of the broken gradient/curl operator to simplify notation. Using the broken differential operators one can alternatively define $W^{1,p}(\mathcal{T}_h) = \{f \in L^p(\Omega) |\ \mathbf{grad}_h f \in L^p(\Omega)^d\}$ and $\boldsymbol{H}(\mathbf{curl};\mathcal{T}_h) = \{\boldsymbol{A} \in L^2(\Omega)^3 |\ \mathbf{curl}_h \boldsymbol{A} \in L^2(\Omega)^3\}$.

Clearly the usual Sobolev spaces are subspaces of their broken versions and one can even show that the broken gradient/curl coincides with the usual gradient/curl on these subspaces. More precisely, we have the following results:

Lemma 3.2.3 ([55, Lemma 1.22])**.** *Let* $s \geq 0$ *integer and* $1 \leq p \leq \infty$*. There holds* $W^{s,p}(\Omega) \subset W^{s,p}(\mathcal{T}_h)$*. Moreover, for all* $f \in W^{1,p}(\Omega)$*,* $\mathbf{grad}_h f = \mathbf{grad}\, f$ *in* $L^p(\Omega)^d$*.*

Lemma 3.2.4. *We have* $\boldsymbol{H}(\mathbf{curl};\Omega) \subset \boldsymbol{H}(\mathbf{curl};\mathcal{T}_h)$ *and for all* $\boldsymbol{A} \in \boldsymbol{H}(\mathbf{curl};\Omega)$*,* $\mathbf{curl}_h \boldsymbol{A} = \mathbf{curl}\,\boldsymbol{A}$ *in* $L^2(\Omega)$*.*

Proof. Let $\boldsymbol{A} \in \boldsymbol{H}(\mathbf{curl};\Omega)$, $T \in \mathcal{T}_h$. Now let $\boldsymbol{\phi} \in C_0^\infty(T)^3$ and denote by $\tilde{\boldsymbol{\phi}}$ its extension by zero to Ω. We then have

$$\begin{aligned} \int_T \mathbf{curl}_h \boldsymbol{A} \cdot \boldsymbol{\phi}\,\mathrm{d}V = \int_T \mathbf{curl}(\boldsymbol{A}|_T) \cdot \boldsymbol{\phi}\,\mathrm{d}V = \int_T \boldsymbol{A} \cdot \mathbf{curl}\,\boldsymbol{\phi}\,\mathrm{d}V \\ = \int_\Omega \boldsymbol{A} \cdot \mathbf{curl}\,\tilde{\boldsymbol{\phi}}\,\mathrm{d}V = \int_\Omega \mathbf{curl}\,\boldsymbol{A} \cdot \tilde{\boldsymbol{\phi}}\,\mathrm{d}V = \int_T \mathbf{curl}\,\boldsymbol{A} \cdot \boldsymbol{\phi}\,\mathrm{d}V \end{aligned}$$

Since $\boldsymbol{\phi}$ is arbitrary this proves that $\mathbf{curl}_h \boldsymbol{A} = \mathbf{curl}\,\boldsymbol{A}$ in $L^2(T)$ and thus $\boldsymbol{A}|_T \in \boldsymbol{H}(\mathbf{curl};T)$. Observing that T is arbitrary finishes the proof. □

Jumps and Averages The broken Sobolev space $W^{1,1}(\mathcal{T}_h)$ is the natural domain of definition for jump and average operators: A function $f \in W^{1,1}(T)$, $T \in \mathcal{T}_h$, has an integrable trace $\gamma_D(f) \in L^1(\partial T)$ by Theorem 2.2.15. Because of this we can *restrict* $\gamma_D(f)$ to an individual face $F \in \mathcal{F}_T$. If now $f \in W^{1,1}(\mathcal{T}_h)$, then f has a (possibly two-valued) trace on every $F \in \mathcal{F}_h$. Therefore, we can define the jump and *weighted* average of $f \in W^{1,1}(\mathcal{T}_h)$ for every face $F \in \mathcal{F}_h$:

$$\begin{aligned} \text{for } F \in \mathcal{F}_h^i,\ F = \partial T_1 \cap \partial T_2, \quad & [\![f]\!] \coloneqq f|_{T_1} - f|_{T_2}\,, \quad & \{\!\{f\}\!\}_\omega \coloneqq \omega_1 f|_{T_1} + \omega_2\, f|_{T_2}\,, \\ \text{for } F \in \mathcal{F}_h^b,\ F = \partial T \cap \partial\Omega, \quad & [\![f]\!] \coloneqq f|_T\,, & \{\!\{f\}\!\}_\omega \coloneqq f|_T\,. \end{aligned}$$

Here the weights $\omega_1, \omega_2 \in [0,1]$ are such that $\omega_1 + \omega_2 = 1$ and will be specified later. If f is a vector valued function, the jump and average operator are defined component wise and are thus also vector valued. In order to simplify notation, we will also introduce the tangential jump of a vector valued function $\boldsymbol{A} \in W^{1,1}(\mathcal{T}_h)^3$ by

$$\begin{aligned} \text{for } F \in \mathcal{F}_h^i,\ F = \partial T_1 \cap \partial T_2, \quad & [\![\boldsymbol{A}]\!]_\tau \coloneqq \boldsymbol{n}_F \times \boldsymbol{A}|_{T_1} - \boldsymbol{n}_F \times \boldsymbol{A}|_{T_2}\,, \\ \text{for } F \in \mathcal{F}_h^b,\ F = \partial T_1 \cap \partial\Omega, \quad & [\![\boldsymbol{A}]\!]_\tau \coloneqq \boldsymbol{n}_F \times \boldsymbol{A}|_{T_1}\,, \end{aligned}$$

where $\boldsymbol{n}_F$ is the outer unit normal of T_1 on F:

Remark 3.2.5. *Every interior face $F = \partial T_1 \cap \partial T_2$ has an intrinsic orientation determined by the order of the two elements T_1, T_2. This order can be chosen arbitrarily but it is important that it is always the same.*

The (tangential) jumps can be used to characterize the spaces $W^{1,p}(\Omega)$, respectively $\boldsymbol{H}(\mathbf{curl};\Omega)$:

Lemma 3.2.6 (Characterization of $W^{1,p}(\Omega)$, [55, Lemma 1.23])**.** *Let $1 \le p \le \infty$. A function $f \in W^{1,p}(\mathcal{T}_h)$ belongs to $W^{1,p}(\Omega)$ if and only if*

$$[\![f]\!] = 0 \quad \textit{almost everywhere on } F,\ \forall F \in \mathcal{F}_h^i.$$

Lemma 3.2.7 (Characterization of $\boldsymbol{H}(\mathbf{curl};\Omega)$)**.** *A function $\boldsymbol{A} \in \boldsymbol{H}(\mathbf{curl};\mathcal{T}_h) \cap W^{1,1}(\mathcal{T}_h)^3$ belongs to $\boldsymbol{H}(\mathbf{curl};\Omega)$ if and only if*

$$[\![\boldsymbol{A}]\!]_\tau = 0 \quad \textit{almost everywhere on } F,\ \forall F \in \mathcal{F}_h^i.$$

Proof. Let $\boldsymbol{A} \in \boldsymbol{H}(\mathbf{curl};\mathcal{T}_h) \cap W^{1,1}(\mathcal{T})^3$ and let $\boldsymbol{\phi} \in C_0^\infty(\Omega)^3$. Then,

$$\begin{aligned} \int_\Omega \boldsymbol{A} \cdot \mathbf{curl}\,\boldsymbol{\phi} &= \sum_{T \in \mathcal{T}_h} \int_T \boldsymbol{A} \cdot \mathbf{curl}\,\boldsymbol{\phi} \\ &= \sum_{T \in \mathcal{T}_h} \left\{ -\int_{\partial T} (\boldsymbol{n}_T \times \boldsymbol{A}) \cdot \boldsymbol{\phi} + \int_T \mathbf{curl}\,\boldsymbol{A} \cdot \boldsymbol{\phi} \right\} \\ &= \int_\Omega \mathbf{curl}_h\,\boldsymbol{A} \cdot \boldsymbol{\phi} - \sum_{F \in \mathcal{F}_h^i} \int_F [\![\boldsymbol{A}]\!]_\tau \cdot \boldsymbol{\phi} \end{aligned} \tag{3.1}$$

Now assume that $[\![\boldsymbol{A}]\!]_\tau = 0$ for all $F \in \mathcal{F}_h^i$. Then (3.1) is exactly the definition of the weak curl operator of $\boldsymbol{A}$, i.e. $\mathbf{curl}\,\boldsymbol{A} = \mathbf{curl}_h\,\boldsymbol{A} \in L^2(\Omega)$ and thus $\boldsymbol{A} \in \boldsymbol{H}(\mathbf{curl};\Omega)$.

Conversely, assume $\boldsymbol{A} \in \boldsymbol{H}(\mathbf{curl};\Omega)$, then (3.1) becomes

$$\begin{aligned}\sum_{F\in\mathcal{F}_h^i}\int_F [\![\boldsymbol{A}]\!]_\tau \cdot \boldsymbol{\phi} &= \int_\Omega \mathbf{curl}_h\,\boldsymbol{A}\cdot\boldsymbol{\phi} - \int_\Omega \boldsymbol{A}\cdot\mathbf{curl}\,\boldsymbol{\phi}\\ &= \int_\Omega (\mathbf{curl}_h\,\boldsymbol{A} - \mathbf{curl}\,\boldsymbol{A})\cdot\boldsymbol{\phi} \overset{\text{Lemma 3.2.4}}{=} 0.\end{aligned}$$

□

3.3 Weighted Interior Penalty Formulation

3.3.1 Generic 3D curl-curl Problem

Having defined the broken Sobolev spaces we can now proceed with the construction of discontinuous Galerkin approximation schemes that rely on a sequence of discrete subspaces V_h, $h \in \mathcal{H}$. In this section, we consider the generic, 3D curl-curl problem posed on a *polyhedral domain* Ω:

$$\begin{cases}\text{Find } \boldsymbol{A} \in V \coloneqq \boldsymbol{H}(\mathbf{curl};\Omega) \text{ subject to}\\ \qquad \mathbf{curl}\,(\mu^{-1}\,\mathbf{curl}\,\boldsymbol{A}) + \kappa\boldsymbol{A} = \boldsymbol{j}^i & L^2(\Omega)^3, & (3.2a)\\ \qquad \gamma_\tau(\boldsymbol{A}) = \boldsymbol{n}\times\boldsymbol{g}_D & \text{on } L^2(\partial\Omega)^3. & (3.2b)\end{cases}$$

Here $\boldsymbol{g_D} \in L^2(\partial\Omega)^3$ is a given function and $\kappa \in L^\infty(\Omega;\mathbb{C}), \mu \in L^\infty(\Omega;\mathbb{R})$ are piecewise constant functions such that $0 < \kappa_{\min} \le |\kappa| \le \kappa_{\max}$, $\operatorname{Re}\kappa \ge 0$, $\operatorname{Im}\kappa \ge 0$, $0 < \mu_{\min} \le \mu \le \mu_{\max}$. I.e. there is a partition $P_\Omega = \{\Omega_i\}_i$ of Ω such that each Ω_i is a polyhedron and such that μ, κ are constant on each Ω_i. Note that the regularized magnetostatic/time-harmonic eddy current problems (2.27) and (2.36) are instances of problem (3.2). We remark that using the lemma of Lax-Milgram 2.1.3, one easily proves that there is a unique solution $\boldsymbol{A}$ of (3.2).

In order to apply the Discontinuous Galerkin (DG) techniques we must make additional assumptions:

Assumption 3.3.1 (Mesh compatibility with P_Ω)**.** *All the meshes $\mathcal{T}_h \in \mathcal{T}_\mathcal{H}$ are* compatible *with the partition P_Ω: Every element $T \in \mathcal{T}_h \subset \Omega_i$ for some i.*

This implies that μ, κ are constant on each $T \in \mathcal{T}_h$. Moreover, we require additional regularity on the solution $\boldsymbol{A}$ such that the jump and average operators are well defined:

Assumption 3.3.2. *The solution $\boldsymbol{A}$ of (2.36) is such that*

$$\boldsymbol{A} \in V^* \coloneqq \left\{ \boldsymbol{A} \in \boldsymbol{H}(\mathbf{curl}; \Omega) \cap H^1(P_\Omega)^3 \middle| \, \mathbf{curl}\, \boldsymbol{A} \in H^1(P_\Omega)^3 \right\}. \tag{3.3}$$

This implies that $\gamma_D(\boldsymbol{A}), \gamma_D(\mathbf{curl}\, \boldsymbol{A}) \in L^2(\partial T)$ for all $T \in \mathcal{T}_h$. This allows us to "split" the integral over the boundary of an element into the contributions of the individual faces.

Remark 3.3.3. *One could incorporate natural/Neumann boundary conditions into problem (3.2) without problems. We will however not need such boundary conditions in the rest of the thesis and thus refrain from introducing them.*

Next, we introduce a sequence of meshes, $\mathcal{T}_\mathcal{H}$ and seek a discrete approximation $\boldsymbol{A}_h$ of the solution $\boldsymbol{A}$ of problem (3.2) in the finite dimensional approximation spaces

$$V_h \subset V_h^* \coloneqq \left\{ \boldsymbol{A} \in H^1(\mathcal{T}_h)^3 \middle| \, \mathbf{curl}\, \boldsymbol{A} \in H^1(\mathcal{T}_h)^3 \right\}. \tag{3.4}$$

Since we assume that the meshes are compatible with P_Ω (Assumption 3.3.1) we have $V^* \subset V_h^*$ for all $h \in \mathcal{H}$.

Assumption 3.3.4 (Inverse Trace inequality)**.** *There exists a constant C_{tr} such that for all $h \in \mathcal{H}$, all $\boldsymbol{A}_h \in V_h$ and all $T \in \mathcal{T}_h$ we have*

$$h_T^{1/2} \left\| \mathbf{curl}\, \boldsymbol{A}_h|_T \right\|_{L^2(\partial T)^3} \leq C_{tr} \left\| \mathbf{curl}\, \boldsymbol{A}_h \right\|_{L^2(T)^3}. \tag{3.5}$$

We will later prove the inverse trace inequality for particular choices of V_h, cf. Remark 3.4.5 and Lemma 3.4.11.

We now introduce the *Symmetric Weighted Interior Penalty (SWIP, $\theta = -1$)* and the *Non-symmetric Weighted Interior Penalty (NWIP, $\theta = 1$)* formulation of (3.2):

$$\begin{cases} \text{Find } \boldsymbol{A}_h \in V_h \text{ subject to} \\ a_h^{\theta\text{WIP}}(\boldsymbol{A}_h, \boldsymbol{A}_h') = \ell_h^\theta(\boldsymbol{A}_h') & \text{for all } \boldsymbol{A}_h' \in V_h. \end{cases} \tag{3.6}$$

The corresponding sesquilinear/semilinear forms are

$$\begin{aligned} a_h^{\theta\text{WIP}}(\boldsymbol{A}_h, \boldsymbol{A}_h') \coloneqq & \int_\Omega \mu^{-1} \mathbf{curl}\, \boldsymbol{A}_h \cdot \overline{\mathbf{curl}\, \boldsymbol{A}_h'} - \sum_{F \in \mathcal{F}_h} \int_F \left\{\!\!\left\{ \mu^{-1} \mathbf{curl}\, \boldsymbol{A}_h \right\}\!\!\right\}_\omega \cdot \overline{\left[\!\left[\boldsymbol{A}_h' \right]\!\right]_\tau} \\ & + \theta \sum_{F \in \mathcal{F}_h} \int_F \overline{\left\{\!\!\left\{ \mu^{-1} \mathbf{curl}\, \boldsymbol{A}_h' \right\}\!\!\right\}_\omega} \cdot \left[\!\left[\boldsymbol{A}_h \right]\!\right]_\tau + \sum_{F \in \mathcal{F}_h} \frac{\eta \gamma_{\mu,F}}{a_F} \int_F \left[\!\left[\boldsymbol{A}_h \right]\!\right]_\tau \cdot \overline{\left[\!\left[\boldsymbol{A}_h' \right]\!\right]_\tau} + \int_\Omega \kappa \boldsymbol{A}_h \cdot \overline{\boldsymbol{A}_h'}, \end{aligned} \tag{3.7}$$

$$\ell_h^\theta(\boldsymbol{A}'_h) \coloneqq \int_\Omega \boldsymbol{j}^i \cdot \overline{\boldsymbol{A}'_h} + \sum_{F\in\mathcal{F}_h^b} \int_F \left\{ \theta \overline{\left\{\!\!\left\{ \mu^{-1} \operatorname{\mathbf{curl}} \boldsymbol{A}'_h \right\}\!\!\right\}_\omega} \cdot (\boldsymbol{n}\times\boldsymbol{g}_D) + \frac{\eta\gamma_{\mu,F}}{a_F} \overline{\left[\!\left[\boldsymbol{A}'_h \right]\!\right]_\tau} \cdot (\boldsymbol{n}\times\boldsymbol{g}_D) \right\}, \tag{3.8}$$

where η is the penalty parameter and $\theta = \pm 1$. The second, third and fourth term of $a_h^{\theta\mathrm{WIP}}$ are called consistency, (non-)symmetry and penalty term, respectively.For an inner face $F \in \mathcal{F}_h^i$, $F = \partial T_1 \cap \partial T_2$, we chose the weights [57]

$$\gamma_{\mu,F} \coloneqq \frac{2}{\mu_1+\mu_2}, \qquad \omega_1 \coloneqq \frac{\mu_1}{\mu_1+\mu_2}, \qquad \omega_2 \coloneqq \frac{\mu_2}{\mu_1+\mu_2}.$$

If F is a boundary face, $F \in \mathcal{F}_h^b$, we choose $\gamma_{\mu,F} \coloneqq \mu^{-1}$. The term a_F is the *local length scale* of face F and can be chosen in different ways (e.g. $a_F = \frac{1}{2}(h_{T_1} + h_{T_2})$). For now, we assume the following:

Assumption 3.3.5. *There exists a constant $\varrho_2 > 0$ such that for all $h \in \mathcal{H}$, all $T \in \mathcal{T}_h$, and all $F \in \mathcal{F}_T$:*

$$0 < a_F \le \varrho_2 h_T. \tag{3.9}$$

In Section 3.6, we will look at concrete choices of a_F and discuss the circumstances under which (3.9) is fulfilled. It will turn out that depending on the choice of a_F we must make additional assumptions about the mesh regularity to guarantee (3.9).

Remark 3.3.6. *If $V_h \subseteq \boldsymbol{H}(\boldsymbol{curl};\Omega)$, then all inner tangential jumps in (3.6) will drop out by Lemma 3.2.7. I.e. only jumps at the boundary remain and we are left with a standard FEM formulation where the inhomogeneous boundary conditions* (3.2b) *are enforced by the penalty terms. If we additionally enforce the boundary conditions in a strong sense using a lifting function, i.e. $V_h \subseteq \boldsymbol{H}_0(\boldsymbol{curl},\Omega)$, the DG boundary terms also drop out.*

The same holds of course if V_h is tangentially continuous in each subdomain of a partition $\tilde{P}_\Omega$ [2] of Ω, but possibly discontinuous across subdomain boundaries (cf. Section 3.5). If the meshes are compatible with $\tilde{P}_\Omega$ then the formulation (3.6) *can be seen as a* domain decomposition method*: Locally, in each subdomain one has a standard FEM formulation but the individual subdomains are coupled to each other by the SWIP/NWIP method.*

A Priori Error Estimate

We will now derive an error estimate for the SWIP ($\theta = -1$) as well as the NWIP ($\theta = 1$) method in a suitable norm (yet to be defined) which will allow us to bound the error $\|\boldsymbol{A} - \boldsymbol{A}_h\|_{\mathrm{WIP}}$ (see (3.12)) by the best approximation error.

We begin our proof by showing that the exact solution $\boldsymbol{A}$ of (3.2) fulfills the variational formulation (3.6):

[2] The partition $\tilde{P}_\Omega$ must not necessarily agree with the partition P_Ω, cf. Section 3.5.

Lemma 3.3.7 (Consistency). *Assume $\boldsymbol{A} \in V^*$ is the exact solution of (3.2). Then for $\theta = \pm 1$ and for all $\boldsymbol{A}'_h \in V_h$,*

$$a_h^{\theta\,WIP}(\boldsymbol{A}, \boldsymbol{A}'_h) = \ell_h^\theta(\boldsymbol{A}'_h).$$

Proof. Since $\boldsymbol{A} \in \boldsymbol{H}(\mathbf{curl}; \Omega)$, $\boldsymbol{A}$ is tangentially continuous across all element boundaries, cf. Lemma 3.2.7. Thus, all inner jump terms drop out,

$$\begin{aligned} a_h^{\theta\mathrm{WIP}}(\boldsymbol{A}, \boldsymbol{A}'_h) = \int_\Omega \frac{1}{\mu}\,\mathbf{curl}\,\boldsymbol{A} \cdot \overline{\mathbf{curl}\,\boldsymbol{A}'_h} - \sum_{F\in\mathcal{F}_h} \int_F \left\{\!\!\left\{\mu^{-1}\,\mathbf{curl}\,\boldsymbol{A}\right\}\!\!\right\}_\omega \cdot \overline{\left[\!\left[\boldsymbol{A}'_h\right]\!\right]_\tau} \\ +\theta \sum_{F\in\mathcal{F}_h^b} \int_F \overline{\left\{\!\!\left\{\mu^{-1}\,\mathbf{curl}\,\boldsymbol{A}'_h\right\}\!\!\right\}_\omega} \cdot \left[\!\left[\boldsymbol{A}\right]\!\right]_\tau + \sum_{F\in\mathcal{F}_h^b} \frac{\eta\gamma_{\mu,F}}{a_F} \int_F \left[\!\left[\boldsymbol{A}\right]\!\right]_\tau \cdot \overline{\left[\!\left[\boldsymbol{A}'_h\right]\!\right]_\tau} + \int_\Omega \kappa\boldsymbol{A} \cdot \overline{\boldsymbol{A}'_h}. \end{aligned} \tag{3.10}$$

Note that the last two sums include only boundary faces. Next, we make use of the following identity (which holds for any interior face $F = \partial T_1 \cap \partial T_2$)

$$\begin{aligned} \left[\!\left[\boldsymbol{a} \times \boldsymbol{b}\right]\!\right] \cdot \boldsymbol{n}_F &= (\boldsymbol{a}_1 \times \boldsymbol{b}_1 - \boldsymbol{a}_2 \times \boldsymbol{b}_2) \cdot \boldsymbol{n}_F \\ &= ((\omega_1\boldsymbol{a}_1 + \omega_2\boldsymbol{a}_2) \times (\boldsymbol{b}_1 - \boldsymbol{b}_2) + (\boldsymbol{a}_1 - \boldsymbol{a}_2) \times (\omega_2\boldsymbol{b}_1 + \omega_1\boldsymbol{b}_2)) \cdot \boldsymbol{n}_F \\ &= -\left\{\!\!\left\{\boldsymbol{a}\right\}\!\!\right\}_\omega \cdot \left[\!\left[\boldsymbol{b}\right]\!\right]_\tau + \left[\!\left[\boldsymbol{a}\right]\!\right]_\tau \cdot (\omega_2\boldsymbol{b}_1 + \omega_1\boldsymbol{b}_2). \end{aligned}$$

Now apply this identity to the second term of (3.10):

$$\begin{aligned} -\sum_{F\in\mathcal{F}_h} \int_F \left\{\!\!\left\{\mu^{-1}\,\mathbf{curl}\,\boldsymbol{A}\right\}\!\!\right\}_\omega \cdot \overline{\left[\!\left[\boldsymbol{A}'_h\right]\!\right]_\tau} &= \sum_{F\in\mathcal{F}_h^i} \int_F \left[\!\!\left[\left(\mu^{-1}\,\mathbf{curl}\,\boldsymbol{A}\right) \times \overline{\boldsymbol{A}'_h}\right]\!\!\right] \cdot \boldsymbol{n}_F \\ -\sum_{F\in\mathcal{F}_h^i} \int_F \underbrace{\left[\!\left[\mu^{-1}\,\mathbf{curl}\,\boldsymbol{A}\right]\!\right]_\tau}_{=0} \cdot \overline{\left(\omega_2\boldsymbol{A}'_{h,1} + \omega_1\boldsymbol{A}'_{h,2}\right)} &- \sum_{F\in\mathcal{F}_h^b} \int_F \left\{\!\!\left\{\mu^{-1}\,\mathbf{curl}\,\boldsymbol{A}\right\}\!\!\right\}_\omega \cdot \overline{\left[\!\left[\boldsymbol{A}'_h\right]\!\right]_\tau}. \end{aligned}$$

The second term on the right-hand side vanishes because $\boldsymbol{A}$ is the solution of the strong formulation (3.2). Indeed, $\mu^{-1}\,\mathbf{curl}\,\boldsymbol{A} \in \boldsymbol{H}(\mathbf{curl}; \Omega)$, which implies that $\mu^{-1}\,\mathbf{curl}\,\boldsymbol{A}$ is tangentially continuous. Note that for all $F \in \mathcal{F}_h^b$: $\left\{\!\!\left\{\mu^{-1}\,\mathbf{curl}\,\boldsymbol{A}\right\}\!\!\right\}_\omega \cdot \overline{\left[\!\left[\boldsymbol{A}'_h\right]\!\right]_\tau} = -\left[\!\!\left[\left(\mu^{-1}\,\mathbf{curl}\,\boldsymbol{A}\right) \times \overline{\boldsymbol{A}'_h}\right]\!\!\right] \cdot \boldsymbol{n}_F$ so we can rearrange the face contributions to the element boundaries,

$$-\sum_{F\in\mathcal{F}_h} \int_F \left\{\!\!\left\{\mu^{-1}\,\mathbf{curl}\,\boldsymbol{A}\right\}\!\!\right\}_\omega \cdot \overline{\left[\!\left[\boldsymbol{A}'_h\right]\!\right]_\tau} = \sum_{T\in\mathcal{T}_h} \int_{\partial T} \left(\mu^{-1}\,(\mathbf{curl}\,\boldsymbol{A}) \times \overline{\boldsymbol{A}'_h}\right) \cdot \boldsymbol{n}_T. \tag{3.11}$$

Now substitute (3.11) into (3.10) and use Green's second formula (2.7) element-wise:

$$a_h^{\theta\mathrm{WIP}}(\boldsymbol{A}, \boldsymbol{A}'_h) = \sum_{T\in\mathcal{T}_h} \int_T \mathbf{curl}\left(\frac{1}{\mu}\,\mathbf{curl}\,\boldsymbol{A}\right) \cdot \overline{\boldsymbol{A}'_h} + \int_\Omega \kappa\boldsymbol{A} \cdot \overline{\boldsymbol{A}'_h}$$

$$+\theta \sum_{F\in\mathcal{F}_h^b} \int_F \overline{\left\{\!\left\{\mu^{-1}\,\mathbf{curl}\,\boldsymbol{A}_h'\right\}\!\right\}_\omega} \cdot [\![\boldsymbol{A}]\!]_\tau + \sum_{F\in\mathcal{F}_h^b} \frac{\eta\gamma_{\mu,F}}{a_F} \int_F [\![\boldsymbol{A}]\!]_\tau \cdot \overline{[\![\boldsymbol{A}_h']\!]_\tau}$$
$$\overset{(3.2)}{=} \ell_h^\theta(\boldsymbol{A}_h').$$

□

Let us introduce the following (semi-)norms on the space V_h^*:

$$\|\boldsymbol{A}\|_{\mathrm{WIP}}^2 \coloneqq \left\|\mu^{-1/2}\,\mathbf{curl}\,\boldsymbol{A}\right\|_{L^2(\Omega)^3}^2 + \left\|\sqrt{|\kappa|}\boldsymbol{A}\right\|_{L^2(\Omega)^3}^2 + |\boldsymbol{A}|_{j,\mu}^2\,, \tag{3.12}$$

$$|\boldsymbol{A}|_{j,\mu}^2 \coloneqq \sum_{F\in\mathcal{F}_h} \frac{\gamma_{\mu,F}}{a_F} \left\|[\![\boldsymbol{A}]\!]_\tau\right\|_{L^2(F)^3}^2, \tag{3.13}$$

$$\|\boldsymbol{A}\|_{\mathrm{WIP},*}^2 \coloneqq \|\boldsymbol{A}\|_{\mathrm{WIP}}^2 + \sum_{T\in\mathcal{T}_h} h_T \left\|\mu^{-1/2}\,\mathbf{curl}\,\boldsymbol{A}\Big|_T\right\|_{L^2(\partial T)^3}^2. \tag{3.14}$$

Lemma 3.3.8 (Bound on consistency term)**.** *For all $\boldsymbol{A}, \boldsymbol{A}' \in V_h^*$ there holds*

$$\left|\sum_{F\in\mathcal{F}_h} \int_F \left\{\!\left\{\mu^{-1}\,\mathbf{curl}\,\boldsymbol{A}\right\}\!\right\}_\omega \cdot \overline{[\![\boldsymbol{A}']\!]_\tau}\right| \leq$$
$$\varrho_2^{1/2} \left\{\sum_{T\in\mathcal{T}_h} h_T \left\|\mu^{-1/2}\,\mathbf{curl}\,\boldsymbol{A}\Big|_T\right\|_{L^2(\partial T)^3}^2\right\}^{1/2} |\boldsymbol{A}'|_{j,\mu}\,.$$

Proof. For an arbitrary inner face $F = \partial T_1 \cap \partial T_2$, we have by the Cauchy-Schwarz (CS) inequality

$$\left|\int_F \left\{\!\left\{\mu^{-1}\,\mathbf{curl}\,\boldsymbol{A}\right\}\!\right\}_\omega \cdot \overline{[\![\boldsymbol{A}']\!]_\tau}\right|$$
$$\leq \left(\int_F \left|\frac{\omega_1}{\mu_1}\,\mathbf{curl}\,\boldsymbol{A}_1 + \frac{\omega_2}{\mu_2}\,\mathbf{curl}\,\boldsymbol{A}_2\right|^2\right)^{1/2} \left(\int_F \left|[\![\boldsymbol{A}']\!]_\tau\right|^2\right)^{1/2}. \tag{3.15}$$

By using Cauchy-Schwarz (CS) again we see that

$$\left|\frac{\omega_1}{\mu_1}\,\mathbf{curl}\,\boldsymbol{A}_1 + \frac{\omega_2}{\mu_2}\,\mathbf{curl}\,\boldsymbol{A}_2\right|$$
$$\leq \left(\frac{\omega_1^2}{\mu_1} + \frac{\omega_2^2}{\mu_2}\right)^{1/2} \left(\left|\mu_1^{-1/2}\,\mathbf{curl}\,\boldsymbol{A}_1\right|^2 + \left|\mu_2^{-1/2}\,\mathbf{curl}\,\boldsymbol{A}_2\right|^2\right)^{1/2}$$
$$\leq a_F^{1/2} \left(\frac{\gamma_{\mu,F}}{a_F}\right)^{1/2} \left(\left|\mu_1^{-1/2}\,\mathbf{curl}\,\boldsymbol{A}_1\right|^2 + \left|\mu_2^{-1/2}\,\mathbf{curl}\,\boldsymbol{A}_2\right|^2\right)^{1/2}.$$

Substitute this back into (3.15) to get

$$\left|\int_F \left\{\!\!\left\{\mu^{-1}\,\mathbf{curl}\,\boldsymbol{A}\right\}\!\!\right\}_\omega \cdot \overline{[\![\boldsymbol{A}']\!]_\tau}\right| \le \left(\frac{\gamma_{\mu,F}}{a_F}\right)^{1/2} \left\|[\![\boldsymbol{A}']\!]_\tau\right\|_{L^2(F)^3} \left[a_F \int_F \left(\left|\mu_1^{-1/2}\,\mathbf{curl}\,\boldsymbol{A}_1\right|^2 + \left|\mu_2^{-1/2}\,\mathbf{curl}\,\boldsymbol{A}_2\right|^2\right)\right]^{1/2}. \quad (3.16)$$

Similarly, for a boundary face $F \in \mathcal{F}_h^b$ we have

$$\left|\int_F \left\{\!\!\left\{\mu^{-1}\,\mathbf{curl}\,\boldsymbol{A}\right\}\!\!\right\}_\omega \cdot \overline{[\![\boldsymbol{A}']\!]_\tau}\right| \overset{\text{(CS)}}{\le} \frac{1}{\sqrt{\mu a_F}} \left\|[\![\boldsymbol{A}']\!]_\tau\right\|_{L^2(F)^3} \left[a_F \int_F \left|\mu^{-1/2}\,\mathbf{curl}\,\boldsymbol{A}\right|^2\right]^{1/2}. \quad (3.17)$$

Now use (3.16-3.17) to bound the sum over all faces,

$$\begin{aligned}
&\left|\sum_{F\in\mathcal{F}_h^b}\int_F \left\{\!\!\left\{\mu^{-1}\,\mathbf{curl}\,\boldsymbol{A}\right\}\!\!\right\}_\omega \cdot \overline{[\![\boldsymbol{A}']\!]_\tau} + \sum_{F\in\mathcal{F}_h^i}\int_F \left\{\!\!\left\{\mu^{-1}\,\mathbf{curl}\,\boldsymbol{A}\right\}\!\!\right\}_\omega \cdot \overline{[\![\boldsymbol{A}']\!]_\tau}\right| \\
&\overset{(3.16\text{-}3.17)}{\le} \sum_{F\in\mathcal{F}_h^b} \frac{1}{\sqrt{\mu a_F}} \left\|[\![\boldsymbol{A}']\!]_\tau\right\|_{L^2(F)^3} \left\{a_F \int_F \left|\mu^{-1/2}\,\mathbf{curl}\,\boldsymbol{A}\right|^2\right\}^{1/2} \\
&\quad + \sum_{F\in\mathcal{F}_h^i} \left(\frac{\gamma_{\mu,F}}{a_F}\right)^{1/2} \left\|[\![\boldsymbol{A}']\!]_\tau\right\|_{L^2(F)^3} \\
&\qquad\qquad \left\{a_F \int_F \left(\left|\mu_1^{-1/2}\,\mathbf{curl}\,\boldsymbol{A}_1\right|^2 + \left|\mu_2^{-1/2}\,\mathbf{curl}\,\boldsymbol{A}_2\right|^2\right)\right\}^{1/2} \\
&\overset{\text{(CS)}}{\le} \left\{\sum_{F\in\mathcal{F}_h} \frac{\gamma_{\mu,F}}{a_F} \left\|[\![\boldsymbol{A}']\!]_\tau\right\|_{L^2(F)^3}^2\right\}^{1/2} \\
&\quad \left\{\sum_{F\in\mathcal{F}_h^i} a_F \int_F \left(\left|\mu_1^{-1/2}\,\mathbf{curl}\,\boldsymbol{A}_1\right|^2 + \left|\mu_2^{-1/2}\,\mathbf{curl}\,\boldsymbol{A}_2\right|^2\right) + \sum_{F\in\mathcal{F}_h^b} a_F \int_F \left|\mu^{-1/2}\,\mathbf{curl}\,\boldsymbol{A}\right|^2\right\}^{1/2} \\
&\le \varrho_2^{1/2} \left\{\sum_{T\in\mathcal{T}_h} h_T \int_{\partial T} \left|\left(\mu^{-1/2}\,\mathbf{curl}\,\boldsymbol{A}\Big|_T\right)\right|^2\right\}^{1/2} |\boldsymbol{A}'|_{j,\mu},
\end{aligned}$$

where we have regrouped the face contributions and used that $a_F \le \varrho_2 h_T$ in the last step, cf. (3.9). □

Using Lemma 3.3.8, we can finally prove discrete coercivity:

Lemma 3.3.9 (Discrete Coercivity). *The sesquilinear form $a_h^{\theta\,WIP}$ is coercive: For $\theta = \pm 1$, for all $\eta > C_{tr}^2 \varrho_2$ and all $h \in \mathcal{H}$ there holds*

$$\left| a_h^{\theta\,WIP}(\boldsymbol{A}_h, \boldsymbol{A}_h) \right| \geq C_{stab} \left\| \boldsymbol{A}_h \right\|_{WIP}^2 \quad \forall \boldsymbol{A}_h \in V_h,$$

with $C_{stab} = \frac{1}{\sqrt{2}} \min\left(\frac{\eta - C_{tr}^2 \varrho_2}{1+\eta}, 1 \right)$. The constant C_{tr} stems from the inverse trace inequality (3.5) and is independent of h, μ, κ, ς_2.

Proof. By definition of $a_h^{\theta\mathrm{WIP}}$ we have

$$\begin{aligned} a_h^{\theta\mathrm{WIP}}(\boldsymbol{A}_h, \boldsymbol{A}_h) = {} & \left\| \mu^{-1/2} \operatorname{\mathbf{curl}} \boldsymbol{A}_h \right\|_{L^2(\Omega)^3}^2 + \eta \left| \boldsymbol{A}_h \right|_{j,\mu}^2 + \int_\Omega \kappa \left| \boldsymbol{A}_h \right|^2 \\ & - \sum_{F \in \mathcal{F}_h} \int_F \left\{ \left\{\!\!\left\{ \mu^{-1} \operatorname{\mathbf{curl}} \boldsymbol{A}_h \right\}\!\!\right\}_\omega \cdot \overline{\left[\!\left[\boldsymbol{A}_h \right]\!\right]_\tau} - \theta \overline{\left\{\!\!\left\{ \mu^{-1} \operatorname{\mathbf{curl}} \boldsymbol{A}_h \right\}\!\!\right\}_\omega} \cdot \left[\!\left[\boldsymbol{A}_h \right]\!\right]_\tau \right\}. \end{aligned} \tag{3.18}$$

Note that the last term of (3.18) is either purely imaginary ($\theta = 1$) or purely real ($\theta = -1$). Moreover, we have assumed $\operatorname{Re}\kappa \geq 0$ and $\operatorname{Im}\kappa \geq 0$ so that we can use the inequality $|z| \geq |\operatorname{Re} z + \operatorname{Im} z| / \sqrt{2}$ to get:

$$\begin{aligned} \left| a_h^{\theta\mathrm{WIP}}(\boldsymbol{A}_h, \boldsymbol{A}_h) \right| \geq \frac{1}{\sqrt{2}} \Bigg\{ & \left\| \mu^{-1/2} \operatorname{\mathbf{curl}} \boldsymbol{A}_h \right\|_{L^2(\Omega)^3}^2 + \eta \left| \boldsymbol{A}_h \right|_{j,\mu}^2 + \int_\Omega |\kappa| \left| \boldsymbol{A}_h \right|^2 \\ & - 2 \left| \sum_{F \in \mathcal{F}_h} \int_F \left\{\!\!\left\{ \mu^{-1} \operatorname{\mathbf{curl}} \boldsymbol{A}_h \right\}\!\!\right\}_\omega \cdot \overline{\left[\!\left[\boldsymbol{A}_h \right]\!\right]_\tau} \right| \Bigg\}. \end{aligned}$$

Now let us give a bound on the last term on the right-hand side using Lemma 3.3.8,

$$\begin{aligned} & \left| \sum_{F \in \mathcal{F}_h} \int_F \left\{\!\!\left\{ \mu^{-1} \operatorname{\mathbf{curl}} \boldsymbol{A}_h \right\}\!\!\right\}_\omega \cdot \overline{\left[\!\left[\boldsymbol{A}_h \right]\!\right]_\tau} \right| \\ & \qquad \leq \varrho_2^{1/2} \left\{ \sum_{T \in \mathcal{T}_h} h_T \left\| \mu^{-1/2} \operatorname{\mathbf{curl}} \boldsymbol{A}_h \big|_T \right\|_{L^2(\partial T)^3}^2 \right\}^{1/2} \left| \boldsymbol{A}_h \right|_{j,\mu} \\ & \qquad \leq C_{\mathrm{tr}} \varrho_2^{1/2} \left\| \mu^{-1/2} \operatorname{\mathbf{curl}} \boldsymbol{A}_h \right\|_{L^2(\Omega)^3} \left| \boldsymbol{A}_h \right|_{j,\mu}, \end{aligned}$$

where we have used the inverse trace inequality (3.5) in the last step. Hence,

$$\begin{aligned} \left| a_h^{\theta\mathrm{WIP}}(\boldsymbol{A}_h, \boldsymbol{A}_h) \right| \geq \frac{1}{\sqrt{2}} \Bigg\{ & \left\| \sqrt{|\kappa|} \boldsymbol{A}_h \right\|_{L^2(\Omega)^3}^2 \\ & + \underbrace{\left\| \mu^{-1/2} \operatorname{\mathbf{curl}} \boldsymbol{A}_h \right\|_{L^2(\Omega)^3}^2}_{:= x^2} - 2 \underbrace{C_{\mathrm{tr}} \varrho_2^{1/2}}_{:= \beta} \left\| \mu^{-1/2} \operatorname{\mathbf{curl}} \boldsymbol{A}_h \right\|_{L^2(\Omega)^3} \left| \boldsymbol{A}_h \right|_{j,\mu} + \eta \underbrace{\left| \boldsymbol{A}_h \right|_{j,\mu}^2}_{:= y^2} \Bigg\}. \end{aligned}$$

Now use the inequality $x^2 - 2\beta xy + \eta y^2 \geq \frac{\eta-\beta^2}{1+\eta}(x^2+y^2)$ which holds for arbitrary β, η, x, y as outlined above (it follows from $(\beta x - \eta y)^2 + (x - \beta y)^2 \geq 0$):

$$\begin{aligned}
&\left|a_h^{\theta\mathrm{WIP}}(\boldsymbol{A}_h, \boldsymbol{A}_h)\right| \\
&\qquad \geq \frac{\eta - C_{\mathrm{tr}}^2\varrho_2}{\sqrt{2}(1+\eta)} \left(\left\| \mu^{-1/2} \operatorname{\mathbf{curl}} \boldsymbol{A}_h \right\|_{L^2(\Omega)^3}^2 + |\boldsymbol{A}_h|_{j,\mu}^2 \right) + \frac{1}{\sqrt{2}} \left\| \sqrt{|\kappa|} \boldsymbol{A}_h \right\|_{L^2(\Omega)^3}^2 \\
&\qquad \geq C_{\mathrm{stab}} \left(\left\| \mu^{-1/2} \operatorname{\mathbf{curl}} \boldsymbol{A}_h \right\|_{L^2(\Omega)^3}^2 + |\boldsymbol{A}_h|_{j,\mu}^2 + \left\| \sqrt{|\kappa|} \boldsymbol{A}_h \right\|_{L^2(\Omega)^3}^2 \right).
\end{aligned}$$

Finally, we note that $C_{\mathrm{stab}} > 0$ if $\eta > C_{\mathrm{tr}}^2\varrho_2$ which completes the proof. □

Remark 3.3.10. *One easily proves that the NWIP formulation* (3.6) *($\theta = 1$) has a unique solution for all $\eta > 0$. Indeed, assume there exists a $\boldsymbol{A}_h \in V_h$ such that $a_h^{\theta\,WIP}(\boldsymbol{A}_h, \boldsymbol{A}_h) = 0$. Equation* (3.18) *implies that $|\boldsymbol{A}_h|_{j,\mu} = \left\| \sqrt{\operatorname{Re}\kappa} \boldsymbol{A}_h \right\|_{L^2(\Omega)^3} = 0$ and hence the consistency and non-symmetry term must be zero and thus $\left\| \sqrt{\operatorname{Im}\kappa} \boldsymbol{A}_h \right\|_{L^2(\Omega)^3} = 0$.*

A closer look at the proof of Lemma 3.3.9 shows that if $a_h^{\theta\mathrm{WIP}}$ is real valued, i.e. $\operatorname{Im}\kappa \equiv 0$, then the divisor $\sqrt{2}$ drops out of C_{stab} because we don't have to consider the real and imaginary parts of $a_h^{\theta\mathrm{WIP}}$ separately. Moreover, the real-valued NWIP formulation ($\theta = 1$) is unconditionally stable since the consistency and non-symmetry term cancel each other:

Corollary 3.3.11. *If the generic curl-curl problem is a real valued problem, the NWIP formulation ($\theta = 1$) is stable for all $\eta > 0$: for all $h \in \mathcal{H}$ there holds*

$$a_h^{\theta\,WIP}(\boldsymbol{A}_h, \boldsymbol{A}_h) \geq C_{stab} \left\| \boldsymbol{A}_h \right\|_{WIP}^2,$$

with $C_{stab} = \min(\eta, 1)$.

Lemma 3.3.12 (Boundedness)**.** *There exists a constant $C_{bnd} > 0$ independent of h, μ, κ such that for all $\boldsymbol{A} \in V_h^*$, all $\boldsymbol{A}_h' \in V_h$, all $h \in \mathcal{H}$*

$$a_h^{\theta\,WIP}(\boldsymbol{A}, \boldsymbol{A}_h') \leq C_{bnd} \left\| \boldsymbol{A} \right\|_{WIP,*} \left\| \boldsymbol{A}_h' \right\|_{WIP}.$$

Here $C_{bnd} = 2 + \eta + \varrho_2^{1/2}(1 + C_{tr})$ with C_{tr} being the inverse trace inequality constant of (3.5).

Proof. We start by splitting the sesquilinear form $a_h^{\theta\mathrm{WIP}}$ into five terms,

$$\begin{aligned}
a_h^{\theta\mathrm{WIP}}(\boldsymbol{A}, \boldsymbol{A}_h') &= \int_\Omega \mu^{-1} \operatorname{\mathbf{curl}} \boldsymbol{A} \cdot \overline{\operatorname{\mathbf{curl}} \boldsymbol{A}_h'} - \sum_{F \in \mathcal{F}_h} \int_F \left\{\!\!\left\{ \mu^{-1} \operatorname{\mathbf{curl}} \boldsymbol{A} \right\}\!\!\right\}_\omega \cdot \overline{[\![\boldsymbol{A}_h']\!]_\tau} \\
&\quad + \theta \sum_{F \in \mathcal{F}_h} \int_F \overline{\left\{\!\!\left\{ \mu^{-1} \operatorname{\mathbf{curl}} \boldsymbol{A}_h' \right\}\!\!\right\}_\omega} \cdot [\![\boldsymbol{A}]\!]_\tau + \sum_{F \in \mathcal{F}_h} \frac{\eta \gamma_{\mu,F}}{a_F} \int_F [\![\boldsymbol{A}]\!]_\tau \cdot \overline{[\![\boldsymbol{A}_h']\!]_\tau} + \int_\Omega \kappa \boldsymbol{A} \cdot \overline{\boldsymbol{A}_h'}
\end{aligned}$$

$$=: T_1 + T_2 + T_3 + T_4 + T_5 \qquad .$$

We can now bound these terms individually,

$$\begin{aligned}
|T_1| &\overset{\text{(CS)}}{\leq} \left\|\mu^{-1/2}\,\mathbf{curl}\,\boldsymbol{A}\right\|_{L^2(\Omega)^3} \left\|\mu^{-1/2}\,\mathbf{curl}\,\boldsymbol{A}'_h\right\|_{L^2(\Omega)^3} \leq \|\boldsymbol{A}\|_{\mathrm{WIP}} \left\|\boldsymbol{A}'_h\right\|_{\mathrm{WIP}}, \\
|T_2| &\overset{\text{Lemma 3.3.8}}{\leq} \varrho_2^{1/2} \|\boldsymbol{A}\|_{\mathrm{WIP},*} \left\|\boldsymbol{A}'_h\right\|_{\mathrm{WIP}}, \\
|T_3| &\overset{\text{Lemma 3.3.8}}{\leq} \varrho_2^{1/2} \left\{ \sum_{T\in\mathcal{T}_h} h_T \left\| \mu^{-1/2}\,\mathbf{curl}\,\boldsymbol{A}'_h\big|_T \right\|^2_{L^2(\partial T)^3} \right\}^{1/2} \|\boldsymbol{A}\|_{\mathrm{WIP}} \\
&\overset{(3.5)}{\leq} C_{\mathrm{tr}}\varrho_2^{1/2} \left\|\mu^{-1/2}\,\mathbf{curl}\,\boldsymbol{A}'_h\right\|_{L^2(\Omega)^3} \|\boldsymbol{A}\|_{\mathrm{WIP}} \\
&\leq C_{\mathrm{tr}}\varrho_2^{1/2} \left\|\boldsymbol{A}'_h\right\|_{\mathrm{WIP}} \|\boldsymbol{A}\|_{\mathrm{WIP}}, \\
|T_4| &\overset{\text{(CS)}}{\leq} \eta\, |\boldsymbol{A}|_{j,\mu} \left|\boldsymbol{A}'_h\right|_{j,\mu} \leq \eta \|\boldsymbol{A}\|_{\mathrm{WIP}} \left\|\boldsymbol{A}'_h\right\|_{\mathrm{WIP}}, \\
|T_5| &\overset{\text{(CS)}}{\leq} \left\|\sqrt{|\kappa|}\boldsymbol{A}\right\|_{L^2(\Omega)^3} \left\|\sqrt{|\kappa|}\boldsymbol{A}'_h\right\|_{L^2(\Omega)^3} \leq \|\boldsymbol{A}\|_{\mathrm{WIP}} \left\|\boldsymbol{A}'_h\right\|_{\mathrm{WIP}}.
\end{aligned}$$

□

Finally, we can combine the previous results into one theorem.

Theorem 3.3.13 (Best Approximation). *Let $\boldsymbol{A} \in V^*$ be a solution of the strong curl-curl problem* (3.2) *and let $\boldsymbol{A}_h \in V_h \subset V_h^*$ solve the variational formulation* (3.6)*. Then for $\theta = \pm 1$, $\eta > C_{tr}^2\varrho_2$ and all $h \in \mathcal{H}$ there holds*

$$\|\boldsymbol{A} - \boldsymbol{A}_h\|_{WIP} < (1 + C_{bnd}/C_{stab}) \inf_{\boldsymbol{v}_h\in V_h} \|\boldsymbol{A} - \boldsymbol{v}_h\|_{WIP,*}, \tag{3.19}$$

and the discrete problem (3.6) *is well-posed, cf. Definition 2.1.1.*

This theorem tells us that the total error is bounded by the best approximation error (w.r.t. suitable norms). Moreover, the total error depends only mildly, namely through the inverse trace inequality constant C_{tr}, on the choice of $V_h \in V_h^*$.

Note that so far, we didn't make any assumption about the mesh sequence $\mathcal{T}_{\mathcal{H}}$. In order to get rates of convergence we will have to introduce such assumptions and make additional ones about the approximation space V_h and the exact solution $\boldsymbol{A}$. This will be the topic of the next Section.

Finally, we would like to point out that for a concrete space V_h one can often compute the value of C_{tr} and ϱ_2 so that it is a-priori clear how to choose η. See the remarks after Lemma 3.4.11 for an example.

Proof of Theorem 3.3.13. We begin by picking an arbitrary $\boldsymbol{v}_h \in V_h$. Then, by the triangle inequality,

$$\|\boldsymbol{A} - \boldsymbol{A}_h\|_{\mathrm{WIP}} \leq \|\boldsymbol{A} - \boldsymbol{v}_h\|_{\mathrm{WIP}} + \|\boldsymbol{v}_h - \boldsymbol{A}_h\|_{\mathrm{WIP}}\,. \tag{3.20}$$

This is almost the statement of Theorem 3.3.13. It remains to bound $\|\boldsymbol{A}_h - \boldsymbol{v}_h\|_{\mathrm{WIP}}$,

$$\begin{aligned}
\|\boldsymbol{A}_h - \boldsymbol{v}_h\|_{\mathrm{WIP}} &\overset{\text{Lemma 3.3.9}}{\leq} C_{\mathrm{stab}}^{-1} \frac{\left|a_h^{\theta\mathrm{WIP}}(\boldsymbol{A}_h - \boldsymbol{v}_h, \boldsymbol{A}_h - \boldsymbol{v}_h)\right|}{\|\boldsymbol{A}_h - \boldsymbol{v}_h\|_{\mathrm{WIP}}} \\
&\overset{\text{Lemma 3.3.7}}{=} C_{\mathrm{stab}}^{-1} \frac{\left|a_h^{\theta\mathrm{WIP}}(\boldsymbol{A} - \boldsymbol{v}_h, \boldsymbol{A}_h - \boldsymbol{v}_h)\right|}{\|\boldsymbol{A}_h - v_h\|_{\mathrm{WIP}}} \\
&\overset{\text{Lemma 3.3.12}}{\leq} C_{\mathrm{stab}}^{-1} C_{\mathrm{bnd}} \frac{\|\boldsymbol{A} - \boldsymbol{v}_h\|_{\mathrm{WIP},*}\, \|\boldsymbol{A}_h - \boldsymbol{v}_h\|_{\mathrm{WIP}}}{\|\boldsymbol{A}_h - \boldsymbol{v}_h\|_{\mathrm{WIP}}} \\
&= C_{\mathrm{stab}}^{-1} C_{\mathrm{bnd}}\, \|\boldsymbol{A} - \boldsymbol{v}_h\|_{\mathrm{WIP},*}\,.
\end{aligned}$$

Inserting this bound into (3.20) (which holds for arbitrary $\boldsymbol{v}_h$) yields the assertion. Note that the sesquilinear form $a_h^{\theta\mathrm{WIP}}$ is coercive (Lemma 3.3.9) and bounded (finite dimensions). Thus, Lax-Milgram assures the well-posedness of the discrete problem. □

Remark 3.3.14. *For a real valued problem and for $\theta = 1$ (NWIP) we can use Corollary 3.3.11 instead of Lemma 3.3.9 in the above proof. In this case the discrete formulation* (3.6) *is stable for all $\eta > 0$ and* (3.19) *holds with $C_{stab} = \min(\eta, 1)$.*

For κ complex valued, numerical experiments show that the NWIP formulation is solvable for all $\eta > 0$ (cf. Remark 3.3.10) and it seems that an a-priori error estimate of the form (3.19) *holds also in this case, cf. Section 5.2. It could be possible to prove the latter using the Banach-Nečas-Babuška (BNB) theorem [60, 55] which gives sufficient and necessary conditions for discrete stability.*

Remark 3.3.15. *Observe that for $\kappa \to 0$ the variational formulation* (3.6) *becomes ill-posed. To see this, we observe that the $\|\cdot\|_{WIP}$ norm "becomes" a semi-norm as $\kappa \to 0$. In order to study the behavior as $\kappa \to 0$ it is thus desirable to state the discrete coercivity (Lemma 3.3.9) w.r.t. a norm that does not depend on κ: We use that $\|\boldsymbol{A}_h\|_{WIP}^2 \geq \kappa_{min} \|\boldsymbol{A}_h\|_{L^2}^2$ and thus Lemma 3.3.9 can be rewritten as*

$$\left|a_h^{\theta\,WIP}(\boldsymbol{A}_h, \boldsymbol{A}_h)\right| \geq \kappa_{min} C_{stab}\, \|\boldsymbol{A}_h\|_{L^2}^2\,. \tag{3.21}$$

We see now clearly that the coercivity constant depends linearly on κ, i.e. the discrete problem becomes ill-posed as $\kappa \to 0$.

Remark 3.3.16. *Instead of enforcing the Dirichlet boundary conditions* (3.2b) *through penalization we can also incorporate them into the trial space (similar to the Poisson problem in Section 2.4). In this case, we don't have to test anymore on the boundary, in fact it suffices to choose the space $V_h \subset \boldsymbol{H}_0(\mathbf{curl}; \Omega)$. In particular, we can restrict the sums in* (3.7) *and* (3.8) *to sums over interior faces $\mathcal{F}_h^i$ and it is not hard to see that the entire analysis of this Section can also be carried out if the jump semi-norm $|\cdot|_{j,\mu}$ sums only over the interior faces $\mathcal{F}_h^i$.*

3.3.2 2D Time-Harmonic Eddy Current Problem

In Chapter 5, we will also consider the 2D, scalar valued eddy current problem. In this section, we will briefly describe the corresponding symmetric/non-symmetric interior penalty formulations but will not delve into the details because the results are classical, see for example [55, Chapter 4]. The 2D scalar valued eddy current problem is obtained from the 3D problem (2.31) by assuming that $\boldsymbol{A} = (0, 0, \varphi)^T$. It reads as follows:

$$\begin{aligned}
&\text{Find } \varphi \in H^1(\Omega) \text{ subject to} \\
&\quad -\operatorname{div}(\mu^{-1}\,\mathbf{grad}\,\varphi) + \kappa\varphi = j^i && \text{in } L^2(\Omega), && \text{(3.22a)}\\
&\qquad\qquad \gamma_D(\varphi) = g_D && \text{on } H^{1/2}(\Gamma_D), && \text{(3.22b)}\\
&\qquad\qquad \gamma_N(\kappa\,\mathbf{grad}\,\varphi) = g_N && \text{on } L^2(\Gamma_N), && \text{(3.22c)}
\end{aligned}$$

where $\operatorname{meas}(\Gamma_D) > 0$ and $\Omega \subset \mathbb{R}^2$ is a bounded, connected polyhedral domain. In comparison to the $3D$ curl-curl problem, this problem is already coercive and regularization is *not* necessary: It suffices to assume that $\kappa \in L^\infty(\Omega;\mathbb{C})$ and $\mu \in L^\infty(\Omega;\mathbb{R})$, $|\kappa| \le \kappa_{\max}$, $\operatorname{Re}\kappa \ge 0$, $0 < \mu_{\min} \le \mu \le \mu_{\max}$, are piecewise constant functions on the partition P_Ω. As for the curl-curl problem, we require additional smoothness for the exact solution φ:

Assumption 3.3.17. *The solution φ of (3.22) is such that*

$$\varphi \in U^* \coloneqq \left\{\varphi \in H^1(\Omega) \cap H^2(P_\Omega)\right\}.$$

We then introduce a sequence of meshes, $\mathcal{T}_\mathcal{H}$ that is compatible with the partition P_Ω. We denote by $\mathcal{F}_h^D \coloneqq \{F \in \mathcal{F}_h^b |\ F \subset \Gamma_D\}$ the subset of boundary faces where the Dirichlet boundary condition (3.22b) is enforced and denote by $\mathcal{F}_h^N \coloneqq \mathcal{F}_h^b \setminus \mathcal{F}_h^D$ the "Neumann faces". We seek the discrete solution φ_h of problem (1.10) in

$$U_h \subset U_h^* \coloneqq H^2(\mathcal{T}_h). \tag{3.23}$$

Assumption 3.3.18 (Inverse Trace Inequality)**.** *There exists a constant C_{tr} such that for all $h \in \mathcal{H}$, all $\varphi_h \in U_h$ and all $T \in \mathcal{T}_h$ we have*

$$h_T^{1/2}\,\|\mathbf{grad}\,\varphi_h|_T \cdot \boldsymbol{n}_T\|_{L^2(\partial T)^2} \le C_{tr}\,\|\mathbf{grad}\,\varphi_h\|_{L^2(T)^2}. \tag{3.24}$$

See Remark 3.4.5 and Lemma 3.4.11 for concrete conditions under which an inverse trace inequality holds.

The Symmetric Weighted Interior Penalty (SWIP, $\theta = -1$) and the Non-symmetric Weighted Interior Penalty (NWIP, $\theta = 1$) formulation of (3.22) is

$$\text{Find } \varphi_h \in U_h \text{ subject to}$$

$$a_h^{\theta\mathrm{WIP}}(\varphi_h, \varphi_h') = \ell_h^\theta(\varphi_h') \qquad \text{for all } \varphi_h' \in U_h. \tag{3.25}$$

Here the sesquilinear/semilinear forms are:

$$\begin{aligned} a_h^{\theta\mathrm{WIP}}(\varphi_h, \varphi_h') &\coloneqq \int_\Omega \mu^{-1} \operatorname{\mathbf{grad}} \varphi_h \cdot \overline{\operatorname{\mathbf{grad}} \varphi_h'} - \sum_{F \in \mathcal{F}_h^i \cup \mathcal{F}_h^D} \int_F \overline{[\![\varphi_h']\!]} \left\{\!\!\left\{ \mu^{-1} \operatorname{\mathbf{grad}} \varphi_h \right\}\!\!\right\}_\omega \cdot \boldsymbol{n}_F \\ &\quad + \theta \sum_{F \in \mathcal{F}_h^i \cup \mathcal{F}_h^D} \int_F [\![\varphi_h]\!] \overline{\left\{\!\!\left\{ \mu^{-1} \operatorname{\mathbf{grad}} \varphi_h' \right\}\!\!\right\}_\omega \cdot \boldsymbol{n}_F} + \sum_{F \in \mathcal{F}_h^i \cup \mathcal{F}_h^D} \frac{\eta \gamma_{\mu,F}}{a_F} \int_F [\![\varphi_h]\!] \overline{[\![\varphi_h']\!]} + \int_\Omega \kappa \varphi_h \overline{\varphi_h'}, \end{aligned} \tag{3.26}$$

$$\begin{aligned} \ell_h^\theta(\varphi_h') \coloneqq \int_\Omega j^i \overline{\varphi_h'} + \sum_{F \in \mathcal{F}_h^N} \int_F g_N \overline{\varphi_h'} + \theta \sum_{F \in \mathcal{F}_h^D} \int_F g_D \overline{\left\{\!\!\left\{ \mu^{-1} \operatorname{\mathbf{grad}} \varphi_h' \right\}\!\!\right\}_\omega \cdot \boldsymbol{n}_F} \\ + \sum_{F \in \mathcal{F}_h^D} \frac{\eta \gamma_{\mu,F}}{a_F} \int_F g_D \overline{[\![\varphi_h']\!]} \end{aligned} \tag{3.27}$$

The weights $\gamma_{\mu,F}$, ω_1, ω_2 are chosen as in Section 3.3.1. Moreover, we assume that there is a ϱ_2 such that (3.9) holds.

Remark 3.3.19. *If $U_h \subset H_0^1(\Omega)$ then all jump terms in* (3.26) *and* (3.27) *will drop out and only a standard FEM formulation remains.*

By using the same procedure as for the curl-curl problem (Section 3.3.1, [55, Chapter 4]) one can derive a best approximation error estimate:

Theorem 3.3.20 (Best approximation)**.** *Let $\varphi \in U^*$ be a solution of the strong 2D eddy current problem* (3.22)*. Moreover, let $\varphi_h \in U_h \subset U_h^*$ solve the variational formulation* (3.25) *with $\theta = \pm 1$. Then for $\eta > C_{tr}^2 \varrho_2$ and all $h \in \mathcal{H}$ there holds*

$$\|\varphi - \varphi_h\|_{WIP} < (1 + C_{bnd}/C_{stab}) \inf_{v_h \in U_h} \|\varphi - v_h\|_{WIP,*},$$

and the discrete problem (3.25) *is well-posed. Here $C_{bnd} = 2 + \eta + \varrho_2^{1/2}(1 + C_{tr})$, $C_{stab} = \frac{1}{\sqrt{2}} \min\left(\frac{\eta - C_{tr}^2 \varrho_2}{1+\eta}, 1\right)$, with C_{tr} being the constant of* (3.24)*.*

Here the corresponding (semi-)norms are defined as:

$$\begin{aligned} \|\varphi\|_{\mathrm{WIP}}^2 &\coloneqq \left\| \mu^{-1/2} \operatorname{\mathbf{grad}}_h \varphi \right\|_{L^2(\Omega)^2}^2 + \left\| \sqrt{|\kappa|} \varphi \right\|_{L^2(\Omega)}^2 + |\varphi|_{j,\mu}^2, \\ |\varphi|_{j,\mu}^2 &\coloneqq \sum_{F \in \mathcal{F}_h^i \cup \mathcal{F}_h^D} \frac{\gamma_{\mu,F}}{a_F} \|[\![\varphi]\!]\|_{L^2(F)}^2, \\ \|\varphi\|_{\mathrm{WIP},*}^2 &\coloneqq \|\varphi\|_{\mathrm{WIP}}^2 + \sum_{T \in \mathcal{T}_h} h_T \left\| \mu^{-1/2} \operatorname{\mathbf{grad}} \varphi|_T \cdot \boldsymbol{n}_T \right\|_{L^2(\partial T)^2}^2. \end{aligned} \tag{3.28}$$

Interestingly, it is possible to extend the Friedrich's inequality (Theorem 2.3.7) to the broken space $H^1(\mathcal{T}_h)$:

Theorem 3.3.21 (Broken Friedrich's Inequality). *Let $\Omega \subset \mathbb{R}^2$ be a bounded, connected polyhedral domain and let $\Gamma_D \subset \partial\Omega$ such that $\operatorname{meas}_1(\Gamma_D) > 0$. Furthermore, let $\mathcal{T}_\mathcal{H}$ be a sequence of shape-regular, affine, conforming, hybrid meshes. For all $\varphi \in H^1(\mathcal{T}_h)$ we have*

$$\|\varphi\|^2_{L^2(\Omega)} \leq C_{F,h} \left[\|\mathbf{grad}\, \varphi\|^2_{L^2(\Omega)^2} + \mu_{max} \, |\varphi|^2_{j,\mu} \right]$$

where $a_F = h_F$ in the definition of $|\varphi|_{j,\mu}$. The constant $C_{F,h}$ depends only on the shape regularity $\sigma_\mathcal{H}$.

We refer the reader to the paper of Brenner [29] for a proof of the above theorem and remark that it can be extended to more general meshes. In particular, it also holds for a quasi-uniform sequence of affine, k-irregular, hybrid meshes.

Using Theorem 3.3.21 we can improve Theorem 3.3.20 for the case $\theta = 1$ (NWIP). In fact, for all $\eta > 0$ we have $\operatorname{Re}\left(a_h^{\theta\mathrm{WIP}}(\varphi_h, \varphi_h)\right) = \left\|\mu^{-1/2} \mathbf{grad}\, \varphi\right\|^2_{L^2(\Omega)^2} + \eta \, |\varphi|^2_{j,\mu} + \left\|\sqrt{\operatorname{Re}\kappa}\, \varphi\right\|^2_{L^2(\Omega)^2} \geq C_{\mathrm{stab}} \, \|\varphi\|^2_{\mathrm{WIP}}$. In other words, we have (cf. Section 3.3.1):

Theorem 3.3.22 (Best approximation for NWIP). *Let $\varphi \in U^*$ be a solution of the strong 2D eddy current problem* (3.22) *and let $\varphi_h \in U_h \subset U_h^*$ solve the variational formulation* (3.25) *for $\theta = 1$ (NWIP). Then for $\eta > 0$ and all $h \in \mathcal{H}$ there holds*

$$\|\varphi - \varphi_h\|_{WIP} < (1 + C_{bnd}/C_{stab}) \inf_{v_h \in U_h} \|\varphi - v_h\|_{WIP,*} \,,$$

and the discrete problem (3.25) *is well-posed. Here $C_{bnd} = 2 + \eta + \varrho_2^{1/2}(1 + C_{tr})$, C_{stab}* depends on $\mu_{\max}$, $\kappa_{\max}$, η, *$C_{F,h}$ and C_{tr} is the constant of the inverse trace inequality* (3.24).

Bibliographical notes The original idea of the symmetric interior penalty method dates back to the paper of Nitsche [108], see also [8]. Later, the idea was picked up by the mortar community [140] and studied in more detail in the DG-framework [55]. Dryja [57] introduced the idea of using weighted averages for the symmetric interior penalty method to compensate large jumps in the coefficient μ for the Poisson equation.

The non-symmetric interior penalty method was introduced by Rivière et al. [122] to derive a simple *hp*-method: At the time, it was not possible to give an exact upper bound for C_{tr} for three-dimensional meshes [148] which complicated the analysis for arbitrary high polynomial degrees. The non-symmetric interior penalty method simplifies this analysis considerably because one does *not* need the inverse trace inequality (the proof is fundamentally different from the one of Theorem 3.3.13 and works only for conforming meshes).

Oden et al. [110] studied the non-symmetric interior penalty formulation with $\eta = 0$ for the Poisson problem. Numerical experiments in [110] suggest that this method behaves

well for polynomials of degree 2 or higher. Rivière et al. [123] have proven later that one can indeed expect optimal rates of convergence for polynomials of degree 2 or higher in 2 and 3 space dimensions.

An alternative to interior penalty type methods is the Locally Discontinuous Galerkin (LDG) method [44] which has been extended to curl-curl type equations by Perugia and Schötzau [116]. As for SWIP method, the LDG method leads to a symmetric, positive definite matrix and also requires the choice of a penalty parameter. But in comparison to the SWIP method there is no lower-bound on the penalty parameter (as for the NWIP method) but the stencil is considerably larger than for the SWIP/NWIP method. The latter is due to the use of so-called discrete lifting operators [55] which leads to an interaction of shape-functions of elements that are not only immediate neighbors but also between elements that are neighbors of neighbors. Castillo [41] shows that the storage requirements for LDG system matrices can be up to 2.5 times higher than for SWIP/NWIP for 2D problems. For 3D problems, this factor will be even higher.

We remark that all the DG-type methods discussed so far have been posed in *primal form*. It is of course possible to recast them into a mixed form where the unknown $\boldsymbol{A}(\varphi)$ and the "flux" $\mu^{-1}\,\mathbf{curl}\,\boldsymbol{A}$ ($\mu^{-1}\,\mathbf{grad}\,\varphi$) appear as unknowns. The different DG-methods can then be characterized by their numerical fluxes which allows for a unified analysis of all these methods, cf. [9]. The mixed formulation also allows for the definition of many other methods which cannot be cast into primal form [55]. We refer the reader to the excellent overviews of [9] and [55, Chapter 4] and to [41] for a numerical comparison between the LDG/SIP/NIP methods.

3.4 Conforming Polynomial Spaces

This section introduces the classical H^1 and $\boldsymbol{H}(\mathbf{curl})$ conforming polynomial spaces that are used by most Finite Element Method (FEM) codes. We will also state some well-known approximation results and provide suitable references for more insights. Note that these spaces are only well defined on *conforming* meshes. In the next Section 3.5, we will then "break" these spaces such that they become non-conforming and extend the approximation results to the interior penalty norms introduced in the previous two sections.

The first subsection 3.4.1 will define an abstract procedure for constructing approximation spaces based on the mapping functions Φ_T which works in principle for all kinds of meshes as long as a *reference finite element* for the reference element (see below) exists. The subsequent sections then introduce such a reference finite element for the tetrahedron that is $H^1/\boldsymbol{H}(\mathbf{curl})$ conforming. We will refrain from introducing other *reference finite element* for general hybrid meshes because this would lengthen the presentation considerably without adding anything new. We refer the reader to the PhD thesis of Bergot [20] which contains reference finite elements for all hybrid element types (cf. Figure 3.1) that are $H^1/\boldsymbol{H}(\mathbf{curl})/\boldsymbol{H}(\mathrm{div})$ conforming.

3.4.1 Abstract (Reference) Finite Elements

We start by introducing the concept of a *finite element*, cf. [42]:

Definition 3.4.1 (Finite Element). *A* finite element *in* $\mathbb{R}^d$ *is a triple* (T, P_T, Σ_T) *where*

i) T *is a geometric domain (e.g. tetrahedron, prism, etc.) in* $\mathbb{R}^d$ *with a non-empty interior and Lipschitz-continuous boundary.*

ii) P_T *is a finite dimensional space of real, possibly vector valued functions defined over the set* T*.*

iii) $\Sigma_T = \{l_i\}_{1 \leq i \leq N_T}$ *is set of* N_T *linearly independent functionals defined over the space* P_T*. These linear functionals are called* Degrees Of Freedom *(DOF).*

Here $T \in \mathcal{T}_h$ is usually an element of the mesh and P_T is a space of polynomials.

We will always assume that the finite elements are *unisolvent*:

Definition 3.4.2 (Unisolvency). *The finite element* (T, P_T, Σ_T) *is said to be* unisolvent *if any set of numbers* α_i*,* $1 \leq i \leq N_T$ *uniquely determines* $p \in P_T$ *such that* $l_i(p) = \alpha_i$*.*

Clearly unisolvency implies that $N_T = \dim(P_T)$. Moreover, there must exist a basis $\{\phi_j\}_{1 \leq j \leq N_T}$ of P_T such that $l_i(\phi_j) = \delta_{i,j}$. The functions ϕ_j are called the *basis- or shape- functions of the finite element.*

Usually the domain of definition of the DOF's l_i can be extended to a larger space $\tilde{P}_T$ (e.g. $C^1(T)$). This allows us to define the interpolation operator $\mathcal{I}_T : \tilde{P}_T \to P_T$ as follows:

$$\mathcal{I}_T(f)(\boldsymbol{x}) = \sum_{i=1}^{N_T} l_i(f)\phi_i(\boldsymbol{x}). \tag{3.29}$$

Clearly this interpolation operator is a projection/idempotent: $\mathcal{I}_T(p) = p$ for all $p \in P_T$.

Definition 3.4.3 (Equality). *We say that two finite elements* (T_1, P_1, Σ_1) *and* (T_2, P_2, Σ_2) *are* equal*, if*

$$T_1 = T_2, \qquad P_1 = P_2, \text{ and} \qquad \mathcal{I}_{T_1} = \mathcal{I}_{T_2},$$

or equivalently, if

$$T_1 = T_2, \qquad P_1 = P_2, \text{ and} \qquad \operatorname{span}(\Sigma_1) = \operatorname{span}(\Sigma_2).$$

It is important to note that the above definition of equality introduces an equivalence class of finite elements.

Next, we would like to construct conforming approximation spaces P_h over a *hybrid* mesh $\mathcal{T}_h$. For this we must define a finite element (T, P_T, Σ_T) for each cell $T \in \mathcal{T}_h$. We do this in the spirit of Section 3.1 and start by defining a finite set of *reference finite elements* $\{(\hat{T}_i, \hat{P}_i, \hat{\Sigma}_i)\}_i$. For each element $T \in \mathcal{T}_h$, there is a mapping $\Phi_T : \hat{T}_i \to T$ where i is chosen to match the reference element type of T. We can then define the mapped function space P_T by the following rules:

$$\text{If } P_h \subset H^1(\Omega): \qquad P_T \coloneqq \hat{P}_i \circ \Phi_T^{-1}. \tag{3.30}$$

$$\text{If } P_h \subset \boldsymbol{H}(\mathbf{curl}; \Omega): \qquad P_T \coloneqq \left\{ (\mathrm{D}\Phi_T)^{-T} (\hat{\boldsymbol{p}} \circ \Phi_T^{-1}) \,\middle|\, \hat{\boldsymbol{p}} \in \hat{P}_i \right\}. \tag{3.31}$$

$$\text{If } P_h \subset \boldsymbol{H}(\mathrm{div}; \Omega): \qquad P_T \coloneqq \left\{ \left(\frac{1}{\det(\mathrm{D}\Phi_T)} \mathrm{D}\Phi_T \right) (\hat{\boldsymbol{p}} \circ \Phi_T^{-1}) \,\middle|\, \hat{\boldsymbol{p}} \in \hat{P}_i \right\}. \tag{3.32}$$

The linear functionals Σ_T are chosen such that $l_i(\hat{p} \circ \Phi_T^{-1}) = \hat{l}_i(\hat{p})$. So, if the reference finite element $(\hat{T}_i, \hat{P}_i, \hat{\Sigma}_i)$ is unisolvent then the mapped finite element (T, P_T, Σ_T) is also unisolvent.

The transformations (3.31) and (3.32) are essentially the pullback of a differential form [74]. In a vector calculus setting they can also be interpreted as **curl**/div preserving transformations see the books of Cohen [45, Appendix A] and Monk [102, Section 3.9] for a derivation. The div preserving transformation in (3.32) is often referred to as the *Piola transformation*, see e.g. [32], [60].

Remark 3.4.4. *In practice, it is often not sufficient to define just one reference finite element because $H^1/H(\mathbf{curl})$ conformity cannot be guaranteed by this simple mapping scheme. Instead one must think of $(\hat{T}_i, \hat{P}_i, \hat{\Sigma}_i)$ as an equivalence class. Depending on the orientation that a mesh element $T \in \mathcal{T}_h$ has w.r.t. its neighbors one then has to pick one particular reference finite element from the equivalence class to construct the shape functions. For low-order finite elements it is often sufficient to just flip the sign of some shape functions but this does not generalize to higher orders.*

Remark 3.4.5. *Under additional assumptions on the mesh-sequence (e.g. shape-regularity), the fact that there are only* finitely *many reference finite elements $(\hat{T}_i, \hat{P}_i, \hat{\Sigma}_i)$ automatically implies the existence of inverse trace inequalities such as* (3.5) *and* (3.24)*. See also Lemma 3.4.11 below.*

3.4.2 A H^1 Conforming, Scalar Finite Element

This section briefly presents an example of a reference finite element that can be used to build the approximation space $V_h \subset H^1(\Omega)$ on a *conforming* mesh $\mathcal{T}_h$. As explained before we will present here only a scalar finite element for the 3D tetrahedron.

First, we define the two fundamental polynomial spaces

$$\mathbb{P}_k \coloneqq \operatorname{span}\left\{\boldsymbol{x}^{\boldsymbol{\alpha}} |\ |\boldsymbol{\alpha}|_{\ell^1} \leq k\right\}, \tag{3.33}$$

$$\mathbb{Q}_k \coloneqq \operatorname{span}\left\{\boldsymbol{x}^{\boldsymbol{\alpha}} |\ |\boldsymbol{\alpha}|_{\ell^\infty} \leq k\right\}. \tag{3.34}$$

Here $\boldsymbol{\alpha} \in \mathbb{N}_0^d$ is a multi-index and $k \in \mathbb{N}$ is the *polynomial degree*. Note that $\dim \mathbb{Q}_k = (k+1)^d$ while $\dim \mathbb{P}_k = \binom{d+k}{d}$.

Remark 3.4.6. *One easily checks that the space $\mathbb{P}_k$ is* invariant *under affine transformations: If $p \in \mathbb{P}_k$ then $p \circ \Phi \in \mathbb{P}_k$ for an affine transformation Φ. Also, note that this is generally not true for the space $\mathbb{Q}_k$.*

One can derive an approximation result for the space $\mathbb{P}_k$ using averaged Taylor polynomials [30]:

Theorem 3.4.7 (Deny-Lions, [102, Theorem 5.5], [58])**.** *Let Ω be a bounded domain with Lipschitz continuous boundary. Let $k \geq 0$ be an integer. Then we have for all $\varphi \in H^s(\Omega)$, $0 \leq s \leq k+1$,*

$$\inf_{p \in \mathbb{P}_k} \|\varphi - p\|_{H^s(\Omega)} \leq C\, |\varphi|_{H^s(\Omega)}.$$

Here C is independent of φ, but depends on Ω, k and s.

Since $\mathbb{P}_k \subset \mathbb{Q}_k$ the same theorem holds for $p \in \mathbb{Q}_k$. Most approximation results for more complex approximation spaces are based on the Deny-Lions Theorem: The idea is mostly to make sure that the approximation space U_h is a superset of $\mathbb{P}_k$ when restricted to an element $T \in \mathcal{T}_h$ or to the reference element $\hat{T}$ (see below), cf. [60, Theorem 1.103].

The following definition is from [102]:

Definition 3.4.8 (Scalar Reference Finite Element)**.** *On the reference tetrahedron $\hat{T}$ (cf. Figure 3.1) we define the reference finite element of order $k \geq 1$ by*

- $\hat{P} = \mathbb{P}_k(\hat{T})$
- *The DOF's fall into four classes, $\hat{\Sigma} = \hat{\Sigma}_v \cup \hat{\Sigma}_e \cup \hat{\Sigma}_f \cup \hat{\Sigma}_V$:*
  - *i)* Vertex DOF's: *Let $\boldsymbol{a}_i$, $1 \leq i \leq 4$ denote the 4 vertices of the reference tetrahedron, then*

$$\hat{\Sigma}_v \coloneqq \{f \mapsto f(\boldsymbol{a}_i) |\ 1 \leq i \leq 4\},$$

  - *ii)* Edge DOF's: *For $k > 1$*

$$\hat{\Sigma}_e \coloneqq \left\{ f \mapsto \frac{1}{\operatorname{meas}(\hat{e})} \int_{\hat{e}} f q \,\mathrm{d}\ell \,\middle|\, q \in \mathbb{P}_{k-2}(\hat{e}),\ \textit{for all edges } \hat{e} \right\},$$

iii) Facet DOF's: *For* $k > 2$

$$\hat{\Sigma}_f \coloneqq \left\{ f \mapsto \frac{1}{\operatorname{meas}(\hat{F})} \int_{\hat{F}} f q \,\mathrm{d}S \,\middle|\, q \in \mathbb{P}_{k-3}(\hat{F}), \forall \hat{F} \in \mathbb{F}_{\hat{T}} \right\},$$

iv) Volume DOF's: *For* $k > 3$

$$\hat{\Sigma}_V \coloneqq \left\{ f \mapsto \frac{1}{\operatorname{meas}(\hat{T})} \int_{\hat{T}} f q \,\mathrm{d}V \,\middle|\, q \in \mathbb{P}_{k-4}(\hat{T}) \right\}.$$

We remark that the above definition does not give an explicit expression for the DOF's since no explicit basis for the spaces $\mathbb{P}_{k-2}$, $\mathbb{P}_{k-3}$, $\mathbb{P}_{k-4}$ is given. The above representation however uniquely defines the *equivalence class* of the reference finite element which is enough for our purposes. One can check that $\dim(\hat{\Sigma}) = \dim(\mathbb{P}_k)$ and that the finite element is unisolvent [102].

We call $\phi_j \in \mathbb{P}_k$ a *facet shape function* of facet F if the corresponding DOF l_j is a facet DOF of F. The other types of DOF's are classified similarly. One can easily show that a vertex/edge/facet shape function is exactly zero on all other vertices/edges/facets except the one where it is defined on. For example, consider the shape function ϕ_j associated with an edge e. This function is clearly zero at all vertices and one can show that it is also zero on all other edges except edge e using partial integration, cf. [102, Lemma 5.47].

The Orientation Problem Let $T \in \mathcal{T}_h$ be any element and $F \in \mathbb{F}_T$ a facet/face of it. Moreover, assume that Φ_T is an affine mapping. It is then easy to see that the *mapped* facet DOF's of face F lie in the space $\Sigma_F = \{\varphi \mapsto \operatorname{meas}(F)^{-1} \int_F \varphi q \,\mathrm{d}S |\ q \in \mathbb{P}_{k-3}(F)\}$. Similarly, the set of mapped edge DOF's of an edge e (of element T) lie in the space $\Sigma_e = \{\varphi \mapsto \operatorname{meas}(e)^{-1} \int_e \varphi q \,\mathrm{d}\ell |\ q \in \mathbb{P}_{k-2}(e)\}$. The important point is that the definition of these spaces is *independent* of the mesh element $T \in \mathcal{T}_h$. In particular, if there are two elements T_i, $T_j \in \mathcal{T}_h$ that share a common face $F = \partial T_i \cap \partial T_j$ then the space of face DOF's Σ_F is the same for both elements and of course the same is true for the three spaces of edge DOF's Σ_e, $e \subset \partial F$.

We can thus choose a (arbitrary) basis $\{l_{F,i}\}_i$ for the space $\Sigma_F = \operatorname{span}\{l_{F,i}\}_i$ that is independent of the two adjacent elements. This basis will then determine a basis of facet DOF's on the reference elements of T_i/T_j. In other words, depending the concrete face basis $\{l_{F,i}\}_i$ we must choose a different reference element for T_i/T_j from the equivalence classes of Definition 3.4.8. This is the reason that we cannot get along with just one reference element but we rather need an equivalence class of reference elements (cf. Remark 3.4.4). The same is of course true for the edge DOF's.

A very important question is whether one can build a $H^1(\Omega)$ conforming basis using the above (mapped) finite elements on $\mathcal{T}_h$. We observe that if we do not impose any

constraints between the basis functions $\phi_{j,T}$ on the different elements $T \in \mathcal{T}_h$ then the resulting space $\mathbb{P}_{k,h}(\mathcal{T}_h) = \{p \in H^1(\mathcal{T}_h) |\ p|_T \in \mathbb{P}_k(T),\ \forall T \in \mathcal{T}_h\}$ is nonconforming in $H^1(\Omega)$ but is still a subspace of $H^1(\mathcal{T}_h)$.

In light of Lemma 3.2.6, the critical question is whether we can identify basis functions from two adjacent elements T_i, T_j with each other such that they are continuous across the common face/facet $F = T_i \cap T_j$. Or equivalently:

$$\begin{gathered}\text{If all vertex, edge and facet DOF's of face } F \text{ vanish for all } p \in \hat{P}_i \\ \text{this must imply } p|_F \equiv 0.\end{gathered} \tag{3.35}$$

Indeed, by picking the right reference finite elements for T_i and T_j we can identify the vertex/edge/facet DOF's of T_i and T_j with each other and thus we can also associate the corresponding basis/shape functions $\phi_{j,T}$ with each other. Now if all vertex, edge, and facet DOF's of the common face F agree, then the jump of the basis/shape functions across F must vanish if we assume the above property (3.35), cf. also [102, Lemma 5.35]. Monk [102, Lemma 5.47] shows that (3.35) holds for the finite element of Definition 3.4.8.

So, for affine meshes the scalar finite element introduced above is H^1 conforming. For non-affine meshes one has to impose additional restrictions on Φ_T; Sloppily speaking the mapping from a facet $\hat{F}$ of the reference element $\hat{T}$ to facet/face $F \in \mathcal{F}_h$ should be "similar" for all facets $\hat{F} \in \mathbb{F}_{\hat{T}}$.

Global approximation space We can thus define the global approximation space (not necessarily meaningful for non-affine meshes)

$$\mathcal{P}_{k,h}(\Omega) \coloneqq \left\{ p_h \in H^1(\Omega) \middle|\ p_h|_T \circ \Phi_T \in \mathcal{P}_k(\hat{T}),\ \forall T \in \mathcal{T}_h \right\}, \tag{3.36}$$

with $\mathcal{P}_k(\hat{T}) = \mathbb{P}_k(\hat{T})$ if $\hat{T}$ is a simplex. Otherwise $\mathcal{P}_k(\hat{T})$ is a more general space (see e.g. [20]) that contains $\mathbb{P}_k(\hat{T})$. Since $\mathbb{P}_k$ is invariant under affine transformations, an equivalent definition for affine, simplicial meshes is

$$\mathcal{P}_{k,h}(\Omega) = \left\{ p_h \in H^1(\Omega) \middle|\ p_h|_T \in \mathbb{P}_k,\ \forall T \in \mathcal{T}_h \right\}.$$

Remark 3.4.9. *One could argue that the introduced framework with (mapped) finite elements is unnecessarily complex and that one could instead just use nodal/Lagrangian shape functions for which the orientation problem is much less severe. The problem with such a point of view is however twofold: On the one hand Lagrangian type elements lead to very ill-conditioned systems of equations for high polynomial degrees. On the other hand, the approach that we introduce here can be applied in the exactly the same way to* $\boldsymbol{H}(\mathbf{curl})$ *conforming Nedelec/edge elements whereas a nodal basis for edge elements is in principle possible but also leads to severe ill-conditioning, [21].*

Interpolation estimate One can show that the DOF's of the (mapped) finite element given in Definition 3.4.8 can be extended to the space $\tilde{\mathbb{P}}(\hat{T}) = H^{\frac{3}{2}+\delta}(\hat{T})$ with $\delta > 0$. So for simplicial meshes we can construct the global projection operator $\pi_h : H^{3/2+\delta}(\Omega) =: \tilde{\mathbb{P}}(\Omega) \to \mathcal{P}_{k,h}(\Omega) \subset H^1(\Omega)$ by

$$(\pi_h \varphi)|_T = \pi_T(\varphi|_T), \quad \forall T \in \mathcal{T}_h,$$

where π_T is defined by (3.29). Using the Deny-Lions Theorem 3.4.7 on the reference element one finds [102, Theorem 5.48]

Theorem 3.4.10. *Let $\mathcal{T}_\mathcal{H}$ be a shape-regular sequence of conforming, tetrahedral, affine meshes of Ω. Then there exists a constant $C(s)$ independent of h and φ such that for all $\varphi \in H^s(\Omega)$,*

$$\|\varphi - \pi_h \varphi\|_{H^1(\Omega)} \leq C(s) h^{s-1} \|\varphi\|_{H^s(\Omega)}, \quad 2 \leq s \leq k+1.$$

This estimate holds tetrahedron by tetrahedron (if Ω, h are replaced by T and h_T, respectively).

Finally, we state an inverse trace inequality for the space $\mathbb{P}_k$:

Lemma 3.4.11 (Inverse Trace Inequality for $\mathbb{P}_k$, [148])**.** *Let $\mathcal{T}_h \subset \mathbb{R}^d$ be a shape regular sequence of affine, simplicial, possibly non-conforming meshes. Then for all $h \in \mathcal{H}$, all $T \in \mathcal{T}_h$, and all $\varphi_h \in \mathbb{P}_k(T)$ we have*

$$h_T^{1/2} \|\varphi_h|_T\|_{L^2(\partial T)} \leq C_{tr} \|\varphi_h\|_{L^2(T)},$$

with $C_{tr} = h_T^{1/2} \sqrt{\frac{(k+1)(k+3)\operatorname{meas}(\partial T)}{3\operatorname{meas}(T)}} = Ck$ where C is independent of T, k but depends on $\sigma_\mathcal{H}$.

So if $U_h \subset \mathbb{P}_{k,h}(\mathcal{T}_h) = \{p \in L^2(\Omega) |\ p|_T \in \mathbb{P}_k(T),\ \forall T \in \mathcal{T}_h\}$ Assumption 3.3.18 holds for affine, shape-regular mesh sequences since $\mathbf{grad}\, \mathbb{P}_k \subset (\mathbb{P}_{k-1})^3$ (for $k \geq 1$). In particular, we see that $C_{\mathrm{tr}} = O(k)$ so that we have to choose the penalty parameter $\eta = O(k^2)$, cf. Theorem 3.3.20.

The same argument is true for the space V_h which is used to discretize the generic $\mathbf{curl}\,\mathbf{curl}$ problem (cf. (3.4)): Assume that $V_h \subset \mathbb{P}_{k,h}(\mathcal{T}_h)^3$. Then Assumption 3.3.4 holds with $C_{\mathrm{tr}} = O(k)$ and we should choose the penalty parameter $\eta = O(k^2)$, cf. Theorem 3.3.13.

3.4.3 The $H(\mathrm{curl})$ Conforming Nédélec/Edge Finite Element

In this section, we will briefly introduce the 3D Nédélec [105] or edge finite element of the *first kind*. The lowest order element with $k = 1$ is sometimes also referred to as the Whitney element/form.

Our presentation follows mostly the one in the excellent book of Monk [102, Section 5.5]. We start by introducing the polynomial spaces

$$\begin{aligned}\tilde{\mathbb{P}}_k &\coloneqq \operatorname{span}\{\boldsymbol{x}^{\boldsymbol{\alpha}} |\ |\boldsymbol{\alpha}|_{\ell^1} = k\},\\ \mathcal{S}_k &\coloneqq \left\{\boldsymbol{p} \in \tilde{\mathbb{P}}_k^3 \,\middle|\, \boldsymbol{x}\cdot\boldsymbol{p} = 0\right\},\\ R_k &\coloneqq \mathbb{P}_{k-1}^3 \oplus \mathcal{S}_k.\end{aligned}$$

The $\boldsymbol{H}(\mathbf{curl})$-conforming reference finite element of the first kind is then defined by [102, Definition 5.30]

Definition 3.4.12 (Reference Nédélec/edge finite element)**.** *On the reference tetrahedron $\hat{T}$ (cf. Figure 3.1) we define the* reference Nédélec/edge finite element *of order $k \geq 1$ by*

- $\hat{P} = R_k$.
- *The DOF's fall into three classes, $\hat{\Sigma} = \hat{\Sigma}_e \cup \hat{\Sigma}_f \cup \hat{\Sigma}_V$:*

  i) Edge DOF's*:*

$$\hat{\Sigma}_e \coloneqq \left\{\boldsymbol{A} \mapsto \int_{\hat{e}} \hat{p}\hat{\boldsymbol{A}}\cdot\boldsymbol{t}\,\mathrm{d}\ell \,\middle|\, \hat{p} \in \mathbb{P}_{k-1}(\hat{e}),\ \textit{for each edge } \hat{e} \textit{ of } \hat{T}\right\},$$

  ii) Facet DOF's*: For $k > 1$*

$$\hat{\Sigma}_f \coloneqq \left\{\boldsymbol{A} \mapsto \frac{1}{\operatorname{meas}(\hat{F})}\int_{\hat{F}} \hat{\boldsymbol{A}}\cdot\hat{\boldsymbol{p}}\,\mathrm{d}S \,\middle|\, \hat{\boldsymbol{p}} \in \mathbb{P}_{k-2}(\hat{F})^3,\ \hat{\boldsymbol{p}}\cdot\boldsymbol{n}_{\hat{F}} = 0,\ \forall \hat{F} \in \mathbb{F}_{\hat{T}}\right\},$$

  iii) Volume DOF's*: For $k > 2$*

$$\hat{\Sigma}_V \coloneqq \left\{\boldsymbol{A} \mapsto \int_{\hat{T}} \boldsymbol{A}\cdot\hat{\boldsymbol{p}}\,\mathrm{d}V \,\middle|\, \hat{\boldsymbol{p}} \in \mathbb{P}_{k-3}(\hat{T})^3\right\}.$$

One can show that this finite element is unisolvent and $\boldsymbol{H}(\mathbf{curl})$ conforming, [102, Theorem 5.37]. The "orientation problem" can be solved in exactly the same way as for the H^1 conforming finite element. Using the mapping procedure from Section 3.4.1 we define the global Nédélec approximation space

$$R_{k,h}(\Omega) \coloneqq \{\boldsymbol{A}_h \in \boldsymbol{H}(\mathbf{curl};\Omega) |\ \boldsymbol{A}|_T \in P_T, \text{ with } (T, P_T, \Sigma_T) \text{ the mapped finite element on } T \in \mathcal{T}_h\}.$$

As for the scalar case, one can show that the DOF's in Definition 3.4.12 can be extended to the space $\tilde{R}(\hat{T}) = \{\boldsymbol{A} \in H^{1/2+\delta}(\hat{T})^3 |\ \mathbf{curl}\,\boldsymbol{A} \in L^p(\hat{T})^3\}$, where $\delta > 0$, $p > 2$ [102, Lemma 5.38]. We can thus define the global interpolation operator $\boldsymbol{r}_h : \tilde{R}(\Omega) \mapsto R_{k,h}(\Omega)$ element by element,

$$(\boldsymbol{r}_h\boldsymbol{A})|_T = \boldsymbol{r}_T(\boldsymbol{A}|_T), \quad \forall T \in \mathcal{T}_h,$$

where $\boldsymbol{r}_T$ is defined by 3.29. The corresponding, classical error estimate is:

Theorem 3.4.13 ([102, Theorem 5.41]). *Let $\mathcal{T}_{\mathcal{H}}$ be a shape-regular sequence of conforming, tetrahedral, affine meshes of Ω. If $\boldsymbol{A} \in H^s(\Omega)^3$ and $\mathbf{curl}\,\boldsymbol{A} \in H^s(\Omega)^3$ for $1/2 + \delta \leq s \leq k$ for $\delta > 0$ then*

$$\|\boldsymbol{A} - \boldsymbol{r}_h\boldsymbol{A}\|_{L^2(\Omega)^3} + \|\mathbf{curl}(\boldsymbol{A} - \boldsymbol{r}_h\boldsymbol{A})\|_{L^2(\Omega)^3} \leq C(s)h^s \left(\|\boldsymbol{A}\|_{H^s(\Omega)^3} + \|\mathbf{curl}\,\boldsymbol{A}\|_{H^s(\Omega)^3}\right),$$

and

$$\|\mathbf{curl}(\boldsymbol{A} - \boldsymbol{r}_h\boldsymbol{A})\|_{L^2(\Omega)^3} \leq C(s)h^s \|\mathbf{curl}\,\boldsymbol{A}\|_{H^s(\Omega)^3}.$$

Here $C(s)$ is independent of h and both estimates hold tetrahedron by tetrahedron.

Note that in the above theorem the interpolation operator $\boldsymbol{r}_h$ is well defined since $\boldsymbol{H}^s(\Omega) \hookrightarrow L^3(\Omega)$ for all $s > 1/2$ by the Sobolev embedding theorem [54, Theorem 6.7].

Discrete De Rahm Diagram It turns out that for conforming, simplicial meshes $\mathcal{T}_h$ there is an intimate connection between $\mathbb{P}_{k,h}(\Omega)$ and $R_{k,h}(\Omega)$. In fact, the (discrete) *de Rahm diagram* commutes, cf. (2.10) and [102]:

$$\begin{array}{ccccccc}
H^1(\Omega) & \xrightarrow{\mathbf{grad}} & \boldsymbol{H}(\mathbf{curl};\Omega) & \xrightarrow{\mathbf{curl}} & \boldsymbol{H}(\mathrm{div};\Omega) & \xrightarrow{\mathrm{div}} & L^2(\Omega) \\
\cup & & \cup & & \cup & & \\
\tilde{\mathbb{P}}(\Omega) & & \tilde{R}(\Omega) & & \tilde{D}(\Omega) & & \\
\pi_h \big\downarrow & & \boldsymbol{r}_h \big\downarrow & & \boldsymbol{w}_h \big\downarrow & & \Pi_h \big\downarrow \\
\mathcal{P}_{k,h}(\Omega) & \xrightarrow{\mathbf{grad}} & R_{k,h}(\Omega) & \xrightarrow{\mathbf{curl}} & D_{k,h}(\Omega) & \xrightarrow{\mathrm{div}} & \mathcal{P}_{k,h}(\mathcal{T}_h).
\end{array} \tag{3.37}$$

Here $D_{k,h}(\Omega)$ is the space spanned by the Raviart-Thomas $\boldsymbol{H}(\mathrm{div})$ conforming finite elements which is defined similar to the spaces $\mathcal{P}_{k,h}(\Omega)$ and $R_{k,h}(\Omega)$, see [102, Section 5.4]. The space $\tilde{D}(\Omega) \coloneqq H^{1/2+\delta}(\Omega)^3$, $\delta > 0$ is the domain of definition of the Raviart-Thomas interpolation operator $\boldsymbol{w}_h$. Finally, $\Pi_h : L^2(\Omega) \to \mathcal{P}_{k,h}(\mathcal{T}_h)$ is the usual L^2 projection, see for example [55].

Theorem 3.4.14 (Exact discrete Sequence, [74, Theorem 3.7]). *If Ω is simply-connected and has connected boundary, then the two horizontal sequences in* (3.37) *are* exact. *I.e. the range of each operator coincides with the kernel of the following operator.*

For spaces with homogeneous boundary conditions a discrete version of the diagram (2.11) exists and commutes. Moreover, Theorem 3.4.14 carries over to this diagram, see [60] and [23].

Bibliographical notes It is quite simple to define scalar reference finite elements for 2D/3D conforming hybrid meshes that are H^1 conforming, see [20] for explicit basis functions. As long as the underlying mesh remains affine it is also quite simple to give estimates for the projection error that are like Theorem 3.4.10. For non-affine meshes one must replace the notion of shape regularity of a mesh sequence $\mathcal{T}_{\mathcal{H}}$ by more complicated requirements to derive error estimates, see for example [22], [60, Definition 1.124]. Further complications arise when the domain is only approximated by the finite element mesh. This case is usually analyzed for *iso-parameteric* finite elements where the mapping function Φ_T is a polynomial (of the same degree) itself. Using the ideas of Lenoir [93] one can devise a procedure for mapping the finite element solution (obtained on the approximate domain) to the real domain and analyze the approximation error. Generally, the order of the polynomials used for Φ_T should match the order of the reference finite element space $\hat{P}_i$, [30, Section 4.7], [60].

For the $\boldsymbol{H}(\mathbf{curl})$ conforming finite elements, the situation is somewhat similar; The corresponding finite elements are quite classical for affine triangles, quadrilaterals, tetrahedrons, prisms and hexahedras [102] but not for *pyramids* [107], [49], [70]. Also, it is not clear how to deal with non-affine hexahedral/prism elements. Bergot and Duruflé [21] discuss these two issues and define 2D/3D Nédélec elements for hybrid meshes based on "first order geometry mappings" (e.g. trilinear on the hexahedral element) that guarantee the correct rates of convergence based on the inclusion $P_T \supset R_k$ for all reference elements, see also [20]. Interestingly the proposed basis of Bergot and Duruflé [21] is *larger* than the standard basis for affine, hybrid elements [102]. For general curvilinear, triangular elements Vardapetyan and Demkowicz [147] propose the mapping approach that we introduced before. They prove convergence using the chain-rule for the case that the domain Ω is exactly represented by the curvilinear mesh.

The "orientation problem" is discussed in much more detail and from a different point of view in the paper of Ainsworth and Coyle [1]. In particular, they show that it is generally not possible to obtain a $H^1/\boldsymbol{H}(\mathbf{curl})$ conforming basis with only one reference finite element for the tetrahedron . This agrees with our concept of "equivalence classes of reference finite elements", see also [156].

Note that the interpolation operators π_h and $\boldsymbol{r}_h$ are somewhat limited because they are not well-defined for functions living only in $H^1(\Omega)$ or $\boldsymbol{H}(\mathbf{curl};\Omega)$. A possible alternative is the Clément interpolation operator [43], [22] which is however not a projection anymore and does not respect homogeneous boundary conditions. Recently Ern and Guermond [61] have proposed interpolation operators for H^1, $\boldsymbol{H}(\mathbf{curl})$ and $\boldsymbol{H}(\mathrm{div})$ that are stable in L^1, that are projections and that respect homogeneous boundary conditions, but the discrete De Rahm diagram (3.37) does not commute.

3.5 Piecewise Conforming Polynomial Spaces

Throughout this thesis, we will consider approximation spaces that are $H^1/\boldsymbol{H}(\mathbf{curl})$ conforming in a large part of the domain but which are broken across some element boundaries. For example, in Chapter 4 we will break the space along the non-conforming interface between two sliding meshes and in Chapter 5 we will break the space along the surface of the conductor so that we can enrich it with additional shape functions.

In mathematical terms this means that we have a domain decomposition of Ω into subdomains $\tilde{P}_\Omega = \{\tilde{\Omega}_i\}_{i\geq 0}$ such that $\overline{\Omega} = \overline{\bigsqcup_i \tilde{\Omega}_i}$ [3].Moreover, we assume that the sequence of meshes $\mathcal{T}_\mathcal{H}$ is compatible with $\tilde{P}_\Omega$ and that all meshes $\mathcal{T}_h$ are conforming within a subdomain. Therefore, we can split the set of inner faces $\mathcal{F}_h^i = \mathcal{F}_h^{ii} \sqcup \mathcal{F}_h^{ib}$ into faces interior to every subdomain and faces that lie between two subdomains:

$$\mathcal{F}_h^{ib} \coloneqq \left\{ F \in \mathcal{F}_h^i \,\middle|\, F \subset \partial\tilde{\Omega}_i \cap \partial\tilde{\Omega}_j \text{ for some } i,j \right\}, \qquad \mathcal{F}_h^{ii} \coloneqq \mathcal{F}_h^i \setminus \mathcal{F}_h^{ib}.$$

The approximation space for the curl-curl problem is then given by

$$R_{k,h}(\tilde{P}_\Omega) \coloneqq \left\{ \boldsymbol{A}_h \in \boldsymbol{H}(\mathbf{curl}; \tilde{P}_\Omega) \,\middle|\, \boldsymbol{A}_h|_T \in \Phi_T(R_k),\, \forall T \in \mathcal{T}_h \right\}, \tag{3.38}$$

where P_T is the polynomial space of the mapped finite element space of $\hat{P}_T = R_k$ (for tetrahedral meshes). Note that a function $\boldsymbol{A} \in R_{k,h}(\tilde{P}_\Omega)$ is tangentially continuous across faces $F \in \mathcal{F}_h^{ii}$ and tangentially discontinuous across $F \in \mathcal{F}_h^{ib}$. Therefore, we call $R_{k,h}(\tilde{P}_\Omega)$ a piecewise $\boldsymbol{H}(\mathbf{curl})$ conforming space.

We would like to prove an approximation result similar to Theorem 3.4.13 but using the $\|\cdot\|_{\mathrm{WIP},*}$ norm. Because the meshes can be non-conforming between the subdomains $\hat{\Omega}_i$ we must make sure that the local length scale a_F in the definition of the $\|\cdot\|_{\mathrm{WIP}}$ norm does not get to small. I.e. we assume that there is a constant ϱ_1 such that for all $h \in \mathcal{H}$, all $T \in \mathcal{T}_h$ and all $F \in \mathcal{F}_T$ we have

$$a_F \geq \varrho_1 h_T. \tag{3.39}$$

Moreover, we need the technical assumption that there is a constant $\varrho_3 \in \mathbb{N}$ such that for all $h \in \mathcal{H}$, $T \in \mathcal{T}_h$,

$$\mathrm{card}(\mathcal{F}_T) \leq \varrho_3. \tag{3.40}$$

We define the global projection operator $\tilde{\boldsymbol{r}}_h : V^* \to R_{k,h}(\tilde{P}_\Omega)$ element-wise (V^* is defined by (3.3)),

$$(\tilde{\boldsymbol{r}}_h \boldsymbol{A})|_T \coloneqq \boldsymbol{r}_T(\boldsymbol{A}|_T), \quad \forall T \in \mathcal{T}_h.$$

[3] The partition $\tilde{P}_\Omega$ does not necessarily agree with the partition P_Ω introduced in Section 3.3.

$\tilde{\boldsymbol{r}}_h \boldsymbol{A}$ is indeed tangentially continuous across conforming faces $F \in \mathcal{F}_h^{ii}$ because the mapped DOF's of the finite elements of Definition 3.4.12 are equal in the sense of Definition 3.4.3. Hence the local projections $\boldsymbol{r}_T \boldsymbol{A}$ restricted to a conforming face agree on both sides. Also, note that $\boldsymbol{r}_h$ is defined in exactly the same way as $\tilde{\boldsymbol{r}}_h$ but the latter maps to the piecewise conforming space $R_{k,h}(\tilde{P}_\Omega)$ and is thus also defined for (piecewise) non-conforming meshes.

The following theorem then gives an upper bound for the best approximation error of Theorem 3.3.13:

Theorem 3.5.1. *Assume that the exact solution of* (3.2) *is such that* $\boldsymbol{A} \in \boldsymbol{H}(\mathbf{curl}; \Omega) \cap H^s(P_\Omega)^3$, $\mathbf{curl}\, \boldsymbol{A} \in H^s(P_\Omega)^3$ *with integer* $1 \leq s \leq k$. *Then*

$$\|\boldsymbol{A} - \tilde{\boldsymbol{r}}_h \boldsymbol{A}\|_{WIP,*} \leq C \max(\mu_{min}^{-1/2}, \kappa_{max}^{1/2})\, h^{s-1} \sum_i \left(\|\boldsymbol{A}\|_{H^s(\Omega_i)^3} + \|\mathbf{curl}\, \boldsymbol{A}\|_{H^s(\Omega_i)^3} \right).$$

Here C *depends on* ϱ_1, ϱ_3, k *but not on* h, κ *and* μ.

Remark 3.5.2. *By combining Theorem 3.5.1 with Theorem 3.3.13, we see that for a sufficiently smooth exact solution* $\boldsymbol{A}$, *the total error* $\|\boldsymbol{A} - \boldsymbol{A}_h\|_{WIP} = O(h^{k-1})$ *if* k*-th order edge functions are used. In comparison to standard FEM on conforming meshes one order of convergence is lost. Theoretically it is possible that there exists a projector* $\tilde{r}_{h,2}$ *which would give a better rate of convergence, but numerical experiments show that Theorem 3.5.1 is sharp for* $k = 1$ *(Chapter 4).*

In order to prove the above theorem, we will make use of two lemmas to bound the face contributions that appear in the $\|\cdot\|_{\mathrm{WIP}}$ norm.

Lemma 3.5.3. *Let* $\mathcal{T}_h$ *be a shape regular sequence of simplicial, affine meshes of the domain* Ω. *Suppose there is an integer* $1 \leq s \leq k$ *such that* $\boldsymbol{u} \in H^s(\tilde{P}_\Omega)^3$ *and* $\mathbf{curl}\, \boldsymbol{u} \in H^s(\tilde{P}_\Omega)^3$. *Then for all* $T \in \mathcal{T}_h \in \mathcal{T}_\mathcal{H}$

$$\|\boldsymbol{u} - \boldsymbol{r}_h \boldsymbol{u}\|_{L^2(\partial T)^3} \leq C h_T^{s-1/2} \left(\|\boldsymbol{u}\|_{H^s(T)^3} + \|\mathbf{curl}\, \boldsymbol{u}\|_{H^s(T)^3} \right),$$

where C *is independent of* h_T, T.

For the proof of Lemma 3.5.3, we refer the reader to [102, Lemma 5.52] (which is proven element-wise).

Lemma 3.5.4. *Let* $\mathcal{T}_h$ *be shape regular sequence of simplicial, affine meshes of* Ω. *Assume* $\boldsymbol{u} \in H^s(\tilde{P}_\Omega)^3$ *for some integer* $1 \leq s \leq k$. *Then the following estimate holds:*

$$\|\boldsymbol{u} - \boldsymbol{w}_T \boldsymbol{u}\|_{L^2(\partial T)^3} \leq C h_T^{s-1/2} \|\boldsymbol{u}\|_{H^s(T)^3} \quad \forall T \in \mathcal{T}_h \in \mathcal{T}_\mathcal{H},$$

where $\boldsymbol{w}_T : \tilde{D}(T) \to D_k$ *is the standard (local) interpolation operator for* k*-th order Thomas-Raviart elements* D_k *[102, Section 5.4]. The constant* C *does not depend on* h_T, T.

Proof. In order to simplify notation, we let C be an arbitrary constant independent of h, T that may take a different value every time it is used. We note that since $\boldsymbol{u} \in H^s(T)^3$, $\boldsymbol{w}_T$ is well-defined by [102, Lemma 5.15]. Now split the integral over ∂T into its facet contributions,

$$\|\boldsymbol{u} - \boldsymbol{w}_T \boldsymbol{u}\|^2_{L^2(\partial T)^3} = \sum_{F_T \in \mathbb{F}_T} \int_{F_T} |\boldsymbol{u} - \boldsymbol{w}_T \boldsymbol{u}|^2 .$$

Since our mesh contains only tetrahedrons we can find for every $F_T \in \mathbb{F}_T$ a linear transformation $\Phi_{T,F_T} : \hat{T} \to T$ which maps the reference element $\hat{T}$ onto the actual element T such that the pre-image $\hat{F}_T$ of facet F_T lies in the $x - y$ plane of $\hat{T}$,

$$\Phi_{T,F_T} : \hat{\boldsymbol{x}} \mapsto \boldsymbol{B}_{T,F_T} \hat{\boldsymbol{x}} + \boldsymbol{b}_{T,F_T},$$

where $\boldsymbol{B}_{T,F_T} \in \mathbb{R}^{3\times 3}$. Now using the usual change of variables together with the Piola transformation (3.32) we obtain

$$\begin{aligned}
&\int_{F_T} |\boldsymbol{u} - \boldsymbol{w}_T \boldsymbol{u}|^2 \\
&\qquad = \int_{\hat{F}_T} \left|\det(\boldsymbol{B}_{T,F_T})^{-1} \boldsymbol{B}_{T,F_T} \left(\hat{\boldsymbol{u}} - \widehat{\boldsymbol{w}_T \boldsymbol{u}}\right)\right|^2 \left|(\boldsymbol{B}_{T,F_T})_{:,1} \times (\boldsymbol{B}_{T,F_T})_{:,2}\right| \\
&\qquad = \frac{\operatorname{meas}(F_T)}{\operatorname{meas}(\hat{F}_T)\ |\det(\boldsymbol{B}_{T,F_T})|^2} \int_{\hat{F}_T} \left|\boldsymbol{B}_{T,F_T}(\hat{\boldsymbol{u}} - \boldsymbol{w}_{\hat{T}} \hat{\boldsymbol{u}})\right|^2 \\
&\qquad \le C h_T^2 \left|\det(\boldsymbol{B}_{T,F_T})\right|^{-2} \|\boldsymbol{B}_{T,F_T}\|^2 \left\|\hat{\boldsymbol{u}} - \boldsymbol{w}_{\hat{T}} \hat{\boldsymbol{u}}\right\|^2_{L^2(\hat{F}_T)^3} . \qquad (3.41)
\end{aligned}$$

Here $(\boldsymbol{B}_{T,F_T})_{:,i}$ denotes the $i-th$ column of $\boldsymbol{B}_{T,F_T}$, $\widehat{\boldsymbol{w}_T \boldsymbol{u}}$ is defined by the Piola transform (3.32), and we have used that $\widehat{\boldsymbol{w}_T \boldsymbol{u}} = \boldsymbol{w}_{\hat{T}} \hat{\boldsymbol{u}}$ [102, Lemma 5.22]. Now notice that $\hat{\boldsymbol{u}} - \boldsymbol{w}_{\hat{T}} \hat{\boldsymbol{u}} \in H^s(\hat{T})^3$ and thus we can use the trace inequality Theorem 2.2.12,

$$\left\|\hat{\boldsymbol{u}} - \boldsymbol{w}_{\hat{T}} \hat{\boldsymbol{u}}\right\|_{L^2(\hat{F}_T)^3} \le \left\|\hat{\boldsymbol{u}} - \boldsymbol{w}_{\hat{T}} \hat{\boldsymbol{u}}\right\|_{L^2(\partial \hat{T})^3} \le C \left\|\hat{\boldsymbol{u}} - \boldsymbol{w}_{\hat{T}} \hat{\boldsymbol{u}}\right\|_{H^1(\hat{T})^3} .$$

For the next step, we note that $\forall \phi \in \mathbb{P}^{k-1}(\hat{T})^3 \subset D_k(\hat{T})$ we have $\phi = \boldsymbol{w}_{\hat{T}} \phi$ by the definition of $\boldsymbol{w}_{\hat{T}}$. Therefore,

$$\left\|\hat{\boldsymbol{u}} - \boldsymbol{w}_{\hat{T}} \hat{\boldsymbol{u}}\right\|_{H^1(\hat{T})^3} \le \left\|(\boldsymbol{I} - \boldsymbol{w}_{\hat{T}})(\hat{\boldsymbol{u}} + \phi)\right\|_{H^1(\hat{T})^3} \le C \left\|\hat{\boldsymbol{u}} + \phi\right\|_{H^1(\hat{T})^3} ,$$

where we have used that $\boldsymbol{w}_{\hat{T}} : H^1(\hat{T})^3 \to D_k$ is a bounded operator, i.e. $\left\|\boldsymbol{w}_{\hat{T}} \hat{\boldsymbol{u}}\right\|_{H^1(\hat{T})^3} \le C \left\|\hat{\boldsymbol{u}}\right\|_{H^1(\hat{T})^3}$ (cf. Proof of [102, Thm. 5.25]). Since ϕ is arbitrary we can use the Deny-Lions theorem 3.4.7

$$\left\|\hat{\boldsymbol{u}} - \boldsymbol{w}_{\hat{T}} \hat{\boldsymbol{u}}\right\|_{L^2(\hat{T})^3} \le C \inf_{\phi \in \mathbb{P}^{k-1}(\hat{T})^3} \left\|\hat{\boldsymbol{u}} + \boldsymbol{\phi}\right\|_{H^1(\hat{T})^3} \le C \left|\hat{\boldsymbol{u}}\right|_{H^s(\hat{T})^3} . \qquad (3.42)$$

Finally, we have to map $\left|\hat{\boldsymbol{u}}\right|_{H^s(\hat{T})^3}$ back to the actual element T. For this observe that using (3.32),

$$\frac{\partial^\alpha}{\partial \hat{\boldsymbol{x}}^\alpha} \hat{\boldsymbol{u}} = \det(\boldsymbol{B}_{T,F_T})\, \boldsymbol{B}^{-1}_{T,F_T} \frac{\partial^\alpha}{\partial \hat{\boldsymbol{x}}^\alpha} (\boldsymbol{u} \circ \Phi_T)$$

with $|\alpha|_{\ell^1} = s$ being a multi-index. Therefore,

$$|\hat{\boldsymbol{u}}|^2_{H^s(\hat{T})^3} = \sum_{|\alpha|_{\ell^1}=s} \int_{\hat{T}} \left| \frac{\partial^\alpha \hat{\boldsymbol{u}}}{\partial \hat{\boldsymbol{x}}^\alpha} \right|^2 \leq |\det(\boldsymbol{B}_{T,F_T})|^2 \left\| \boldsymbol{B}^{-1}_{T,F_T} \right\|^2 \sum_{|\alpha|_{\ell^1}=s} \int_{\hat{T}} \left| \frac{\partial^\alpha (\boldsymbol{u} \circ \Phi_T)}{\partial \hat{\boldsymbol{x}}^\alpha} \right|^2$$
$$\leq C \, |\det(\boldsymbol{B}_{T,F_T})|^2 \left\| \boldsymbol{B}^{-1}_{T,F_T} \right\|^2 \|\boldsymbol{B}_{T,F_T}\|^{2s} \, |\det(\boldsymbol{B}_{T,F_T})|^{-1} \, |\boldsymbol{u}|^2_{H^s(T)^3} \,, \qquad (3.43)$$

where we have used [102, Lemma 5.9] in the last step. Now combining (3.41-3.43) gives

$$\|\boldsymbol{u} - \boldsymbol{w}_T \boldsymbol{u}\|^2_{L^2(F_T)^3}$$
$$\leq C \, |\det(\boldsymbol{B}_{T,F_T})|^{-1} \, h_T^2 \, \|\boldsymbol{B}_{T,F_T}\|^2 \left\| \boldsymbol{B}^{-1}_{T,F_T} \right\|^2 \|\boldsymbol{B}_{T,F_T}\|^{2s} \, |\boldsymbol{u}|^2_{H^s(T)^3}$$
$$\leq C h_T^{2s-1} \, |\boldsymbol{u}|^2_{H^s(T)^3} \,.$$

Here we have used [102, Lemma 5.10] together with the fact that the mesh sequence is shape regular. Now summing over all facets $F_T \in \mathbb{F}_T$ yields the assertion. □

Using these lemmas, we can finally give a bound for $\|\boldsymbol{A} - \tilde{\boldsymbol{r}}_h \boldsymbol{A}\|_{\mathrm{WIP},*}$.

Proof of Theorem 3.5.1. In this proof C denotes an arbitrary positive constant that is independent of h, μ, κ. Since $\tilde{\boldsymbol{r}}_h \boldsymbol{A}$ is tangentially continuous across $F \in \mathcal{F}_h^{ii}$ and since $\boldsymbol{A}$ is tangentially continuous across all inner faces $F \in \mathcal{F}_h^i$ only jump terms across $F \in \mathcal{F}_h^{ib} \cup \mathcal{F}_h^b$ remain in the definition of the jump semi-norm $|\cdot|_{j,\mu}$, i.e. we have to bound

$$\|\boldsymbol{A} - \tilde{\boldsymbol{r}}_h \boldsymbol{A}\|^2_{\mathrm{WIP},*} = \underbrace{\left\| \mu^{-1/2} \, \mathbf{curl}(\boldsymbol{A} - \tilde{\boldsymbol{r}}_h \boldsymbol{A}) \right\|^2_{L^2(\Omega)^3}}_{:=T_1} + \underbrace{\left\| \sqrt{|\kappa|} (\boldsymbol{A} - \tilde{\boldsymbol{r}}_h \boldsymbol{A}) \right\|^2_{L^2(\Omega)^3}}_{:=T_2}$$
$$+ \underbrace{\sum_{F \in \mathcal{F}_h^b \cup \mathcal{F}_h^{ib}} \frac{\gamma_{\mu,F}}{a_F} \, \|[\![\boldsymbol{A} - \tilde{\boldsymbol{r}}_h \boldsymbol{A}]\!]_\tau\|^2_{L^2(F)^3}}_{:=T_3} + \underbrace{\sum_{T \in \mathcal{T}_h} h_T \left\| \mu^{-1/2} \, \mathbf{curl} \, (\boldsymbol{A} - \tilde{\boldsymbol{r}}_h \boldsymbol{A})|_T \right\|^2_{L^2(\partial T)^3}}_{:=T_4} .$$

Since μ and κ are constant on each element T_1 and T_2 are easily bounded using 3.4.13 (which holds element-wise!):

$$T_1 + T_2 \leq 2 \max(\mu_{\min}^{-1}, \kappa_{\max}) \left\{ \|\mathbf{curl}(\boldsymbol{A} - \tilde{\boldsymbol{r}}_h \boldsymbol{A})\|^2_{L^2(\Omega)^3} + \|\boldsymbol{A} - \tilde{\boldsymbol{r}}_h \boldsymbol{A}\|^2_{L^2(\Omega)^3} \right\},$$
$$\leq C \max(\mu_{\min}^{-1}, \kappa_{\max}) h^{2s} \sum_i \left(\|\boldsymbol{A}\|^2_{H^s(\Omega_i)^3} + \|\mathbf{curl} \, \boldsymbol{A}\|^2_{H^s(\Omega_i)^3} \right).$$

The term T_3 is bounded using Lemma 3.5.3,

$$T_3 \leq \mu_{\min}^{-1} \sum_{F \in \mathcal{F}_h^b \cup \mathcal{F}_h^{ib}} a_F^{-1} \left(\|\boldsymbol{A} - \tilde{\boldsymbol{r}}_h \boldsymbol{A}|_{T_1}\|^2_{L^2(F)^3} + \|\boldsymbol{A} - \tilde{\boldsymbol{r}}_h \boldsymbol{A}|_{T_2}\|^2_{L^2(F)^3} \right)$$

$$
\begin{aligned}
&\leq C\mu_{\min}^{-1} \sum_{T\in\mathcal{T}_h} \sum_{F\in\mathcal{F}_T\cap(\mathcal{F}_h^b\cup\mathcal{F}_h^{ib})} h_T^{-1} \left\|\boldsymbol{A}-\tilde{\boldsymbol{r}}_h\boldsymbol{A}|_T\right\|_{L^2(F)^3}^2 \\
&\leq C\mu_{\min}^{-1} \sum_{T\in\mathcal{T}_h} \sum_{F\in\mathcal{F}_T\cap(\mathcal{F}_h^b\cup\mathcal{F}_h^{ib})} h_T^{2s-2} \left(\|\boldsymbol{A}\|_{H^s(T)^3}^2 + \|\mathbf{curl}\,\boldsymbol{A}\|_{H^s(T)^3}^2\right) \\
&\leq C\mu_{\min}^{-1} h^{2s-2} \sum_i \left(\|\boldsymbol{A}\|_{H^s(\Omega_i)^3}^2 + \|\mathbf{curl}\,\boldsymbol{A}\|_{H^s(\Omega_i)^3}^2\right).
\end{aligned}
$$

Here we have used that $a_F \geq \varrho_1 h_T$ and $\operatorname{card}(\mathcal{F}_T) < \varrho_3$.

To bound the term T_4, we first note that the local Thomas-Raviart interpolation operator w_T is well defined by [102, Lemma 5.15]. Thus, $\mathbf{curl}\,[\boldsymbol{r}_T\boldsymbol{A}] = \boldsymbol{w}_T(\mathbf{curl}\,\boldsymbol{A})$ by [102, Lemma 5.40] and we can bound T_4 as follows:

$$
\begin{aligned}
T_4 &\leq \mu_{\min}^{-1} \sum_{T\in\mathcal{T}_h} h_T \left\|\mathbf{curl}\,\boldsymbol{A} - \boldsymbol{w}_T(\mathbf{curl}\,\boldsymbol{A})\right\|_{L^2(\partial T)^3}^2 \\
&\leq C\mu_{\min}^{-1} \sum_{T\in\mathcal{T}_h} h_T^{2s} \left\|\mathbf{curl}\,\boldsymbol{A}\right\|_{H^s(T)^3}^2 \leq C\mu_{\min}^{-1} h^{2s} \sum_i \left\|\mathbf{curl}\,\boldsymbol{A}\right\|_{H^s(\Omega_i)^3}^2,
\end{aligned}
$$

where we have used Lemma 3.5.4 and the fact that $h_T \leq h \leq \operatorname{diam}(\Omega)$. □

Remark 3.5.5. *The proof of Theorem 3.5.1 shows that for h sufficiently small the term T_3 dominates the other three terms and is thus responsible for the loss of one order of convergence as pointed out in Remark 3.5.2. Interestingly T_3 sums the jump terms only over the faces $\mathcal{F}_h^b \cup \mathcal{F}_h^{ib}$. This suggests that it suffices to use $(k+1)$-th order edge functions in elements adjacent to $\mathcal{F}_h^b \cup \mathcal{F}_h^{ib}$ and k-th order edge functions everywhere else to achieve $O(h^k)$ order convergence. This can be implemented easily by using a hierarchical basis for the edge functions [21].*

Moreover, if the whole mesh $\mathcal{T}_h$ is conforming and if we incorporate the Dirichlet boundary conditions (3.2b) *into the trial space (cf. Remark 3.3.16) we see that term T_3 completely drops out of the above proof and we get $O(h^k)$ order of convergence with k-th order edge functions. This is not surprising because in this case the WIP-formulation* (3.6) *reduces to the standard FEM formulation for which convergence of order $O(h^k)$ is easily proven.*

3.5.1 Interpolation Estimate for the Broken Polynomial Space $\mathbb{P}_{k,h}(\mathcal{T}_h)$

We remark that Theorem 3.5.1 is very general because it employs the interpolation operator $\tilde{\boldsymbol{r}}_h$ which guarantees that $\tilde{\boldsymbol{r}}_h\boldsymbol{A}$ is tangentially continuous across conforming, interior faces of the mesh. On the other hand, this "generality" complicates the proof considerably because the local interpolation operator $\boldsymbol{r}_T$ must be defined using the notion of a *Finite Element*. An alternative would be to use the *completely discontinuous* approximation space

$$
\mathbb{P}_{k,h}(\mathcal{T}_h) \coloneqq \left\{ f \in L^2(\Omega) \,\middle|\, \forall T \in \mathcal{T}_h,\, f|_T \in \mathbb{P}_k \right\},
$$

and to use the L^2 projection operator $\Pi_h^3 : L^2(\Omega)^3 \to \mathbb{P}_{k,h}(\mathcal{T}_h)^3$. This is the approach taken by many texts on DG, see for example [55]. In the following we shortly present an interpolation estimate for such an approach.

We first state the following well-known interpolation estimates for the L^2 projection operator:

Lemma 3.5.6. *Let $\mathcal{T}_\mathcal{H}$ be a shape-regular sequence of hybrid, affine meshes. Let Π_h be the L^2 projection operator onto $\mathbb{P}_{k,h}(\mathcal{T}_h)$. Then for all $s \in \{0, \dots, k+1\}$, all $h \in \mathcal{H}$, all $T \in \mathcal{T}_h$, and all $f \in H^s(T)$,*

$$|f - \Pi_h f|_{H^m(T)} \leq C h_T^{s-m} |f|_{H^s(T)} \quad \forall m \in \{0, \dots, s\},$$

where C is independent of T and h.

The proof applies the Deny-Lions Theorem 3.4.7 on the reference element and then uses the inverse inequality to estimate the derivatives of $f - \Pi_h f$, cf. proof of [55, Lemma 1.62] (which also holds for the more general mesh sequence considered here).

Lemma 3.5.7. *Under the assumptions of Lemma 3.5.6 assume additionally that $s \geq 1$. Then for all $h \in \mathcal{H}$, all $T \in \mathcal{T}_h$, and all $F \in \mathcal{F}_T$,*

$$\|f - \Pi_h f\|_{L^2(F)} \leq C_1 h_T^{s-1/2} |f|_{H^s(T)},$$

and if $s \geq 2$,

$$\|\mathbf{grad}\,(f - \Pi_h f)\|_{L^2(F)^3} \leq C_2 h_T^{s-3/2} |f|_{H^s(T)},$$

where C_1, C_2 are independent of T, h.

The proof of this Lemma first employs the trace theorem 2.2.15 on the reference element and then uses the above Lemma 3.5.6, see also [55, Lemma 1.59].

Finally, we can give a bound on the interpolation error:

Theorem 3.5.8. *Let $\mathcal{T}_\mathcal{H}$ be a shape-regular sequence of hybrid, affine meshes and let $\Pi_h^3 : L^2(\Omega)^3 \to \mathbb{P}_{k,h}(\mathcal{T}_h)^3$ be the L^2 projection operator. Assume that the exact solution of (3.2) is such that $\boldsymbol{A} \in \boldsymbol{H}(\mathbf{curl}; \Omega) \cap H^{s+1}(P_\Omega)^3$ with integer $1 \leq s \leq k$. Then*

$$\left\| \boldsymbol{A} - \Pi_h^3 \boldsymbol{A} \right\|_{WIP,*} \leq C h^s \max(\mu_{min}^{-1/2}, \kappa_{max}^{1/2}) \sum_i \|\boldsymbol{A}\|_{H^{s+1}(\Omega_i)^3},$$

where C is independent of h, μ, κ but depends on ϱ_1, ϱ_3, k.

Proof. Let C denote an arbitrary positive constant that is independent of h, μ, κ. We must bound:

$$\left\|\boldsymbol{A}-\Pi_h^3\boldsymbol{A}\right\|_{\mathrm{WIP},*}^2 = \underbrace{\left\|\mu^{-1/2}\,\mathbf{curl}(\boldsymbol{A}-\Pi_h^3\boldsymbol{A})\right\|_{L^2(\Omega)^3}^2}_{:=T_1} + \underbrace{\left\|\sqrt{|\kappa|}(\boldsymbol{A}-\Pi_h^3\boldsymbol{A})\right\|_{L^2(\Omega)^3}^2}_{:=T_2}$$
$$+ \underbrace{\sum_{F\in\mathcal{F}_h}\frac{\gamma_{\mu,F}}{a_F}\left\|\left[\!\left[\boldsymbol{A}-\Pi_h^3\boldsymbol{A}\right]\!\right]_\tau\right\|_{L^2(F)^3}^2}_{:=T_3} + \underbrace{\sum_{T\in\mathcal{T}_h} h_T\left\|\mu^{-1/2}\,\mathbf{curl}\,(\boldsymbol{A}-\Pi_h^3\boldsymbol{A})|_T\right\|_{L^2(\partial T)^3}^2}_{:=T_4}.$$

In order to bound T_1 we use that $\|\mathbf{curl}\,\boldsymbol{u}\|_{L^2(T)^3}^2 \le 2\,|\boldsymbol{u}|_{H^1(T)^3}^2$ and apply Lemma 3.5.6:

$$T_1 \le \mu_{\min}^{-1}\sum_{T\in\mathcal{T}_h}\left|\boldsymbol{A}-\Pi_h^3\boldsymbol{A}\right|_{H^1(T)^3}^2 \le \mu_{\min}^{-1}C\sum_{T\in\mathcal{T}_h} h_T^{2s}\,|\boldsymbol{A}|_{H^{s+1}(T)^3}^2.$$

Term T_2 is also bounded using Lemma 3.5.6, $T_2 \le \kappa_{\max}Ch^{2s}\,|\boldsymbol{A}|_{H^{s+1}(P_\Omega)^3}^2$. For term T_3, we use of Lemma 3.5.7 component wise and (3.40) to get

$$T_3 \le \mu_{\min}^{-1}\sum_{T\in\mathcal{T}_h}\sum_{F\in\mathcal{F}_T}\frac{1}{a_F}\left\|\boldsymbol{A}-\Pi_h^3\boldsymbol{A}\right\|_{L^2(F)^3}^2 \le C\mu_{\min}^{-1}\sum_{T\in\mathcal{T}_h}\sum_{F\in\mathcal{F}_T}\frac{h_T^{2s+1}}{h_T}\,|\boldsymbol{A}|_{H^{s+1}(T)^3}^2.$$

Finally, for the last term T_4 we use the second part of Lemma 3.5.7 component wise,

$$T_4 \le 2\mu_{\min}^{-1}\sum_{T\in\mathcal{T}_h} h_T\left|\boldsymbol{A}-\Pi_h^3\boldsymbol{A}\right|_{H^1(\partial T)^3}^2 \le C\mu_{\min}^{-1}\sum_{T\in\mathcal{T}_h} h_T h_T^{2s-1}\,|\boldsymbol{A}|_{H^{s+1}(T)^3}^2.$$

□

Remark 3.5.9. *Choosing $V_h = \mathbb{P}_{k,h}(\mathcal{T}_h)^3$ in Theorem 3.3.13 we see that $\|\boldsymbol{A}-\boldsymbol{A}_h\|_{WIP} = O(h^k)$, i.e. we* don't *lose one order of convergence. The reason for this is that the space $\mathbb{P}_{k,h}(\mathcal{T}_h)^3$ spans the whole space $\mathbb{P}_k(F)^3$ on each face $F\in\mathcal{F}_h$ whereas the restriction of the space $R_{k,h}(\tilde{P}_\Omega)$ to a face F only includes the space $\mathbb{P}_{k-1}(F)^3$. Therefore, the interpolation estimates in the $|\cdot|_{j,\mu}$ semi-norm are one order higher for $\mathbb{P}_{k,h}(\mathcal{T}_h)^3$ than for $R_{k,h}(\tilde{P}_\Omega)$. See also Remark 3.5.2.*

Finally, we would like to point out that a similar analysis can be carried out for the scalar valued, 2D eddy current problem (3.22), see e.g. [57], [55]. The results are very similar to the one for the generic curl-curl problem but *one does not lose one order of convergence* because one chooses $V_h = \mathbb{P}_{k,h}(\tilde{P}_\Omega)$ (piecewise conforming), respectively $V_h = \mathbb{P}_{k,h}(\mathcal{T}_h)$ (completely discontinuous).

3.6 The Local Length Scale a_F

So far, we have assumed that the local length-scale a_F fulfills (3.9), (3.39), (3.40) to derive a-priori error estimates, i.e. $0 < \varrho_1 h_T < a_F < \varrho_2 h_T$. We will now study the following three concrete choices for a_F:

- $a_F^{(1)} := \frac{1}{2}(h_{T_1} + h_{T_2})$ if $F \in \mathcal{F}_h^i$ and $a_F^{(1)} = h_T$ for $F \in \mathcal{F}_h^b$, see [55, Remark 4.6],
- $a_F^{(2)} := \min(h_{T_1}, h_{T_2})$ if $F \in \mathcal{F}_h^i$ and $a_F^{(2)} = h_T$ for $F \in \mathcal{F}_h^b$, see [79],
- $a_F^{(3)} := h_F$ if $F \in \mathcal{F}_h$, see [55, 140],

where h_{T_1}, h_{T_2} are the diameters of the adjacent elements of face F and h_F is the diameter of face F. It turns out that for each choice of a_F we must make additional assumptions on the mesh such that a_F fulfills (3.9), (3.39). So once we have chosen a concrete a_F we can think of ϱ_1, ϱ_2 as mesh dependent parameters. The important point is that the constants in Theorems 3.3.13, 3.3.20 and 3.4.13 depend on the constants $\sigma_{\mathcal{H}}$, ϱ_1, ϱ_2 but they do not depend in any other way on the shape of the underlying meshes. So the question is under what conditions does a sequence of meshes $\mathcal{T}_{\mathcal{H}}$ have ϱ_1, ϱ_2 that are independent of h? The following result gives a sufficient condition for this to hold:

Lemma 3.6.1 (Local Quasi-Uniformity). *Let $\mathcal{T}_{\mathcal{H}}$ be a sequence of meshes and assume there is a constant $0 < C \leq 1$ such that for all $h \in \mathcal{H}$, all pairs of elements T_1, $T_2 \in \mathcal{T}_h$ that share face $F = \partial T_1 \cap \partial T_2$:*

$$Ch_{T_1} \leq h_{T_2} \leq C^{-1} h_{T_1}. \tag{3.44}$$

Then $a_F^{(1)}$ and $a_F^{(2)}$ fulfill conditions (3.9) *and* (3.39) *and ϱ_1, ϱ_2 depend only on C. Moreover* (3.40) *holds.*

Remark 3.6.2. *If $\mathcal{T}_{\mathcal{H}}$ is a shape-regular sequence of affine meshes, condition* (3.44) *holds automatically for a* conforming *face $F = \partial T_1 \cap \partial T_2$ since $h_{T_1} \leq \sigma_{\mathcal{H}} \rho_{T_1} \leq \sigma_{\mathcal{H}} h_F \leq \sigma_{\mathcal{H}} h_{T_2}$. So for shape-regular sequences of affine meshes condition* (3.44) *must only be checked for non-conforming intersections.*

Assume for a moment that $\mathcal{T}_h$ is partitioned into two conforming, shape-regular, affine sequences of submeshes, $\mathcal{T}_{\mathcal{H},1}$ and $\mathcal{T}_{\mathcal{H},2}$ that slide against each other, cf. Chapter 4. Then Lemma 3.6.1 implies that there is an upper bound on the total error $\|\boldsymbol{A} - \boldsymbol{A}_h\|_{\mathrm{WIP}}$ that is independent of the relative position of $\mathcal{T}_{\mathcal{H},1}$ to $\mathcal{T}_{\mathcal{H},2}$ and that tends to 0 as $h \to 0$.

Finally note that $a_F^{(3)}$ clearly fulfills conditions (3.9), (3.39) for a shape-regular sequence of conforming, affine meshes. However for non-conforming mesh sequences (3.39) does generally not hold because h_F can become arbitrarily small. In particular it does not hold for sliding meshes as discussed in Chapter 4. Nevertheless, using $a_F^{(3)}$ in the WIP-formulation (3.6) seems to work in practice for sliding meshes.

4 DG Treatment of Non-Conforming Interfaces

In some applications, such as the simulation of electric machines or magnetic actuators, magnetic fields must be computed in the presence of moving, rigid parts. Then one may use separate, moving sub-meshes for them to avoid remeshing. However, this leads to so-called "sliding-interfaces", i.e. meshes with hanging nodes (cf. Figure 4.1).

Figure 4.1: *Sliding Meshes.* Initially conforming sub-meshes become non-conforming when the upper sub-mesh starts moving.

In this chapter, we aim at constructing a method that approximates the solution of the regularized magnetostatic/eddy current problem in a way that is independent of the "non-conformity" of the sub-meshes at the common interface. This problem has been tackled successfully in the framework of Mortar methods where the continuity constraints are incorporated directly into the trial space [118, 119, 37] or they are enforced by additional Lagrange multipliers [151, 19]. However, they come at the price of introducing either non-local shape functions or additional unknowns.

A more elegant approach is the hybrid coupling introduced by Rodríguez et al. [125]: The idea is to use an $\boldsymbol{E}$ based eddy current formulation in the insulator Ω_0 and a $\boldsymbol{H}$ based formulation inside the conductor Ω_σ. Using integration by parts in each subdomain, the two formulations are naturally coupled to each other across a non-conforming mesh interface. It is not clear whether this simple scheme is discretely stable but it can be stabilized by placing additional constraints on the edge element space [125, Section 3.2].

Another approach uses the Discontinuous Galerkin (DG) framework to deal with hanging nodes. In [7] the 2D eddy current problem is coupled across the non-conforming interface by the Locally Discontinuous Galerkin method (LDG), see also [115] and our remarks at the end of Section 3.3. This technique is extended to the 3D (time-harmonic) eddy current problem to deal with hanging nodes introduced by *hp*-refinement [116]. In this work the eddy current problem is *ellipticized* by introducing an additional **grad**(div) term and hence additional assumptions on the smoothness of the solution must be made to prove convergence.

Alternatively, one can use a mixed DG-formulation and enforce the gauge condition $\operatorname{div}(\mu^{-1}\boldsymbol{A}) = 0$ explicitly to avoid the introduction of a regularization term [79]. The stability of this method for arbitrary, sliding meshes remains unclear: In [79] it is proven that the mixed method yields the expected rates of convergence on conforming meshes and the experimental results in [78] show that it works on k-irregular meshes obtained from *hp*-refinement. However, considering the results of Section 4.1.2 and in [38], it is not clear that the constant in the inf-sup condition [79] is independent of the "non-conformity" of the sub-meshes at the common interface.

Hollaus et al. [77] have successfully used the symmetric interior penalty method to couple the full, *time-harmonic* Maxwell's equations across sliding interfaces. The formulation is very similar to the SWIP formulation (3.6) but it has two additional "twists": First the solution $\boldsymbol{A}$ is represented by a high-order B-spline basis along the sliding interface which makes the numerical integration over the non-conforming meshes easier. Secondly, an additional scalar field is introduced along the sliding interface to avoid over-penalization of gradient fields and to achieve better stability at low-frequencies. Finally, we remark that edge elements of the second kind, which span the full polynomial space $\mathbb{P}_k^3$, have been used in Hollaus et al. [77] so that $O(h^k)$ convergence can be expected, cf. Remark 3.5.9. Unfortunately, a full error analysis for this method was never published.

Since our code, HyDi, can integrate shape functions also over non-conforming interfaces (Chapter 6) and since we are only interested in the eddy current problem we don't need the additional "twists" of [77] and can apply the SWIP formulation directly. We will first consider the regularized magnetostatic problem on arbitrary, non-conforming meshes and then present a method for the simulation of the 3D eddy current problem in the time-domain for moving bodies.

4.1 Magnetostatics

This section presents a series of numerical experiments where the regularized magnetostatic problem (2.25) is solved on a 3D sphere with radius 1 using the SWIP ($\theta = -1$) formulation (3.6). This sphere is split into two hemispheres, $\tilde{\Omega}_0$ and $\tilde{\Omega}_1$ (cf. Section 3.5). We generate a sequence of quasi-uniform meshes $\mathcal{T}_h$ that are compatible with the partition $\tilde{P}_\Omega = \{\tilde{\Omega}_0, \tilde{\Omega}_1\}$ using first order tetrahedrons. The two sub-meshes can

then be rotated by an angle ϑ against each other to create meshes with arbitrary "non-conformity", cf. Figure 4.2.

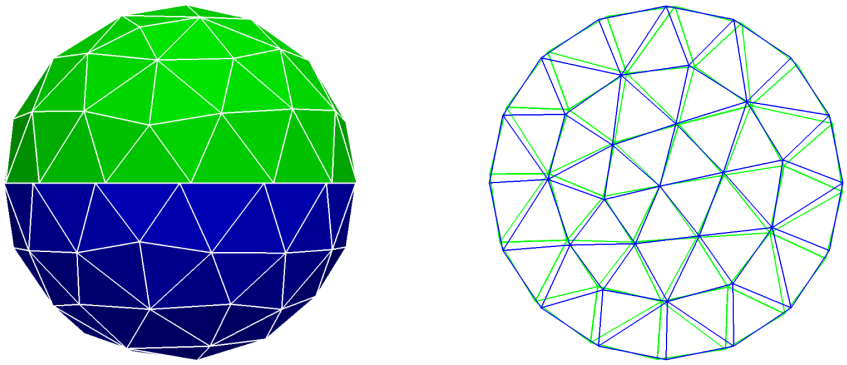

Figure 4.2: *The meshes for the two half spheres.* The upper hemisphere is turned against the lower hemisphere by $\vartheta = 0.05\,\text{rad}$ to create a non-conforming mesh.

4.1.1 Choice of Local Length Scale, h-Convergence

In Section 3.6, we have introduced three choices for the local length scale a_F in (3.6). We will now study these three choices numerically: We impose the analytical solution $\boldsymbol{A} = (\sin y, \cos z, \sin x)$ and choose $\boldsymbol{j}^i$, $\boldsymbol{g}_d$ such that they fulfill (3.2) with $\kappa \equiv \varepsilon = 10^{-6}$, $\mu \equiv 1$.

Figure 4.3 shows the error in the curl-semi norm $|\cdot|_{\boldsymbol{H}(\mathbf{curl};\Omega)}$ for different angles of rotation, for all three choices of a_F and for different mesh-sizes h. We can see that although the error depends slightly on the angle, it converges to zero in all three formulations as h is decreasing. Moreover, we see that the choices $a_F^{(1)}$, $a_F^{(2)}$ yield similar results which are slightly better than the choice $a_F^{(3)}$.

In order to illustrate the best approximation estimates of Theorems 3.3.13 and 3.5.1 we plot the error for a series of quasi-uniform meshes in Figure 4.4 for $a_F = a_F^{(3)}$ [1]. We observe no convergence for first order edge functions which implies that Theorem 3.5.1 is sharp for $k = 1$. For $k = 2$ and $k = 3$ we observe rates of convergence $O(h^{1.5})$ and $O(h^{2.7})$, respectively, which corroborates Theorems 3.3.13 and 3.5.1.

We note that for $V_h = \mathbb{P}_{k,h}(\mathcal{T}_h)$ we observe the rate of convergence $O(h)$, i.e. we do not lose one order of convergence. This agrees with Theorem 3.5.8.

Remark 4.1.1. *The observed rates for $k = 2$ and $k = 3$ are higher than the rates $O(h)$, $O(h^2)$ guaranteed by Theorem 3.5.1. This is due to the better approximation properties of edge functions in the* inside *of the two hemispheres, cf. Remark 3.5.5.*

[1] Based on the results of Figure 4.3 we can expect similar behavior for all three choices of a_F.

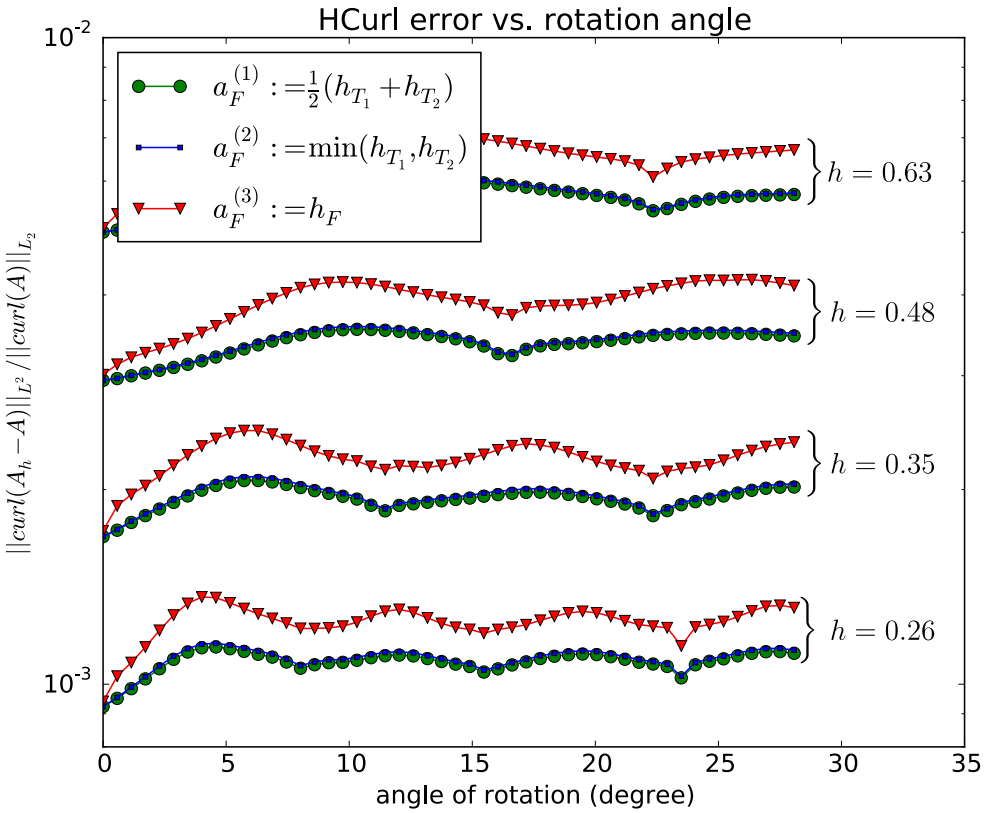

Figure 4.3: The relative L^2 error in $\boldsymbol{B}_h = \mathbf{curl}\, \boldsymbol{A}_h$ vs. the rotation angle for three different choices of a_F and four different mesh-sizes. Second order edge functions, $V_h = R_{2,h}(\tilde{P}_\Omega)$, were used for discretization, and $\eta = 50$. Note that the curve for $a_F^{(2)}$ is partially hidden by the one of $a_F^{(1)}$.

Remark 4.1.2. *Figure 4.4 also contains the errors for the angle $\vartheta = 0$ for which the meshes $\mathcal{T}_h$ are conforming. But since we still enforce the inhomogeneous Dirichlet boundary conditions* (3.2b) *on $\partial\Omega$ by penalization, we do not get the expected order $O(h^k)$ for k-th order edge functions, cf. Remark 3.5.5. Alternatively, one could try to incorporate the inhomogeneous Dirichlet boundary conditions into the approximation spaces V_h, cf. Remark 3.3.16. It is however not clear how this should be done for the case that we consider here because the mesh is non-conforming and there are very small, non-conforming boundary faces $F \in \mathcal{F}_h^b$ for $\vartheta > 0$ on which the boundary condition* (3.2b) *should also be enforced.*

Remark 4.1.3. *Strictly speaking our computational domain Ω is not exactly a sphere, i.e. there is a sequence of polyhedral domains Ω_h that converge to Ω for $h \to 0$. In particular, we enforce the inhomogeneous Dirichlet boundary condition* (3.2b) on $\partial\Omega_h$

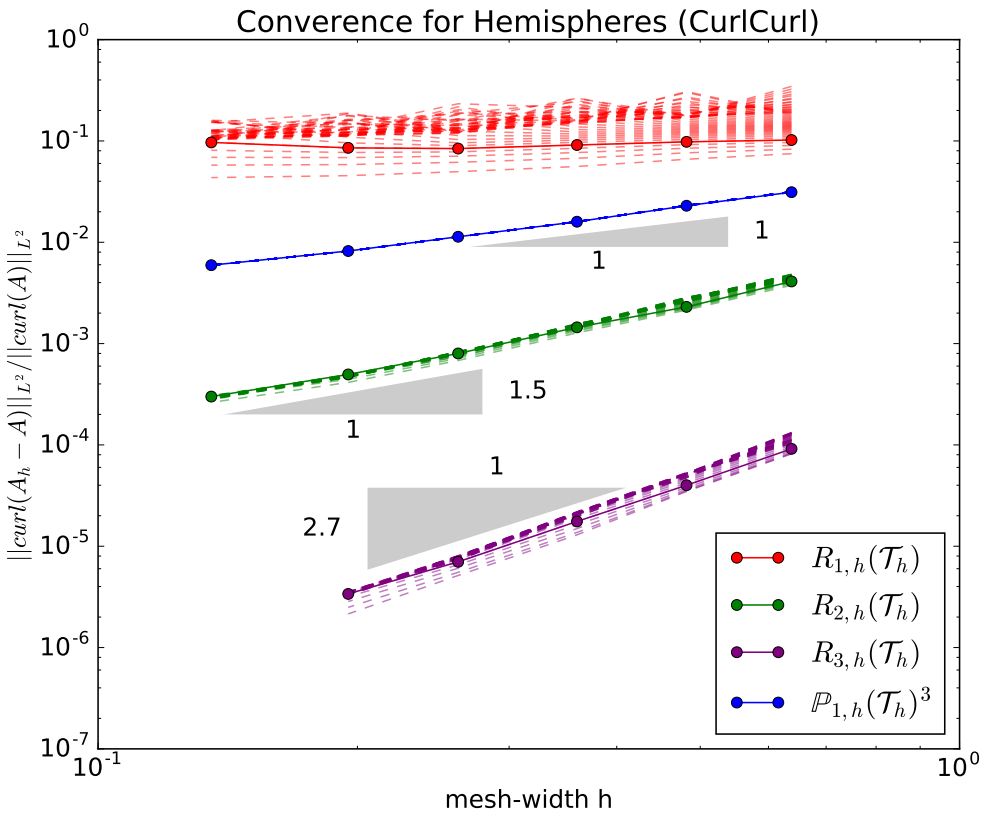

Figure 4.4: The relative L^2 error in $\boldsymbol{B}_h = \mathbf{curl}\,\boldsymbol{A}_h$ vs. the mesh size h for rotation angle $\vartheta = 5 \cdot 10^{-2}$ rad (solid lines). The dashed lines correspond to $\vartheta = n \cdot 10^{-2}$ rad, $n \in \{0, 1, \ldots, 49\}$. $a_F = h_F$, $\kappa \equiv 10^{-6}$, $\eta = 50$, $\mu \equiv 1$.

and not on $\partial\Omega$. Therefore, the numerical experiment does not exactly fit the framework developed in Chapter 3 because Ω changes as $h \to 0$. However, Figure 4.4 suggests that the order of convergence for $k = 2$, $k = 3$ is the same as if Ω was a polyhedron.

4.1.2 Regularization

So far, we have looked at the regularized system (2.25) and it was shown that the SWIP method yields the expected rates of convergence for $\kappa = \varepsilon > 0$ (κ defined as in (3.2)). However, genuine magnetostatics amounts to choosing $\kappa \equiv \varepsilon \equiv 0$. We will consider two approaches to obtain an approximate solution $\boldsymbol{A}_h$ for $\varepsilon = 0$: First, we will try to set $\varepsilon = 0$ directly in the SWIP formulation (3.6) and secondly, we will study the effect of choosing ε small enough such that the error due to regularization is negligible, cf. Section 2.5.1.

The case $\kappa \equiv \varepsilon = 0$

Setting $\kappa = 0$ in (3.6) is equivalent to solving the ungauged magnetostatic problem (2.21) which does not have a unique solution. Indeed, the continuous $\mathbf{curl} - \mathbf{curl}$ operator has an infinite dimensional kernel and the non-zero eigenvalues are well separated from 0 (Section 4.1). If one uses $\boldsymbol{H}(\mathbf{curl})$ conforming edge elements on a conforming mesh this property carries over (Theorem 3.4.14), i.e. edge functions of the first kind yield a spectrally accurate discretization of the $\mathbf{curl} - \mathbf{curl}$ operator. It has been shown that this property also holds for the SWIP formulation on *conforming meshes* [34]. However, the numerical experiments in [38] suggest that spurious eigenvalues appear on general non-conforming meshes.

Therefore, we investigate the spectrum of the $a_h^{\theta\text{WIP}}$ bilinear form ($\theta = -1$) in a numerical experiment. The setup is like the one in the previous section: The domain Ω consists of two half-spheres which can be rotated against each other by an angle ϑ. However, this time we only assemble the matrix of the $a_h^{\theta\text{WIP}}$ bilinear form with $\kappa \equiv \varepsilon = 0$, $a_F = a_F^{(3)}$ [2] and compute its eigenvalues using the `eig` routine of MATLAB R2013a.

Figure 4.5 shows the smallest and largest non-zero eigenvalues of the SWIP formulation for different mesh-widths h and different angles ϑ (dashed, blue lines) [3]. For comparison, we have also plotted the eigenvalues of a standard $\boldsymbol{H}(\mathbf{curl})$ conforming discretization using second order edge functions on the conforming grid $\vartheta = 0$ (green lines).

We see that the bandwidth of the SWIP eigenvalues is comparable to the bandwidth of the $\boldsymbol{H}(\mathbf{curl})$ conforming discretization for many angles. But we also observe that for some angles the lower end of the spectrum tends to zero. In order to better understand this phenomenon, we plotted the smallest and the largest non-zero eigenvalues of the SWIP discretization against ϑ for one mesh-size (Figure 4.6). We see now that the lower end of the spectrum deteriorates as $\vartheta \to 0$, i.e. we can expect spectral pollution for very small angles. This agrees with the observations of [38].

The previous considerations indicate that the $a_h^{\theta\text{WIP}}$ bilinear form with ($\theta = -1$) is not suitable to solve the Maxwell eigenvalue problem on non-conforming meshes. However in this work we are concerned with the solution of the generic $\mathbf{curl} - \mathbf{curl}$ source problem (3.2). Although the Galerkin matrix becomes singular for $\varepsilon = 0$ we can in principle still solve the linear system if it is consistent, i.e. if the right-hand side lies in the range of the system matrix. In this case the solution $\boldsymbol{A}_h$ is not unique anymore, but $\mathbf{curl}\,\boldsymbol{A}_h$ still is.

We attempt to solve the linear system of equations using the conjugate gradient (CG) method. In [84] it is shown that the CG method converges for consistent, symmetric positive semi-definite problems and that its rate of convergence is determined by the non-zero eigenvalues. In particular, the number of CG iterations is related to the generalized

[2] The choices $a_F^{(1)}$ and $a_F^{(2)}$ yield qualitatively the same results. In particular the smallest non-zero eigenvalues also tend to 0 as $\varepsilon \to 0$, cf. Figure 4.6.

[3] An eigenvalue has been classified as non-zero if its absolute value is greater that 10^{-12}

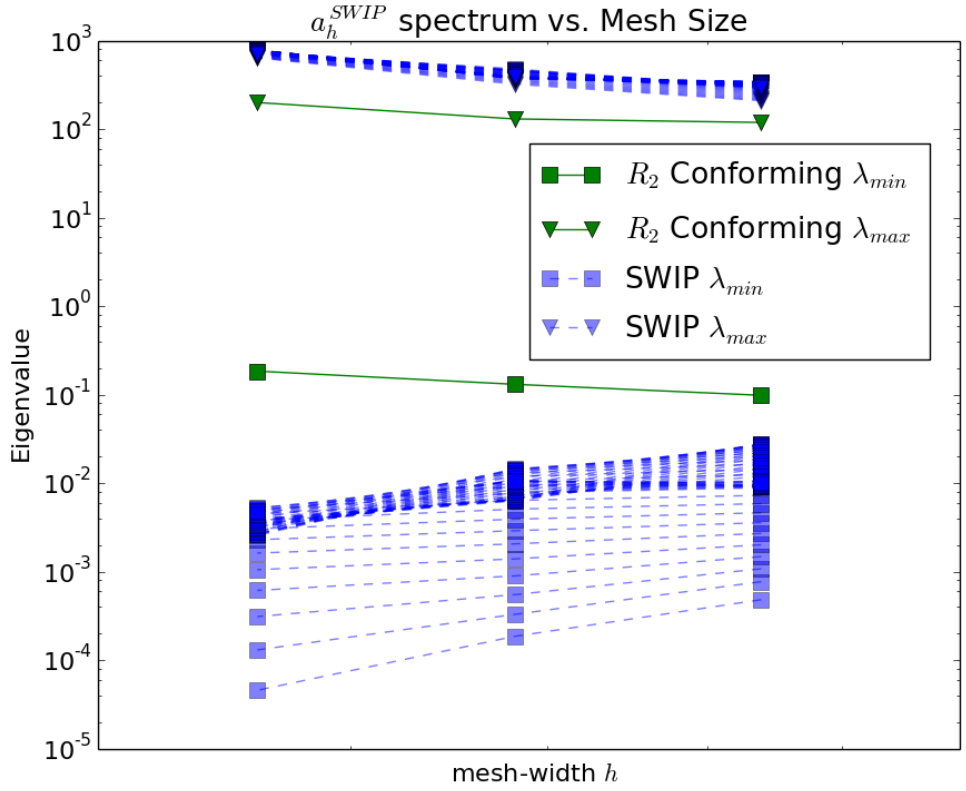

Figure 4.5: The smallest and the largest non-zero eigenvalues for $\varepsilon = 0$ vs. the mesh-width for 50 different angles of rotation (dashed lines). For comparison the smallest and the largest non-zero eigenvalues of an $\boldsymbol{H}(\mathbf{curl})$ conforming discretization based on second order edge functions are plotted as well. The angles are $\vartheta = 0.01n$ rad, $n \in 0, \ldots, 49$ and $R_{2,h}(\tilde{P}_\Omega)$ edge functions were used to discretize $a_h^{\theta\text{WIP}}$, $\mu \equiv 1$.

condition number $\kappa_{\text{cond}} = \frac{\lambda_{\max}}{\lambda_{\min}}$ where $\lambda_{\min}$ is the smallest, non-zero eigenvalue of the system matrix. If, again, we look at Figure 4.6 it becomes clear that $\kappa_{\text{cond}} \to \infty$ as $\vartheta \to 0$. I.e. the number of CG iterations should increase as $\vartheta \to 0$.

This has been confirmed in a numerical experiment: We take the example from Section 4.1.1 with the same analytical solution and choose the right-hand side $\boldsymbol{j}^i = \mathbf{curl}\,\mathbf{curl}\,\boldsymbol{A}$ ($\varepsilon = 0$, $\mu \equiv 1$). Table 4.1 shows the number of CG iterations required to reach the prescribed, relative tolerance 10^{-6}. We see that without a preconditioner the computational cost for the angle $\vartheta = 10^{-6}$ is almost 6 times larger than for $\vartheta = 10^{-1}$. For comparison, we also list the number of iterations needed when the multi-level ILU decomposition

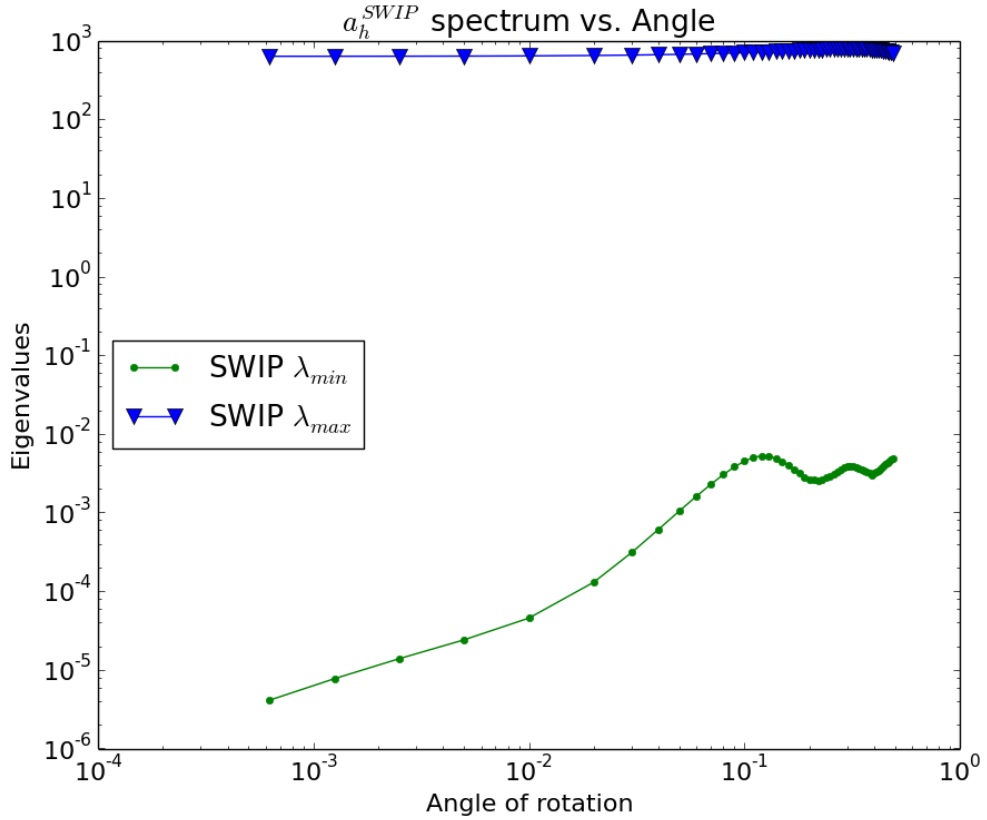

Figure 4.6: The smallest and the largest non-zero eigenvalues vs. the rotation angle ϑ for $h \cong 0.36$, $\varepsilon = 0$, $\mu \equiv 1$. The discretization is based on R_2 edge functions.

ILUPACK is employed [4] [25]. In this case the number of iterations also increases but the factor 6 is reduced to ≈ 3.2.

Remark 4.1.4. *Although the right-hand side $\boldsymbol{j}^i$ that we have chosen in the numerical experiment, is clearly divergence free, there is no guarantee that its discrete counterpart ℓ_h is so too, i.e. it is not clear that the right-hand side vector $\mathbf{b}$, that is associated with ℓ_h, lies in the range of the system matrix. We have investigated this by splitting the right-hand side vector $\mathbf{b}$ into a part that lies in the kernel of the system matrix, $\tilde{\mathbf{b}}$, and into its orthogonal complement, $\tilde{\mathbf{b}}^{\perp}$. It turns out that for all angles $\left|\tilde{\mathbf{b}}^{\perp}\right|_2 / |\mathbf{b}|_2 \approx 10^{-9}$, which seems to be sufficient for CG to converge.*

We can conclude that setting $\kappa \equiv \varepsilon = 0$ is in principle possible if the right-hand side

[4] The ILU factorization is built from the system matrix with $\varepsilon = 10^{-6}$ and the parameters for ILUPACK are: `type sol = 0`, `partitioning=3`, `flags=-1,-1`, `inv. droptol=5`, `threshold ILU=0.1`, `condest=1e-2`, `residual tol. = 5e-6`.

Table 4.1: Number of CG iterations for $\vartheta \to 0$, $h \cong 0.36$, $\varepsilon = 0$. The discretization is based on R_2 edge functions.

ϑ [rad]	No Preconditioner	ILUPACK
10^{-1}	1118	135
10^{-2}	3705	214
10^{-3}	3731	320
10^{-4}	6102	426

vector $\boldsymbol{b}$ lies in the range of the system matrix. However, checking this for a non-zero right-hand side $\boldsymbol{j}^i$ is a non-trivial task because we don't know a-priori the kernel of the system matrix $a_h^{\theta\mathrm{WIP}}$. Moreover, the system matrix becomes ill-conditioned as the angle $\theta \to 0$ which causes he number of CG iterations to increase.

Remark 4.1.5. *If the standard FEM is used together with $\boldsymbol{H}(\mathbf{curl})$ conforming edge elements, then the kernel of the system matrix is explicitly known, see the discrete de Rahm diagram Theorem 3.4.14. In particular, it is easily proven that if* $\operatorname{div} \boldsymbol{j}^i = 0$ *on a continuous level, then ℓ_h lies in the range of the system matrix. Also, if $\boldsymbol{j}^i = \sigma \,\mathbf{grad}\, \varphi_h$ where φ_h is the discrete solution of the stationary electric current problem* (1.13) *it is easily seen that $\sigma \,\mathbf{grad}\, \varphi_h$ is orthogonal to all discrete gradient fields and the corresponding right-hand side vector must thus lie in the range of the system matrix, cf. Theorem 3.4.14. This trait is used widely to solve the singular system using an iterative method because it avoids the introduction of a regularization term and/or additional Lagrange multipliers, see for example [141], [75], [17].*

The case $0 \leq \varepsilon \ll 1$

We saw in the previous section that setting $\varepsilon = 0$ is not feasible in practice. Therefore, we study a different approach: We choose ε so small that the error due to regularization becomes negligible. To make this more explicit we bound the total error between the discrete, regularized solution $\boldsymbol{A}_h^\varepsilon$ and the exact solution of (2.21), $\boldsymbol{A}^0$, by two contributions:

$$\left\|\mu^{-1/2}\,\mathbf{curl}\,(\boldsymbol{A}_h^\varepsilon - \boldsymbol{A}^0)\right\|_{L^2(\Omega)^3} \leq \left\|\mu^{-1/2}\,\mathbf{curl}\,(\boldsymbol{A}_h^\varepsilon - \boldsymbol{A}^\varepsilon)\right\|_{L^2(\Omega)^3} + \left\|\mu^{-1/2}\,\mathbf{curl}(\boldsymbol{A}^\varepsilon - \boldsymbol{A}^0)\right\|_{L^2(\Omega)^3}.$$

Herein $\boldsymbol{A}^\varepsilon$ is the exact solution of the regularized problem (2.25). Clearly the second component is independent of the discretization and thus h, but it depends on ε for a given problem. In fact, Corollary 2.5.3 shows that $\left\|\mu^{-1/2}\,\mathbf{curl}(\boldsymbol{A}^0 - \boldsymbol{A}^\varepsilon)\right\|_{L^2(\Omega)^3} = O(\varepsilon)$ and it even gives us an a-priori bound for $\left\|\mu^{-1/2}\,\mathbf{curl}(\boldsymbol{A}^0 - \boldsymbol{A}^\varepsilon)\right\|_{L^2(\Omega)^3} / \left\|\mathbf{curl}\,\boldsymbol{A}^0\right\|_{L^2(\Omega)^3}$

if Ω is convex. Moreover, the first term depends on h but is independent of ε, since the constants C_{bnd}, C_{stab}, C in Theorems 3.3.13 and 3.5.1 are independent of $\kappa = \varepsilon$. Theorems 3.3.13 and 3.5.1 also tell us that $\left\|\mu^{-1/2}\,\mathbf{curl}(\boldsymbol{A}^\varepsilon - \boldsymbol{A}^0)\right\|_{L^2(\Omega)^3} = O(h^{k-1})$. I.e. it is recommended to choose $\varepsilon = O(h^{k-1})$ to obtain $\left\|\mu^{-1/2}\,\mathbf{curl}(\boldsymbol{A}^\varepsilon - \boldsymbol{A}^0)\right\|_{L^2(\Omega)^3} \ll \left\|\mu^{-1/2}\,\mathbf{curl}(\boldsymbol{A}_h^\varepsilon - \boldsymbol{A}^\varepsilon)\right\|_{L^2(\Omega)^3}$ for all $h \in \mathcal{H}$.

However, as $\varepsilon \to 0$ the discrete problem becomes ill-posed and solvers typically fail to converge, cf. Remark 3.3.15. We try to circumvent this problem by two approaches:

i) For small problems, we use the sparse Cholesky decomposition of PARDISO [130] (Intel MKL Version 11.2) and solve the linear system of equations directly.

ii) For problems, whose Cholesky decomposition does not fit into memory, we use the Conjugate Gradient (CG) method together with ILUPACK [25] as a preconditioner (using the settings of the previous sub-section).

Remark 4.1.6. *We are only interested in the curl of the solution, i.e. the magnetic induction $\boldsymbol{B}$. If we were to look at $\boldsymbol{A}$ instead of $\mathbf{curl}\,\boldsymbol{A}$ then $\|\boldsymbol{A}_h^\varepsilon - \boldsymbol{A}^\varepsilon\|_{L^2(\Omega)^3}$ would not be independent of ε as can be seen from Theorem 3.3.13.*

Numerical example We consider the same setup as in Section 4.1.1 (cf. Figure 4.2) but we choose a different μ in the upper and lower hemisphere. The analytic solution is chosen as $\boldsymbol{A}^0 = (\sin y, 0, \mu \sin x)$ and $\boldsymbol{j}^i$ is chosen such that $\boldsymbol{A}^0$ fulfills (2.21).

We solve the system of linear equations using PARDISO for different values of ε and μ (as in the previous Section we choose $a_F = a_F^{(3)}$). Figure 4.7 shows the total relative error $\left\|\mu^{-1/2}\,\mathbf{curl}(\boldsymbol{A}_h^\varepsilon - \boldsymbol{A}^0)\right\|_{L^2(\Omega)^3} / \left\|\mu^{-1/2}\,\mathbf{curl}\,\boldsymbol{A}^0\right\|_{L^2(\Omega)^3}$ as a function of ε for various mesh-sizes. The solid lines show the error for $\mu_{\text{upper}}/\mu_{lower} = 10^2$ whereas the dashed lines show it for $\mu_{\text{upper}}/\mu_{\text{lower}} = 10^7$.

We note that the errors are almost identical for both choices of μ. Moreover, we observe that for $\varepsilon < 10^{-3}$ the *discretization error* $\left\|\mu^{-1/2}\,\mathbf{curl}(\boldsymbol{A}_h^\varepsilon - \boldsymbol{A}^\varepsilon)\right\|_{L^2(\Omega)^3}$ dominates the *regularization error* $\left\|\mu^{-1/2}\,\mathbf{curl}(\boldsymbol{A}^\varepsilon - \boldsymbol{A}^0)\right\|_{L^2(\Omega)^3}$ whereas for $\varepsilon > 10^{-3}$ the regularization error is dominated by the discretization error. This is what we can expect from the previous discussion. In fact, from Corollary 2.5.3 we can expect that the relative regularization error is bounded by $\frac{4\mu_{\max}}{\pi^2\mu_{\min}}\varepsilon$. The black, dashed line in Figure 4.7 visualizes this estimate for $\frac{\mu_{\max}}{\mu_{\min}} = 1$ and we see that for ε large the behavior is clearly linear, as proven in Corollary 2.5.3, and that the estimate is valid even though $\boldsymbol{g}_D \neq 0$ and $\mu_{\max}/\mu_{\min} \gg 1$.

Remark 4.1.7. *The same results are obtained if CG together with ILUPACK is used. For brevity, we omit these results here.*

We would like to point out that by using the direct solver PARDISO we could solve the resulting system of linear equations for ε as small as 10^{-10} and that the time needed to

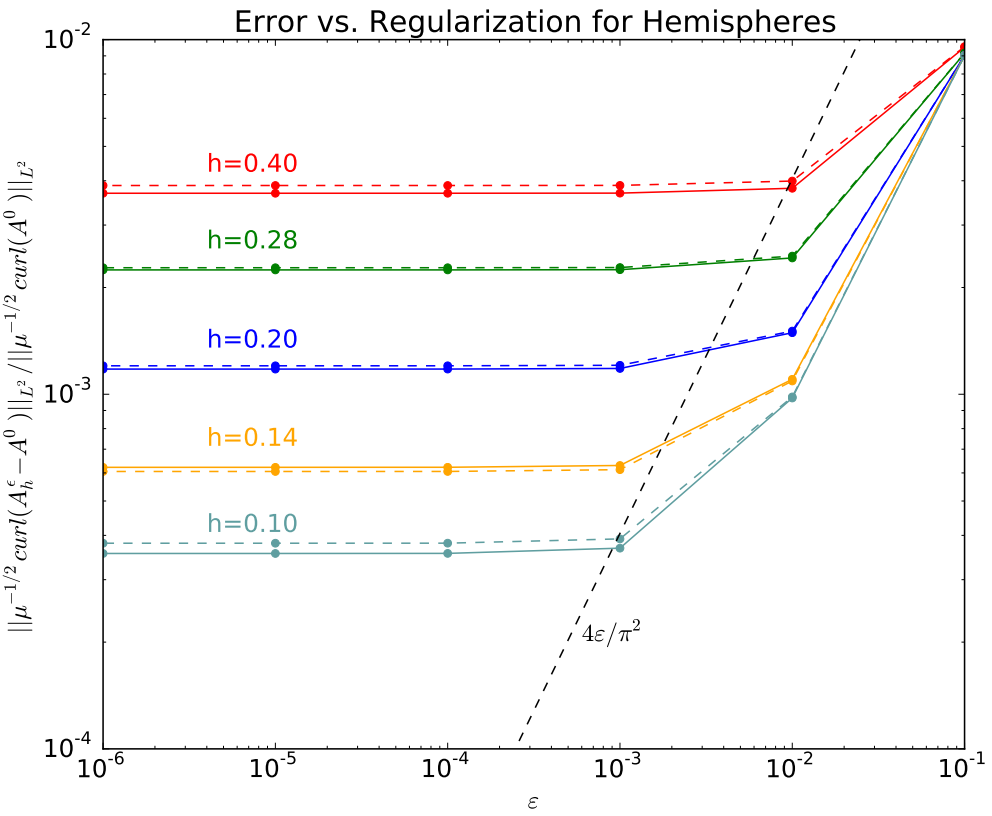

Figure 4.7: Relative L^2-error in $\boldsymbol{B}_h = \mathbf{curl}\, \boldsymbol{A}_h$ vs. ε for multiple mesh-sizes h. The solid lines show the error for $\mu_{\text{upper}} = 10$, $\mu_{\text{lower}} = 0.1$ whereas the dashed lines show it for $\mu_{\text{upper}} = 10^6$, $\mu_{\text{lower}} = 0.1$. The meshes have been rotated against each other by $\vartheta = 10^{-3}$ rad and second order edge functions ($k = 2$) were used for discretization.

solve the system seems to be independent of ε (see Table 4.2). A similar result holds for preconditioned CG with the ILUPACK preconditioner where the system is solvable for arbitrary small ε (cf. our discussion for $\varepsilon = 0$) and the solution time seems to be independent of ε for ε small enough.

We can thus choose an ε that is (almost) arbitrarily small without affecting the discretization error $\left\|\mu^{-1/2}\,\mathbf{curl}(\boldsymbol{A}_h^\varepsilon - \boldsymbol{A}^\varepsilon)\right\|_{L^2(\Omega)}$ and without incurring rising cost for solving the resulting linear systems of equations. In other words, one should choose ε as small as possible such that the resulting linear system can still be solved.

Table 4.2: Relative runtimes for $\varepsilon \to 0$, $h \cong 0.36$. The discretization is based on R_2 edge functions and $\vartheta = 10^{-4}$ rad. The runtimes have been normalized with the runtime for $\varepsilon = 10^{-1}$.

ε	PARDISO[a]	ILUPACK[b]
10^{-1}	1	1
10^{-2}	1.01	1.41
10^{-3}	1.01	1.42
10^{-4}	1.02	1.43
10^{-5}	0.98	1.42

[a] Time includes Cholesky factorization and back-substitution
[b] Time includes ILU factorization and CG iterations

4.2 Eddy Current Problem with Moving Bodies

It is in principle possible to use the magnetostatic problem of the previous section to simulate devices with moving parts by solving the magnetostatic problem (2.25) (possibly also the stationary electric current problem (1.13)) in each time step. By doing so one completely ignores the temporal derivatives in Maxwell's equations and in particular one neglects Faraday's law of induction. This simplification can be justified for some special settings such as the formation of an electric arc in a circuit breaker.

On the other hand, there are important applications such as electric motors/generators, magnetic actuators or eddy current breaks where Faraday's law of induction is essential for the functioning of the device. In this case the magnetostatic model is clearly inappropriate but it often suffices to consider the eddy current problem in the time-domain, cf. Section 1.2.

However, the solution of the eddy current problem in the presence of moving components is not straightforward. In fact, if an Eulerian description of the field quantities is used one must use *upwinding* [124] or other stabilization techniques to deal with the advective term $\boldsymbol{V} \times \boldsymbol{B}$ in (1.11). Moreover, if an Eulerian description is employed one has to take care that the material boundaries are properly resolved by the mesh for every time-step.

Because of these difficulties, it is usually easier to use a Lagrangian description for the simulation. Thereby one gets rid of the term $\boldsymbol{V} \times \boldsymbol{B}$, and the material boundaries are easily resolved by the underlying (moving) mesh.

In the following we will first study how the eddy current equation looks in any moving frame of reference and in particular we derive a rule to transform the vector potential $\boldsymbol{A}$ from one frame of reference to another. We then fix the moving frame of reference so that it coincides with the motion of the underlying bodies to dispose of the convective term $\boldsymbol{V} \times \boldsymbol{B}$. In other words, we derive a *Lagrangian description* for each moving body. These

descriptions must be coupled with each other by transforming the vector potential $\boldsymbol{A}$ to a common frame of reference. Interestingly we can show that this special transformation is not needed in the absence of sliding contacts which simplifies the treatment considerably and is henceforth assumed.

Subsection 4.2.2 presents a variational framework into which we cast the previously introduced Lagrangian formulation. We continue to prove convergence of an implicit Euler time stepping scheme for the case that all bodies are at rest but for arbitrary-nonconforming-meshes (Subsection 4.2.3). Finally, we present two numerical experiments in Subsection 4.2.4 that underline the developed theory and in particular suggest that the method also works for moving bodies.

4.2.1 Eddy Current Equation in a Moving Frame of Reference

In this section, we derive a vector potential formulation of the eddy current problem (1.10) in a moving frame of reference. As in Chapter 1 we will first analyze the problem in an unbounded domain and assume that the electromagnetic fields are smooth enough.

We recall that in the presence of moving parts we have to use the generalized form of Ohm's law (1.11):

$$\boldsymbol{j} = \sigma(\boldsymbol{E} + \boldsymbol{V} \times \boldsymbol{B}) + \boldsymbol{j}^i, \tag{4.1}$$

with $\boldsymbol{V}(t) : \mathbb{R}^3 \to \mathbb{R}^3$ being the velocity of the underlying material (w.r.t. to the laboratory frame of reference). Using the appropriate constitutive laws, the eddy current problem in the *laboratory frame of reference* thus reads as (cf. Section 1.2)

$$\begin{cases} \text{Find } \boldsymbol{E}(\boldsymbol{x},t),\, \boldsymbol{B}(\boldsymbol{x},t) \text{ subject to:} & & \\ \qquad \mathbf{curl}\, \boldsymbol{E} + \dfrac{\partial \boldsymbol{B}}{\partial t} = 0 & \text{for all } t > 0, & \text{(4.2a)} \\ \qquad \mathbf{curl}\, \mu^{-1}\boldsymbol{B} - \sigma \boldsymbol{E} = \sigma \boldsymbol{V} \times \boldsymbol{B} + \boldsymbol{j}^i & \text{for all } t > 0, & \text{(4.2b)} \\ \qquad \operatorname{div} \boldsymbol{B} = 0 & \text{for all } t > 0, & \text{(4.2c)} \\ \qquad \boldsymbol{B}(\boldsymbol{x},0) = \boldsymbol{B}_{\text{init}} & \text{in } \Omega_\sigma. & \text{(4.2d)} \end{cases}$$

Remark 4.2.1. *As in the time-harmonic eddy current problem of Section 2.6, the electric field $\boldsymbol{E}$ is also not uniquely determined by* (4.2) *inside insulators: We can add any gradient field with support in Ω_0 to $\boldsymbol{E}$ and* (4.2) *is still fulfilled.*

Remark 4.2.2. *We have omitted an initial condition for $\boldsymbol{E}(\boldsymbol{x},t)$ because, sloppily speaking, the temporal derivative of $\boldsymbol{E}$ does not appear in* (4.2). *See Section 4.2.2 for a more rigorous explanation.*

Remark 4.2.3. *Considering Faraday's law* (4.2a), *it is clear that the magnetic Gauss' law* (4.2c) $\operatorname{div} \boldsymbol{B} = 0$ *if and only if* $\operatorname{div} \boldsymbol{B}_{init} = 0$, *cf. [60, Lemma 6.3]. So it suffices to require* $\operatorname{div} \boldsymbol{B}_{init} = 0$.

Later, we attach the electromagnetic fields to the mesh and "advect" them together with the mesh. We will assume that our sub-meshes (and hence the moving frame of reference) move as a rigid body, i.e. they are not stretched or otherwise deformed. Thus, the coordinates $(\check{\boldsymbol{x}}, \check{t})$ of the moving frame of reference are related to the coordinates of the laboratory frame $(\boldsymbol{x}, t)$ by the *extended Galilei transformation* [5]

$$\boldsymbol{x} = \boldsymbol{T}(t)\check{\boldsymbol{x}} + \boldsymbol{r}(t), \tag{4.3a}$$

$$t = \check{t}. \tag{4.3b}$$

Here $\boldsymbol{T} \in C^1\left(\mathbb{R}^+; \mathbb{R}^{3\times 3}\right)$ is an orthogonal rotation matrix at every time t, i.e. we have $\boldsymbol{T}(t)\boldsymbol{T}(t)^T = \mathrm{Id}$, $\det \boldsymbol{T}(t) = 1$ for all $t \in \mathbb{R}^+$, and $\boldsymbol{r} \in C^1\left(\mathbb{R}^+; \mathbb{R}^3\right)$ describes the motion of the origin of the moving frame of reference ($\check{\boldsymbol{x}} = 0$).

The velocity w.r.t. the laboratory frame of a point $\check{\boldsymbol{x}}$ that is fixed in the moving frame is given by:

$$\mathcal{V}(\boldsymbol{x}, t) \coloneqq \frac{\partial \boldsymbol{x}(\check{\boldsymbol{x}}, t)}{\partial t} = \frac{\partial \boldsymbol{T}(t)}{\partial t}\check{\boldsymbol{x}} + \frac{\partial \boldsymbol{r}(t)}{\partial t} = \frac{\partial \boldsymbol{T}(t)}{\partial t}\boldsymbol{T}(t)^T(\boldsymbol{x} - \boldsymbol{r}(t)) + \frac{\partial \boldsymbol{r}(t)}{\partial t}. \tag{4.4}$$

Note that $\mathcal{V}$ is not necessarily the same as $\boldsymbol{V}$ in (4.1) because the moving frame of reference can be chosen arbitrarily. Later, we will choose the moving frame of reference such that $\mathcal{V} = \boldsymbol{V}$ but for the moment we consider any moving frame of reference.

It is well-known that the eddy current problem is invariant under transformations of the form (4.3) if the motion can be regarded as quasi-stationary with respect to electrodynamics [87, 86, 65]:

Theorem 4.2.4 (Extended Galilean invariance of Eddy Current Problem [40])**.** *The system of equations* (4.2) *is invariant under the transformation* (4.3) *if the field quantities transform in the following form (cf. [86]):*

$$\begin{aligned} \boldsymbol{T}\check{\boldsymbol{E}} &= \boldsymbol{E} + \mathcal{V} \times \boldsymbol{B}, & \boldsymbol{T}\check{\boldsymbol{B}} &= \boldsymbol{B}, \\ \boldsymbol{T}\check{\boldsymbol{j}}^i &= \boldsymbol{j}^i, & \boldsymbol{T}\check{\boldsymbol{H}} &= \boldsymbol{H}, \\ \boldsymbol{T}\check{\boldsymbol{j}} &= \boldsymbol{j}, & \boldsymbol{T}\check{\boldsymbol{V}} &= \boldsymbol{V} - \mathcal{V}. \end{aligned} \tag{4.5}$$

Here the vectors $\check{\boldsymbol{E}}$, $\check{\boldsymbol{B}}$, $\check{\boldsymbol{j}}^i$, $\check{\boldsymbol{H}}$ and $\check{\boldsymbol{j}}$ are defined w.r.t. the basis spanned by the columns of $\boldsymbol{T}(t)$.

Remark 4.2.5. *Interestingly the relations* (4.5) *can be obtained formally from the ones of the Lorentz transformation [80] (Remark 1.1.1) by taking the limit for the speed of light $c \to \infty$. This is in some sense not surprising since we have seen in Section 1.2 that we can interpret the eddy current problem formally as a limit of the full Maxwell's equations for $c \to \infty$.*

Remark 4.2.6. *The relations* (4.5) *show that the constitutive laws $\boldsymbol{B} = \mu\boldsymbol{H}$ and the generalized Ohm's law* (4.1) *hold in exactly the same way in the moving frame of reference. This is not the case for the full Maxwell's equations, cf. Remark 1.1.4.*

[5] Note that our definition allows for rigid-body rotation and so we term it the extended Galilei transformation. Most authors assume that a Galilei transformation is characterized by translation only, cf. [80, Section 11.1].

Temporally gauged formulation As in Section 2.6, we can derive a *temporally gauged formulation* [6] of problem (4.2): Let us assume that ($\boldsymbol{E}$, $\boldsymbol{B}$) is a (typically not unique) solution of the eddy current problem (4.2) and define the vector potential

$$\boldsymbol{A}(\boldsymbol{x},t) \coloneqq \boldsymbol{A}_{\text{init}}(\boldsymbol{x}) - \int_0^t \boldsymbol{E}(\boldsymbol{x},s)\,\mathrm{d}s, \tag{4.6}$$

where $\boldsymbol{A}_{\text{init}}(\boldsymbol{x})$ is any vector potential such that $\boldsymbol{B}_{\text{init}} = \mathbf{curl}\,\boldsymbol{A}_{\text{init}}$ (cf. Remark 4.2.3 and Theorem 2.3.3). By differentiating (4.6) w.r.t. time we get

$$\boldsymbol{E}(\boldsymbol{x},t) = -\frac{\partial \boldsymbol{A}}{\partial t}(\boldsymbol{x},t).$$

Substituting this into Faradays law (4.2a) and using that $\boldsymbol{B}_{\text{init}} = \mathbf{curl}\,\boldsymbol{A}_{\text{init}}$ we see that

$$\boldsymbol{B}(\boldsymbol{x},t) = \mathbf{curl}\,\boldsymbol{A}(\boldsymbol{x},t)$$

Using these two relations we can rewrite the first-order system (4.2) as the second-order *temporally gauged formulation*

$$\begin{cases} \text{Find } \boldsymbol{A}(\boldsymbol{x},t) \text{ subject to:} \\ \sigma\dfrac{\partial \boldsymbol{A}}{\partial t} + \mathbf{curl}\left(\mu^{-1}\,\mathbf{curl}\,\boldsymbol{A}\right) = \boldsymbol{j}^i + \sigma(\boldsymbol{V}\times\mathbf{curl}\,\boldsymbol{A}), \qquad \text{for } t>0 & \text{(4.7a)} \\ \boldsymbol{A}(\boldsymbol{x},0) = \boldsymbol{A}_{\text{init}}. & \text{(4.7b)} \end{cases}$$

Proposition 4.2.7. *The formulations* (4.2) *and* (4.7) *are equivalent: If* $\boldsymbol{B}(\boldsymbol{x},t)$, $\boldsymbol{E}(\boldsymbol{x},t)$ *are a solution of* (4.2) *then* $\boldsymbol{A}(\boldsymbol{x},t)$, *defined by* (4.6), *is a solution of* (4.7). *Also, if* $\boldsymbol{A}(\boldsymbol{x},t)$ *is a solution of* (4.7) *then* $\boldsymbol{E} = -\frac{\partial \boldsymbol{A}}{\partial t}$, $\boldsymbol{B} = \mathbf{curl}\,\boldsymbol{A}$ *are a solution of* (4.2).

The question is now how we have to transform $\boldsymbol{A}$ when we switch to the moving frame of reference (4.3):

Corollary 4.2.8. *The temporally gauged formulation* (4.7) *is invariant under the transformation* (4.3) *if we transform*

$$\boldsymbol{T}(0)\check{\boldsymbol{A}}_{init}(\check{\boldsymbol{x}}) = \boldsymbol{A}_{init}(\boldsymbol{x}(\check{\boldsymbol{x}},0)), \tag{4.8}$$

$$\boldsymbol{T}(t)\check{\boldsymbol{A}}(\check{\boldsymbol{x}},t) = \boldsymbol{A}(\boldsymbol{x}(\check{\boldsymbol{x}},t),t) - \boldsymbol{T}(t)\int_0^t \boldsymbol{T}(s)^T\left[\mathbf{grad}_{\boldsymbol{x}}\left(\mathcal{V}\cdot\boldsymbol{A}\right)(\boldsymbol{x}(\check{\boldsymbol{x}},s),s)\right]\mathrm{d}s. \tag{4.9}$$

Moreover, we have

$$-\frac{\partial \check{\boldsymbol{A}}(\check{\boldsymbol{x}},t)}{\partial t} = \check{\boldsymbol{E}}(\check{\boldsymbol{x}},t), \qquad \check{\mathbf{curl}}\check{\boldsymbol{A}}(\check{\boldsymbol{x}},t) = \check{\boldsymbol{B}}(\check{\boldsymbol{x}},t). \tag{4.10}$$

[6] As we will see this formulation doesn't have a unique solution, i.e. it is not fully gauged, cf. Remark 2.6.2

Remark 4.2.9. *The integral in* (4.9) *is a path integral over the line* $(\boldsymbol{x}(\check{\boldsymbol{x}}, s), s)$, $s \in [0, t]$ *for* $\check{\boldsymbol{x}}$ *fixed.*

Proof. We already know from Theorem 4.2.4 that problem (4.2) is invariant under transformation (4.3). So we can define $\check{\boldsymbol{A}}$ by (4.6) (in the moving frame) which immediately gives the relations (4.10). It remains to show that $\check{\boldsymbol{A}}$ can be equally expressed by (4.9).

First, we note that we can express the velocity $\mathcal{V}$ also in terms of the angular velocity $\boldsymbol{\omega} \in C^1(\mathbb{R}^+; \mathbb{R}^3)$:

$$\mathcal{V}(\boldsymbol{x}, t) = \boldsymbol{\omega}(t) \times (\boldsymbol{x} - \boldsymbol{r}(t)) + \frac{\partial \boldsymbol{r}(t)}{\partial t}.$$

Comparing this to the expression (4.4) we see that for any vector $\boldsymbol{a} \in \mathbb{R}^3$:

$$\frac{\partial \boldsymbol{T}(t)}{\partial t} \boldsymbol{T}(t)^T \boldsymbol{a} = \boldsymbol{W}(t)\boldsymbol{a} = \boldsymbol{\omega}(t) \times \boldsymbol{a}, \qquad \text{with } \boldsymbol{W} = \begin{pmatrix} 0 & -\omega_3 & \omega_2 \\ \omega_3 & 0 & -\omega_1 \\ -\omega_2 & \omega_1 & 0 \end{pmatrix}.$$

Now define $\check{\boldsymbol{A}}$ by

$$\begin{aligned} \check{\boldsymbol{A}}(\check{\boldsymbol{x}}, t) - \check{\boldsymbol{A}}_{\text{init}}(\check{\boldsymbol{x}}) &= -\int_0^t \check{\boldsymbol{E}}(\check{\boldsymbol{x}}, s)\, \mathrm{d}s \\ &\overset{(4.5)}{=} \int_0^t -\boldsymbol{T}(s)^T \boldsymbol{E}(\boldsymbol{x}(\check{\boldsymbol{x}}, s), s) - \boldsymbol{T}(s)^T \left[\mathcal{V}(\boldsymbol{x}(\check{\boldsymbol{x}}, s), s) \times \boldsymbol{B}(\boldsymbol{x}(\check{\boldsymbol{x}}, s), s)\right] \mathrm{d}s \\ &= \int_0^t \boldsymbol{T}(s)^T \frac{\partial \boldsymbol{A}}{\partial t}(\boldsymbol{x}(\check{\boldsymbol{x}}, s), s) - \boldsymbol{T}(s)^T \left[\mathcal{V}(\boldsymbol{x}(\check{\boldsymbol{x}}, s), s) \times \boldsymbol{B}(\boldsymbol{x}(\check{\boldsymbol{x}}, s), s)\right] \mathrm{d}s. \end{aligned}$$

Note that

$$\begin{aligned} \frac{\mathrm{d}(\boldsymbol{T}(s)^T \boldsymbol{A}(\boldsymbol{x}(\check{\boldsymbol{x}}, s), s))}{\mathrm{d}s} = \frac{\partial \boldsymbol{T}^T}{\partial t}(s) \boldsymbol{A}(\boldsymbol{x}(\check{\boldsymbol{x}}, s), s) + \boldsymbol{T}(s)^T \frac{\partial \boldsymbol{A}}{\partial t}(\boldsymbol{x}(\check{\boldsymbol{x}}, s), s) \\ + \boldsymbol{T}(s)^T (\mathcal{V}(\boldsymbol{x}(\check{\boldsymbol{x}}, s), s) \cdot \nabla_{\boldsymbol{x}}) \boldsymbol{A}(\boldsymbol{x}(\check{\boldsymbol{x}}, s), s) \end{aligned}$$

so that we get

$$\begin{aligned} \check{\boldsymbol{A}}(\check{\boldsymbol{x}}, t) &= \boldsymbol{T}(t)^T \boldsymbol{A}(\boldsymbol{x}(\check{\boldsymbol{x}}, t), t) \\ &\quad \underbrace{- \int_0^t \frac{\partial \boldsymbol{T}(s)^T}{\partial s} \boldsymbol{A}(\boldsymbol{x}(\check{\boldsymbol{x}}, s), s) + \boldsymbol{T}(s)^T \left[(\mathcal{V} \cdot \nabla_{\boldsymbol{x}}) \boldsymbol{A} + \mathcal{V} \times \boldsymbol{B}\right](\boldsymbol{x}(\check{\boldsymbol{x}}, s), s)\, \mathrm{d}s}_{:=\alpha}. \end{aligned}$$

Next, we use that $0 = \frac{\partial (\boldsymbol{T}(s)\boldsymbol{T}(s)^T)}{\partial s} = \frac{\partial \boldsymbol{T}(s)}{\partial s} \boldsymbol{T}(s)^T + \boldsymbol{T}(s) \frac{\partial \boldsymbol{T}(s)^T}{\partial s}$ so that

$$\frac{\partial \boldsymbol{T}(s)^T}{\partial s} = -\boldsymbol{T}(s)^T \frac{\partial \boldsymbol{T}(s)}{\partial s} \boldsymbol{T}(s)^T = -\boldsymbol{T}(s)^T \boldsymbol{W}(s).$$

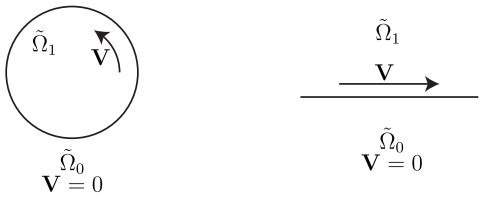

(a) Rotation (b) Translation

Figure 4.8: Two possible domain decompositions with respective velocity fields

Moreover, we use the identity $\mathbf{grad}\,(\boldsymbol{a}\cdot\boldsymbol{b}) = (\boldsymbol{a}\cdot\nabla)\boldsymbol{b} + (\boldsymbol{b}\cdot\nabla)\boldsymbol{a} + \boldsymbol{a}\times\mathbf{curl}\,\boldsymbol{b} + \boldsymbol{b}\times\mathbf{curl}\,\boldsymbol{a}$ to get

$$\alpha = -\int_0^t \boldsymbol{T}(s)^T \left[\mathbf{grad}_{\boldsymbol{x}}\,(\mathcal{V}\cdot\boldsymbol{A}) - (\boldsymbol{A}\cdot\nabla_{\boldsymbol{x}})\mathcal{V} - \boldsymbol{A}\times\mathbf{curl}_{\boldsymbol{x}}\,\mathcal{V} - \boldsymbol{\omega}\times\boldsymbol{A}\right](\boldsymbol{x}(\check{\boldsymbol{x}},s),s)\,\mathrm{d}s$$

Finally, we use $(\boldsymbol{A}\cdot\nabla_{\boldsymbol{x}})\mathcal{V} = \boldsymbol{\omega}\times\boldsymbol{A}$ and $\mathbf{curl}_{\boldsymbol{x}}\,\mathcal{V} = 2\boldsymbol{\omega}$ to get the assertion. □

Remark 4.2.10 (Inverse Transformation)**.** *Let us apply the transformation* (4.9) *twice, i.e. first for the reference frame*

$$\check{\boldsymbol{x}} = \boldsymbol{T}(t)^T(\boldsymbol{x} - \boldsymbol{r}(t)), \qquad \text{and then for} \qquad \check{\check{\boldsymbol{x}}} = \boldsymbol{T}(t)\check{\boldsymbol{x}} + \boldsymbol{r}(t).$$

This transforms $\boldsymbol{A}$ and the associated $\boldsymbol{E}$, $\boldsymbol{B}$ fields (cf. (4.10)*) from the laboratory system to the moving system and back. Using the transformation rules* (4.5)*, we clearly have $\check{\check{\boldsymbol{B}}} = \boldsymbol{B}$ and thus $\check{\check{\boldsymbol{E}}} = \boldsymbol{E}$. I.e. $\frac{\partial\check{\check{\boldsymbol{A}}}}{\partial t} = \frac{\partial\boldsymbol{A}}{\partial t}$ for all $t > 0$. Moreover, we have $\check{\check{\boldsymbol{A}}}(\check{\check{\boldsymbol{x}}},0) = \check{\check{\boldsymbol{A}}}_{init} = \boldsymbol{A}_{init} = \boldsymbol{A}(\boldsymbol{x},0)$ so that we must have $\check{\check{\boldsymbol{A}}} = \boldsymbol{A}$ for all $t > 0$ (for $\boldsymbol{A}$ sufficiently smooth).*

Lagrangian formulation

We will now derive a *Lagrangian formulation* of (4.7) which requires some additional assumptions on the velocity field $\boldsymbol{V}$:

Assumption 4.2.11. *There is a partition $\tilde{P}_\Omega = \{\tilde{\Omega}_0, \tilde{\Omega}_1\}$ of $\Omega = \mathbb{R}^3$ (cf. Section 3.5) such that the velocity $\boldsymbol{V} = 0$ in $\tilde{\Omega}_0$. Moreover, we assume that there is a moving frame of reference, $(\boldsymbol{T}(t), \boldsymbol{r}(t))$, such that $\boldsymbol{V}(\boldsymbol{x},t) = \mathcal{V}(\boldsymbol{x},t)$ in $\tilde{\Omega}_1$ (cf.* (4.4)*).*

Note that Ω is still an unbounded domain and so the two subdomains $\tilde{\Omega}_0$, $\tilde{\Omega}_1$ can, but need not be unbounded. Figure 4.8 shows two such possible domain decompositions $\tilde{P}_\Omega$ with the corresponding velocity fields $\boldsymbol{V} = \mathcal{V}$.

Let us introduce some additional notation: As in Section 2.6, $\Omega_\sigma \subset \mathbb{R}^3$ denotes the open subset where $\sigma > 0$ (cf. Assumption 2.4.1), and we define the insulator $\Omega_0 \coloneqq \Omega\setminus\overline{\Omega_\sigma}$. For

each subdomain, we define the conductors/insulators as $\tilde{\Omega}_{\sigma,i} \coloneqq \Omega_\sigma \cap \tilde{\Omega}_i$, $\tilde{\Omega}_{0,i} \coloneqq \Omega_0 \cap \tilde{\Omega}_i$ for $i = 0, 1$. Finally, we denote by $\Gamma = \partial\tilde{\Omega}_0 \cap \partial\tilde{\Omega}_1$ the common intersection.

We now decompose the eddy current problem (4.7) into two smaller sub-problems posed on $\tilde{\Omega}_0$ and $\tilde{\Omega}_1$. In each subdomain, we employ a *Lagrangian description* of problem (4.7); That is, we choose the frame of reference (4.3) for $\tilde{\Omega}_1$ such that it agrees with the velocity $\boldsymbol{V}$ in $\tilde{\Omega}_1$. Because of this $\check{\boldsymbol{V}}$ will be zero in $\tilde{\Omega}_1$ and we can solve the coupled Initial Value Problem (IVP)

$$
\begin{cases}
\text{Find } \boldsymbol{A}_0,\ \check{\boldsymbol{A}}_1 \text{ subject to} & \\
\sigma\dfrac{\partial \boldsymbol{A}_0}{\partial t} + \mathbf{curl}\,\mu^{-1}\,\mathbf{curl}\,\boldsymbol{A}_0 = \boldsymbol{j}^i & \text{in } \tilde{\Omega}_0,\ t > 0, \qquad (4.11a)\\
\sigma\dfrac{\partial \check{\boldsymbol{A}}_1}{\partial t} + \check{\mathbf{curl}}\,\mu^{-1}\check{\mathbf{curl}}\,\check{\boldsymbol{A}}_1 = \check{\boldsymbol{j}}^i & \text{in } \tilde{\Omega}_1,\ t > 0, \qquad (4.11b)\\
\check{\boldsymbol{n}}_\Gamma \times \check{\boldsymbol{A}}_0 = \check{\boldsymbol{n}}_\Gamma \times \check{\boldsymbol{A}}_1 & \text{on } \Gamma,\ t > 0, \qquad (4.11c)\\
\check{\boldsymbol{n}}_\Gamma \times \mu^{-1}\check{\mathbf{curl}}\,\check{\boldsymbol{A}}_0 = \check{\boldsymbol{n}}_\Gamma \times \mu^{-1}\check{\mathbf{curl}}\,\check{\boldsymbol{A}}_1 & \text{on } \Gamma,\ t > 0, \qquad (4.11d)\\
\boldsymbol{A}_0(\boldsymbol{x}, 0) = \boldsymbol{A}_{\text{init}} & \text{in } \tilde{\Omega}_{\sigma,0}, \qquad (4.11e)\\
\check{\boldsymbol{A}}_1(\check{\boldsymbol{x}}, 0) = \check{\boldsymbol{A}}_{\text{init}} & \text{in } \tilde{\Omega}_{\sigma,1}. \qquad (4.11f)
\end{cases}
$$

Here $\check{\boldsymbol{n}}_\Gamma = \boldsymbol{T}^T\boldsymbol{n}_\Gamma$ is the interface normal written using the basis vectors of the moving frame of reference (4.3). Note that we have transformed $\boldsymbol{A}_0$ from the laboratory frame to the moving frame of reference by means of (4.9) in order to state the transmission conditions (4.11c), (4.11d) between $\tilde{\Omega}_0$ and $\tilde{\Omega}_1$.

The coupled problem (4.11) is clearly not well-posed because we can add any gradient field to $\boldsymbol{A}_0$ ($\check{\boldsymbol{A}}_1$) that has compact support in $\tilde{\Omega}_{0,0}$ ($\tilde{\Omega}_{0,1}$) and the equations (4.11) are still fulfilled. This is expected because the electric field $\boldsymbol{E}$ is not uniquely determined by (4.2) inside insulators Ω_0. Interestingly this gauge freedom allows us to get rid of the transformation rule (4.9) in transmission condition (4.11c):

Lemma 4.2.12. *Suppose that the conductors Ω_σ are such that there are no* sliding contacts, *i.e. $\Omega_\sigma \cap \Gamma = \emptyset$ for all $t \geq 0$. Then the transmission condition* (4.11c) *can be replaced by*

$$
\boldsymbol{n}_\Gamma \times \boldsymbol{A}_0 = \boldsymbol{n}_\Gamma \times (\boldsymbol{T}\check{\boldsymbol{A}}_1), \qquad \text{on } \Gamma, t > 0 \qquad (4.12)
$$

without affecting the physically observable fields. I.e. if $\boldsymbol{A}_0$, $\check{\boldsymbol{A}}_1$ are a solution of (4.11) *then there are fields $\boldsymbol{a}_0$, $\check{\boldsymbol{a}}_1$ that solve* (4.11) *with* (4.11c) *replaced by* (4.12)*, and such that*

$$
\begin{aligned}
\mathbf{curl}\,\boldsymbol{A}_0(\boldsymbol{x}, t) &= \mathbf{curl}\,\boldsymbol{a}_0(\boldsymbol{x}, t) && \text{in } \tilde{\Omega}_0, t > 0, && (4.13a)\\
\check{\mathbf{curl}}\,\check{\boldsymbol{A}}_1(\check{\boldsymbol{x}}, t) &= \check{\mathbf{curl}}\,\check{\boldsymbol{a}}_1(\check{\boldsymbol{x}}, t) && \text{in } \tilde{\Omega}_1, t > 0, && (4.13b)\\
\frac{\partial \boldsymbol{A}_0}{\partial t}(\boldsymbol{x}, t) &= \frac{\partial \boldsymbol{a}_0}{\partial t}(\boldsymbol{x}, t) && \text{in } \tilde{\Omega}_{\sigma,0}, t > 0, && (4.13c)
\end{aligned}
$$

$$\frac{\partial \check{\boldsymbol{A}}_1}{\partial t}(\check{\boldsymbol{x}},t) = \frac{\partial \check{\boldsymbol{a}}_1}{\partial t}(\check{\boldsymbol{x}},t) \qquad \text{in } \tilde{\Omega}_{\sigma,1}, t>0. \tag{4.13d}$$

Moreover, the reverse also holds: if $\boldsymbol{a}_0$, $\check{\boldsymbol{a}}_1$ *solve* (4.11) *with* (4.11c) *replaced by* (4.12), *then there are* $\boldsymbol{A}_0$, $\check{\boldsymbol{A}}_1$ *solving* (4.11) *such that relations* (4.13) *hold.*

Proof. The idea is to transform $\boldsymbol{A}_0$ locally around the interface Γ into the moving frame of reference and to define this as $\boldsymbol{a}_0$: Since there are no sliding contacts it is possible to find a function $\chi \in C^\infty(\mathbb{R}^3)$ such that $\chi = 1$ in a neighborhood of Γ and $\chi = 0$ in a neighborhood of Ω_σ. We now define, cf. (4.9)

$$\boldsymbol{a}_0(\boldsymbol{x},t) \coloneqq \boldsymbol{A}_0(\boldsymbol{x},t) - \boldsymbol{T}(t)\int_0^t \boldsymbol{T}^T(s)\left[\mathbf{grad}_{\boldsymbol{x}}(\chi\mathcal{V}\cdot\boldsymbol{A}_0)(\boldsymbol{x}(\check{\boldsymbol{x}}(\boldsymbol{x},t),s),s)\right]\mathrm{d}s. \tag{4.14}$$

Since χ is zero in $\tilde{\Omega}_{\sigma,0}$ for all $t>0$ (4.13c) clearly holds. Moreover, by using the curl- and div-preserving transformation rules (cf. (3.32), [40, Appendix A], [102, Corollary 3.58])

$$\begin{aligned}
\check{\mathbf{grad}}\, f(\boldsymbol{x}(\check{\boldsymbol{x}})) &= \boldsymbol{T}^T \mathbf{grad}\, f(\boldsymbol{x}(\check{\boldsymbol{x}})) && \text{for all } f,\\
\check{\mathbf{curl}}\, \boldsymbol{Y}(\boldsymbol{x}(\check{\boldsymbol{x}})) &= \det(\boldsymbol{T})\boldsymbol{T}^{-1}\mathbf{curl}\,(\boldsymbol{T}\boldsymbol{Y})(\boldsymbol{x}(\check{\boldsymbol{x}}))\\
&= \boldsymbol{T}^T\mathbf{curl}\,(\boldsymbol{T}\boldsymbol{Y})(\boldsymbol{x}(\check{\boldsymbol{x}})) && \text{for all } \boldsymbol{Y},
\end{aligned} \tag{4.15}$$

we get

$$\begin{aligned}
\check{\mathbf{curl}}\,\left(\boldsymbol{T}(t)^T\boldsymbol{a}_0(\boldsymbol{x}(\check{\boldsymbol{x}},t),t)\right) &= \boldsymbol{T}(t)^T\mathbf{curl}\,\boldsymbol{A}_0(\boldsymbol{x}(\check{\boldsymbol{x}},t),t)\\
&\quad - \int_0^t \underbrace{\check{\mathbf{curl}}\,\check{\mathbf{grad}}\,(\chi\mathcal{V}\cdot\boldsymbol{A}_0)(\boldsymbol{x}(\check{\boldsymbol{x}}(\boldsymbol{x},t),s),s)}_{=0}\mathrm{d}s.
\end{aligned}$$

On the other hand

$$\check{\mathbf{curl}}\,\left(\boldsymbol{T}(t)^T\boldsymbol{a}_0(\boldsymbol{x}(\check{\boldsymbol{x}},t),t)\right) = \boldsymbol{T}(t)^T\mathbf{curl}\,\boldsymbol{a}_0(\boldsymbol{x}(\check{\boldsymbol{x}},t),t),$$

so that (4.13a) holds. Now choose $\check{\boldsymbol{a}}_1 = \check{\boldsymbol{A}}_1$ so that (4.13b) and (4.13d) clearly hold. Finally, we note that (4.12) holds:

$$0 \overset{(4.11c)}{=} \check{\boldsymbol{n}}_\Gamma \times (\check{\boldsymbol{A}}_0 - \check{\boldsymbol{A}}_1) \overset{(4.9)}{=} \check{\boldsymbol{n}}_\Gamma \times (\boldsymbol{T}^T\boldsymbol{a}_0 - \check{\boldsymbol{a}}_1) = \boldsymbol{T}^T(\boldsymbol{n}_\Gamma \times (\boldsymbol{a}_0 - \boldsymbol{T}\check{\boldsymbol{a}}_1)),$$

where we have used the identity $(\boldsymbol{M}\boldsymbol{a})\times(\boldsymbol{M}\boldsymbol{b}) = (\det\boldsymbol{M})\boldsymbol{M}^{-T}(\boldsymbol{a}\times\boldsymbol{b})$, which holds for every invertible matrix $\boldsymbol{M}\in\mathbb{R}^3$.

In order to show the reverse statement, assume $\boldsymbol{a}_0$, $\check{\boldsymbol{a}}_1$ are such that (4.11) holds with (4.11c) replaced by (4.12). The idea is now to transform $\check{\boldsymbol{a}}_1$ locally around Γ into the moving frame of reference and define this as $\check{\boldsymbol{A}}_1$ so that when $\boldsymbol{a}_0$ is transformed by (4.9) we have again equality. I.e. we choose $\boldsymbol{A}_0 = \boldsymbol{a}_0$ and

$$\check{\boldsymbol{A}}_1(\check{\boldsymbol{x}},t) = \check{\boldsymbol{a}}_1(\check{\boldsymbol{x}},t) - \int_0^t \check{\mathbf{grad}}\left(\chi(\boldsymbol{T}(s)^T\boldsymbol{\mathcal{V}})\cdot\check{\boldsymbol{a}}_1\right)(\check{\boldsymbol{x}}(\boldsymbol{x}(\check{\boldsymbol{x}},t),s),s)\,\mathrm{d}s.$$

Using the same ideas as in the first part of the proof it is now possible to show that the relations (4.13) hold and that $\boldsymbol{A}_0$, $\check{\boldsymbol{A}}_1$ are a solution of (4.11). □

The above lemma tells us that we can consider an alternative formulation of (4.11) which does not use the transformation rule (4.9) (if there are no sliding contacts). As we will see this simplified formulation has a lot of advantages when it comes to the numerical implementation and analysis (cf. Remark 4.2.30) and it will therefore be our primary subject of study for the rest of this chapter.

Remark 4.2.13. *A simple but less rigorous argument for the validity of lemma 4.2.12 is the following: In the eddy current model, the electric field $\boldsymbol{E}$ has no meaning in insulators and it suffices to consider the magnetic field $\boldsymbol{B}$ in Ω_0. So if there are no sliding contacts it should suffice to couple only the $\boldsymbol{B}$ fields with each other, i.e. $[\![\boldsymbol{B}]\!]\cdot\boldsymbol{n}_\Gamma = 0$. Since there is no special transformation rule for $\boldsymbol{B}$ (as opposed to $\boldsymbol{A}$, cf.* (4.5), (4.9)*) it suffices to require $[\![\boldsymbol{A}]\!]_\tau = 0$ on Γ.*

4.2.2 Variational Framework

In the previous section, we have studied the eddy current problem on an unbounded space-time domain and we have always assumed that the involved functions are smooth enough. We will now restrict the problem to the (open) space-time domain $\wr\!\!\wr := \{(\boldsymbol{x},t)|\ t \in (0,t_F), \boldsymbol{x} \in \Omega(t)\}$ where $\Omega(t)$ can *change over time* and t_F is an arbitrary but finite end time.

We assume that $\Omega(t)$ is a bounded domain with Lipschitz boundary for all $t \in [0,t_F]$. In the spirit of the previous section and Section 3.5 we split $\Omega(t)$ into two subdomains [7] $\tilde{P}_\Omega(t) = \{\tilde{\Omega}_0(t), \tilde{\Omega}_1(t)\}$ such that $\overline{\Omega} = \overline{\tilde{\Omega}_0(t) \sqcup \tilde{\Omega}_1(t)}$. As before, we denote the common intersection by $\Gamma(t) = \partial\tilde{\Omega}_0(t) \cap \partial\tilde{\Omega}_1(t)$ and the conductor by the open subset $\Omega_\sigma(t) := \{\boldsymbol{x} \in \Omega|\ \sigma(x,t) > 0\}$. We assume that there are no sliding contacts so that we can split $\Omega_\sigma(t)$ into the two, well-separated subsets $\tilde{\Omega}_{\sigma,0}(t) := \Omega_\sigma(t) \cap \tilde{\Omega}_0(t)$, and $\tilde{\Omega}_{\sigma,1}(t) := \Omega_\sigma(t) \cap \tilde{\Omega}_1(t)$. Similarly, we define the two insulator domains $\tilde{\Omega}_{0,0}(t) := \tilde{\Omega}_0(t) \setminus \overline{\tilde{\Omega}_{\sigma,0}}(t)$ and $\tilde{\Omega}_{0,1}(t) := \tilde{\Omega}_1(t) \setminus \overline{\tilde{\Omega}_{\sigma,1}}(t)$. As before we make the following assumption about the velocity field:

Assumption 4.2.14. *Subdomain $\tilde{\Omega}_0(t)$ is at rest, i.e. $\tilde{\Omega}_0(t) = \tilde{\Omega}_0(0)$ for all $t \geq 0$. Moreover, we assume that $\tilde{\Omega}_1(t)$ is moving as a rigid body, i.e. there is a rotation matrix $\tilde{\boldsymbol{T}} \in C^1(\mathbb{R}^+;\mathbb{R}^{3\times3})$ and offset function $\tilde{\boldsymbol{r}} \in C^1(\mathbb{R}^+;\mathbb{R}^3)$ such that $\tilde{\Omega}_1(t) = \tilde{\boldsymbol{T}}(t)\tilde{\Omega}_1(0) + \tilde{\boldsymbol{r}}(t)$. In other words: We assume that the velocity field $\boldsymbol{V}$ is exactly zero in $\tilde{\Omega}_0$ and that it matches the motion of $\tilde{\Omega}_1$, i.e. $\tilde{\Omega}_1$ is* advected *by $\boldsymbol{V}$.*

Moreover, we assume that σ is independent of time w.r.t. each subdomain, i.e. $\sigma|_{\tilde{\Omega}_0}(\boldsymbol{x},t)$ is a function of $\boldsymbol{x}$ only and $\sigma|_{\tilde{\Omega}_1}(\boldsymbol{x}(\check{\boldsymbol{x}},t),t)$ is a function of $\check{\boldsymbol{x}}$ only.

We can now interpret the Lagrangian formulation (4.11) on two space-time cylinders $(0,t_F)\times\tilde{\Omega}_0$ and $(0,t_F)\times\tilde{\Omega}_1$(in the coordinates of the moving frame of reference) which are coupled to each other (note that $\wr\!\!\wr$ is *not* a space-time cylinder). For this we change

[7] The generalization to more than two subdomains is straightforward.

our point of view slightly and interpret $\boldsymbol{A}_0$ (respectively $\check{\boldsymbol{A}}_1$) as a Banach-space valued function [62, Chapter 7], [121, Chapter 11], [28, Section II.5.4],

$$\boldsymbol{A}_0 : (0, t_F) \to V_0.$$

It remains to define the space V_0 (V_1): We assume that the magnetic field energy $\frac{1}{2} \left\| \mu^{-1/2} \boldsymbol{B} \right\|^2_{L^2(\Omega)^3}$ is finite which implies that $\boldsymbol{B}_0 = \mathbf{curl}\, \boldsymbol{A}_0 \in L^2(\tilde{\Omega}_0)^3$ (for almost every time t). So the natural choice is $V_0 \coloneqq \boldsymbol{H}(\mathbf{curl}; \tilde{\Omega}_0)$ or using the notion of *Bochner spaces* [128, Section 2.3]: $\boldsymbol{A}_0 \in L^2((0, t_F); V_0)$, where $L^2((0, t_F); V_0)$ is a Bochner L^p space.

Definition 4.2.15 (Bochner L^p space, [62, 121, 128])**.** *For a* separable *Banach space X we define*

$$L^p((0, t_F); X) \coloneqq \left\{ f : (0, t_F) \to X \,\middle|\, \int_0^{t_F} \|f\|_X^p \, \mathrm{d}t < \infty \right\}.$$

Finally, let us multiply (4.11a) with a smooth function $\boldsymbol{\varphi} \in C^\infty(\overline{\tilde{\Omega}_0})^3$, integrate by parts over $\tilde{\Omega}_0$ and *note that σ is independent of t* to get

$$\int_{\tilde{\Omega}_0} \frac{\partial(\sigma \boldsymbol{A}_0)}{\partial t} \cdot \boldsymbol{\varphi} = \int_{\tilde{\Omega}_0} \boldsymbol{j}^i \cdot \boldsymbol{\varphi} - \int_{\tilde{\Omega}_0} \mu^{-1} \, \mathbf{curl}\, \boldsymbol{A}_0 \cdot \mathbf{curl}\, \boldsymbol{\varphi} - \int_{\partial \tilde{\Omega}_0} (\boldsymbol{n} \times (\mu^{-1} \, \mathbf{curl}\, \boldsymbol{A}_0)) \cdot \boldsymbol{\varphi}.$$

In other words, we can interpret $\frac{\partial(\sigma \boldsymbol{A}_0)}{\partial t} \in \boldsymbol{H}(\mathbf{curl}; \tilde{\Omega}_0)'$ as a functional with $L^2(\tilde{\Omega}_0)^3$ as a *pivot space*: $\boldsymbol{H}(\mathbf{curl}; \tilde{\Omega}_0) \subset L^2(\tilde{\Omega}_0)^3 \simeq \left(L^2(\tilde{\Omega}_0)^3 \right)' \subset \boldsymbol{H}(\mathbf{curl}; \tilde{\Omega}_0)'$, cf. Remark 2.2.11. Using again the notion of Bochner spaces this can be written as

$$\boldsymbol{A}_0 \in \mathscr{V}(\tilde{\Omega}_0) \coloneqq \left\{ \boldsymbol{A} \in L^2\left((0, t_F); \boldsymbol{H}(\mathbf{curl}; \tilde{\Omega}_0)\right) \,\middle|\, \frac{\partial(\sigma \boldsymbol{A})}{\partial t} \in L^2\left((0, t_F); \boldsymbol{H}(\mathbf{curl}; \tilde{\Omega}_0)'\right) \right\}.$$

Similar to the classical Sobolev embedding of $H^1((0, t_F)) \hookrightarrow C^0((0, t_F))$, the fact that the temporal derivative of $\boldsymbol{A}_0 \in \mathscr{V}(\tilde{\Omega}_0)$ is in L^2 gives some extra (time-) regularity for $\boldsymbol{A}_0$.

Lemma 4.2.16. *Suppose that $\boldsymbol{A} \in \mathscr{V}(\tilde{\Omega}_0)$. Then in fact, $(\sqrt{\sigma}\boldsymbol{A}) \in C^0\left([0, T]; L^2(\tilde{\Omega}_0)^3\right)$.*

Proof. The proof is analogous to the one of [121, Lemma 11.4] and is left out for brevity. See also [60, Lemma 6.2], [62, Theorem 3, 5.9.2]. □

The above lemma shows that $\sqrt{\sigma}\boldsymbol{A}_0$ is continuous in time and we can thus enforce an initial condition on $\boldsymbol{A}_0$ for $t = 0$ in the $L^2(\tilde{\Omega}_{\sigma,0})^3$ sense. But note that Lemma 4.2.16 does not give us time continuity in the insulator $\tilde{\Omega}_{0,0}$ which we can also not expect since the temporal derivative of $\boldsymbol{A}_0$ disappears in (4.11) inside $\tilde{\Omega}_{0,0}$. Furthermore, Lemma 4.2.16 suggests that $\boldsymbol{A}_0 \in \mathscr{V}(\tilde{\Omega}_0)$ cannot be continuously differentiated in time so we

cannot expect time continuity of $\boldsymbol{E}_0 = -\frac{\partial \boldsymbol{A}_0}{\partial t}$. I.e. we cannot enforce an initial condition on the electric field (cf. Remark 4.2.2).

The above discussion thus motivates the following Initial Boundary Value Problem (IBVP),

$$
\begin{cases}
\text{Find } \boldsymbol{A}_0 \in \mathscr{V}(\tilde{\Omega}_0), \check{\boldsymbol{A}}_1 \in \mathscr{V}(\tilde{\Omega}_1) \text{ subject to} & \\
\dfrac{\partial(\sigma \boldsymbol{A}_0)}{\partial t} + \mathbf{curl}\, \mu^{-1} \mathbf{curl}\, \boldsymbol{A}_0 = \boldsymbol{j}^i & \text{in } \boldsymbol{H}(\mathbf{curl}; \tilde{\Omega}_0)', \text{ a.e. } t, \quad (4.16a) \\
\dfrac{\partial(\sigma \check{\boldsymbol{A}}_1)}{\partial t} + \check{\mathbf{curl}}\, \mu^{-1} \check{\mathbf{curl}}\, \check{\boldsymbol{A}}_1 = \check{\boldsymbol{j}}^i & \text{in } \boldsymbol{H}(\mathbf{curl}; \tilde{\Omega}_1)', \text{ a.e. } t, \quad (4.16b) \\
\boldsymbol{n}_\Gamma \times \big(\boldsymbol{A}_0 - (\boldsymbol{T} \check{\boldsymbol{A}}_1)\big) = 0 & \text{on } (H^{1/2}_{00}(\Gamma)')^3, \text{ a.e. } t, \quad (4.16c) \\
\boldsymbol{n}_\Gamma \times \big(\mu^{-1} \mathbf{curl}\, \boldsymbol{A}_0 - \mu^{-1} \boldsymbol{T} \check{\mathbf{curl}}\, \check{\boldsymbol{A}}_1\big) = 0 & \text{on } (H^{1/2}_{00}(\Gamma)')^3, \text{ a.e. } t, \quad (4.16d) \\
\boldsymbol{n} \times \boldsymbol{A} = 0 & \text{on } \boldsymbol{H}^{-1/2}(\mathrm{div}_{\partial\Omega}; \partial\Omega), \quad (4.16e) \\
\boldsymbol{A}_0(\boldsymbol{x}, 0) = \boldsymbol{A}_{\mathrm{init}}(\boldsymbol{x}) & \text{a.e. in } \tilde{\Omega}_{\sigma,0}, \quad (4.16f) \\
\check{\boldsymbol{A}}_1(\check{\boldsymbol{x}}, 0) = \check{\boldsymbol{A}}_{\mathrm{init}}(\check{\boldsymbol{x}}) & \text{a.e. in } \tilde{\Omega}_{\sigma,1}. \quad (4.16g)
\end{cases}
$$

Note that we have replaced the transmission condition (4.11c) by the transmission condition (4.12), i.e. we assume that there are *no sliding contacts* (cf. Lemma 4.2.12). The transmission condition (4.16c) thus implies that $\boldsymbol{A}_0$ and $\boldsymbol{T}\check{\boldsymbol{A}}_1$ are tangentially continuous across Γ for a.e. $t \in (0, t_F)$, i.e. the function

$$
\boldsymbol{A}(\boldsymbol{x}, t) \coloneqq \begin{cases} \boldsymbol{A}_0(\boldsymbol{x}, t) & \text{if } \boldsymbol{x} \in \tilde{\Omega}_0, \\ \boldsymbol{T}\check{\boldsymbol{A}}_1(\check{\boldsymbol{x}}(\boldsymbol{x}, t), t) & \text{if } \boldsymbol{x} \in \tilde{\Omega}_1(t) \end{cases}, \tag{4.17}
$$

lies in $\boldsymbol{H}(\mathbf{curl}; \Omega)$ (cf. Proposition 2.2.28). Therefore, the trace $\boldsymbol{n} \times \boldsymbol{A} \in \boldsymbol{H}^{-1/2}(\mathrm{div}_{\partial\Omega}; \partial\Omega)$ and we can enforce the homogeneous Dirichlet boundary condition (4.16e). This implies in turn $\boldsymbol{B} \cdot \boldsymbol{n} = 0$ on $\partial\Omega$ which reflects the decay of the magnetic fields far away from the sources.

For the other transmission condition (4.11d) we have used that $\check{\boldsymbol{n}}_\Gamma \times \check{\mathbf{curl}}\, \check{\boldsymbol{A}}_0 = (\boldsymbol{T}^T \boldsymbol{n}_\Gamma) \times (\boldsymbol{T}^T \mathbf{curl}\, \boldsymbol{A}_0) = \boldsymbol{T}^T (\boldsymbol{n}_\Gamma \times \mathbf{curl}\, \boldsymbol{A}_0)$. Moreover, we assume that $\boldsymbol{j}^i \in L^2((0, t_F); L^2(\Omega)^3)$, so that in a neighborhood of Γ (there are no sliding contacts) $\mathbf{curl}\, \mu^{-1} \mathbf{curl}\, \boldsymbol{A}_0$ is square integrable and thus the trace $\boldsymbol{n}_\Gamma \times (\mu^{-1} \mathbf{curl}\, \boldsymbol{A}_0)$ can be restricted to $(H^{1/2}_{00}(\Gamma)')^3$.

Using the *energy method*, we can show that there is at most one solution of (4.16):

Lemma 4.2.17 (Uniqueness). *Let $\boldsymbol{A}^1$ and $\boldsymbol{A}^2$ be two solutions of the coupled IBVP (4.16) (defined by (4.17)). Then for almost every $t \in (0, t_F)$: $\boldsymbol{A}^1(t) = \boldsymbol{A}^2(t)$ a.e. in Ω_σ and $\mathbf{curl}\, \boldsymbol{A}^1(t) = \mathbf{curl}\, \boldsymbol{A}^2(t)$ a.e. in Ω.*

Proof. We define $\boldsymbol{Z} = \boldsymbol{A}^1 - \boldsymbol{A}^2$ and denote by $\boldsymbol{Z}_0$ and $\boldsymbol{Z}_1$ its restrictions to $\tilde{\Omega}_0$, $\tilde{\Omega}_1$, respectively. Since $\boldsymbol{Z}(t) \in \boldsymbol{H}_0(\mathbf{curl}; \Omega)$ for a.e. t there are approximations $\boldsymbol{z}^n \in C_0^\infty(\Omega)^3$

such that $\boldsymbol{z}^n \to \boldsymbol{Z}(t)$ in $\boldsymbol{H}_0(\mathbf{curl};\Omega)$ for $n \to \infty$. We denote by $\boldsymbol{z}_0^n$ and $\boldsymbol{z}_1^n$ the restrictions to $\tilde{\Omega}_0$ and $\tilde{\Omega}_1$. Since $\boldsymbol{A}^1$ and $\boldsymbol{A}^2$ both solve (4.16a) and (4.16b) we have

$$\left\langle \frac{\partial(\sigma \boldsymbol{Z}_0)}{\partial t}, \boldsymbol{z}_0^n \right\rangle_{\boldsymbol{H}(\mathbf{curl};\tilde{\Omega}_0)} + \left\langle \mathbf{curl}\, \mu^{-1}\, \mathbf{curl}\, \boldsymbol{Z}_0, \boldsymbol{z}_0^n \right\rangle_{\boldsymbol{H}(\mathbf{curl};\tilde{\Omega}_0)} = 0, \quad (4.18a)$$

$$\left\langle \frac{\partial(\sigma \boldsymbol{T}^T \boldsymbol{Z}_1)}{\partial t}, \boldsymbol{T}^T \boldsymbol{z}_1^n \right\rangle_{\boldsymbol{H}(\mathbf{curl};\tilde{\Omega}_1)} + \left\langle \check{\mathbf{curl}}\, \mu^{-1} \check{\mathbf{curl}}\, (\boldsymbol{T}^T \boldsymbol{Z}_1), \boldsymbol{T}^T \boldsymbol{z}_1^n \right\rangle_{\boldsymbol{H}(\mathbf{curl};\tilde{\Omega}_1)} = 0. \quad (4.18b)$$

Here $\langle \cdot, \cdot \rangle_{\boldsymbol{H}(\mathbf{curl};\tilde{\Omega}_i)}$ denotes the duality product between $\boldsymbol{H}(\mathbf{curl};\tilde{\Omega}_i)'$ and $\boldsymbol{H}(\mathbf{curl};\tilde{\Omega}_i)$ for $i = 0, 1$. Now observe that

$$\begin{aligned} &\left\langle \mathbf{curl}\, \mu^{-1}\, \mathbf{curl}\, \boldsymbol{Z}_0, \boldsymbol{z}_0^n \right\rangle_{\boldsymbol{H}(\mathbf{curl};\tilde{\Omega}_0)} + \left\langle \check{\mathbf{curl}}\, \mu^{-1} \check{\mathbf{curl}}\, (\boldsymbol{T}^T \boldsymbol{Z}_1), \boldsymbol{T}^T \boldsymbol{z}_1^n \right\rangle_{\boldsymbol{H}(\mathbf{curl};\tilde{\Omega}_1)} \overset{(4.16d)}{=} \\ &\qquad \left(\mu^{-1}\, \mathbf{curl}\, \boldsymbol{Z}_0, \mathbf{curl}\, \boldsymbol{z}^n\right)_{L^2(\tilde{\Omega}_0)^3} + \left(\mu^{-1} \check{\mathbf{curl}}\, (\boldsymbol{T}^T \boldsymbol{Z}_1), \check{\mathbf{curl}}\, \boldsymbol{T}^T \boldsymbol{z}^n\right)_{L^2(\tilde{\Omega}_1)^3} \overset{(4.15)}{=} \\ &\qquad\qquad \left(\mu^{-1}\, \mathbf{curl}\, \boldsymbol{Z}, \mathbf{curl}\, \boldsymbol{z}^n\right)_{L^2(\Omega)^3}. \end{aligned}$$

So adding the two equations (4.18) we get

$$\begin{aligned} &\left\langle \frac{\partial(\sigma \boldsymbol{Z}_0)}{\partial t}, \boldsymbol{z}_0^n \right\rangle_{\boldsymbol{H}(\mathbf{curl};\tilde{\Omega}_0)} + \left\langle \frac{\partial(\sigma \boldsymbol{T}^T \boldsymbol{Z}_1)}{\partial t}, \boldsymbol{T}^T \boldsymbol{z}_1^n \right\rangle_{\boldsymbol{H}(\mathbf{curl};\tilde{\Omega}_1)} \\ &\qquad\qquad + \left(\mu^{-1}\, \mathbf{curl}\, \boldsymbol{Z}, \mathbf{curl}\, \boldsymbol{z}^n\right)_{L^2(\Omega)^3} = 0 \end{aligned}$$

Now let $n \to \infty$, integrate over $(0, t)$ and use [28, Theorem II.5.12]

$$\left\| \sqrt{\sigma} \boldsymbol{Z}_0(t) \right\|^2_{L^2(\tilde{\Omega}_0)^3} - \left\| \sqrt{\sigma} \boldsymbol{Z}_0(0) \right\|^2_{L^2(\tilde{\Omega}_0)^3} = \int_0^t \left\langle \frac{\partial(\sigma \boldsymbol{Z}_0)}{\partial t}(s), \boldsymbol{Z}_0(s) \right\rangle_{\boldsymbol{H}(\mathbf{curl};\tilde{\Omega}_0)} \mathrm{d}s,$$

together with $\boldsymbol{Z}_0(0) = \boldsymbol{Z}_1(0) = 0$ (cf. (4.16f), (4.16g)) to get

$$\left\| \sqrt{\sigma} \boldsymbol{Z}_0(t) \right\|^2_{L^2(\tilde{\Omega}_0)^3} + \left\| \sqrt{\sigma} \boldsymbol{T}^T \boldsymbol{Z}_1(t) \right\|^2_{L^2(\tilde{\Omega}_1)^3} + \int_0^t \left\| \mu^{-1/2}\, \mathbf{curl}\, \boldsymbol{Z}(s) \right\|^2_{L^2(\Omega)^3} \mathrm{d}s = 0.$$

Since this holds for a.e. $t \in (0, t_F)$ this yields the assertion. □

Using Galerkin's method (see e.g. [62, Section 7.1.2], [121, Theorem 11.3]) and the techniques of the proof of Theorem 2.6.5 it should be possible to show the existence of a weak solution of (4.16) and thus the well-posedness of the problem. However, because of the rather complicated transmission/boundary conditions (which are different for every time t!) this is rather technical and so we just *assume* that the IBVP (4.16) is well-posed.

4.2.3 Symmetric Weighted Interior Penalty Approximation

We now turn to the task of approximating the solution of (4.16) numerically on a computer. For this we first discretize the problem in space using the SWIP formulation and then discretize this finite dimensional system of Ordinary Differential Equations (ODE) in time using *implicit Euler* time stepping. This is often referred to as the *method of lines*. We first present the fully discrete problem in space and time and then continue to prove an error estimate for the case that the meshes are *not* moving (but can intersect arbitrarily).

We assume that we are given two conforming sequences of meshes $\mathcal{T}_{\mathcal{H},0}$ and $\mathcal{T}_{\mathcal{H},1}$ of the subdomains $\tilde{\Omega}_0(0)$ and $\tilde{\Omega}_1(0)$ at time $t = 0$. For $t > 0$ the mesh sequence $\mathcal{T}_{\mathcal{H},1}$ is advected together with the subdomain $\tilde{\Omega}_1(t)$ so that for every time $t \in [0, t_F]$ we have a global, usually non-conforming sequence of meshes $\mathcal{T}_{\mathcal{H}}(t) \coloneqq \{\mathcal{T}_{h,0} \cup \mathcal{T}_{h,1}(t) |\ \mathcal{T}_{h,0} \in \mathcal{T}_{\mathcal{H},0}, \mathcal{T}_{h,1}(t) \in \mathcal{T}_{\mathcal{H},1}(t)\}$.

Let us split the time interval $(0, t_F)$ into N equally sized segments of size $\Delta t = t_F/N$ and let $t^i \coloneqq i\,\Delta t$ for $i \in \{0, \dots, N\}$. At every time step t^i we seek two discrete solutions $\boldsymbol{A}_{h,0}^i \in V_{h,0}^i$, $\check{\boldsymbol{A}}_{h,1}^i \in V_{h,1}^i$. Here $V_{h,j}^i \subset V_{h,j}^{*,i} \coloneqq \{\boldsymbol{A} \in H^1(\mathcal{T}_{h,j}(t^i))^3 |\ \mathbf{curl}\,\boldsymbol{A} \in H^1(\mathcal{T}_{h,j}(t^i))^3\}$, $j = 0, 1$, are finite dimensional subspaces, cf. (3.4). Analogous to the previous section we define

$$\boldsymbol{A}_h^i(\boldsymbol{x}) \coloneqq \begin{cases} \boldsymbol{A}_{h,0}^i(\boldsymbol{x}) & \text{if } \boldsymbol{x} \in \tilde{\Omega}_0, \\ \boldsymbol{T}(t^i)\check{\boldsymbol{A}}_{h,1}^i(\boldsymbol{x}) & \text{if } \boldsymbol{x} \in \tilde{\Omega}_1(t^i). \end{cases} \tag{4.19}$$

At every time step $i > 0$ we solve the following problem:

$$\begin{cases} \text{Find } \boldsymbol{A}_{h,0}^i \in V_{h,0}^i,\ \check{\boldsymbol{A}}_{h,1}^i \in V_{h,1}^i \text{ s.t. for all } \boldsymbol{A}_{h,0}' \in V_{h,0}^i,\ \boldsymbol{A}_{h,1}' \in V_{h,1}^i \\ \qquad \left(\sigma_\varepsilon \frac{\boldsymbol{A}_{h,0}^i - \boldsymbol{A}_{h,0}^{i-1}}{\Delta t}, \boldsymbol{A}_{h,0}'\right)_{L^2(\tilde{\Omega}_0)^3} + \left(\sigma_\varepsilon \frac{\check{\boldsymbol{A}}_{h,1}^i - \check{\boldsymbol{A}}_{h,1}^{i-1}}{\Delta t}, \check{\boldsymbol{A}}_{h,1}'\right)_{L^2(\tilde{\Omega}_1)^3} \\ \qquad\qquad + a_{h,\kappa=0}^{\theta\mathrm{WIP}}(\boldsymbol{A}_h^i, \boldsymbol{A}_h') = \left(\boldsymbol{j}^i(t^i), \boldsymbol{A}_h'\right)_{L^2(\Omega)^3}. \end{cases} \tag{4.20}$$

Here $\boldsymbol{A}_h'$ is defined analogously to $\boldsymbol{A}_h^i$, cf. (4.19), and we choose $\theta = -1$, i.e. the Symmetric Weighted Interior Penalty (SWIP) formulation. The bilinear form $a_{h,\kappa=0}^{\theta\mathrm{WIP}}$ is defined by (3.7) with $\kappa = 0$ and $\boldsymbol{g}_D = 0$ (homogeneous Dirichlet boundary conditions).

Note that problem (4.20) is generally not solvable with $\sigma = 0$ in Ω_0, cf. Remark 3.3.15. Similar to the magnetostatic/time-harmonic eddy current problem we thus regularize the system by setting

$$\sigma_\varepsilon(\boldsymbol{x}) \coloneqq \begin{cases} \sigma(\boldsymbol{x}) & \text{if } \boldsymbol{x} \in \Omega_\sigma, \\ \varepsilon & \text{else,} \end{cases}$$

with $0 < \varepsilon \ll \sigma_{\min}$.

Finally, we remark that the initial conditions $\boldsymbol{A}^0_{h,0}$ and $\check{\boldsymbol{A}}^0_{h,1}$ must be provided and should in some sense be good approximations of $\boldsymbol{A}_{\text{init}}$. This will be made more precise in the next section, cf. Theorem 4.2.21.

A Priori Error Estimate

Let us now analyze the behavior of the above method for the case that $\tilde{\Omega}_1$ is at rest but such that the submeshes of $\tilde{\Omega}_0$ and $\tilde{\Omega}_1$ can still intersect in a non-conforming way. Without loss of generality we can then assume that $\boldsymbol{T}$ is the identity so that the coupled problem (4.16) can be rewritten as (in regularized form)

$$\begin{cases} \text{Find } \boldsymbol{A} \in \mathscr{V}(\Omega) \text{ subject to} \\ \dfrac{\partial(\sigma_\varepsilon \boldsymbol{A})}{\partial t} + \mathbf{curl}\,\mu^{-1}\,\mathbf{curl}\,\boldsymbol{A} = \boldsymbol{\jmath}^i & \text{in } \boldsymbol{H}(\mathbf{curl};\Omega)', \text{ for a.e. } t, \quad (4.21a) \\ \boldsymbol{n}\times\boldsymbol{A} = 0 & \text{on } \boldsymbol{H}^{-1/2}(\mathrm{div}_{\partial\Omega};\partial\Omega), \text{ for a.e. } t, \quad (4.21b) \\ \boldsymbol{A}(\boldsymbol{x},0) = \boldsymbol{A}_{\text{init}}(\boldsymbol{x}) & \text{a.e. in } \Omega_\sigma. \quad (4.21c) \end{cases}$$

Similarly, the discrete SWIP formulation (4.20) simplifies to

$$\begin{cases} \text{Find } \boldsymbol{A}^i_h \in V_h \text{ s.t. for all } \boldsymbol{A}'_h \in V_h \\ \left(\sigma_\varepsilon \dfrac{\boldsymbol{A}^i_h - \boldsymbol{A}^{i-1}_h}{\Delta t}, \boldsymbol{A}'_h\right)_{L^2(\Omega)^3} + a^{\theta\text{WIP}}_{h,\kappa=0}(\boldsymbol{A}^i_h, \boldsymbol{A}'_h) = \left(\boldsymbol{\jmath}^i(t^i), \boldsymbol{A}'_h\right)_{L^2(\Omega)^3}. \end{cases} \quad (4.22)$$

Here $V_h \subset V^*_h := \{\boldsymbol{A} \in H^1(\mathcal{T}_h)^3 |\ \mathbf{curl}\,\boldsymbol{A} \in H^1(\mathcal{T}_h)^3\}$, cf. (3.4). Furthermore, let $\|\cdot\|_{V^{*,r}}$ be any norm (yet to be defined) and define $V^{*,r} := V^* \cap \{\boldsymbol{A} |\ \|\boldsymbol{A}\|_{V^{*,r}} < \infty\}$, where $V^* := \{\boldsymbol{A} \in \boldsymbol{H}(\mathbf{curl};\Omega) \cap H^1(P_\Omega)^3 |\ \mathbf{curl}\,\boldsymbol{A} \in H^1(P_\Omega)^3\}$ [8], cf. (3.3).

Assumption 4.2.18 (Approximation Property). *The space V_h is such that for every $\boldsymbol{A} \in V^{*,r}$ we have*

$$\inf_{\boldsymbol{v}_h \in V_h} \|\boldsymbol{A} - \boldsymbol{v}_h\|_{WIP,*} \leq C h^r \|\boldsymbol{A}\|_{V^{*,r}}.$$

Here $\|\cdot\|_{WIP,*}$ is defined by (3.14) with $\kappa = \sigma_\varepsilon$, and C is independent of $\boldsymbol{A}$, h, σ_ε, μ.

The above assumption holds for example if $V_h = R_{r+1,h}(\tilde{P}_\Omega)$ with (cf. Theorem 3.5.1)

$$\|\boldsymbol{A}\|_{V^{*,r}} = \max(\mu_{\min}^{-1/2}, \sigma_{\max}^{1/2}) \sum_j \left(\|\boldsymbol{A}\|_{H^{r+1}(\Omega_j)^3} + \|\mathbf{curl}\,\boldsymbol{A}\|_{H^{r+1}(\Omega_j)^3}\right),$$

[8] The partiton P_Ω is defined in Section 3.3.1 and is generally not the same as $\tilde{P}_\Omega$.

Another possible choice would be the completely discontinuous space $V_h = \mathbb{P}_{r,h}(\mathcal{T}_h)$ with (cf. Theorem 3.5.8)

$$\|\boldsymbol{A}\|_{V^{*,r}} = \max(\mu_{\min}^{-1/2}, \sigma_{\max}^{1/2}) \sum_j \|\boldsymbol{A}\|_{H^{r+1}(\Omega_j)^3}.$$

For the analysis of the discrete IBVP (4.22) we will need the

Definition 4.2.19 (Elliptic/Ritz Projector). *For every $\boldsymbol{A} \in V^*$ we define $R_h\boldsymbol{A} \in V_h$ by*

$$a_{h,\kappa=0}^{\theta\,WIP}(R_h(\boldsymbol{A}), \boldsymbol{A}_h') + \left(\sigma_\varepsilon R_h(\boldsymbol{A}), \boldsymbol{A}_h'\right)_{L^2(\Omega)^3} = a_{h,\kappa=0}^{\theta\,WIP}(\boldsymbol{A}, \boldsymbol{A}_h') + \left(\sigma_\varepsilon \boldsymbol{A}, \boldsymbol{A}_h'\right)_{L^2(\Omega)^3} \quad (4.23)$$

for all $\boldsymbol{A}_h' \in V_h$.

Proposition 4.2.20 (Ritz Projection Error). *Let V_h be such that Assumption 4.2.18 holds. Then we have for the penalty parameter η large enough:*

$$\|\boldsymbol{A} - R_h(\boldsymbol{A})\|_{WIP} \leq C_1 \inf_{\boldsymbol{v}_h \in V_h} \|\boldsymbol{A} - \boldsymbol{v}_h\|_{WIP,*} \leq C_2 h^r \|\boldsymbol{A}\|_{V^{*,r}} \quad (4.24)$$

Here C_1, C_2 are independent of $\boldsymbol{A}$, μ, σ_ε, h.

Proof. Let $\boldsymbol{v}_h \in V_h$ be arbitrary. Then

$$\|\boldsymbol{A} - R_h(\boldsymbol{A})\|_{\mathrm{WIP}} \leq \|\boldsymbol{A} - \boldsymbol{v}_h\|_{\mathrm{WIP}} + \|\boldsymbol{v}_h - R_h\boldsymbol{A}\|_{\mathrm{WIP}}.$$

The second term on the right-hand side can be bounded by

$$\begin{aligned}
\|\boldsymbol{v}_h - R_h\boldsymbol{A}\|_{\mathrm{WIP}} &\leq C_{\mathrm{stab}}^{-1} \frac{a_{h,\kappa=\sigma_\varepsilon}^{\theta\mathrm{WIP}}(\boldsymbol{v}_h - R_h\boldsymbol{A}, \boldsymbol{v}_h - R_h\boldsymbol{A})}{\|\boldsymbol{v}_h - R_h(\boldsymbol{A})\|_{\mathrm{WIP}}}, \\
&= C_{\mathrm{stab}}^{-1} \frac{a_{h,\kappa=\sigma_\varepsilon}^{\theta\mathrm{WIP}}(\boldsymbol{v}_h - \boldsymbol{A}, \boldsymbol{v}_h - R_h\boldsymbol{A})}{\|\boldsymbol{v}_h - R_h(\boldsymbol{A})\|_{\mathrm{WIP}}}, \\
&\leq C_{\mathrm{bnd}} C_{\mathrm{stab}}^{-1} \|\boldsymbol{v}_h - \boldsymbol{A}\|_{\mathrm{WIP},*}.
\end{aligned}$$

Here we have used Lemma 3.3.9, the definition of the Ritz projector and Lemma 3.3.12. Since $\boldsymbol{v}_h$ is arbitrary the assertion follows. □

Theorem 4.2.21. *Let $\boldsymbol{A} \in C^1([0,t_F]; V^{*,r}) \cap C^2([0,t_F]; L^2(\Omega)^3)$ solve (4.21) and choose $\boldsymbol{A}_h^0 = R_h(\boldsymbol{A}_{init})$. Then*

$$\left\|\mu^{-1/2}\,\mathbf{curl}\,(\boldsymbol{A}_h^N - \boldsymbol{A}(t_F))\right\|_{L^2(\Omega)^3}^2 + \left|\boldsymbol{A}_h^N - \boldsymbol{A}(t_F)\right|_{j,\mu}^2 \leq C\left(h^{2r}\chi_1^2 + \Delta t^2 \chi_2^2\right),$$

with $\chi_1^2 := (1+t_F)\,\|\boldsymbol{A}\|_{C^1([0,t_F];V^{*,r})}^2$, $\chi_2^2 = \int_0^{t_F} \left\|\sqrt{\sigma_\varepsilon}\frac{\partial^2 \boldsymbol{A}}{\partial t^2}\right\|_{L^2(\Omega)^3}^2$. The constant C is independent of μ, σ_ε, $\boldsymbol{A}$, h, t_F and $|\cdot|_{j,\mu}$ is defined by (3.13).

In the theorem above, the space $C^k([0,t_F];X)$ is the space of k-times *Fréchet differentiable* functions $f:[0,t_F]\to X$ equipped with the supremum norm (cf. [46])

$$\|\boldsymbol{A}\|_{C^k([0,t_F];X)} \coloneqq \max_{0\le l\le k}\sup_{t\in[0,t_F]}\left\|\frac{\partial^l \boldsymbol{A}}{\partial t^l}(t)\right\|_X.$$

Proof. Since $\boldsymbol{A}$ is sufficiently regular we see that $\frac{\partial(\sigma_\varepsilon \boldsymbol{A})}{\partial t}=\sigma_\varepsilon\frac{\partial \boldsymbol{A}}{\partial t}\in L^2(\Omega)^3$ so that

$$\boldsymbol{j}^i-\sigma_\varepsilon\frac{\partial \boldsymbol{A}}{\partial t}=\mathbf{curl}\,\mu^{-1}\,\mathbf{curl}\,\boldsymbol{A}\in L^2(\Omega)^3.$$

Using the consistency of $a^{\theta\mathrm{WIP}}_{h,\kappa=0}$, Lemma 3.3.7 (which also holds for $\kappa=0$), we see ($\theta=-1$)

$$\left(\sigma_\varepsilon\frac{\partial \boldsymbol{A}}{\partial t},\boldsymbol{A}_h'\right)_{L^2(\Omega)^3}+a^{\theta\mathrm{WIP}}_{h,\kappa=0}(\boldsymbol{A},\boldsymbol{A}_h')=\left(\boldsymbol{j}^i,\boldsymbol{A}_h'\right)_{L^2(\Omega)^3}\quad\forall \boldsymbol{A}_h'\in V_h, t\in[0,t_F]. \tag{4.25}$$

We split the error as

$$\boldsymbol{A}_h^i-\boldsymbol{A}(t^i)=\underbrace{\boldsymbol{A}_h^i-R_h\boldsymbol{A}(t^i)}_{\coloneqq\xi_h^i}+\underbrace{R_h\boldsymbol{A}(t^i)-\boldsymbol{A}(t^i)}_{\coloneqq\xi_\pi^i}.$$

In order to simplify notation, let us formally introduce $\overline{\partial}^i\boldsymbol{A}_h^i\coloneqq\frac{\boldsymbol{A}_h^i-\boldsymbol{A}_h^{i-1}}{\Delta t}$. For any $\boldsymbol{A}_h'\in V_h$ we have

$$\begin{aligned}
&\left(\sigma_\varepsilon\overline{\partial}^i\xi_h^i,\boldsymbol{A}_h'\right)_{L^2(\Omega)^3}+a^{\theta\mathrm{WIP}}_{h,\kappa=0}(\xi_h^i,\boldsymbol{A}_h')\\
&\quad= \left(\sigma_\varepsilon\overline{\partial}^i\boldsymbol{A}_h^i,\boldsymbol{A}_h'\right)_{L^2(\Omega)^3}-\left(\sigma_\varepsilon R_h(\overline{\partial}^i\boldsymbol{A}),\boldsymbol{A}_h'\right)_{L^2(\Omega)^3}+a^{\theta\mathrm{WIP}}_{h,\kappa=0}(\boldsymbol{A}_h^i-R_h\boldsymbol{A}(t^i),\boldsymbol{A}_h')\\
&\quad\overset{(4.22)}{=} \left(\boldsymbol{j}^i,\boldsymbol{A}_h'\right)_{L^2(\Omega)^3}-\left(\sigma_\varepsilon R_h(\overline{\partial}^i\boldsymbol{A}),\boldsymbol{A}_h'\right)_{L^2(\Omega)^3}-a^{\theta\mathrm{WIP}}_{h,\kappa=0}(R_h\boldsymbol{A}(t^i),\boldsymbol{A}_h')\\
&\quad\overset{(4.23),(4.25)}{=} \left(\sigma_\varepsilon\left[\frac{\partial \boldsymbol{A}}{\partial t}(t^i)-R_h(\overline{\partial}^i\boldsymbol{A})\right],\boldsymbol{A}_h'\right)_{L^2(\Omega)^3}+\left(\sigma_\varepsilon(\boldsymbol{A}(t^i)-R_h\boldsymbol{A}(t^i),\boldsymbol{A}_h'\right)_{L^2(\Omega)^3}\\
&\quad=: \left(\sigma_\varepsilon\boldsymbol{z}^i,\boldsymbol{A}_h'\right)_{L^2(\Omega)^3}.
\end{aligned}\tag{4.26}$$

Now choose $\boldsymbol{A}_h'=\overline{\partial}^i\xi_h^i$ to get

$$\begin{aligned}
a^{\theta\mathrm{WIP}}_{h,\kappa=0}(\xi_h^i,\overline{\partial}^i\xi_h^i)&=\left(\sigma_\varepsilon\boldsymbol{z}^i,\overline{\partial}^i\xi_h^i\right)_{L^2(\Omega)^3}-\left(\sigma_\varepsilon\overline{\partial}^i\xi_h^i,\overline{\partial}^i\xi_h^i\right)_{L^2(\Omega)^3}\\
&=-\frac{1}{2}\left\|\sqrt{\sigma_\varepsilon}(\boldsymbol{z}^i-\overline{\partial}^i\xi_h^i)\right\|^2_{L^2(\Omega)^3}+\frac{1}{2}\left\|\sqrt{\sigma_\varepsilon}\boldsymbol{z}^i\right\|^2_{L^2(\Omega)^3}-\frac{1}{2}\left\|\sqrt{\sigma_\varepsilon}\overline{\partial}^i\xi_h^i\right\|^2_{L^2(\Omega)^3}\\
&\le\frac{1}{2}\left\|\sqrt{\sigma_\varepsilon}\boldsymbol{z}^i\right\|^2_{L^2(\Omega)^3}.
\end{aligned}\tag{4.27}$$

Therefore,

$$\begin{aligned}\overline{\partial}^i a^{\theta\mathrm{WIP}}_{h,\kappa=0}(\xi^i_h,\xi^i_h) &:= \frac{a^{\theta\mathrm{WIP}}_{h,\kappa=0}(\xi^i_h,\xi^i_h) - a^{\theta\mathrm{WIP}}_{h,\kappa=0}(\xi^{i-1}_h,\xi^{i-1}_h)}{\Delta t}\\ &= \frac{2a^{\theta\mathrm{WIP}}_{h,\kappa=0}(\xi^i_h,\xi^i_h) - 2a^{\theta\mathrm{WIP}}_{h,\kappa=0}(\xi^i_h,\xi^{i-1}_h) - a^{\theta\mathrm{WIP}}_{h,\kappa=0}(\xi^i_h-\xi^{i-1}_h,\xi^i_h-\xi^{i-1}_h)}{\Delta t}\\ &\le \left\|\sqrt{\sigma_\varepsilon}\boldsymbol{z}^i\right\|^2_{L^2(\Omega)^3}.\end{aligned}$$

So summing over all time steps we get

$$a^{\theta\mathrm{WIP}}_{h,\kappa=0}(\xi^N_h,\xi^N_h) \le \Delta t\sum_{i=1}^N \left\|\sqrt{\sigma_\varepsilon}\boldsymbol{z}^i\right\|^2_{L^2(\Omega)^3} + a^{\theta\mathrm{WIP}}_{h,\kappa=0}(\xi^0_h,\xi^0_h), \tag{4.28}$$

where the last term is zero since $\boldsymbol{A}^0_h = R_h(\boldsymbol{A}_{\mathrm{init}})$. It remains to give a bound for the sum over the $\boldsymbol{z}^i$. For this we split

$$\boldsymbol{z}^i = \underbrace{\frac{\partial \boldsymbol{A}}{\partial t}(t^i) - \overline{\partial}^i\boldsymbol{A}}_{:=\boldsymbol{z}^i_1} + \underbrace{\overline{\partial}^i\boldsymbol{A} - R_h(\overline{\partial}^i\boldsymbol{A})}_{:=\boldsymbol{z}^i_2} + \underbrace{\boldsymbol{A}(t^i) - R_h(\boldsymbol{A}(t^i))}_{:=\boldsymbol{z}^i_3}.$$

In order to bound $\boldsymbol{z}^i_1$, we use a Taylor expansion of $\boldsymbol{A}$ around t^i,

$$\boldsymbol{A}(t^i) - \boldsymbol{A}(t^{i-1}) = \Delta t\frac{\partial \boldsymbol{A}}{\partial t}(t^i) + \int_{t^{i-1}}^{t^i}(t^{i-1}-t)\frac{\partial^2\boldsymbol{A}}{\partial t^2}(t)\,\mathrm{d}t, \tag{4.29}$$

to get for $1 \le p < \infty$ (the forthcoming proof of Theorem 4.2.22 will require $p = 1$)

$$\begin{aligned}\Delta t\sum_{i=1}^N \left\|\sqrt{\sigma_\varepsilon}\boldsymbol{z}^i_1\right\|^p_{L^2(\Omega)^3} &= \Delta t^{1-p}\sum_{i=1}^N \left\|\sqrt{\sigma_\varepsilon}\int_{t^{i-1}}^{t^i}(t^{i-1}-t)\frac{\partial^2\boldsymbol{A}}{\partial t^2}(t)\,\mathrm{d}t\right\|^p_{L^2(\Omega)^3}\\ &\le \Delta t^{1-p}\sum_{i=1}^N \left(\int_{t^{i-1}}^{t^i}\left\|\sqrt{\sigma_\varepsilon}(t^{i-1}-t)\frac{\partial^2\boldsymbol{A}}{\partial t^2}(t)\right\|_{L^2(\Omega)^3}\mathrm{d}t\right)^p\\ &\le \sum_{i=1}^N\int_{t^{i-1}}^{t^i}\left\|\sqrt{\sigma_\varepsilon}(t^{i-1}-t)\frac{\partial^2\boldsymbol{A}}{\partial t^2}(t)\right\|^p_{L^2(\Omega)^3}\mathrm{d}t\\ &\le \Delta t^p\int_0^{t_F}\left\|\sqrt{\sigma_\varepsilon}\frac{\partial^2\boldsymbol{A}}{\partial t^2}\right\|^p_{L^2(\Omega)^3},\end{aligned} \tag{4.30}$$

where we have used Jensen's inequality in the second last step. In order to bound the term $\boldsymbol{z}^i_2$, we first observe that

$$\boldsymbol{z}^i_2 = (I-R_h)\Delta t^{-1}\int_{t^{i-1}}^{t^i}\frac{\partial\boldsymbol{A}}{\partial t}(t)\,\mathrm{d}t = \Delta t^{-1}\int_{t^{i-1}}^{t^i}(I-R_h)\frac{\partial\boldsymbol{A}}{\partial t}(t)\,\mathrm{d}t,$$

to conclude that

$$\begin{aligned}\Delta t\sum_{i=1}^{N}\left\|\sqrt{\sigma_\varepsilon}\boldsymbol{z}_2^i\right\|_{L^2(\Omega)^3}^p &= \Delta t^{1-p}\sum_{i=1}^{N}\left\|\sqrt{\sigma_\varepsilon}\int_{t^{i-1}}^{t^i}(I-R_h)\frac{\partial \boldsymbol{A}}{\partial t}(t)\,\mathrm{d}t\right\|_{L^2(\Omega)^3}^p\\ &\le \int_0^{t_F}\left\|\sqrt{\sigma_\varepsilon}(I-R_h)\frac{\partial \boldsymbol{A}}{\partial t}(t)\right\|_{L^2(\Omega)^3}^p\mathrm{d}t\\ &\overset{(4.24)}{\le} Ch^{p\,r}\int_0^{t_F}\left\|\frac{\partial \boldsymbol{A}(t)}{\partial t}\right\|_{V^*,r}^p\mathrm{d}t \le Ch^{p\,r}t_F\left\|\boldsymbol{A}\right\|_{C^1([0,t_F];V^{*,r})}^p,\end{aligned} \tag{4.31}$$

where we have used that $\left\|\sqrt{\sigma_\varepsilon}\boldsymbol{a}\right\|_{L^2(\Omega)^3} \le \|\boldsymbol{a}\|_{\mathrm{WIP}}$ in the second last step, cf. (3.12). Finally, the term $\boldsymbol{z}_3^i$ is easily bounded by

$$\Delta t\sum_{i=1}^{N}\left\|\sqrt{\sigma_\varepsilon}\boldsymbol{z}_3^i\right\|_{L^2(\Omega)^3}^p \le \Delta t\sum_{i=1}^{N}Ch^{p\,r}\left\|\boldsymbol{A}(t^i)\right\|_{V^{*,r}}^p \le Ch^{p\,r}t_F\left\|\boldsymbol{A}\right\|_{C^0([0,t_F];V^{*,r})}^p. \tag{4.32}$$

Now using the discrete coercivity (Lemma 3.3.9) and the estimates (4.24), (4.28) we get

$$\begin{aligned}&\left\|\mu^{-1/2}\,\mathbf{curl}\,(\boldsymbol{A}_h^N-\boldsymbol{A}(t_F))\right\|_{L^2(\Omega)^3}^2+\left|\boldsymbol{A}_h^N-\boldsymbol{A}(t_F)\right|_{j,\mu}^2\\ &\le 2\left\|\mu^{-1/2}\,\mathbf{curl}\,\xi_\pi^N\right\|_{L^2(\Omega)^3}^2+2\left|\xi_\pi^N\right|_{j,\mu}^2+2C_{\mathrm{stab}}^{-1}a_{h,\kappa=0}^{\theta\mathrm{WIP}}(\xi_h^N,\xi_h^N),\\ &\le C\left(h^{2r}\left\|\boldsymbol{A}(t_F)\right\|_{V^{*,r}}^2+\Delta t\sum_{i=1}^{N}\left\|\sqrt{\sigma_\varepsilon}\boldsymbol{z}^i\right\|_{L^2(\Omega)^3}^2\right).\end{aligned}$$

Finally, we use the estimates (4.30), (4.31), (4.32) with $p=2$ to finish the proof. □

By modifying the proof of the above theorem slightly we can also give a bound for $\sigma_\varepsilon\boldsymbol{A}$:

Theorem 4.2.22. *Under the assumptions of Theorem 4.2.21, we have*

$$\left\|\sqrt{\sigma_\varepsilon}(\boldsymbol{A}_h^N-\boldsymbol{A}(t_F))\right\|_{L^2(\Omega)^3} \le C\left(\chi_1 h^r+\tilde{\chi}_2\Delta t\right),$$

with $\chi_1=\sqrt{1+t_F}\,\|\boldsymbol{A}\|_{C^1([0,t_F];V^{*,r})}$, $\tilde{\chi}_2=\int_0^{t_F}\left\|\sqrt{\sigma_\varepsilon}\frac{\partial^2\boldsymbol{A}}{\partial t^2}\right\|_{L^2(\Omega)^3}$. *The constant C is independent of μ, σ_ε, $\boldsymbol{A}$, h and t_F.*

Proof. We choose $\boldsymbol{A}'=\xi_h^i$ in (4.26) to get

$$\left(\sigma_\varepsilon\xi_h^i,\xi_h^i\right)_{L^2(\Omega)^3}+\Delta t a_{h,\kappa=0}^{\theta\mathrm{WIP}}(\xi_h^i,\xi_h^i)=\left(\sigma_\varepsilon\xi_h^{i-1},\xi_h^i\right)_{L^2(\Omega)^3}+\Delta t\left(\sigma_\varepsilon\boldsymbol{z}^i,\xi_h^i\right)_{L^2(\Omega)^3}.$$

Since the term $\Delta t a_{h,\kappa=0}^{\theta\mathrm{WIP}}(\xi_h^i,\xi_h^i)\ge 0$, we can neglect it and use Cauchy-Schwarz on the right-hand side to get

$$\left\|\sqrt{\sigma_\varepsilon}\xi_h^i\right\|_{L^2(\Omega)^3} \le \left\|\sqrt{\sigma_\varepsilon}\xi_h^{i-1}\right\|_{L^2(\Omega)^3}+\Delta t\left\|\sqrt{\sigma_\varepsilon}\boldsymbol{z}^i\right\|_{L^2(\Omega)^3}.$$

Summing over all the time steps we thus have

$$\begin{aligned}\left\|\sqrt{\sigma_\varepsilon}\xi_h^N\right\|_{L^2(\Omega)^3} &\leq \left\|\sqrt{\sigma_\varepsilon}\xi_h^0\right\|_{L^2(\Omega)^3} + \Delta t\sum_{i=1}^{N}\left\|\sqrt{\sigma_\varepsilon}\boldsymbol{z}^i\right\|_{L^2(\Omega)^3},\\ &\leq \Delta t\int_0^{t_F}\left\|\sqrt{\sigma_\varepsilon}\frac{\partial^2\boldsymbol{A}}{\partial t^2}(t)\right\|_{L^2(\Omega)^3}\mathrm{d}t + Ct_Fh^r\left\|\boldsymbol{A}\right\|_{C^1([0,t_F];V^{*,r})}.\end{aligned}$$

We have used that $\xi_h^0 = 0$ since $\boldsymbol{A}_h^0 = R_h(\boldsymbol{A}_{\text{init}})$ and we have bounded the terms $\boldsymbol{z}_1^i$, $\boldsymbol{z}_2^i$, $\boldsymbol{z}_3^i$ using (4.30), (4.31) and (4.32), respectively, with $p = 1$. Finally, we remark that

$$\left\|\sqrt{\sigma_\varepsilon}(\boldsymbol{A}_h^N - \boldsymbol{A}(t_F))\right\|_{L^2(\Omega)^3} \leq \left\|\sqrt{\sigma_\varepsilon}\xi_h^N\right\|_{L^2(\Omega)^3} + \left\|\sqrt{\sigma_\varepsilon}\xi_\pi^N\right\|_{L^2(\Omega)^3},$$

and use (4.24) to bound $\left\|\sqrt{\sigma_\varepsilon}\xi_\pi^N\right\|_{L^2(\Omega)^3}$. □

Finally, let us analyze the convergence of the electric field $\boldsymbol{E} = -\frac{\partial\boldsymbol{A}}{\partial t}$ as $h, \Delta t \to 0$.

Theorem 4.2.23. *Under the assumptions of Theorem 4.2.21 assume additionally $\boldsymbol{A} \in C^2([0,t_F];V^{*,r})$. Then*

$$\Delta t\sum_{i=1}^{N}\left\|\sqrt{\sigma_\varepsilon}\left(\frac{\boldsymbol{A}_h^i - \boldsymbol{A}_h^{i-1}}{\Delta t} - \frac{\partial\boldsymbol{A}}{\partial t}(t^i)\right)\right\|_{L^2(\Omega)^3}^2 \leq C\left(\chi_1^2h^{2r} + \chi_2^2\Delta t^2 + \chi_3^2h^{2r}\Delta t^2\right), \tag{4.33}$$

with $\chi_1^2 = (1+t_F)\left\|\boldsymbol{A}\right\|_{C^1([0,t_F];V^{*,r})}^2$, $\chi_2^2 = \int_0^{t_F}\left\|\sqrt{\sigma_\varepsilon}\frac{\partial^2\boldsymbol{A}}{\partial t^2}\right\|^2$, $\chi_3^2 = t_F\left\|\boldsymbol{A}\right\|_{C^2([0,t_F];V^{*,r})}^2$. The constant C is independent of μ, σ_ε, $\boldsymbol{A}$, h and t_F.

Remark 4.2.24. *The above theorem does not give us an estimate for the error in $\frac{\partial\boldsymbol{A}}{\partial t}$ at a given time step t^i, but rather an ℓ^2 average over time (in a discrete sense).*

Proof. Let split the left-hand side of (4.33) into three contributions:

$$\begin{aligned}\Delta t\sum_{i=1}^{N}\left\|\sqrt{\sigma_\varepsilon}\left(\overline{\partial}^i\boldsymbol{A}_h^i - \frac{\partial\boldsymbol{A}}{\partial t}(t^i)\right)\right\|_{L^2(\Omega)^3}^2 &\leq 3\Delta t\sum_{i=1}^{N}\Bigg[\left\|\sqrt{\sigma_\varepsilon}\overline{\partial}^i\xi_h^i\right\|_{L^2(\Omega)^3}^2\\ &\quad + \left\|\sqrt{\sigma_\varepsilon}\overline{\partial}^i\xi_\pi^i\right\|_{L^2(\Omega)^3}^2 + \left\|\sqrt{\sigma_\varepsilon}\left(\overline{\partial}^i\boldsymbol{A}(t^i) - \frac{\partial\boldsymbol{A}}{\partial t}(t^i)\right)\right\|_{L^2(\Omega)^3}^2\Bigg],\\ &=: 3(\eta_1+\eta_2+\eta_3),\end{aligned}$$

where we have used the notations from the proof of Theorem 4.2.21. To bound the first term, η_1, we use that

$$\Delta t\left(\sigma_\varepsilon\overline{\partial}^i\xi_h^i, \overline{\partial}^i\xi_h^i\right)_{L^2(\Omega)^3} \overset{(4.27)}{=} \Delta t\left(\sigma_\varepsilon\boldsymbol{z}^i, \overline{\partial}^i\xi_h^i\right) - \Delta t a_{h,\kappa=0}^{\theta\text{WIP}}(\xi_h^i, \overline{\partial}^i\xi_h^i),$$

$$
\begin{aligned}
&= \Delta t \left(\sigma_\varepsilon \boldsymbol{z}^i, \overline{\partial}^i \xi_h^i\right) - \frac{1}{2} a_{h,\kappa=0}^{\theta\mathrm{WIP}}(\xi_h^i - \xi_h^{i-1}, \xi_h^i - \xi_h^{i-1}) \\
&\qquad - \frac{1}{2} a_{h,\kappa=0}^{\theta\mathrm{WIP}}(\xi_h^i, \xi_h^i) + \frac{1}{2} a_{h,\kappa=0}^{\theta\mathrm{WIP}}(\xi_h^{i-1}, \xi_h^{i-1}), \\
&\leq \Delta t \left(\sigma_\varepsilon \boldsymbol{z}^i, \overline{\partial}^i \xi_h^i\right) - \frac{1}{2} a_{h,\kappa=0}^{\theta\mathrm{WIP}}(\xi_h^i, \xi_h^i) + \frac{1}{2} a_{h,\kappa=0}^{\theta\mathrm{WIP}}(\xi_h^{i-1}, \xi_h^{i-1}).
\end{aligned}
$$

Now sum over all time-steps to get the following bound for η_1:

$$
\begin{aligned}
\eta_1 &\leq \Delta t \sum_{i=1}^{N} \left(\sigma_\varepsilon \boldsymbol{z}^i, \overline{\partial}^i \xi_h^i\right) + \frac{1}{2} a_{h,\kappa=0}^{\theta\mathrm{WIP}}(\xi_h^0, \xi_h^0) \\
&\overset{\mathrm{CS}}{\leq} \Delta t \left(\sum_{i=1}^{N} \left(\sigma_\varepsilon \boldsymbol{z}^i, \boldsymbol{z}^i\right)\right)^{1/2} \underbrace{\left(\sum_{i=1}^{N} \left(\sigma_\varepsilon \overline{\partial}^i \xi_h^i, \overline{\partial}^i \xi_h^i\right)\right)^{1/2}}_{\sqrt{\eta_1}} \\
&\leq 3\Delta t \sum_{i=1}^{N} \left[\left\|\sqrt{\sigma_\varepsilon} \boldsymbol{z}_1^i\right\|_{L^2(\Omega)^3}^2 + \left\|\sqrt{\sigma_\varepsilon} \boldsymbol{z}_2^i\right\|_{L^2(\Omega)^3}^2 + \left\|\sqrt{\sigma_\varepsilon} \boldsymbol{z}_3^i\right\|_{L^2(\Omega)^3}^2\right] \\
&\leq 3\Delta t^2 \int_0^{t_F} \left\|\sqrt{\sigma_\varepsilon} \frac{\partial^2 \boldsymbol{A}}{\partial t^2}\right\|_{L^2(\Omega)^3}^2 + Ch^{2r}(1 + t_F) \left\|\boldsymbol{A}\right\|_{C^1([0,t_F];V^{*,r})}^2,
\end{aligned}
$$

where we have used that $\xi_h^0 = 0$ by assumption together with the estimates (4.30), (4.31), (4.32) for $p = 2$. Let us continue with the second term, η_2: we first check that

$$
\begin{aligned}
\left\|\sqrt{\sigma_\varepsilon} \overline{\partial}^i \xi_\pi^i\right\|_{L^2(\Omega)^3} &= \left\|\sqrt{\sigma_\varepsilon}(R_h - I)\overline{\partial}^i \boldsymbol{A}\right\|_{L^2(\Omega)^3} \\
&\overset{(4.29)}{\leq} \left\|\sqrt{\sigma_\varepsilon}(R_h - I)\frac{\partial \boldsymbol{A}}{\partial t}(t^i)\right\|_{L^2(\Omega)^3} \\
&\qquad + \left\|\frac{\sqrt{\sigma_\varepsilon}}{\Delta t} \int_{t^{i-1}}^{t^i} (t^{i-1} - t)(R_h - I)\frac{\partial^2 \boldsymbol{A}}{\partial t^2}(t)\,\mathrm{d}t\right\|_{L^2(\Omega)^3}, \\
&\overset{(4.24)}{\leq} Ch^r \left\|\frac{\partial \boldsymbol{A}}{\partial t}\right\|_{C^0([0,t_F];V^{*,r})} + \int_{t^{i-1}}^{t^i} \left\|\sqrt{\sigma_\varepsilon}(R_h - I)\frac{\partial^2 \boldsymbol{A}}{\partial t^2}(t)\right\|_{L^2(\Omega)^3} \mathrm{d}t, \\
&\overset{(4.24)}{\leq} Ch^r \left\|\frac{\partial \boldsymbol{A}}{\partial t}\right\|_{C^0([0,t_F];V^{*,r})} + Ch^r \Delta t \left\|\frac{\partial^2 \boldsymbol{A}}{\partial t^2}\right\|_{C^0([0,t_F];V^{*,r})},
\end{aligned}
$$

to conclude

$$
\eta_2 \leq Ch^{2r} t_F \left(\left\|\frac{\partial \boldsymbol{A}}{\partial t}\right\|_{C^0([0,t_F];V^{*,r})}^2 + \Delta t^2 \left\|\frac{\partial^2 \boldsymbol{A}}{\partial t^2}\right\|_{C^0([0,t_F];V^{*,r})}^2\right).
$$

It remains to bound the term η_3: We first note that

$$
\left\|\sqrt{\sigma_\varepsilon}\left(\overline{\partial}^i \boldsymbol{A}(t^i) - \frac{\partial \boldsymbol{A}}{\partial t}(t^i)\right)\right\|_{L^2(\Omega)^3} = \left\|\frac{\sqrt{\sigma_\varepsilon}}{\Delta t} \int_{t^{i-1}}^{t^i} (t^{i-1} - t)\frac{\partial^2 \boldsymbol{A}}{\partial t^2}(t)\,\mathrm{d}t\right\|_{L^2(\Omega)^3}
$$

$$\leq \int_{t^{i-1}}^{t^i} \left\| \sqrt{\sigma_\varepsilon} \frac{\partial^2 \boldsymbol{A}}{\partial t^2}(t) \right\|_{L^2(\Omega)^3} \mathrm{d}t,$$

so that using Jensen's inequality we get

$$\eta_3 = \Delta t \sum_{i=1}^{N} \left\| \sqrt{\sigma_\varepsilon} \left(\overline{\partial}^i \boldsymbol{A}(t^i) - \frac{\partial \boldsymbol{A}}{\partial t}(t^i) \right) \right\|_{L^2(\Omega)^3}^2 \leq \Delta t^2 \int_0^{t_F} \left\| \sqrt{\sigma_\varepsilon} \frac{\partial^2 \boldsymbol{A}}{\partial t^2} \right\|_{L^2(\Omega)^3}^2 \mathrm{d}t.$$

Combining the estimates for η_1, η_2, and η_3 yields the assertion. □

Remark 4.2.25. *The three theorems above give only first order convergence in time. With a bit more effort and using higher order time-integration, one can show that higher-order convergence in time is possible, cf. [145, Chapter 7].*

Remark 4.2.26. *It should be possible to show similar estimates also for the case of moving meshes. In this case the bilinear form $a_{h,\kappa=0}^{\theta\,WIP}$ changes over time since the grid $\mathcal{T}_h$ looks different at every time step. This complicates the analysis considerably since one must show that $a_{h,\kappa=0}^{\theta\,WIP}$ is "differentiable" in time. In fact, let $\boldsymbol{j}^i \in L^2(\Omega)^3$ be arbitrary but fixed in time ($\check{\boldsymbol{j}}^i$ is advected with $\tilde{\Omega}_1$), let $\boldsymbol{A}(t)$ be the solution of $\mathbf{curl}\,\mu^{-1}\,\mathbf{curl}\,\boldsymbol{A} + \sigma_\varepsilon \boldsymbol{A} = \boldsymbol{j}^i$ in $\Omega(t)$ and let $\boldsymbol{A}_h(t)$ be the solution of $a_{h,\kappa=\sigma_\varepsilon}^{\theta\,WIP}(t; \boldsymbol{A}_h, \boldsymbol{A}_h') = (\boldsymbol{A}_h, \boldsymbol{A}_h')_{L^2(\Omega(t))^3}$. It suffices then to show that [145, Chapter 4]*

$$\left\| \frac{\partial \boldsymbol{A}_h(t)}{\partial t} - \frac{\partial \boldsymbol{A}(t)}{\partial t} \right\|_{L^2(\Omega)^3} \leq C h^r \left\| \boldsymbol{j}^i \right\|_{L^2(\Omega)^3}.$$

Figure 4.3 suggests that this holds since the derivative of the error w.r.t. the angle seems to be bounded.

4.2.4 Numerical Experiments

In this section, we would like to study the behavior of the approximation error of the SWIP method (4.20) for two concrete, numerical examples. We will first consider a case where the two sub-domains are at rest and then look at a more complete example where one sub-domain is in motion.

Fixed Meshes

We consider a numerical experiment that is similar to the one of Section 4.1: The domain is again a 3D sphere with radius 1 that is split into two hemispheres, $\tilde{\Omega}_0$ and $\tilde{\Omega}_1$, which are meshed individually, cf. Figure 4.2. We will rotate the two meshes against each other (but not over time!) by an angle ϑ to create arbitrary, non-conforming intersections. Thus, the theory from the previous section is applicable and we can expect convergence in Δt and h.

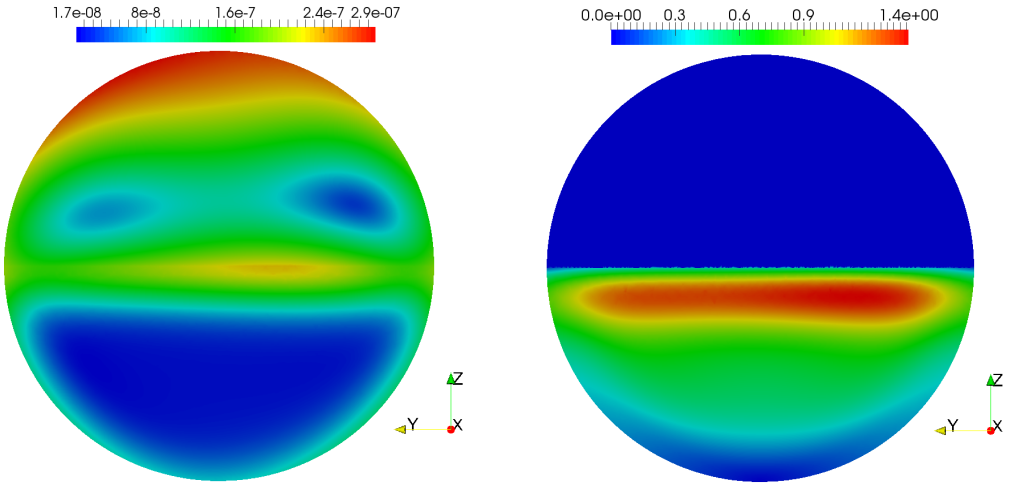

(a) Magnitude of magnetic induction $\boldsymbol{B} = \mathbf{curl}\, \boldsymbol{A}$

(b) Induced curent $-\sigma_\varepsilon \frac{\partial \boldsymbol{A}}{\partial t}$

Figure 4.9: Reference solution on cross section through sphere at time $t_F = 1.0$, $N = 200$, $h = 0.05$, $V_h = R_2(\Omega)$.

We use the SWIP formulation (4.22) with $\boldsymbol{A}_{\text{init}} \equiv 0$, $\boldsymbol{g}_D \equiv 0$ (cf. (3.2b)) , $\mu^{-1} \equiv 8 \cdot 10^5 \cong \mu_0^{-1}$, $\boldsymbol{j}^i = (\sin y, \cos z, \sin x / \cosh t)^T$ and

$$\sigma_\varepsilon(x) \coloneqq \begin{cases} 6 \cdot 10^7 & \text{in } \tilde{\Omega}_0, \\ 10^{-2} & \text{in } \tilde{\Omega}_1, \end{cases}$$

I.e. the southern hemisphere $\tilde{\Omega}_0$ is a good conductor (copper) while $\tilde{\Omega}_1$ is filled with air (we assume that the regularization error is negligible, cf. Section 4.1.2). Let $\Gamma = \partial\tilde{\Omega}_0 \cap \partial\tilde{\Omega}_1$ be the non-conforming interface. We note that $\boldsymbol{j}^i$ fulfills the compatibility condition $\int_\Gamma \boldsymbol{n}_\Gamma \cdot \boldsymbol{j}^i = 0$ (cf. (2.33)), so we can expect that the IBVP (4.21) has a weak solution.

We compute a (regularized) reference solution using the standard finite element method on a very fine, conforming mesh ($h = 0.05$) using third order edge functions $R_3(\Omega)$ in space. For the time-discretization we split $(0, t_F)$ into 200 time steps and use a second-order time-stepping Runge-Kutta scheme (SDIRK2 [2, Theorem 5]), cf. Figure 4.9.

This reference solution is then compared to the "approximate solution" which is obtained by the SWIP time-stepping on possibly non-conforming meshes using piecewise second order edge functions $V_h = R_2(\tilde{P}_\Omega)$, cf. Section 3.5. Figure 4.10 shows the relative error

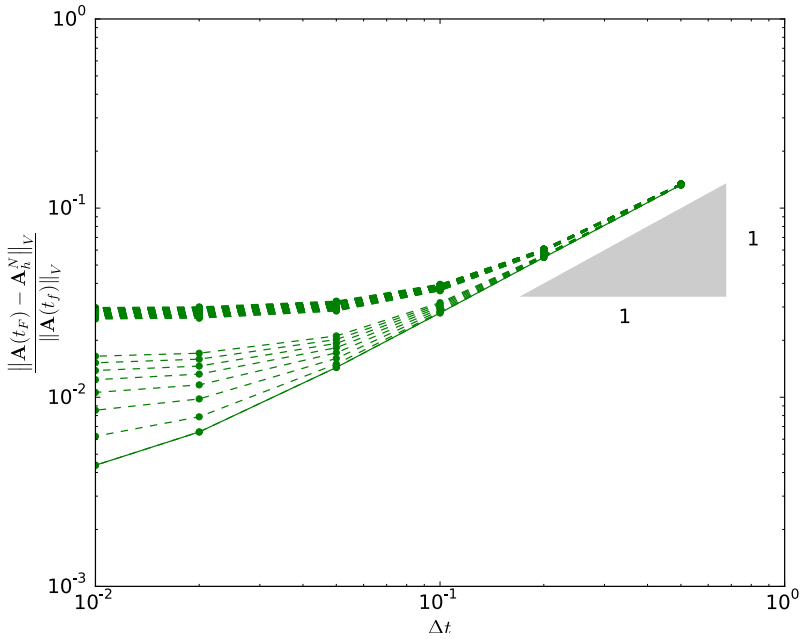

Figure 4.10: Relative error in energy norm vs. time-step size Δt, $h = 0.135$, $t_F = 1$. The dashed lines correspond to $\vartheta = 0.01n$, $n \in \{1, 2, \ldots, 49\}$ and the solid line to the conforming mesh with $\vartheta = 0$, $a_F = h_F$, $\eta = 50$, $V_h = R_3(\tilde{P}_\Omega)$. The apparent gap for small Δt vanishes if the angular resolution is increased.

in the energy norm [9]

$$\|\boldsymbol{A}\|_V^2 := \|\sqrt{\sigma_\varepsilon}\boldsymbol{A}\|_{L^2(\Omega)^3}^2 + \left\|\mu^{-1}\,\mathbf{curl}\,\boldsymbol{A}\right\|_{L^2(\Omega)^3}^2$$

for fixed mesh-size $h = 0.13$, different sizes of the time step Δt and for 50 different angles of rotation ϑ (dashed lines). We see that we obtain first order convergence in Δt for all angles and for Δt large enough. This agrees with Theorems (4.2.21) and (4.2.22) which also predict that the error stagnates for $\Delta t \to 0$ because the mesh-size h is kept fixed, i.e. the spatial error starts to dominate as $\Delta t \to 0$.

We study now the h-convergence: Theorems (4.2.21) and (4.2.22) guarantee here also at least first order convergence in h (for Δt fixed). Figure 4.11 shows that we get almost second-order convergence in h which is somewhat expected because we use second order edge elements, $R_2(\tilde{P}_\Omega)$, so we "loose" one order of accuracy only for $\vartheta > 0$ and only at the interface Γ, cf. Remark 4.1.1. We also see that for h small, the rate of convergence deteriorates and the error is dominated by the $O(\Delta t)$ term in Theorems 4.2.21, 4.2.22.

Remark 4.2.27. *If we compare Figure 4.4 against Figure 4.11 we see that in the latter the rate of convergence for second-order edge functions is slightly higher (almost* 2 *instead of*

[9] Here we compute the error roughly speaking only over a sphere of radius ≈ 0.95 to avoid problems with mapping a very coarse mesh onto the fine, reference mesh, cf. Remark 4.1.3.

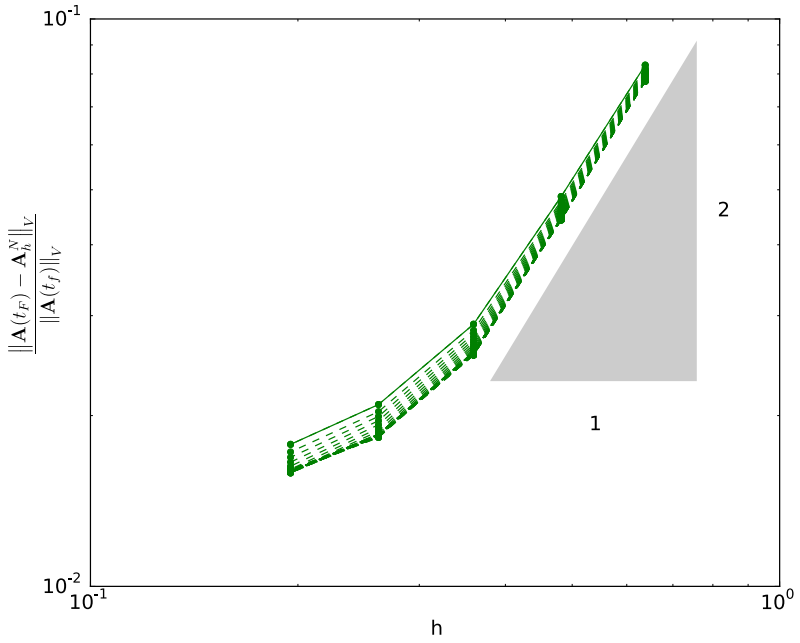

Figure 4.11: Relative error in energy norm vs. mesh-width h, $\Delta t = 10^{-5}$, $t_F = 10^{-4}$. The dashed lines correspond to $\vartheta = 0.01n$, $n \in \{1, 2, \ldots, 49\}$ and the solid line to the conforming mesh with $\vartheta = 0$, $a_F = h_F$, $\eta = 50$, $V_h = R_2(\tilde{P}_\Omega)$.

1.5*). This is most probably due to the homogeneous boundary conditions which were used in Figure 4.11, and which can be approximated exactly by second order edge functions. I.e. the term T_3 in the proof of Theorem 3.5.1 reduces the order of approximation only at the non-conforming interface Γ but not on the boundary $\partial\Omega$ and is thus less dominant than in the case considered in Figure 4.4. See also Remark 3.5.5.*

Moving meshes

In Remark 4.2.26, we have already hypothesized that we should also observe convergence in the case that $\tilde{\Omega}_1$ is in motion. We shall now investigate this case by simulating a well-known experiment from physics: We consider a loop of wire/metal that is introduced into a magnetic field generated by two permanent magnets, cf. Figure 4.12[10].

The domain Ω is split into two subdomains: $\tilde{\Omega}_0$ contains the two airboxes and is at rest while $\tilde{\Omega}_1$ is a very thin but long domain containing the wire loop. It slides through the

[10] The square loop of wire has outer sidelengths $(0.1, 1, 0.1)$, its cross-section is a square with side-length 0.1 and it is centered between the two cubic permanent magnets which are the rectangular cuboids $[-5,5]\times[-5,5]\times[1.5,5.5]$ and $[-5,5]\times[-5,5]\times[-5.5,-1.5]$, respectively (cf. Figures 4.12 and 4.13b). The two stationary airboxes have dimensions $[-15,15]\times[-15,15]\times[0.5,15]$, $[-15,15]\times[-15,15]\times[-15,-0.5]$ whereas the middle airbox at $t = 0$ is the rectangular cuboid $[-15,15]\times[-35,15]\times[-0.5,0.5]$.

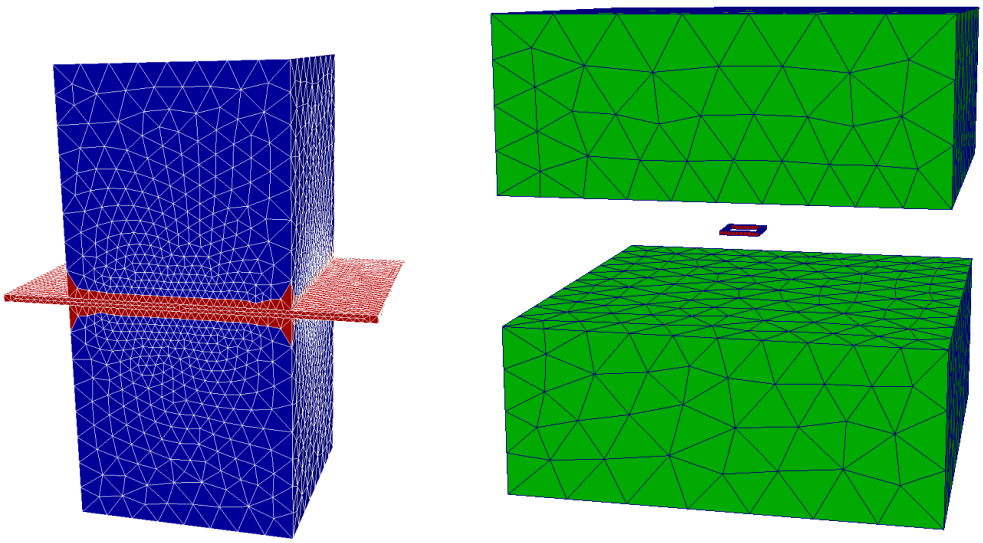

(a) Mesh with airbox. The blue mesh cells use first-order edge elements whereas the red cells use second-order edge elements (edge and face degrees are selected by minimum rule).

(b) Mesh without airbox showing the two permanent magnets (green) and the loop of wire (red)

Figure 4.12: The coarsest mesh $\mathcal{T}_h$, $h = 0.1$, at $t = 21$.

two connected components of $\tilde{\Omega}_0$ with velocity $\boldsymbol{V} = (0, 0.5, 0)^T$, cf. Figure 4.12. The total simulation time is $t_F = 40$ and the conductivity inside the wire loop is $6 \cdot 10^7$ while in the airbox it is set to $10^{-6}/\mu$, $\mu \equiv \mu_0 = 4\pi \cdot 10^{-7}$. The magnetization of the permanent magnets is realized by the extended constitutive law $\boldsymbol{B} = \mu(\boldsymbol{H} + \boldsymbol{M})$ with $\boldsymbol{M} = (0, 0, 1/(4\pi \cdot 10^{-7}))^T$ being the magnetization inside the permanent magnets, cf. (1.7).

For the approximation space V_h, we use second order edge elements in all mesh elements that share at least a node with the sliding interface, while we use first-order edge elements everywhere else, cf. Figure 4.12a. The polynomial degree of the facet- and edge DOF's (see Definition 3.4.12) is chosen using the *minimum rule*: The polynomial degree of an edge/facet is the minimum of the polynomial degree of all adjacent elements.

The simulation is carried out using the more general SWIP formulation (4.20) using implicit Euler time-stepping, $a_F = a_F^{(1)}$, $\eta = 500$ [11]. The initial solution $\boldsymbol{A}_h^0$ is obtained by solving $a_{h,\kappa=\sigma_\varepsilon}^{\theta\text{WIP}}(\boldsymbol{A}_h^0, \boldsymbol{A}_h') = -(\boldsymbol{M}, \mathbf{curl}\, \boldsymbol{A}_h')_{L^2(\Omega)^3}$ for all $\boldsymbol{A}_h' \in V_h$. Figure 4.13 shows the simulated magnetic field and the induced current in the wire loop. We see that the magnetic field is approximately homogeneous in between the two permanent magnets and has an approximate magnitude of 0.2[12]. Using Faraday's law (1.1a), we can thus give

[11] The penalty parameter η is chosen so that it is large enough, cf. Theorem 3.3.13

[12] The slight asymmetry of the magnetic field lines in Figure 4.13a is a visualization artifact.

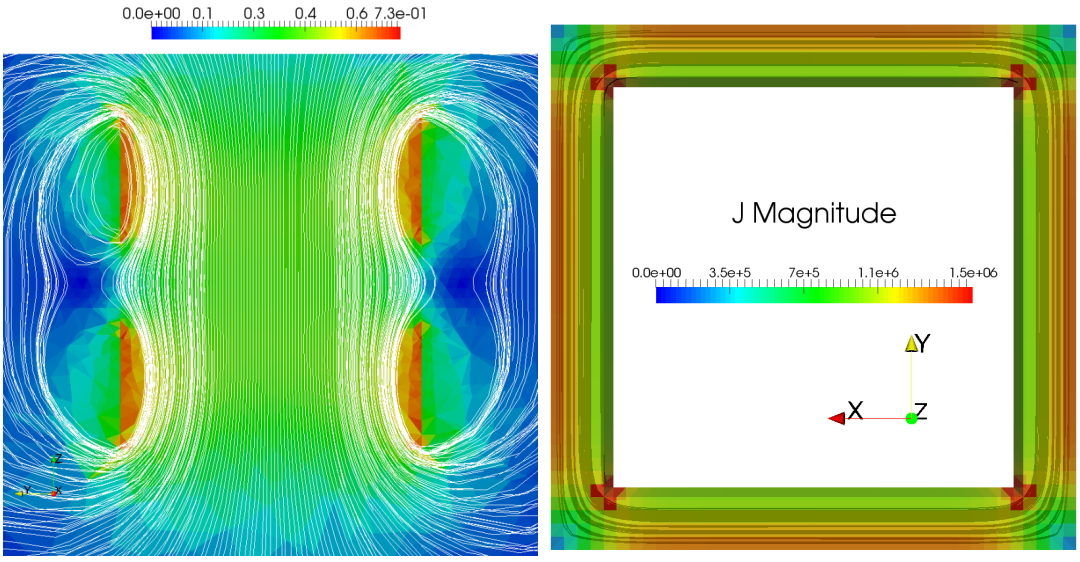

(a) Magnitude of magnetic induction (background) and magnetic field-lines for $t = 20$.

(b) Magnitude of induced current (background) and current streamlines for $t = 10$.

Figure 4.13: Magnetic field and induced current on finest mesh $\mathcal{T}_h$, $h = 0.025$.

a crude estimate for the induced current density: $4l\,|\boldsymbol{E}| = |\boldsymbol{B}|\,l\,|\boldsymbol{V}|$ where $l = 1$ is the side-length of the wire-loop and therefore the induced current should be approximately $\sigma\,|\boldsymbol{E}| = 6 \cdot 10^7\,\frac{0.2 \cdot 0.5}{4} = 1.5 \cdot 10^6$. This matches more or less the magnitude of the current density shown in Figure 4.13b.

Finally, Figure 4.14 plots the induced current density over time for different values of h and Δt. We see that if either h or Δt is reduced the discrete solution converges to some solution, cf. Theorem 4.2.23. Moreover, our crude estimate of $1.5 \cdot 10^6$ for the induced current density matches more or less the observed, maximal current densities in Figure 4.14.

Remark 4.2.28 (Permanent Magnets). *In order to simulate permanent magnets, the right-hand side of* (4.16a) *takes the weak form* $(-\boldsymbol{M}, \mathbf{curl}\,\boldsymbol{A}')$ *with* $\boldsymbol{A}' \in \boldsymbol{H}(\mathbf{curl}; \Omega)$ *being a test function. So the right-hand side is in the dual space* $\boldsymbol{H}(\mathbf{curl}; \Omega)'$ *(more precisely in* $\boldsymbol{H}_0(\mathbf{curl}; \Omega)$*) and does* not *lie in* $L^2(\Omega)^3$ *as we have assumed in Section 3.3. In fact, it is not so easy to come up with a Discontinuous Galerkin method that can handle such rough right-hand sides [55]. However, in our case the situation is less severe because the permanent magnets are surrounded by a conforming mesh so that the SWIP method reduces locally to the standard FEM method which can handle such right-hand sides without problems, cf. Remark 3.3.6.*

Remark 4.2.29 (Remeshing). *Instead of using a fixed mesh for* $\tilde{\Omega}_1$ *we could have also remeshed the insulator* $\tilde{\Omega}_{0,1}$ *in every time step (or just stretched the corresponding part of the mesh) because the temporal derivatives of* $\boldsymbol{A}$ *are anyway not defined in insulators. In*

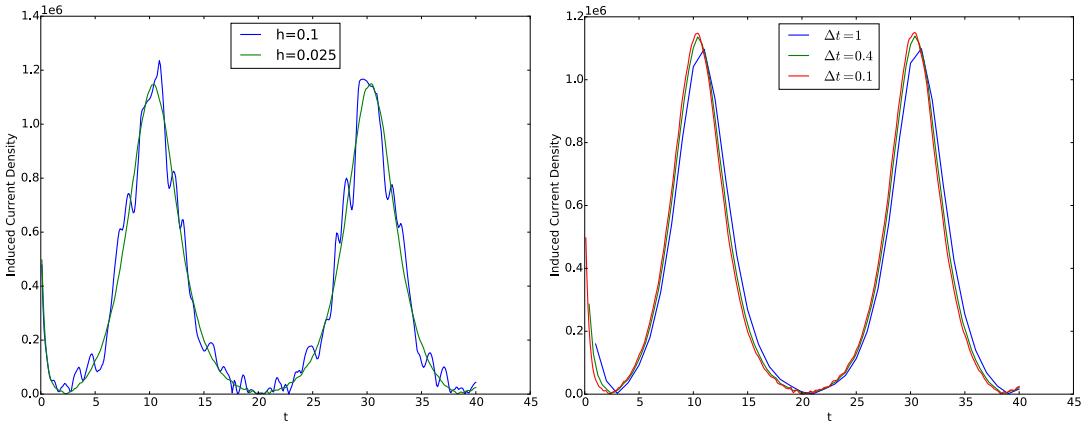

(a) For different mesh-widths, $\Delta t = 0.1$ (b) For different time step sizes, $h = 0.025$

Figure 4.14: Averaged, induced current density $\left|\sigma_\varepsilon \frac{\boldsymbol{A}^i - \boldsymbol{A}^{i-1}}{\Delta t}\right|$ over cross section $x = 0$

this case the domain Ω would have stayed the same for all $t > 0$. However, in practice we regularize the system by setting $\sigma_\varepsilon = \varepsilon$ in the insulator so that the temporal derivatives of $\boldsymbol{A}$ do not vanish. But it should be possible to replace the time stepping scheme in the insulator with the regularized magnetostatic operator for small ε.

Remark 4.2.30 (Sliding Contacts). *In the presence of sliding contacts one cannot make the simplification of Lemma 4.2.12 and the Galilean-type transformation rule* (4.9) *must be taken into account for the transmission conditions, cf.* (4.11c) *[124]. This complicates the analysis however drastically: First, the variational framework (Section 4.2.2) must be altered considerably because globally $\boldsymbol{A} \notin \boldsymbol{H}(\mathbf{curl}; \Omega)$ anymore ($\boldsymbol{A}$ defined by* (4.17)*). In fact, assume that $\boldsymbol{A} \in \boldsymbol{H}(\mathbf{curl}; \Omega)$ and transform $\boldsymbol{A}$ inside $\tilde{\Omega}_0$ from the rest frame into the moving frame by* (4.9) *(cf.* (4.17)*):*

$$\hat{\boldsymbol{A}}(\check{\boldsymbol{x}}, t) := \begin{cases} \boldsymbol{T}(t)^T \boldsymbol{A}(\boldsymbol{x}(\check{\boldsymbol{x}}, t), t) - \int_0^t \boldsymbol{T}(s)^T \left[\mathbf{grad}_{\boldsymbol{x}} (\mathcal{V} \cdot \boldsymbol{A})(\boldsymbol{x}(\check{\boldsymbol{x}}, s), s)\right] \mathrm{d}s & \text{if } \boldsymbol{x}(\check{\boldsymbol{x}}, t) \in \tilde{\Omega}_0, \\ \check{\boldsymbol{A}}_1(\check{\boldsymbol{x}}, t) & \text{else.} \end{cases}$$

Clearly, $\hat{\boldsymbol{A}}$ is the solution of problem (4.7) *expressed in the moving frame of reference. Therefore $\mathbf{curl}\, \hat{\boldsymbol{A}} = \check{\boldsymbol{B}} \in L^2(\Omega)^3$, i.e. $\hat{\boldsymbol{A}}$ must be tangentially continuous across the sliding interface (cf. Proposition 2.2.28). Looking at the above transformation it should be clear that this does not hold for general $\boldsymbol{A}$, i.e. we have a contradiction.*

Secondly, the numerical method must be altered as well to include a streamline-time-integration (cf. Remark 4.2.9) along the sliding contact which complicates the numerical implementation considerably. In particular, the term $\mathbf{grad}\,(\boldsymbol{A} \cdot \boldsymbol{V})$ is not easily calculated in terms of discrete shape-functions. See also [124] for an alternative approach.

Bibliographical remarks The (extended) Galilean invariance of the eddy current problem (Theorem 4.2.4) is well-known and has been used in numerous works to derive Lagrangian formulations [87, 86, 26, 155, 37]. However, it seems to be less known that in the absence of sliding contacts one can replace the transformation rules $\boldsymbol{T}\check{\boldsymbol{E}} = \boldsymbol{E} + \mathcal{V} \times \boldsymbol{B}$ and (4.9) by $\boldsymbol{T}\check{\boldsymbol{E}} = \boldsymbol{E}$ and (4.12), respectively, to derive the coupling conditions, but some authors make this assumption implicitly, cf. [119, 65, 37].

Buffa et al. [37] show existence of a solution of an IBVP that is very similar to problem (4.16) under the assumption that all conductors are in motion ($\Omega_{\sigma,0} = \emptyset$). In [35] the existence and uniqueness of the solution of the time-dependent eddy current problem in the absence of moving parts is proven using the Fourier transform.

The idea of using the Ritz-projector to give L^2 / energy estimates for the approximation error is inspired by the work of Wheeler [150], see also the excellent monograph by Thomée [145].

5 Enriched DG for Time-Harmonic Eddy Current Problems

In Chapter 3, we have seen that the interior penalty method can deal with very general, non-conforming approximation spaces V_h. In the previous chapter, we have then used this flexibility to couple $\boldsymbol{H}(\mathbf{curl})$ conforming, polynomial shape functions across arbitrary non-conforming mesh interfaces. In this chapter, we will use the interior penalty method to deal with *non-polynomial*, *non-*$\boldsymbol{H}(\mathbf{curl})$*-conforming* shape functions on *conforming* meshes. To be more specific, *we will enrich the standard polynomial approximation space with additional shape functions* to improve its approximation properties. Sloppily speaking Theorem 3.3.13 then implies that the discrete interior penalty solution $\boldsymbol{A}_h$ is also more accurate.

The idea of using a-priori knowledge about the problem at hand to improve the discrete approximation space has been around for a while and has been applied to a variety of problems: In 1973 Fix et al. [64] have proposed to enrich the classical FEM approximation space with singular basis functions to get higher orders of convergence in the presence of corner/interface singularities, see also [142, Chapter 8]. In their work, polynomial cutoff functions have been used to restrict the support of the singular basis functions to a few mesh-cells and hence obtain a sparse stiffness matrix. Later, this idea was generalized and popularized by Babuška and Melenk [10] with the introduction of the *Partition of Unity Method (PUM)*. This method takes a set of *local approximation spaces* and glues them together to a globally conforming approximation space by multiplying them with functions forming a partition of unity. In [10] it is shown that the local approximation properties carry over to the global approximation space. The PUM has been applied to a variety of problems, including the approximation of harmonic functions by harmonic polynomials [97], the approximation of Helmholtz's equation using plane waves [97, 10] and for the approximation of problems with rough coefficients [98].

In this chapter, we will restrict ourselves to the study of electromagnetic boundary layers of the time-harmonic eddy current problem. We will see that this phenomenon can be characterized by the *skin-depth* δ which measures the thickness of the boundary layer. Our goal will be to construct a numerical method that is *robust w.r.t.* δ, i.e. the approximation error should be independent of δ. Moreover, we strive for an *efficient method* that offers a reasonable rate of convergence for all δ (see Section 5.1). In order to achieve this, we will also use a-priori knowledge about the problem to enrich the approximation space but we will not use the PUM to couple the basis functions with each other. Instead we employ the NWIP formulation introduced in Chapter 3.

In contrast to the previous chapters we will not delve too much into the theory because it is rather complicated and there are still a number of open questions. Instead we will present some instructive numerical examples and appeal to the intuition of the reader.

Section 5.1 will consider a 1D version of the time-harmonic eddy current problem that exhibits exponential boundary layers. This very simple problem has been analyzed numerous times in the literature and we will briefly present the standard methods for its numerical approximation. We will then consider the 3D time-harmonic eddy current problem in Section 5.2 and use the previously presented 1D boundary layers to enrich the polynomial approximation spaces. We will see that this simple method resolves the boundary layers successfully but it also becomes apparent that one cannot easily improve the quality of approximation due to singularities in edges/corners of the conductors. Therefore, we study a simple, 2D time-harmonic eddy current problem that exhibits these singularities but not the boundary layers (Section 5.3). In the spirit of Section 5.2, we propose an enriched approximation space so that we can resolve the singular behavior without refining the mesh. Finally, we will combine the ideas of Sections 5.2 and 5.3 in Section 5.4 to devise a method for the 2D eddy current problem that is robust in δ (without proof).

5.1 Resolution of 1D Boundary Layers

Before we turn to the approximation of 3D boundary layers, let us study an instructive 1D problem: We consider the eddy current problem on the 1D domain $\Omega = (-1, 1)$ with the conductor $\Omega_\sigma = (-1, 0)$ having constant conductivity σ. Setting $\boldsymbol{A} = (0, 0, u^\delta(x))^T$ (δ will be defined later) in (2.31) and assuming $\mu = const$, we obtain

$$\begin{cases} \text{Find } u^\delta \in H^1(\Omega) \text{ subject to} \\ \qquad -\dfrac{\partial^2 u^\delta}{\partial x^2} + i\dfrac{2}{\delta^2}\chi_{\Omega_\sigma} u^\delta = \mu j^i \qquad \text{in } L^2(\Omega), & \text{(5.1a)} \\ \qquad\qquad u(-1) = g_{-1}, & \text{(5.1b)} \\ \qquad\qquad \dfrac{\partial u}{\partial x}(1) = g_1'. & \text{(5.1c)} \end{cases}$$

Here χ_{Ω_σ} is the characteristic function of the conductor Ω_σ, the skin-depth

$$\delta = \sqrt{\frac{2}{\mu\omega\sigma}}, \tag{5.2}$$

and the magnetic field is given by $\boldsymbol{B} = \mathbf{curl}\, \boldsymbol{A} = (0, -\frac{\partial u^\delta}{\partial x}, 0)^T$. Note that we have set the inhomogeneous Neumann boundary condition $\frac{\partial u}{\partial x}(1) = -B_2(1) = g_1'$ which prescribes the value of an external magnetic field at $x = 1$. Therefore, the above problem can be used to calculate the current $-i\omega\sigma\boldsymbol{A}$ induced by such an external magnetic field.

The corresponding energy norm for an open subset $\mathcal{O} \subseteq \Omega$ is defined by

$$\left\|u^\delta\right\|^2_{U^\delta(\mathcal{O})} \coloneqq \left\|\frac{\partial u^\delta}{\partial x}\right\|^2_{L^2(\mathcal{O})} + \frac{2}{\delta^2}\left\|u^\delta\right\|^2_{L^2(\mathcal{O}\cap\Omega_\sigma)}. \tag{5.3}$$

It is very well-known that the above model problem (5.1) features sharp boundary layers of thickness δ. In fact, it is easy to check that

$$u^\delta_{b,1}(x) \coloneqq \begin{cases} \exp\left(\frac{1+i}{\delta}x\right) & \text{if } x \in \Omega_\sigma, \\ \frac{1+i}{\delta}x + 1 & \text{else,} \end{cases} \quad u^\delta_{b,2}(x) \coloneqq \begin{cases} \exp\left(\frac{1+i}{\delta}(-x-1)\right) & \text{if } x \in \Omega_\sigma, \\ (1-\frac{1+i}{\delta}x)\exp\left(-\frac{1+i}{\delta}\right) & \text{else,} \end{cases} \tag{5.4}$$

are two weak solutions of (5.1a) for $j^i = 0$, i.e. they are *Trefftz functions* since they fulfill the PDE (5.1a) exactly. So if $j^i = 0$ they can be linearly combined to match the boundary conditions (5.1b), (5.1c). In particular, for $g_1' = 1$ the solution $w^\delta \coloneqq \frac{\delta}{1+i}u^\delta_{b,1}$ describes the behavior of the electromagnetic fields induced by an external magnetic field at $x = 1$ quite well (g_{-1} must be chosen correspondingly).

Let us briefly study the behavior of the solution w^δ for $\delta \to 0$. First of all, we note that $\left|w^\delta(x)\right| < \left|\frac{\delta}{1+i}\right|$ for all $x < 0$ so that $w^\delta \to 0$ in Ω_σ as $\delta \to 0$. I.e. $\lim_{\delta\to 0} w^\delta$ is the solution of the Perfect Electric Conductor (PEC) limit problem (still assuming $j^i = 0$)

$$\begin{cases} \text{Find } u \in H^1(\Omega_0) \text{ subject to} \\ \qquad -\dfrac{\partial^2 u}{\partial x^2} = 0 \qquad \text{in } L^2(\Omega_0), & \text{(5.5a)} \\ \qquad u(0) = 0, & \text{(5.5b)} \\ \qquad \dfrac{\partial u}{\partial x}(1) = 1. & \text{(5.5c)} \end{cases}$$

Also, note that

i) $\|\boldsymbol{B}\|_{L^2(\Omega_\sigma)} = \left\|\frac{\partial w^\delta}{\partial x}\right\|_{L^2(\Omega_\sigma)} = O(\delta^{1/2})$,

ii) $\|\boldsymbol{E}\|_{L^2(\Omega_\sigma)} = \left\|\omega w^\delta\right\|_{L^2(\Omega_\sigma)} = O(\omega\delta^{3/2})$, and hence

iii) $\left\|w^\delta\right\|_{U^\delta(\Omega_\sigma)} = O(\delta^{1/2})$.

This implies that for $\sigma \to \infty$, $\boldsymbol{E}$, $\boldsymbol{B}$ will vanish inside the conductor and in particular the energy in the conductor, $\left\|w^\delta\right\|_{U^\delta(\Omega_\sigma)}$, will also vanish. Finally, we remark that for $j^i \neq 0$ we have the following result:

Proposition 5.1.1. *Let $j^i \in \mathbb{P}_{k,h}(\{\Omega_\sigma, \Omega_0\})$. Then there are coefficients α_1, $\alpha_2 \in \mathbb{C}$ and a piecewise polynomial function $v \in C^1(\Omega)$, $v|_{\Omega_\sigma} \in \mathbb{P}_k(\Omega_\sigma)$, $v|_{\Omega_0} \in \mathbb{P}_{k+2}(\Omega_0)$ such that the unique solution u of (5.1) is*

$$u = \alpha_1 u_{b,1} + \alpha_2 u_{b,2} + v.$$

In other words: If $j^i \neq 0$ is polynomial we can split the solution into a boundary layer part and a polynomial remainder.

Proof. Let us define v in Ω_σ by

$$v(x)|_{\Omega_\sigma} = \sum_{l=0}^{\lceil k/2 \rceil} (i\omega\sigma)^{-l-1} \mu^{-l} \frac{\partial^{2l} j^i}{\partial x^{2l}}(x).$$

It is now easy to check that $-\frac{\partial^2 v}{\partial x^2} + i\mu\omega\sigma v = \mu j^i$ in Ω_σ. Since j^i is also polynomial in Ω_0 there is a polynomial $w \in \mathbb{P}_{k+2}(\Omega_0)$ such that $-\frac{\partial^2 w}{\partial x^2} = \mu j^i$ in Ω_0. Now choose $v(x)|_{\Omega_0} = w(x) + a_1 x + a_2$ with $a_1, a_2 \in \mathbb{C}$ such that $v \in C^1(\Omega)$. Therefore, v is a solution of (5.1a) but does not yet fulfill the boundary conditions (5.1b) and (5.1c). But since $u_{b,1}$ and $u_{b,2}$ are solutions of the homogeneous equation we can choose α_1, $\alpha_2 \in \mathbb{C}$ such that $\alpha_1 u_{b,1} + \alpha_2 u_{b,2} + v$ is a solution of the inhomogeneous problem (5.1). □

Remark 5.1.2. *Proposition 5.1.1 can be generalized to arbitrary $j^i \in H^{4m+2}(\Omega)$ and sharp estimates can be given for α_1, α_2 and $\left|j^i\right|_{H^l}$, $l \in \{0, 1, \ldots, 2m\}$ that make explicit the dependence on δ, cf. [134, Theorem 3.50]. However, in most engineering problems involving the time-harmonic eddy current problem $j^i \equiv 0$ or $j^i = const$ piecewise so that not much is gained by allowing $j^i \in H^{4m+2}(\Omega)$.*

Numerical approximation

Let us now discuss how the solution of problem (5.1) can be approximated numerically. The main problem lies in the resolution of the boundary layer which can get very thin if σ, μ or ω are large. Ideally, we would like to have a method where the approximation error is independent of δ. The following definition is a weaker form of [134, Definition 3.54], see also [129]:

Definition 5.1.3 (Robustness in δ)**.** *A numerical method using N unknowns to approximate the solution of problem* (5.1) *is said to be* robust in δ *with order $\lambda(N)$ if and only if*

$$\limsup_{N\to\infty} \left(\sup_{\delta\in(0,1]} \left\| u^\delta - u_N^\delta \right\|_{U^\delta(\Omega)} \right) \frac{1}{\lambda(N)} = C < \infty, \tag{5.6}$$

where u_N^δ is the numerical solution and C may depend on j^i, μ but not on δ.

We will now briefly summarize the δ-robustness of the most common (finite element based) numerical methods to solve problem (5.1) under the assumption that $j^i \equiv 0$:

(Quasi-)Uniform h-refinement If the sequences of meshes $\mathcal{T}_{\mathcal{H}}$ is quasi uniform and polynomials of order p are used, convergence of order h^p in the energy norm is observed if a condition of the form $h < C\delta$ is fulfilled [134, 129]. For arbitrary δ the method is still robust in δ (w.r.t. $\|\cdot\|_{L^2}$) but with a reduced order of convergence: Schatz and Wahlbin [129, Theorem A.2] show that if $p = 1$ then $\left\|u^\delta - u_N^\delta\right\|_{L^2(\Omega)} \leq C/\sqrt{N}$ uniformly in δ, i.e. $\lambda(N) = 1/\sqrt{N}$.

Graded h-refinement Instead of decreasing the mesh-width h uniformly, one can choose the element-size non-uniform but *depending on* δ and keep the polynomial degree p fixed. If an exponential grading [153, Lemma 2.4.5] is used, the method is δ-robust with $\lambda(N) = N^{-p}$ [153, Theorem 2.4.6].

p-refinement Instead of refining the mesh one can also increase the polynomial degree p globally in every element but keep h constant. Such a method is δ-robust with $CN^{-1} \leq \lambda(N) \leq CN^{-1}\sqrt{\log N}$, [136, Theorem 4.2] [134, Theorem 3.72] [13].

hp-refinement Finally one can adapt the mesh and change the polynomial degree p at the same time to obtain exponential convergence. In fact, Schwab [134, Theorem 3.74] shows that it suffices to consider a mesh consisting of three elements: $\mathcal{T}_h = \{(-1, -C_1(p + 1/2)\delta), (-C_1(p + 1/2)\delta, 0), (0, 1)\}$ with corresponding polynomial degrees $\boldsymbol{p} = (1, p, 1)$ so that $\lambda(N) = C_2^{N\ 1}$ with C_1, C_2 being independent of δ, p. See also [136, Theorem 4.3] for the case of complex valued boundary layers.

From the above list, the graded h-refinement and the hp-refinement are the only *efficient* [2] options for approximating the boundary layer robustly in δ. Unfortunately, both of these methods also require specialized meshes to resolve the boundary layer. This is not so much of a problem in $1D$ but can become a *non-trivial task in higher dimensions*: Often one is given a rather coarse 2D/3D mesh from a mesh generator that does not resolve the boundary layer and the surface of the conductor can be very complex, so that is not easy to refine the mesh without creating hanging nodes, and without introducing to many additional mesh cells.

On the other hand, we see that if we include the boundary layer functions $u_{b,1}$, $u_{b,2}$ into the approximation space V_h we can solve the 1D eddy current problem (5.1) with $j^i \equiv 0$ *exactly*. Moreover, Proposition (5.1.1) tells us that even with j^i polynomial we will be able to solve the problem exactly if we include polynomials of sufficiently high degree p in V_h. With a bit more work, it should also be possible to show that for j^i being analytic, exponential convergence in p can be achieved if the p-refined approximation space is enriched with $u_{b,1}$, $u_{b,2}$.

Similarly, it is possible to show that *quasi-uniform* h-refinement is robust in δ and recovers the expected algebraic rates of convergence (known for problems without boundary

[1] For large δ one has to switch to global p-refinement.

[2] With efficient we mean that the method can in principle achieve any algebraic rate of convergence (robust in δ) by increasing the polynomial degree p.

layers) if the approximation space is enriched with the exponential boundary layer functions $u_{b,1}$, $u_{b,2}$, see [10, Section 4.1].

Remark 5.1.4 (Approximation of boundary layer). *Let $w^\delta = \frac{\delta}{1+i} u_{b,1}^\delta$ be again the standard boundary layer solution (as before) and observe that $\left\|w^\delta\right\|_{U^\delta(\Omega_\sigma)} \to 0$ as $\delta \to 0$. I.e. the energy inside the conductor tends to zero as $\delta \to 0$ and is eventually dominated by the energy in Ω_0. For standard FEM and DG, we have best approximation results such as Theorem 3.3.13 which are stated w.r.t. energy norms that resemble the norm $\|\cdot\|_V$ of (5.3). Since the energy of w^δ is mostly concentrated in Ω_0 for δ small, we cannot expect a robust approximation of the boundary layer, i.e. we cannot expect that $\left\| \left(w^\delta - w_h^\delta\right)|_{\Omega_\sigma} \right\|_V / \left\| w^\delta|_{\Omega_\sigma} \right\|_V < C$ with C being independent of δ.*

In other words: FEM and DG methods generally try to optimize the overall error and not the error inside the conductor. Therefore, the approximation of the boundary layer itself may become worse as $\delta \to 0$ but the overall quality of approximation (measured in $\|\cdot\|_V$) should be independent of δ (if the method is robust in δ).

5.2 Approximation of 3D Boundary Layers

We are interested in solving the *regularized*, 3D eddy current problem (2.36) using an *enriched approximation space*. We strive for a method that is robust in δ w.r.t. p-refinement. For this we assume that the conductors Ω_σ are polyhedral and that we are given one (rather coarse) mesh $\mathcal{T}_h$, i.e. $\mathcal{T}_\mathcal{H}$ consists of one mesh only. Furthermore, we presume that the exact solution has well-defined jumps and averages, $\boldsymbol{A}^{\varepsilon,\delta} \in V^*$, so that we can approximate it using the NWIP formulation ($\theta = 1$) (3.6) with a discrete approximation space V_h. Considering the best approximation Theorem 3.3.13, we are thus left with the task of constructing a suitable approximation space V_h that can approximate the solution $\boldsymbol{A}^{\varepsilon,\delta}$ well for all values of δ.

The discussion from the previous Section 5.1 motivates the following choice for the approximation space:

$$V_h \coloneqq R_{k,h,0}(\tilde{P}_\Omega) \oplus \mathcal{A}_l(\mathcal{T}_h^\mathcal{A}).$$

Here $R_{k,h,0}(\tilde{P}_\Omega)$ consists of (broken) edge functions of order k defined on all of Ω. This space is enriched by the space $\mathcal{A}_l(\mathcal{T}_h^\mathcal{A})$ containing (modulated) Trefftz functions of the form (5.4). In the following we describe both spaces in more detail.

Modulated Trefftz Functions As in the 1D case, the solution $\boldsymbol{A}^{\varepsilon,\delta}$ of (2.36) exhibits also thin boundary layers along the surface of conductors for large σ, ω or μ. We can derive an explicit solution for the case of an infinite conductor: Let us consider the problem (2.36) on the whole space $\mathbb{R}^3$ such that σ is zero in the upper-half space $\Omega_0 = \{\boldsymbol{x} \in \mathbb{R}^3 |\ x_3 > 0\}$ and equal to a constant in the lower half space $x_3 < 0$, cf. Figure

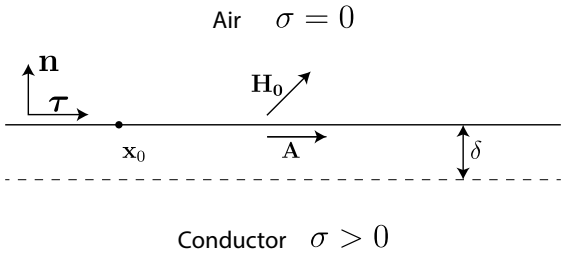

Figure 5.1: Construction of Trefftz functions at surface of conductor

5.1. Furthermore, assume that there is an external excitation by a magnetic field $\boldsymbol{H}_0$ which is constant along the surface $F \coloneqq \{\boldsymbol{x} \in \mathbb{R}^3 | x_3 = 0\}$ and that $\mu = const$, $\boldsymbol{j}^i = 0$ in Ω_σ. For $x_3 < 0$ we can then write the solution $\boldsymbol{A}^{\varepsilon,\delta}$ of (2.36) in the conductor explicitly as

$$\boldsymbol{A}^{\varepsilon,\delta}(\boldsymbol{x}) = \boldsymbol{A}_{F,\boldsymbol{\tau}}(\boldsymbol{x}) \coloneqq |\boldsymbol{H}_0|\, \delta/(1+i)\, \boldsymbol{\tau}\, \exp\left((1+i)(\boldsymbol{x}-\boldsymbol{x}_0)\cdot \boldsymbol{n}/\delta\right), \tag{5.7}$$

where $\boldsymbol{x}_0 \in F$, $\boldsymbol{n} = (0,0,1)^T$ is the surface normal of F, pointing from Ω_σ to Ω_0, $\boldsymbol{\tau} \in \mathbb{R}^3$ is a unit vector orthogonal to $\boldsymbol{n}$ and $\boldsymbol{H}_0$, and δ is the skin-depth (cf. Figure 5.1). Note that $\boldsymbol{A}_{F,\boldsymbol{\tau}}(\boldsymbol{x})$ is essentially a vector-valued version of the Trefftz function $u_{b,1}$ introduced in the previous section.

Remark 5.2.1 (Impedance Boundary Conditions (IBC))**.** *One can check that the solution* $\boldsymbol{A}_{F,\boldsymbol{\tau}}$ *fulfills*

$$\frac{1+i}{\delta}\boldsymbol{A}_{F,\boldsymbol{\tau}} = -\boldsymbol{n} \times \mathbf{curl}\, \boldsymbol{A}_{F,\boldsymbol{\tau}}$$

in Ω_σ*. Or equivalently,*

$$\boldsymbol{E} = (1+i)\sqrt{\frac{\omega\mu}{2\sigma}}\, \boldsymbol{n} \times \boldsymbol{H}. \tag{5.8}$$

This holds on the inside of the surface F *(i.e. in the conductor* Ω_σ*) and because* $\boldsymbol{E}$ *and* $\boldsymbol{H}$ *are tangentially continuous it also holds on the outside. Using relation* (5.8) *one can devise yet another numerical method to model the boundary layer in* Ω_σ *approximately: One can remove the conductors* Ω_σ *altogether from the computational domain* Ω *and replace them with the Robin-type boundary condition* (5.8)*. Relation* (5.8) *is often referred to as* Impedance Boundary Condition *(IBC) [112], see also [100] for higher order IBCs and estimates for the IBC modeling error, which are however only valid for smooth surfaces [51].*

Unfortunately, the conductors Ω_σ are usually not infinite half-spaces but rather bounded polyhedrons and the external magnetic field $\boldsymbol{H}_0$ is not constant along the surface of the

polyhedron. But usually $\boldsymbol{H}_0$ varies mildly along a face $F \in \mathcal{F}_h^i, F \subset \partial\Omega_\sigma$ which motivates that we *modulate* $\boldsymbol{A}_{F,\boldsymbol{\tau}}$ with polynomials: For each element $T \in \mathcal{T}_h$, $T \subset \Omega_\sigma$ we define the space

$$\mathcal{A}_l(T) \coloneqq \left\{ p\boldsymbol{A}_{F,\boldsymbol{\tau}} |\ p \in \mathbb{P}_l(T),\ F \in \mathcal{F}_h^i,\ F \subset \partial T \cap \partial\Omega_0,\ \boldsymbol{\tau} \text{ tangential of } F \right\}.$$

Note that the dimension of the space $\mathcal{A}_l(T)$ is $2n \dim(\mathbb{P}_l(T))$, where n is the number of faces of T that are at the conductor surface, since for every flat surface there are only two linearly independent tangentials $\boldsymbol{\tau}$. We define $\mathcal{T}_h^{\mathcal{A}} \coloneqq \{T \in \mathcal{T}_h |\ \dim(\mathcal{A}_0(T)) > 0, \sigma(T) > 0\}$ to be the set of elements with at least one adjacent boundary layer and we let $\overline{\Omega_{\mathcal{A}}} \coloneqq \bigcup_{T \in \mathcal{T}_h^{\mathcal{A}}} \overline{T}$. We then define the *broken, modulated Trefftz approximation space* by

$$\mathcal{A}_l(\mathcal{T}_h^{\mathcal{A}}) \coloneqq \left\{ \boldsymbol{A} \in L^2(\Omega_{\mathcal{A}})^3 |\ \ \boldsymbol{A}|_T \in \mathcal{A}_l(T)\ \forall T \in \mathcal{T}_h^{\mathcal{A}} \right\}. \tag{5.9}$$

Broken Edge Element Space Our idea is to use a conforming edge element space wherever possible and to "break" this space only around elements containing the modulated Trefftz functions. For this we define the domain decomposition $\tilde{P}_\Omega \coloneqq \{\Omega \setminus \overline{\Omega_{\mathcal{A}}}\} \cup \mathcal{T}_h^{\mathcal{A}}$ and define (cf. (3.38))

$$R_{k,h,0}(\tilde{P}_\Omega) \quad \coloneqq \quad \left\{ \boldsymbol{A} \in \boldsymbol{H}(\mathbf{curl}; \tilde{P}_\Omega) \middle|\ \boldsymbol{A}|_T \in \Phi_T(R_k)\, \forall T \in \mathcal{T}_h,\ \boldsymbol{n} \times \boldsymbol{A} = 0 \text{ on } \partial\Omega \right\}.$$

Note that we incorporate the Dirichlet boundary condition $\boldsymbol{n} \times \boldsymbol{A}$ directly into the approximation space so that the sums over $\mathcal{F}_h^b$ in (3.6) drop out, cf. Remark 3.3.16.

We also remark that the space $V_h = R_{k,h,0}(\tilde{P}_\Omega) \oplus \mathcal{A}_l(\mathcal{T}_h^{\mathcal{A}})$ is tangentially continuous across a face $F \in \mathcal{F}_h^i$ if and only if both the adjacent elements do *not* belong to $\mathcal{T}_h^{\mathcal{A}}$. I.e. the DG-terms on these faces drop out of the NWIP formulation (3.6) and the method resembles "locally" the standard finite element method, cf. Remark 3.3.6.

Moreover, we note that V_h is a superset of the space of conforming edge elements, $R_{k,h,0}(\Omega)$. Considering the best approximation result (3.19), we can thus expect that the space V_h has equal or better approximation properties than the space $R_{k,h,0}(\Omega)$. In fact, we have that $1 + C_{\text{bnd}}/C_{\text{stab}}$ is a function of C_{tr} (cf. Remark 3.4.5), η and ρ_2, of which only C_{tr} depends on the choice of V_h. If we assume that C_{tr} does not drastically increase by adding $\mathcal{A}_k(\mathcal{T}_h^{\mathcal{A}})$ to V_h, we see that we obtain almost the same error as for the choice $V_h = R_{k,h,0}(\Omega)$ (C_{tr} is the same for $R_{k,h}(\Omega)$ and $R_{k,h,0}(\mathcal{T}_h^{\mathcal{A}})$).

Remark 5.2.2 (SWIP vs. NWIP)**.** *In principle one could also use the SWIP formulation* (3.6) *($\theta = -1$) with the approximation space V_h to solve the time-harmonic eddy current problem* (2.36) *numerically. However, because of the complex valued mass term, the system will still be non-symmetric and it is not clear a-priori how the penalty parameter η must be chosen since the inverse trace inequality constant, C_{tr}, is not known for the space V_h, cf. Assumption 3.3.4. On the other hand, we have observed experimentally that the NWIP formulation works robustly for $\eta = 1$ for most spaces V_h. We suspect that this is always true but we have no rigorous proof, cf. Remarks 3.3.14 and 3.3.10.*

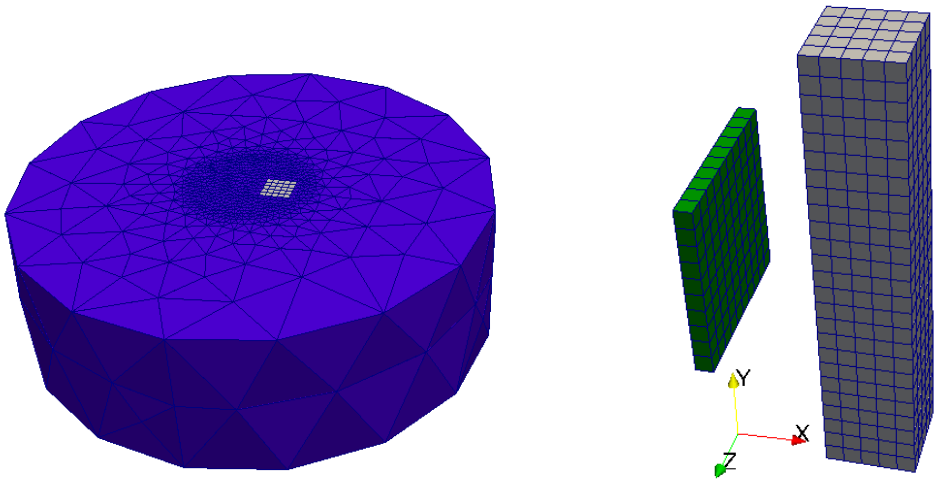

(a) With airbox. (b) Without airbox.

Figure 5.2: Coarse, hybrid mesh of domain Ω, $h = 0.2$

Numerical Example

We pose problem (2.36) on a cylindrically shaped domain Ω with two conductors constituting Ω_σ as shown in Figure 5.2: The "plate" Ω_{plate} (green) is the cuboid $(-0.7, -0.5) \times (-1, 1)^2$ whereas the "bar" Ω_{bar} (gray) has dimensions $(0.5, 1.5) \times (-2.5, 2.5) \times (-0.5, 0.5)$. We mesh Ω with the coarse, hybrid mesh $\mathcal{T}_h$ shown in Figure 5.2 that has only one layer of elements across the plate. This reflects the constraints encountered with more complex geometries where it is prohibitively expensive to resolve the boundary layers with a fine mesh.

The system is excited by a homogeneous generator current, $\boldsymbol{j}^i = (0, 2000, 0)$ in Ω_{bar}, which induces an electric current in the plate. We will vary σ_{plate} to simulate boundary layers of arbitrary thickness in the plate and keep all other (material) parameters constant: $\mu \equiv \mu_0 = 4\pi \cdot 10^{-7}$ globally, $\sigma_{\text{bar}} = 10^4$, $\omega = 50$, and $\varepsilon = 10^{-6}$.

Figure 5.3 shows a first, qualitative comparison of the current distribution in a cross section of the plate. Comparing the reference solution[3] with the solution obtained using the standard, first order FEM, we see that the top and bottom boundary layers are not resolved at all and that the behavior in the edges is completely wrong. The proposed (modulated) Trefftz method can resolve the bottom and top boundary layer much better but the error is still considerable at the edges.

[3] The reference solution was obtained on an refined mesh, which is adapted to the local features of the solution and uses second order edge elements $R_{2,h}(\Omega)$.

Figure 5.3: Current distribution $|\boldsymbol{j}| = \left|\omega\sigma \boldsymbol{A}^{\varepsilon,\delta}\right|$ in plate plotted over cross-section $y = 0$ for $\sigma_{\text{plate}} = 5 \cdot 10^7$, $\delta_{\text{plate}}/h = 0.063$, $k = l = 1$

Figure 5.4 shows the local surface error $\left\|\sqrt{\sigma\omega}\boldsymbol{n} \times (\boldsymbol{A}^{\varepsilon,\delta} - \boldsymbol{A}_h^{\varepsilon,\delta})\right\|_{L^2(\partial\Omega_{\text{plate}})^3}$ (cf. definition of 1D energy norm (5.3)) for different values of σ_{plate} (and hence δ_{plate}). We observe that the error of the enriched method is always equal or better than simple first-order edge functions $R_{1,h}(\Omega)$. In particular, for $\delta \ll h$ the modulated Trefftz functions clearly outperform the classical edge elements, cf. Fig. 5.3. For reference, we also show the error for a standard, first-order FEM formulation where the plate has been replaced by IBC, cf. Remark 5.2.1. We see that the IBC approximation becomes valid as $\delta_{\text{plate}} \to 0$ and does in fact reach the precision of the enriched method with $k = l = 1$ for small δ. We conclude that the modulated Trefftz functions work well for small and large δ and in particular they outperform the standard FEM as well as IBC in the transition zone $0.2 < \delta/h < 0.5$.

It seems that the error in Figure 5.4 increases for all three methods as $\delta \to 0$ so it is not clear whether they are robust in δ, cf. Definition 5.1.3. To better understand the reason for this we have plotted the pointwise distribution of the error in current density $\left|\sigma\omega(\boldsymbol{A}^{\varepsilon,\delta} - \boldsymbol{A}_h^{\varepsilon,\delta})\right|$ for different values of δ (respectively σ) over a cross-section in Figure 5.5. We observe that the boundary layers at the flat surfaces are approximated rather well which confirms the observations from Figure 5.3. However, the smaller δ, the more the error is concentrated in the edges (corners) of the plate. At the same time the maximum error in current density, $\left\|\sigma\omega(\boldsymbol{A}^{\varepsilon,\delta} - \boldsymbol{A}_h^{\varepsilon,\delta})\right\|_{L^\infty(\Omega_\sigma)}$, increases as $\delta \to 0$ (from 63 to $2.9 \cdot 10^4$) so that the overall surface error in Figure 5.4 increases.

This is not a surprise because the edges of the plate are exactly the locations where the Trefftz basis functions $\boldsymbol{A}_{F,\boldsymbol{\tau}}$ cease to be meaningful. Furthermore, we can expect singularities at the edges (and corners) of the plate due to the jump in σ and the non-smooth boundary $\partial\Omega_{\text{plate}}$ (see next section). So the problem is twofold:

i) The solution $\boldsymbol{A}^{\varepsilon,\delta}$ is not very smooth at edges/corners and increasing the polynomial

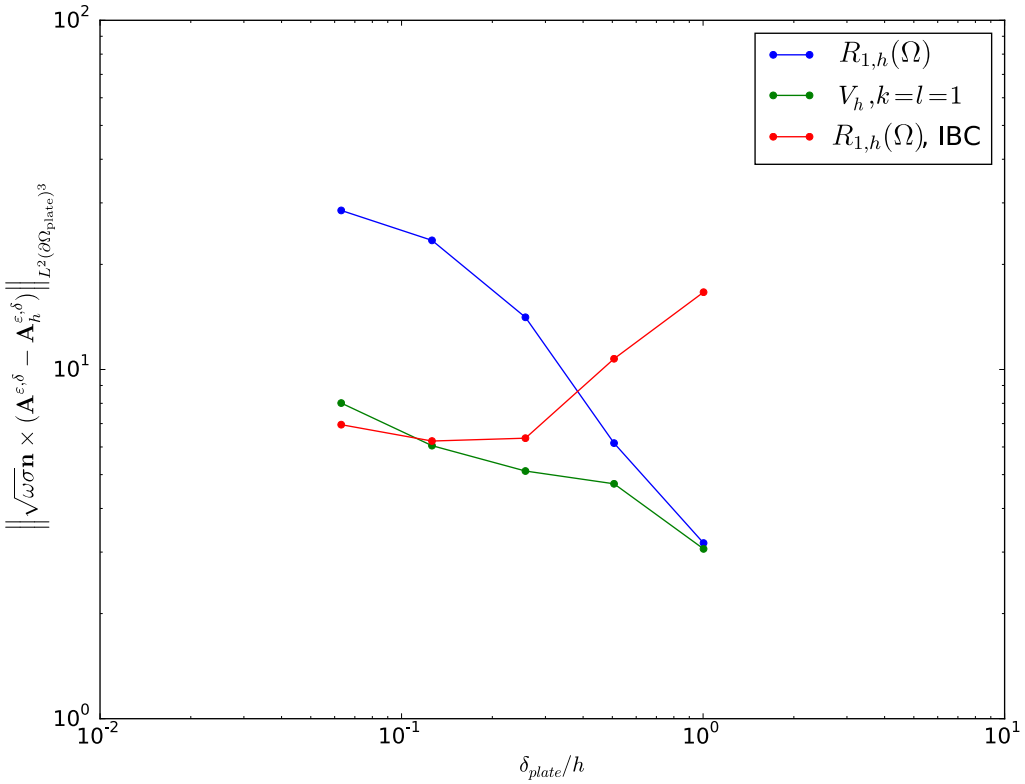

Figure 5.4: Local surface error vs. skin-depth δ for the mesh shown in Fig. 5.2.

degree k, l will not help much: Due to the lack of smoothness we can only expect an algebraic rate of convergence.

ii) The boundary layer also exists in edges/corners and we do not have an explicit expression for this component of the solution. Because of this we can only expect a δ robust rate of convergence of $O(k^{-1})$, cf. Section 5.1.

We will address problem i) in the next section and problem ii) in Section 5.4.

5.3 Approximation of 2D Eddy Current Singularities

In the previous section, we have seen that we cannot neglect the singularities in the edges/corners of the conductor for the design of the discrete approximation space V_h. We will now try to incorporate explicit expressions of the singularities of the eddy current problem into the approximation space V_h. Thereby we can absorb the singular components of the solution so that the remainder is smooth enough to be approximated

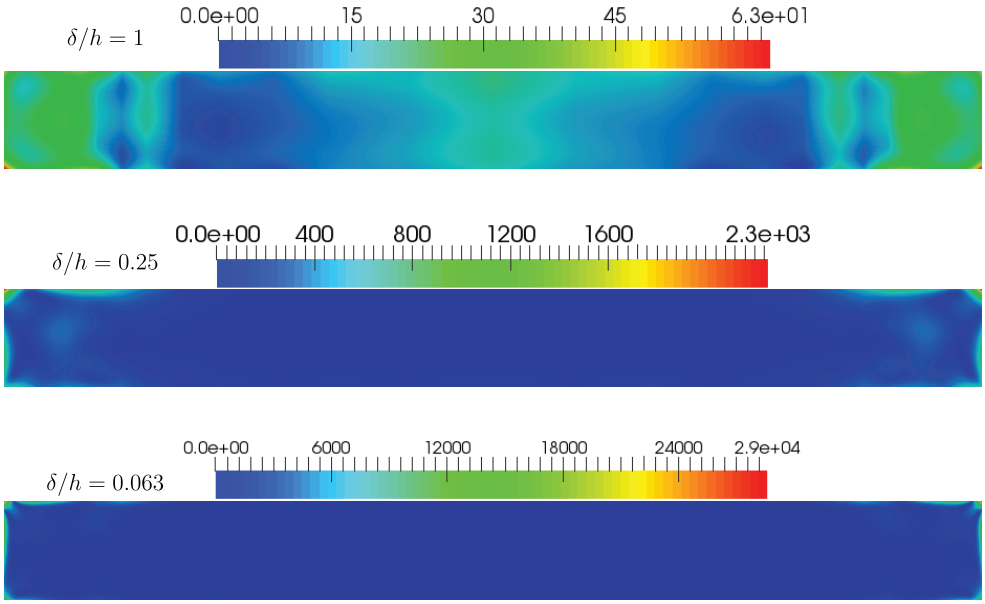

Figure 5.5: Pointwise distribution of the error $\left|\sigma\omega(\boldsymbol{A}^{\varepsilon,\delta} - \boldsymbol{A}_h^{\varepsilon,\delta})\right|$ plotted over cross section $y = 0$ of plate for enriched method with $k = l = 1$.

efficiently by high-order polynomials. Our goal will be to construct a method that shows an exponential rate of convergence for a *fixed* δ. The issue of δ-robustness will be discussed in the next section.

Unfortunately, it is prohibitively expensive to calculate a reference solution for the plate/bar geometry of the previous section that is accurate enough to study exponential convergence reliably. Moreover, the full 3D geometry features singularities along edges as well as singularities in corners of the conductor and for the latter there are no known explicit expressions [50]. We will therefore consider the simpler, 2D, scalar-valued time-harmonic eddy current problem (cf. (3.22)), cf. [39]: We assume that $\mu \equiv const$, $\boldsymbol{j}^i = \boldsymbol{0}$ in the vicinity of the corner, $\boldsymbol{A} = (0, 0, \varphi(x, y))^T$ and substitute this into the 3D eddy current problem (2.31) to obtain

$$\begin{cases} \text{Find } \varphi \in H^1(\Omega) \text{ subject to} \\ \qquad -\Delta\varphi + \dfrac{2i}{\delta^2}\chi_{\Omega_\sigma}\varphi = 0 & \text{in } L^2(\Omega), \qquad (5.10a) \\ \qquad \boldsymbol{n} \cdot \mathbf{grad}\,\varphi = 1 & \text{on } L^2(\Gamma_{N,1}), \qquad (5.10b) \\ \qquad \boldsymbol{n} \cdot \mathbf{grad}\,\varphi = 0 & \text{on } L^2(\Gamma_{N,0}). \qquad (5.10c) \end{cases}$$

Here Ω consists of a square-shaped conductor Ω_σ with side-length 0.05 and an L-shaped air-region Ω_0 surrounding the conductor, cf. Figure 5.6a. As before, the skin-depth $\delta = \sqrt{\frac{2}{\mu\omega\sigma}}$ and χ_{Ω_σ} denotes the characteristic function of Ω_σ. Since $\boldsymbol{n} \cdot \mathbf{grad}\,\varphi =$

$-\boldsymbol{n} \times \mathbf{curl}\,\varphi$, the inhomogeneous Neumann boundary condition (5.10b) represents an external magnetic field that excites the system, cf. (5.1c). In the 3D plate/bar example this field was generated by the current $\boldsymbol{j}^i$ in Ω_{bar}.

In order to motivate the homogeneous Neumann boundary condition (5.10c), we recall from the previous section that a boundary layer is formed along the surface of the conductor $\Gamma = \partial\Omega_\sigma \cap \partial\Omega_0$. Far away from the singularity, i.e. at $\Gamma_{N,0}$ the boundary layer will have (almost) the form $\boldsymbol{A}_{F,\boldsymbol{\tau}}$, cf. (5.7) and in particular its variation in normal direction (w.r.t. $\Gamma_{N,0}$) will be (almost) zero, i.e. $\boldsymbol{n} \cdot \mathbf{grad}\,\varphi = 0$.

We compute a reference solution φ of (5.10) using the standard FEM with 15-th order polynomials on an extremely fine, graded mesh. Figure 5.6b shows the induced current of this reference solution. Comparing it to Figure 5.3 we see that the 2D solution φ reproduces the current distribution of the 3D plate/bar example in an edge of the plate: In particular, we observe a boundary layer and we can expect the same singular behavior.

Remark 5.3.1. *The variable φ can be interpreted in two ways: So far, we have set φ equal to the z-component of the vector potential $\boldsymbol{A}$ and therefore $\mathbf{curl}\,\varphi = \boldsymbol{B} \in L^2(\Omega)^2$ is vector valued while the electric field $E = -i\omega\varphi$ is scalar valued. This is often referred to as the* transverse magnetic (TM) formulation*, cf. [80, Section 8.2]. The* transverse electric (TE) formulation *assumes that the magnetic field is scalar valued, $B = \varphi$, and thus $\boldsymbol{E} = \mu^{-1}\sigma^{-1}\,\mathbf{curl}\,B$ is vector valued in Ω_σ. I.e. the model problem* (5.10) *can be used to study both cases, but φ must be interpreted differently.*

5.3.1 Asymptotic Corner Expansion

Dauge et al. [51] give explicit expressions for the singularities of problem (5.10c), that is functions that describe the behavior of φ close to the corner $(0,0)$, see also [39]. In order to describe these singularities, we introduce the polar coordinate system (r,θ) and the opening angle α shown in Figure 5.6a. Since the singular behavior stems from the non-principal part of the elliptic operator one constructs explicit expressions for the singularities using an iterative procedure: We start from any (real valued) harmonic polynomial $\mathfrak{s}_0^{m,p} := r^m \cos(m\theta - p\pi/2)$, $m \in \mathbb{N}$, $p = 0, 1$, and construct the first order shadow $\mathfrak{s}_1^{m,p}$ by solving the problem [51, Equation (19)]

$$\begin{cases} \text{Find } \mathfrak{s}_j^{m,p} \in S^{m+2j} \text{ subject to} \\ \qquad\qquad \Delta\mathfrak{s}_j^{m,p} = 4\mathfrak{s}_{j-1}^{m,p}, \end{cases} \tag{5.11}$$

with $j = 1$. Here the space of quasi-homogeneous functions is defined by

$$S^l := \operatorname{span}\left\{ r^l \log^q r\, \Phi(\theta) \,\middle|\, q \in \mathbb{N},\ \Phi \in C^1([-\pi,\pi]),\ \Phi|_{\Omega_\sigma} \text{ smooth},\ \Phi|_{\Omega_0} \text{ smooth} \right\}.$$

This process can be repeated j times to get the shadow of order j.

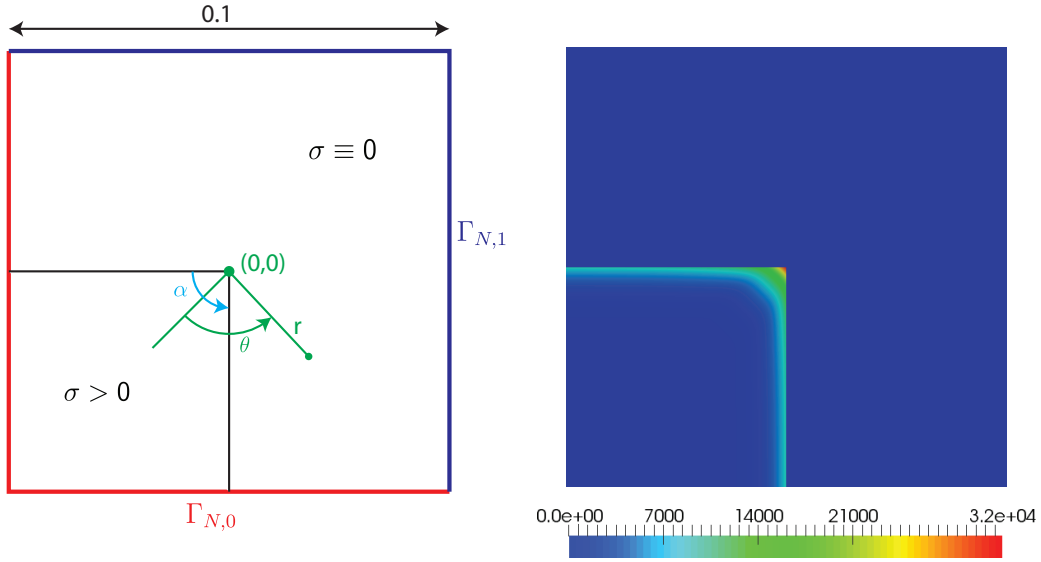

(a) Domain Ω with the boundary parts $\overline{\partial\Omega} = \overline{\Gamma_{N,0} \sqcup \Gamma_{N,1}}$. The associated polar coordinate system is shown in green.

(b) Reference solution showing induced current $|\omega\sigma\chi_{\Omega_\sigma} u|$ for $\mu = \sigma = 1$, $\omega = 367514$, $\delta/0.05 = 0.063$

Figure 5.6: The simple 2D eddy current model problem

Following Dauge et al. [51], we will describe the shadow functions $\mathfrak{s}_j^{m,p}$ using complex valued functions: We associate with every point $(r, \theta) \in \Omega$ the complex number $z = r\exp(i\theta)$, cf. Figure 5.6a. Every pair of real valued shadow functions $(\mathfrak{s}_j^{m,0}\mathfrak{s}_j^{m,1})$ is then associated with the complex valued shadow $s_j^m(z) \coloneqq \mathfrak{s}_j^{m,0}(r,\theta) + i\mathfrak{s}_j^{m,1}(r,\theta)$.

In general, one can write such a complex shadow as follows:

Proposition 5.3.2. *[51, Proposition A.9] Let $m \in \mathbb{N}$ and $j \geq 1$. Then*

$$\begin{aligned} s_j^m(z)\big|_{\Omega_\sigma} &= a_{mj} z^{m+2j} \log^j z + a'_{mj} \overline{z}^{m+2j} \log^j \overline{z} \\ &\quad + \sum_{n=0}^{j-1}\sum_{i=0}^{j-n} b_{mj,ni} z^{m+2j-i}\, \overline{z}^i \log^n z + \sum_{n=0}^{j-1}\sum_{i=0}^{j-n} c_{mj,ni} z^i\, \overline{z}^{m+2j-i} \log^n \overline{z}, \\ s_j^m(z_0)\big|_{\Omega_0} &= (-1)^m a_{mj} z_0^{m+2j} \log^j z_0 + (-1)^m a'_{mj} \overline{z}_0^{m+2j} \log^j \overline{z}_0 \\ &\quad + \sum_{n=0}^{j-1}\sum_{i=0}^{j-n} b'_{mj,ni} z_0^{m+2j-i}\, \overline{z}_0^i \log^n z_0 + \sum_{n=0}^{j-1}\sum_{i=0}^{j-n} c'_{mj,ni} z_0^i\, \overline{z}^{m+2j-i} \log^n \overline{z}_0, \end{aligned}$$

where $z_0 \coloneqq -z$ and a_{mj}, a'_{mj}, $b_{mj,ni}$, $b'_{mj,ni}$, $c_{mj,ni}$, $c'_{mj,ni}$ are real coefficients.

Remark 5.3.3 (Coefficients). *For $j = 1$ the coefficients a_{mj}, a'_{mj}, $b_{mj,ni}$, $b'_{mj,ni}$, $c_{mj,ni}$, $c'_{mj,ni}$ can be obtained from [51, Proposition 4.3] so that the corresponding shadow functions $\mathfrak{s}_1^{m,p}$ could be directly used as basis functions of a discrete approximation space.*

Unfortunately, there are no explicit expressions available for the coefficients if $j > 1$; but one could use the (rather complicated) induction process described in [51, Appendix A]. Fortunately, we don't need to do this because we can let the NWIP formulation select the proper value of the coefficients for us.

From the complex shadow functions s_j^m, we can recover the real-valued shadow functions simply by $\mathfrak{s}_j^{m,0} = \operatorname{Re} s_j^m$, $\mathfrak{s}_j^{m,1} = \operatorname{Im} s_j^m$. Using the fact that $r\frac{\partial}{\partial r} = z\frac{\partial}{\partial z} + \overline{z}\frac{\partial}{\partial \overline{z}}$ and $\frac{\partial}{\partial \theta} = i(z\frac{\partial}{\partial z} - \overline{z}\frac{\partial}{\partial \overline{z}})$ [51] one easily deduces that $\mathfrak{s}_j^{m,p}\Big|_\Omega \in H^{m+2j}(\{\Omega_\sigma, \Omega_0\})$, but $\mathfrak{s}_j^{m,p}\Big|_\Omega \notin H^{m+2j+1}(\{\Omega_\sigma, \Omega_0\})$ for $p = 0, 1$. It is even possible to prove the following decomposition [51, Equations (21), (22)], [50], [85]:

Theorem 5.3.4 (Decomposition). *Let $\varphi \in H^1(\Omega)$ be the solution of (5.10) and let $s \in \mathbb{N}$, $s \geq 1$ be fixed. Furthermore, let $\chi \in C_0^\infty(\Omega; \mathbb{R})$ be a smooth cutoff function such that $\chi = 1$ inside a ball $B(0; r)$. Then there exist coefficients $\Lambda^{m,p,j} \in \mathbb{C}$ such that*

$$\varphi = \chi \sum_{m=0}^{s-2} \sum_{p=0}^{1} \sum_{j=1}^{\lfloor \frac{s-m}{2} \rfloor} \Lambda^{m,p,j} \mathfrak{s}_j^{m,p} + \mathcal{R}_{s+1}, \tag{5.12}$$

where the remainder $\mathcal{R}_{s+1} \in H^{s+1}(\{\Omega_\sigma, \Omega_0\})$.

The above theorem tells us in particular that $\varphi \in H^2(\{\Omega_\sigma, \Omega_0\})$, i.e. $\varphi \in C^0(\Omega)$ by the Sobolev imbedding. Also, $\varphi \in U^*$ so that Assumption 3.3.17 holds.

Remark 5.3.5. *The above theory generalizes straightforwardly to any conductor $\Omega_\sigma \subset \mathbb{R}^2$ with piecewise smooth boundary. Interestingly the type of singularity does not depend on the opening angle α at the singular point: The leading singularity is always of type $r^2 \log r$.*

5.3.2 Algebraic Convergence

For $j, s \in \mathbb{N}$, $j \geq 1$, $s \geq 2j$ we define the singular space

$$\mathcal{S}_j^s(\Omega) \coloneqq \operatorname{span}\Big\{ \operatorname{Re} f(z), \operatorname{Im} f(z) \Big|\ f(z) = z^{s'-i}\ \overline{z}^i \log^{j'} z,\ z \in \Omega,\ 0 \leq s' \leq s, \\ 1 \leq j' \leq j,\ 0 \leq i \leq j - j' \Big\}.$$

For a partition $P_\Omega = \{\Omega_i\}_{i \geq 0}$ of Ω we furthermore define the broken, singular space

$$\mathcal{S}_j^m(P_\Omega) \coloneqq \left\{ f \in L^2(\Omega) \Big|\ f|_{\Omega_i} \in \mathcal{S}_j^m(\Omega_i)\, \forall \Omega_i \in P_\Omega \right\}. \tag{5.13}$$

In order to define the discrete approximation space, we assume that there is an *affine* (coarse) mesh $\mathcal{T}_h$ of Ω that is compatible with μ, σ, i.e. Assumption 3.3.1 holds. We

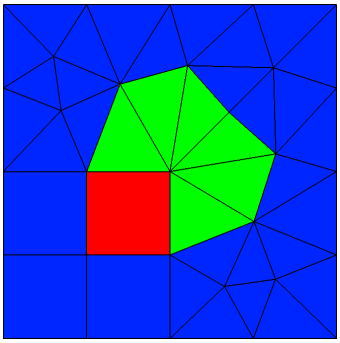

Figure 5.7: Domain decomposition $\tilde{P}_\Omega$ for a concrete mesh $\mathcal{T}_h$ of Ω, cf. Figure 5.6a. Every color corresponds to one subdomain $\tilde{\Omega}_i \in \tilde{P}_\Omega$. The partition $P_\mathcal{S}$ contains only the red and the green subdomains.

denote by $\mathcal{T}_h^\mathcal{S} \subset \mathcal{T}_h$ the set of all mesh elements that touch node $(0,0)$ and we define $\Omega_\mathcal{S}$ by $\overline{\Omega_\mathcal{S}} \coloneqq \overline{\bigcup_{T\in\mathcal{T}_h^\mathcal{S}} T}$. Furthermore, we define the partitions $P_\mathcal{S} \coloneqq \{\Omega_0 \cap \Omega_\mathcal{S}, \Omega_\sigma \cap \Omega_\mathcal{S}\}$ and $\tilde{P}_\Omega \coloneqq P_\mathcal{S} \cup \{\Omega \setminus \overline{\Omega_\mathcal{S}}\}$, cf. Figure 5.7.

Based on Theorem 5.3.4, we propose the following discrete approximation space

$$U_h^{s,k} \coloneqq \mathcal{S}^s_{\lfloor s/2\rfloor}(P_\mathcal{S}) \oplus \mathcal{P}_{k,h}(\tilde{P}_\Omega), \tag{5.14}$$

where $s \geq 2$ determines the smoothness of the remainder $\mathcal{R}_{s+1}$ and is kept fixed; $k \geq 1$ is the polynomial degree. Note that generally $\mathfrak{s}_j^{m,p}\big|_\Omega \notin \mathcal{S}_j^{m+2j}(\{\Omega_0, \Omega_\sigma\})$ for $p = 0, 1$, but $\mathfrak{s}_j^{m,p}\big|_\Omega \in U_h^{2m+j,2m+j}$ and hence the triple sum in (5.12) belongs to $U_h^{s,s}$.

Let now $\varphi_h \in U_h^{s,k}$, $k \geq s$ be the NWIP ($\theta = 1$) solution of (5.10), (3.22). Using Theorem 5.3.4 with a cutoff function χ that fulfills $\chi \equiv 1$ in $\Omega_\mathcal{S}$ together with Theorem 3.3.20 we see that

$$\begin{aligned}\|\varphi - \varphi_h\|_{\mathrm{WIP}} < C \Bigg[&\inf_{v_h \in \mathcal{P}_{k,h}(P_\mathcal{S})} \|\mathcal{R}_{s+1} - v_h\|_{\mathrm{WIP},*(\Omega_\mathcal{S})} \\ &+ \inf_{v_h \in \mathcal{P}_{k,h}(\Omega\setminus\overline{\Omega_\mathcal{S}})} \|\varphi - v_h\|_{\mathrm{WIP},*(\Omega\setminus\overline{\Omega_\mathcal{S}})} \Bigg],\end{aligned} \tag{5.15}$$

where C is a generic constant that depends on k only through the inverse trace-inequality constant of $U_h^{s,k}$ (cf. Assumption 3.3.18) and $\|\cdot\|_{\mathrm{WIP},*(X)}$ is the WIP,* norm (3.28) restricted to $X \subset \Omega$. The two infima on the right-hand side of (5.15) are easily estimated using standard interpolation theory [12, 13] but unfortunately, we do not know how C_{tr} depends on k.

Let us therefore study the approximation properties of $U_h^{s,k}$ in a numerical experiment: We set $\mu \equiv \sigma \equiv 1$ and solve (5.10) using the NWIP ($\theta = 1$) formulation (3.25) with penalty parameter $\eta = 1$ and local length scale $a_F = h_F$. The linear system of equations

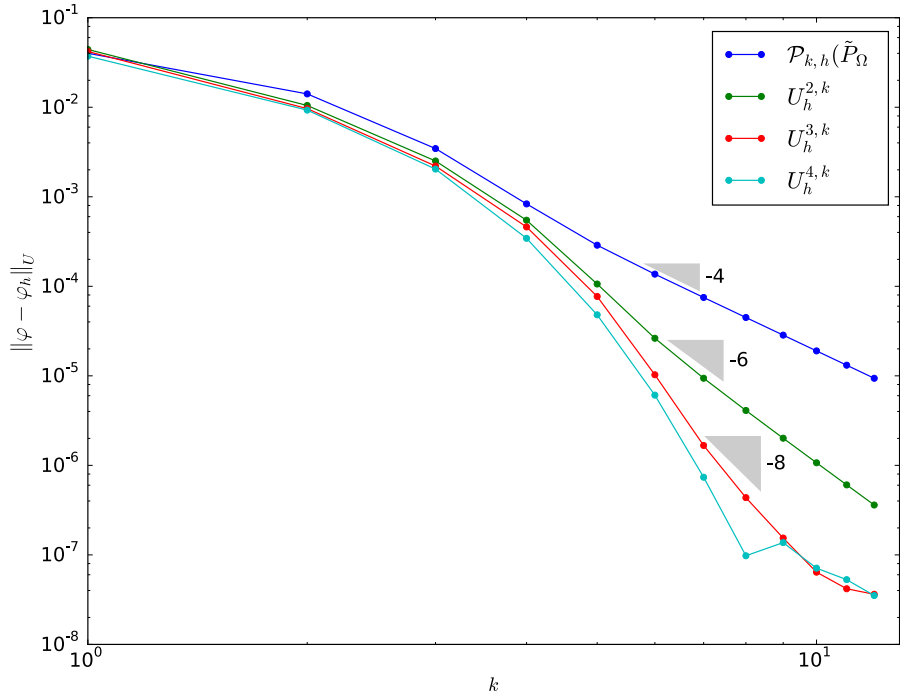

Figure 5.8: Energy error vs. polynomial degree for fixed s on the mesh $\mathcal{T}_h$ shown in Figure 5.7.

is solved using the sparse LU decomposition of PARDISO [130]. Figure 5.8 shows the energy error

$$\|\varphi - \varphi_h\|_U \coloneqq \left(|\varphi - \varphi_h|^2_{H^1(\Omega)} + \frac{2}{\delta^2} \|\varphi - \varphi_h\|^2_{L^2(\Omega_\sigma)} \right)^{1/2} \tag{5.16}$$

against the polynomial degree k for different choices of s [4].

We see that already the polynomial space $\mathcal{P}_{k,h}(\tilde{P}_\Omega)$ achieves algebraic convergence of order $O(k^{-4})$. If we additionally include the singularities $\mathcal{S}^s_{\lfloor s/2 \rfloor}$, we get even order $O(k^{-2(s+1)})$. This is somewhat expected due to the special form of the singularities: Assume that a function u can be written as

$$u = u_1 + \chi \sum_{j=1}^{n} C_j r^{\beta_j} \log^{\gamma_j} r\Phi(\theta), \tag{5.17}$$

with $u_1 \in H^{q+1}(\Omega)$, $\beta_1 > 0, \gamma_j > 0$, $\beta_{j+1} \geq \beta_j$, Φ being a C^∞ function and χ being a smooth cutoff function (cf. Theorem 5.3.4). Then Babuška and Suri [13, Theorem 6.1]

[4] The reference solution φ is computed using the FEM on a very fine, graded mesh with 15-th order polynomial shape-functions.

show that there exists a polynomial $u_h \in \mathcal{P}_{k,h}(\Omega)$ such that

$$\|u - u_h\|_{H^1(\Omega)} \leq C k^{-\min(q,2\beta_1)} (\log k)^{\gamma_{\max}} \left(\|u_1\|_{H^{q+1}(\Omega)} + \sum_{j=1}^{n} |C_j| \right), \tag{5.18}$$

where $\gamma_{\max} = \max_{j,\beta_j=\beta_1} \gamma_j$ and the constant C is independent of k.

Theorem 5.3.4 assures that $\mathcal{R}_{s+1}$ can be written in the form (5.17) with $\beta_1 = s+1$, $\gamma_{\max} = \lfloor (s+1)/2 \rfloor$. Therefore, we expect that the first infimum in 5.15 has order $O(k^{-2(s+1)}(\log k)^{\lfloor (s+1)/2 \rfloor})$. Up to the logarithmic factor this is exactly the rate of convergence measured in Figure 5.8.

Remark 5.3.6 (Numerical Quadrature). *The approximation space $U_h^{s,k}$ contains non-polynomial basis functions that belong only to H^2. It is therefore not advisable to use high-order quadrature rules to evaluate the surface and line integrals of* (3.26) *and* (3.27) *since the quadrature error would dominate the overall error, cf. [60, Lemma 2.27(Strang 1)]. Instead our implementation uses composite, hp-quadrature rules that refine towards the singularity [135].*

5.3.3 Exponential convergence

In the previous section, we have seen that the approximation space $U_h^{s,k}$ leads to algebraic convergence if s is kept fixed and only k increases. We have not been able to prove this rigorously because we do not know how fast C_{tr} increases with k but the method seems to work in practice. Let us now investigate whether we can even obtain exponential convergence if we increase s and k at the same time. The numerical analysis of this problem is even more complicated because the constant C in (5.18) depends on q and s. Moreover, one would need an estimate for $\|\mathcal{R}_{s+1}\|_{H^{s+1}}$ that is independent of s in order to estimate the truncation error; this seems very ambitious [50].

Let us therefore study the behavior of the error using the same setup as in the previous section. But this time we choose the approximation space $U_h = U_h^{k,k}$. Figure 5.9 shows the convergence of the energy error [4] for this choice. We observe an exponential rate up to about $k = 7$. For higher values of k numerical instabilities are observed which are due to a severe ill-conditioning of the Galerkin matrix. In other words, it is not possible to push the energy error below 10^{-6} due to numerical round-off errors. The same effect is observed for the approximation space $U^{s,k}$ of the previous section, cf. Figure 5.8.

For comparison, Figure 5.9 shows also the convergence of the standard *hp*-FEM which can be characterized by two parameters: The mesh-grading factor $\sigma_{\mathcal{T}_h}$ determines how the mesh $\mathcal{T}_h$ is refined towards the singularity and the slope μ_p determines at what rate the polynomial degree decreases towards the singularity, cf. [134, Section 4.5]. To the best of the author's knowledge it is not possible to determine a-priori the optimal values of $\sigma_{\mathcal{T}_h}$ and μ_p. We have therefore determined the optimal choice $\sigma_{\mathcal{T}_h} = 0.35$, $\mu_p = 1$ manually by brute-force testing. For comparison we also plot the standard

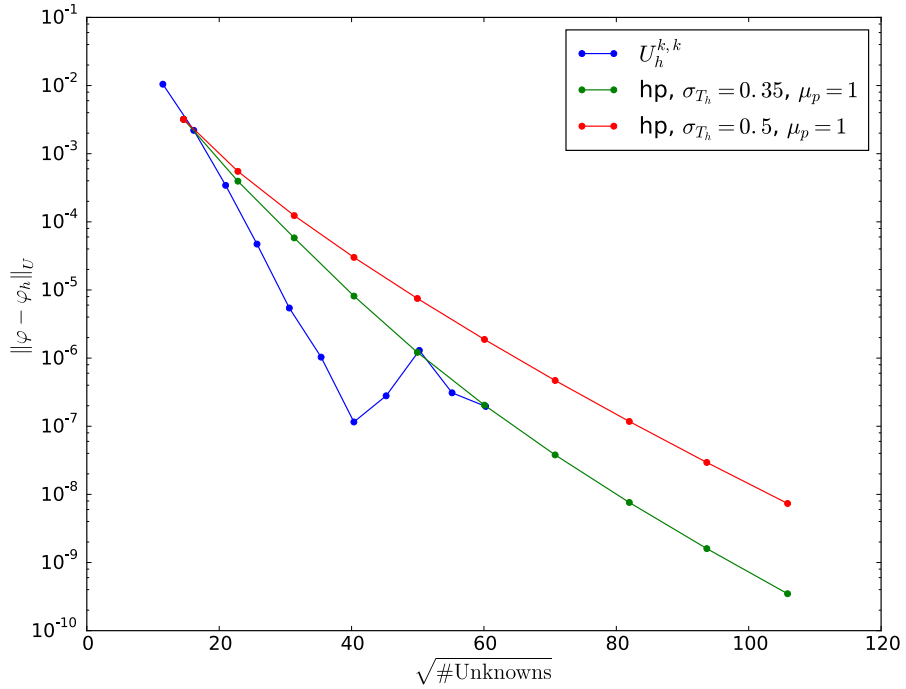

Figure 5.9: Energy error vs. square-root of number of unknowns for the enriched method with $U_h = U_h^{k,k}$ on the mesh shown in Figure 5.7. For comparison also the performance of the *hp*-FEM is shown.

choice $\sigma_{\mathcal{T}_h} = 0.5$, $\mu_p = 1$. We note that in both cases the *hp*-FEM needs considerably more unknowns to reach an accuracy that is comparable to the enriched method with $U_h = U_h^{k,k}$. In fact, in order to reach the accuracy 10^{-6}, the enriched method requires 1253 unknowns whereas the *hp*-FEM needs 2494 and 3609 unknowns, respectively. We also observe that the *hp*-FEM is numerically much more robust and can achieve an error of 10^{-9} in the energy norm easily.

Remark 5.3.7 (Numerical instability)**.** *The numerical instability of the enriched method for high polynomial degrees seems to be due to the very-high linear dependence between the basis functions (which are essentially the expressions of Proposition 5.3.2 plus a set of almost orthogonal polynomials): The condition number of the Galerkin matrix of* $U_h^{2,2}$ *is already in the order of* 10^{14}*.*

We have tried to improve the numerical stability of the enriched method using two techniques: Firstly, we have tried to orthogonalize the basis functions w.r.t. the L^2 *inner product locally in each mesh cell* $T \in \mathcal{T}_h^S$ *using the SVD decomposition and 64-bit double precision (for this the approximation space must be discontinuous across all elements* $T \in \mathcal{T}_h^S$*). Unfortunately, this had absolutely no effect and the outcome was identical to the one shown in Figure 5.9. Secondly, we have orthogonalized the basis functions w.r.t. the* L^2 *inner product in a ball around the corner using the arbitrary precision functionality of Mathematica [152]. This improved the situation a little bit (instability*

was observed around 10^{-7}*) but lead to extremely complex shape functions so it is not worth the effort.*

Bibliographical Remarks Babuška and Oh [11] introduced the *method of auxiliary mapping* to deal with infinite domains and corner singularities. Here a special mapping is used to transform the solution locally around the singularity into an auxiliary space. By doing so one can get rid of the singular behavior and use standard polynomials in the mapped space to approximate the solution efficiently. However, special *circular mesh elements* must be used in the vicinity of the corner singularity to apply the method.

5.4 2D Singularly Perturbed Problem

In the previous section, we have studied the singular behavior of the solution φ of problem (5.10) for a fixed δ and we have presented two numerical methods to approximate φ. We will now consider the case where $\delta \in (0, 0.05]$ (0.05 is the side length of the conductor Ω_σ) and we want to construct a numerical method that is robust in δ and shows exponential convergence.

At the end of Section 5.2, we concluded that the solution of the time-harmonic eddy current problem poses two major challenges:

i) It shows singular behavior close to (2D) corners of the conductor.

ii) There is no analytic expression that describes the boundary layer in (2D) corners of the conductor.

The previous section presented the key idea to solve problem i), but additional ingredients are needed to make this idea work robustly in δ. Moreover, we must tackle problem ii) somehow.

5.4.1 Scale Invariance

We note that the PDE (5.10a) is *scale-invariant*: Let us assume that $\tilde{\varphi}^1 \in H^1(\mathbb{R}^2)$ fulfills (5.10a) with $\delta = 1$ in the whole space $\mathbb{R}^2$ (the conductor is defined by $\Omega_\sigma = \{(r, \theta) |\ |\theta| \leq \alpha/2\}$, $\Omega_0 \coloneqq \mathbb{R}^2 \setminus \overline{\Omega_\sigma}$). It is then easily checked that $\tilde{\varphi}^\delta = \tilde{\varphi}^1 \circ \Phi_\delta$, with $\Phi_\delta : \mathbb{R}^2 \to \mathbb{R}^2$, $\boldsymbol{x} \mapsto \boldsymbol{x}/\delta$, is a solution of (5.10a) for any δ.

Furthermore, let us define the energy norm over a bounded set $\mathcal{O} \subset \mathbb{R}^2$ for a given δ by (cf. (5.16))

$$\|u\|^2_{U^\delta(\mathcal{O})} \coloneqq |u|^2_{H^1(\mathcal{O})} + \frac{2}{\delta^2} \|u\|^2_{L^2(\Omega_\sigma \cap \mathcal{O})} .$$

It is easy to check that the energy norm of $\tilde{\varphi}^1$ and $\tilde{\varphi}^\delta$ is exactly the same when the integration domain is shrunk by a factor of δ:

$$\left\|\tilde{\varphi}^\delta\right\|_{U^\delta(\Phi_\delta^{-1}(\mathcal{O}))} = \left\|\tilde{\varphi}^1 \circ \Phi_\delta\right\|_{U^\delta(\Phi_\delta^{-1}(\mathcal{O}))} = \left\|\tilde{\varphi}^1\right\|_{U^1(\mathcal{O})},$$

for any open, bounded set $\mathcal{O} \in \mathbb{R}^2$. So inside a ball $\mathcal{O} = B(\mathbf{0}, \delta)$, the solution φ^δ of BVP (5.10) is essentially a downscaled version of the solution φ^1 for $\delta = 1$ (neglecting the effect of the boundary conditions).

Let us now apply the scale invariance to the decomposition Theorem 5.3.4: We choose an open subset $\mathcal{O} \subset \mathbb{R}^2$ that contains the origin $(0,0)$ and we write $\tilde{\varphi}^1 = \chi\mathfrak{S}_s + \mathcal{R}_{s+1}$ such that $\chi \in C_0^\infty(\mathbb{R}^2)$, $\chi = 1$ in $\mathcal{O}$, $\mathcal{R}_{s+1} \in H^{s+1}(\{\Omega_\sigma, \Omega_0\})$ and $\mathfrak{S}_s$ contains the triple sum of (5.12). Then clearly $\tilde{\varphi}^\delta = \tilde{\varphi}^1 \circ \Phi_\delta = (\chi \circ \Phi_\delta)(\mathfrak{S}_s \circ \Phi_\delta) + \mathcal{R}_{s+1} \circ \Phi_\delta$, and in particular, $\|\mathcal{R}_{s+1} \circ \Phi_\delta\|_{U^\delta(\Phi_\delta^{-1}(\mathcal{O}))} = \|\mathcal{R}_{s+1}\|_{U^1(\mathcal{O})}$. Therefore, the error $\left\|\tilde{\varphi}^\delta - \mathfrak{S}_s\right\|_{U^\delta(\Phi_\delta^{-1}(\mathcal{O}))} = \|\mathcal{R}_{s+1}\|_{U^1(\mathcal{O})}$ for all δ, i.e. $\mathfrak{S}_s$ is a good approximation of $\tilde{\varphi}^\delta$ for all δ inside $\Phi_\delta^{-1}(\mathcal{O})$. Since the leading term of $\mathfrak{S}$ is of the form $r^2 \log r$ (cf. Proposition 5.3.2) we can deduce that inside a region $\Phi_\delta^{-1}(\mathcal{O})$, $\tilde{\varphi}^\delta$ will resemble the function $r^2 \log r$ (for $\operatorname{diam}\mathcal{O}$ small enough). Neglecting again the boundary conditions we can argue that the same holds for the solution φ^δ of the BVP (5.10), cf. Figure 5.10.

The question is now of course how the solution φ^δ of (5.10) behaves in the region $\mathcal{O}' \setminus \overline{\Phi_\delta^{-1}(\mathcal{O})}$ where $\mathcal{O}'$ is another open neighborhood of the origin. For this we note that in the limit $\delta \to 0$ the solution of problem (5.10) converges to the solution of the following Laplace problem, cf. Problem (5.5)

$$\begin{cases} \text{Find } \varphi^0 \in H^1(\Omega_0) \text{ subject to} & \\ \qquad -\Delta\varphi^0 = 0, & \text{in } \Omega_0, \qquad (5.19a) \\ \qquad \varphi^0 = 0 & \text{on } \Gamma \coloneqq \Omega_0 \cap \Omega_\sigma, \qquad (5.19b) \\ \qquad \boldsymbol{n} \cdot \mathbf{grad}\,\varphi^0 = 1 & \text{on } \Gamma_{N,1}. \qquad (5.19c) \end{cases}$$

It is well-known [90, 142] that this problem features singularities of type

$$\mathfrak{l}^j \coloneqq r^{\frac{j\pi}{2\pi-\alpha}} \sin\left(\frac{j\pi}{2\pi-\alpha}\theta\right), \tag{5.20}$$

at the origin, $j \in \{1, 2, \ldots\}$. Moreover, a decomposition similar to the one in Theorem 5.3.4 holds for φ^0. Finally, we note that the leading singularity of the Laplace problem (5.19) is of type $r^{2/3}$ (for $\alpha = \pi/2$) and hence we can expect that the function $\varphi^\delta \overset{r,\delta\to 0}{\sim} r^{2/3}$ in $\mathcal{O}'$ (for $\operatorname{diam}\mathcal{O}'$ small enough).

Figure 5.10 shows the radial derivative of the solution φ^δ of (5.10) along the line $\theta = \pi$ and confirms the previous analysis: We see that the first derivative does not blowup as $r \to 0$ which is expected since $\varphi^\delta \overset{r\to 0}{\sim} r^2 \log r$. Moreover, we see that for $r \in [0, \delta]$ the behavior of $\frac{\partial\varphi}{\partial r}$ is well described by the derivative of the singular function $r \log r$ plus a first-order polynomial whereas for $\delta \in [1.5, 9]$ $\frac{\partial\varphi}{\partial r}$ is very well approximated by the derivatives of the first two Laplace singularities $\mathfrak{l}^1$, $\mathfrak{l}^2$ plus a constant.

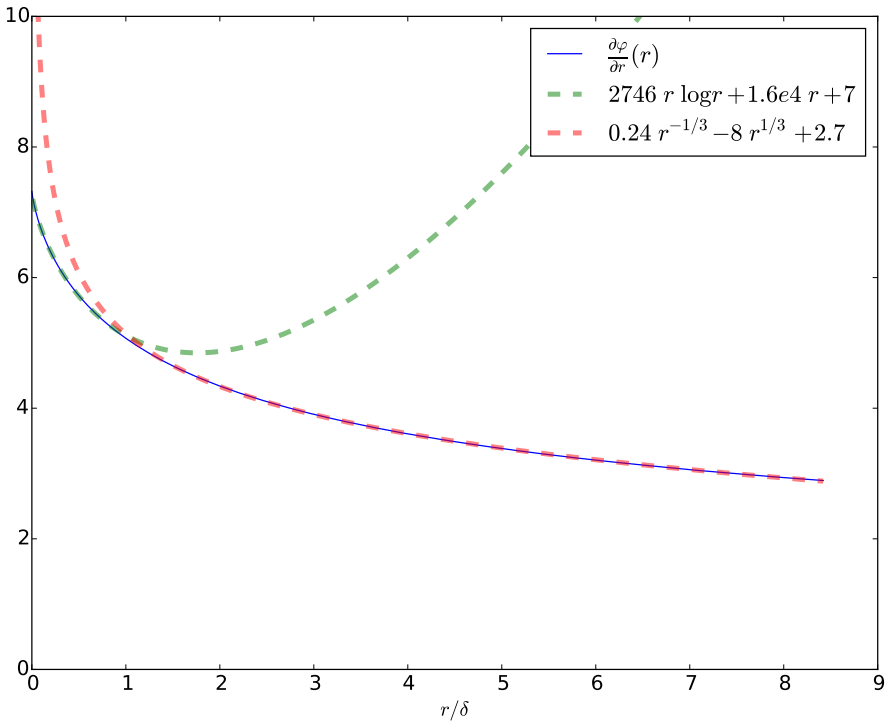

Figure 5.10: Plot of the radial derivative of the reference solution $\varphi^\delta(r, \pi)$ of (5.10) and two fitting functions with leading terms $r \log r$, $r^{-1/3}$, respectively. Here $\delta = 5 \cdot 10^{-4}$.

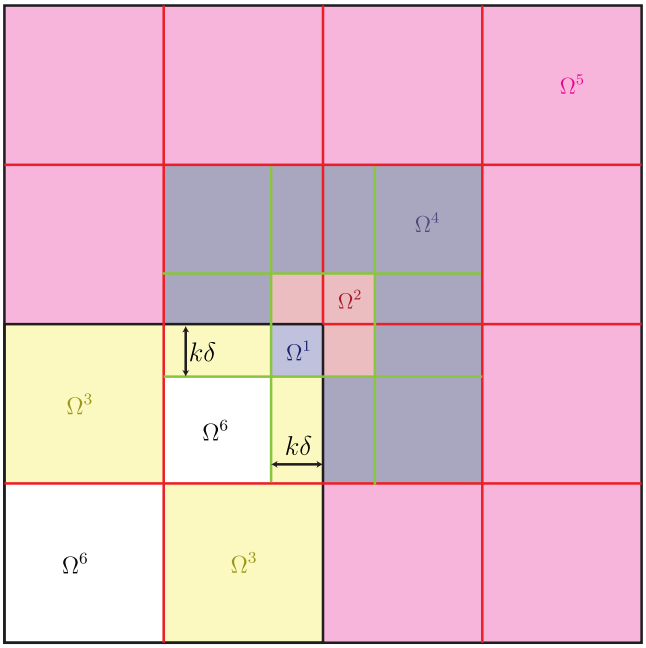

Figure 5.11: Adapted mesh for the domain Ω of Figure 5.6a showing the subdomains Ω^i.

5.4.2 Enriched Approximation Space

In order to come-up with an efficient, numerical method that is robust in δ we must resolve both the singular shadow functions $\mathfrak{s}_j^{m,p}$ as well as the singularities $\mathfrak{l}^j$ of the Laplace operator. Since the support of the cutoff functions (cf. Theorem 5.3.4) of the two types of singularities must scale differently as $\delta \to 0$ we propose to refine a given, coarse mesh around the corner of the conductor using *hanging node-refinement* such that an area of size $\approx k\delta$ is resolved by the mesh (k being the global polynomial degree). The prefactor k stems from the theory of the *hp*-approximation of the 1D boundary layer, cf. Section 5.1 and [154].

Figure 5.11 shows such a mesh for the simple BVP (5.10): The black lines show the original geometry of the conductor Ω_σ and the airbox Ω_0, the red lines show an initial, coarse mesh and the green lines show the additional, hanging-node refinement of size $k\delta$.

Let us now state the global approximation space in terms of the domain decomposition $\overline{\Omega} = \overline{\bigsqcup_{j=1}^6 \Omega^j}$ shown in Figure 5.11:

$$U_h^{s,k} \coloneqq \mathcal{S}^s_{\lfloor s/2 \rfloor}(\{\Omega^1, \Omega^2\}) \oplus \mathcal{L}^s(\overline{\Omega^2 \cup \Omega^4}) \oplus \mathcal{A}_k(\mathcal{T}_h^{\Omega^3}) \oplus \mathcal{P}_{k,h}(\{\Omega^j\}_{j=1}^6). \tag{5.21}$$

The space $\mathcal{S}_j^m$ is defined by (5.13) and its purpose is to absorb the singular shadow functions $\mathfrak{s}_j^{m,p}$. Based on the previous discussion we have defined this space only in a

neighborhood of size $k\delta$ around the origin. The space $\mathcal{L}^s$ is spanned by the singularities of the Laplace operator,

$$\mathcal{L}^s(X) \coloneqq \operatorname{span}\left\{ \left.\mathfrak{l}^j\right|_X \mid \mathfrak{l}^j \notin H^{s+1}(X)\right\}, \qquad X \subset \Omega,$$

where the singularities $\mathfrak{l}^j$ are defined by (5.20). Note that $\mathcal{L}^s(\overline{\Omega^2 \cup \Omega^4})$ is defined on a subset of Ω that does *not* shrink as $\delta \to 0$. The space $\mathcal{A}_k(\mathcal{T}_h^{\Omega^3})$ is the scalar, 2D version of the space defined in (5.9) with $\mathcal{T}_h^{\Omega^3} \coloneqq \{T \in \mathcal{T}_h \mid T \subset \Omega^3\}$. Finally, the space of piecewise polynomials $\mathcal{P}_{k,h}(\{\Omega^j\}_{j=1}^6)$ is formally defined by (3.36).

We would like to point out that this approximation space can solve problems i) and ii) mentioned at the beginning of this section: it can approximate the singular behavior and the boundary layer of φ in the vicinity of the corner $(0,0)$, cf. Section 5.1.

5.4.3 Numerical Experiments

Let us now investigate the approximation properties of the space $U_h^{s,k}$ defined by (5.21): We solve the BVP (5.10) using the NWIP formulation (3.25) ($\theta = 1$) with the approximation space $U_h = U_h^{k,k}$.

Figure 5.12 shows the energy error $\|\varphi_h - \varphi\|_{U^\delta(\Omega)}$ for different skin-depths δ and different choices of k. We observe that for k fixed, and $\delta \to 0$ the error at first decreases until it reaches a constant level for δ very small. This can be explained as follows: From Section 5.1, we expect that $\left\|\varphi^\delta\right\|_{U^\delta(\Omega_\sigma)} = O(\delta^{1/2})$ so that for δ moderate the overall energy error $\left\|\varphi^\delta - \varphi_h^\delta\right\|_{U^\delta(\Omega)}$ is dominated by the error in the conductor, $\left\|\varphi^\delta - \varphi_h^\delta\right\|_{U^\delta(\Omega_\sigma)}$, which decreases as $\delta \to 0$. For δ small enough, the boundary layer is almost inexistent and thus the overall error $\left\|\varphi^\delta - \varphi_h^\delta\right\|_{U^\delta(\Omega)}$ is dominated by the error in the airbox, $\left\|\varphi^\delta - \varphi_h^\delta\right\|_{U^\delta(\Omega_0)}$, i.e. the energy error reaches a plateau for $\delta \to 0$.

Figure 5.13 shows the energy error against the polynomial degree k for different values of δ. We see that for δ large we get clearly exponential convergence which agrees with the observations from Section 5.3. For smaller δ the error unfortunately stagnates already for $k = 3$ due to numerical errors.

Finally let us study the strength of the two types of singularities for different values of δ: Figure 5.14 shows the energy error for $k = 3$ plotted against δ for the case that either the singular shadows $\mathfrak{s}_j^{m,p}$ or the Laplace singularities $\mathfrak{l}^j$ are not included in the approximation space $U_h^{k,k}$. We see that the singular shadows $\mathfrak{s}_j^{m,p}$ dominate the approximation error for large δ but for smaller δ's the Laplace singularities $\mathfrak{l}^j$ become much more important. This agrees with our discussion in Section 5.4.1.

Remark 5.4.1 (Singularity and NWIP). *In this section, we have enriched the polynomial space with singularities of the Laplace equation. The leading singularity is of type $r^{2/3}$, i.e. $U_h^{k,k} \not\subset U_h^*$ so that strictly speaking we cannot use the approximation space $U_h^{k,k}$ with*

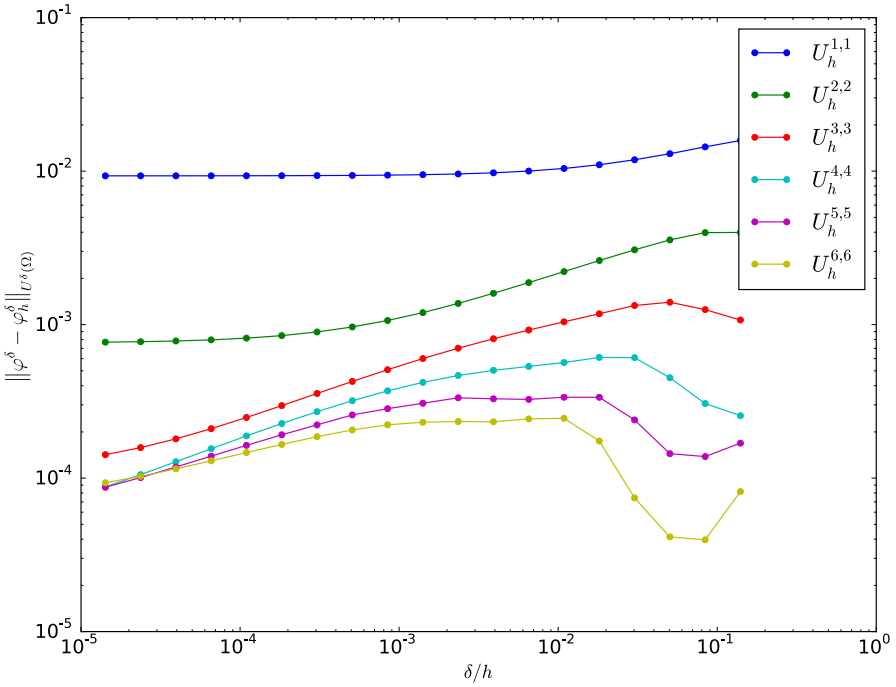

Figure 5.12: Energy error vs. δ for different values of k

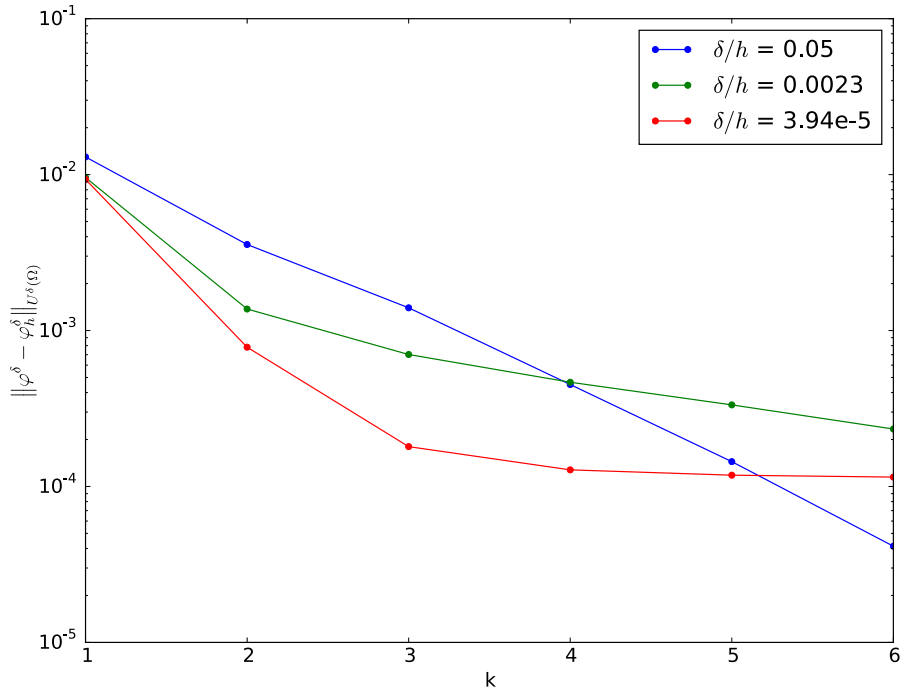

Figure 5.13: Energy error vs. k for different values of δ

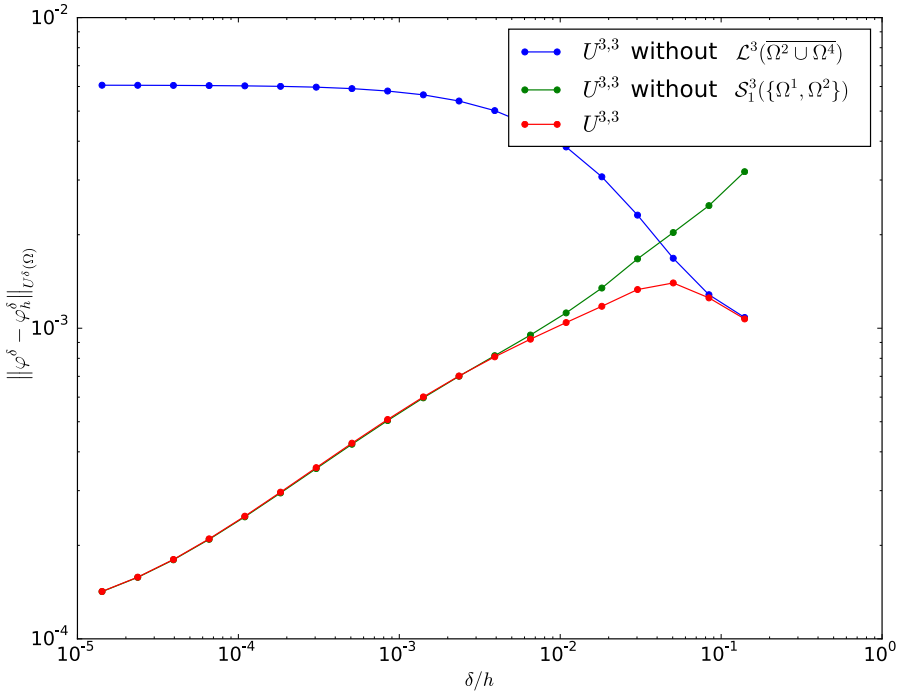

Figure 5.14: Energy error vs. δ for different types of singularities

the NWIP formulation (3.25), *cf.* (3.23). *However, condition* (3.23) *can be relaxed since its only purpose is to make sure that the trace of a function* $\varphi_h \in U_h^{k,k}$ *lies in* $L^2(F)$, $F \in \mathcal{F}_h$. *It is now easy to check that the trace of* $\mathfrak{V}^j$ *is square integrable over all faces* $F \in \mathcal{F}_h$ *(for* $\alpha = \pi/2$*) so that the NWIP formulation still works as expected.*

Bibliographical Notes Xenophontos [154] studies δ-robust numerical methods for the 2D reaction-diffusion equation which is essentially the BVP (5.10) with $\Omega = \Omega_\sigma$. The idea of shrinking the mesh together with δ to approximate the singularity uniformly in δ can also be found in [154]. In contrast to our method, the singularity is in that work not resolved by enriching the approximation space but rather by an *hp*-refinement towards the corner.

6 HyDi

In the previous two chapters, we have shown extensive numerical studies to support the developed theory and to get new insights. But so far, we have tactically omitted the details of the implementation of the numerical experiments and we will *continue to do so* in this chapter. In fact, this chapter is not about the concrete implementation of the numerical methods that we have introduced previously. It is much more about *the philosophy behind the implementation* which turns out to be interesting in its own right.

The material of this Chapter is mostly based on the experiences that the author and Christoph Winkelmann have collected while working with HyDi over the past 3.5 years. But many of the conclusions and ideas apply to numerical software in general.

HyDi has been developed as part of a collaboration between ABB corporate research and ETH Zürich entitled "High resolution simulation tool for power devices". It is a set of C++11 libraries to solve partial differential equations with the finite element method (or variants of it). HyDi runs on Windows and Linux and supports **Hy**brid meshes and **Di**scontinuous approximation spaces. HyDi is also the basis for a 3D hybrid electromagnetic solver used intensively by the project partner ABB for magneto-hydrodynamic plasma simulations of electric arcs in circuit breakers. It successfully combines academic flexibility with industrial speed.

The first section of this chapter gives a brief overview of HyDi and presents the fundamental design ideas behind it. The next sections present some specific features of HyDi: Section 6.2 will summarize the authors thoughts on unit tests while Section 6.3 presents the composite grid manager that is used to merge multiple conforming grids into one (possibly non-conforming) grid. In particular, this section gives more details about the numerically robust algorithm that has been used to determine the faces $F \in \mathcal{F}_h$ that lie in between two conforming sub-grids. Finally, Section 6.4 demonstrates how the observer pattern [66] can be used to deal with changes in the underlying grid.

6.1 Overview

Design Philosophy It is important to be aware that HyDi itself is a set of C++11 libraries, i.e. it is not an executable and it is also not a software framework. The latter

means that HyDi takes a mostly *unopinionated approach* and allows the user [1] to solve problems in a variety of ways; there is not one guiding principle that the user has to follow to work with HyDi. In particular, the user must write his own `main()` routine and call HyDi from there.

In order to give the user as much freedom as possible we have minimized the required external dependencies to two well-known libraries: the Boost libraries [53] and the Eigen3 library [72]. Nevertheless, there is a list of other, optional, external libraries that can be linked to HyDi such as sparse direct solvers.

One of the most important guiding principles in the (object oriented) software design of HyDi is *extensibility*: By this we mean that new functionality can be added to HyDi *without modifying internals of the existing code.* In HyDi extensibility is mostly achieved by (class level) *modularity*: Almost every (C++) class in HyDi implements an abstract interface and can be replaced by any other class that implements the same abstract interface. I.e. the classes are *loosely coupled* to each other.

Extensibility is closely linked to *maintainability*: a new developer should be able to extend HyDi without understanding all its internals. Clearly extensibility facilitates this considerably because the developer only needs to know about the relevant interfaces in order to extend it. However, this does not guarantee maintainability: Sometimes one needs to refactor parts of the existing code (e.g. an interface). But in order to do so the person that makes the change must understand all the consequences in order not to break anything. If there are no unit tests in place this often means that the person committing the changes must first understand a big part of the code which contradicts maintainability. This is one of the reasons that HyDi uses unit tests to test almost every single class (cf. Section 6.2). Moreover, HyDi provides a comprehensive documentation to further support extensibility and maintainability.

Remark 6.1.1 (Interfaces). *In HyDi, interfaces are realized by either runtime or compile-time polymorphism and it is not always straightforward to determine which is the better choice.* Runtime polymorphism *is always implemented using abstract base classes in combination with virtual member functions. The memory management is often realized by using* `std::shared_ptr`*. The biggest advantage of runtime polymorphism is that it is simple and compilation time is not negatively affected. It is therefore the method of choice for all interfaces that are not instantiated in massive amounts and where there are not too many virtual function calls. Unfortunately, runtime polymorphism leads to runtime overhead, i.e. the program is slowed down because every call to a virtual function implies a lookup in the corresponding virtual function table. Moreover, virtual functions cannot be function templates which limits the possible applications somewhat.*

Because of this HyDi makes extensive use of compile-time polymorphism *which can be implemented with either one of three techniques:*

[1] With *user* we mean a programmer that uses the HyDi libraries and that does not necessarily understand all of its details.

Curiously Recurring Template Pattern (CRTP) *Is the method of choice for objects that are not copyable. See the HyDi documentation and [83, Section 16.3] for more information.*

Compile-time Strategy Pattern *Is used if the class should be copyable but implements at most one interface, cf. [66].*

Boost Concept Check Library *Is used if neither one of the above options is applicable, cf. [138].*

All of these techniques lead to compile-time overhead (i.e. compilation is slower) but not to runtime overhead. Compile-time polymorphism is mostly used for very fundamental interfaces that are used heavily, such as the grid interface (see Section 6.3).

Functionality So far, we have described the design philosophy behind HyDi and how it is put into practice. From a user's point of view, the most important functionality of HyDi is the

- Abstract grid interface that is compatible with the Distributed and Unified Numerics Environment (DUNE) [16, 15].
- Support for 2D and 3D hybrid, conforming grids with first order geometry mapping. Adaptive h-refinement is experimentally supported in 2D.
- Composite grid manager that can combine multiple conforming grids into one (possibly non-conforming) grid, cf. Section 6.3.
- Grid readers for GMSH and Abaqus file formats.
- Automatic update of data-structures upon a change in the grid, cf. Section 6.4.
- Hierarchic, H^1 conforming polynomial basis of any order for hybrid, 2D meshes that enables local p-refinement [20].
- Hierarchic, $\boldsymbol{H}(\mathbf{curl})$ conforming edge/Nédélec elements of any order for hybrid, 2D and 3D meshes that enables local p-refinement [21].
- First order polynomial basis for hybrid 3D meshes.
- Ability to break approximation spaces across any face $F \in \mathcal{F}_h$ and combine them with other approximation spaces to construct more complex approximation spaces (composite pattern [66]).
- Numerical quadrature of any order for hybrid, 2D and 3D meshes.
- hp-quadrature to integrate singular shape-functions [135].
- Parallelized assembly routines (shared-memory) that scale very well up to 12 threads.
- Parallelized static condensation (shared-memory).

- First and second order time-stepping.
- Conjugate Gradient (CG) and BiCGSTAB iterative solvers.
- Numerous interfaces to 3rd-party linear solvers: PARDISO (Intel Math Kernel Library), PARDISO (by Schenk and Gärtner [130]), UMFPACK, ILUPACK [25].
- Support for writing and reading matrices/vectors in MATLAB's `.mat` format.
- Output to VTK files. Non-linear shape functions can be visualized by refining the mesh locally. Functions can be visualized on surface and/or volume elements.
- Efficient interpolation between geometrically overlapping but otherwise unrelated meshes using R^* trees [68].
- Intuitive handling of functions defined on a grid thanks to C++ operator overloading.

6.2 Unit tests

As we have already mentioned in the previous section, *unit tests* are used by HyDi to increase its maintainability. It turns out that *unit tests* have many other advantages, some of which are not so obvious and which came as a surprise to the author himself. The author is convinced that the unit tests of HyDi are *one of the most outstanding features of HyDi*.

In the following we will give some arguments to support this claim. But first we should agree on what a unit test is:

Definition 6.2.1 (Unit Test [111, Definition 1.2])**.** *A* unit test *is an automated piece of code that invokes the unit of work being tested, and then checks some assumptions about a single end result of that unit. A unit test is almost always written using a unit testing framework. It can be written easily and runs quickly. It's trustworthy, readable, and maintainable. It's consistent in its results as long as production code hasn't changed.*

Here a *unit of work* is the "sum of actions that take place between the invocation of a public method in the system and a single noticeable end result" [111]. A unit of work should be as small as possible so that a failure of a unit test gives a clear indication of what went wrong. In order to do so, the code, which should be tested, must be *testable*, i.e. it must be possible to isolate small units of work and test them independently. This must already be taken into consideration *before* the code itself is written. Often extensibility and modularity go hand in hand with testability.

A *unit testing framework* organizes the unit tests in a structure and allows to run all of them upon request (or automatically whenever a change is committed). Usually a unit testing framework also provides a human-readable output that details the tests that

have failed and why they failed. HyDi relies on the Boost test framework [126] to carry out these tasks.

In order to show the wide applicability of unit tests to numerical software, let us describe a few unit tests from HyDi:

Inter-element continuity Implementing a new approximation space U_h or V_h that is H^1 or $\boldsymbol{H}(\mathbf{curl})$ conforming is not a simple task because one must ensure that the basis functions are (tangentially) continuous across element boundaries, cf. Lemmas 3.2.6, 3.2.7. However, testing continuity is extremely simple: One only needs to evaluate every basis function at a few points on the inside and the outside of an inner face $F \in \mathcal{F}_h^i$ and check that they are continuous. Moreover, this idea works for all approximation spaces, so one can write an abstract unit test [2] to test (tangential) continuity for all approximation spaces (that implement an interface).

Numerical differentiation Once the basis functions have been implemented one can use numeric differentiation to test if the derivatives of the basis functions are also correctly implemented. This is again applicable to any approximation space so it can be refactored into an abstract unit test.

Testing the assembly routine One can write a small, mock approximation space that has basis functions which are globally constant and assemble the corresponding mass matrix. Compare this assembled mass matrix with the correct, analytical form of the mass matrix (which is easily computed).

Numerical Quadrature Use a quadrature rule of order p to integrate monomials of orders $0, \dots, p$ and check that the result is correct.

Interpolation The efficient implementation of a routine to interpolate a function from one mesh to another, unrelated mesh (of the same domain) is not easy. But testing is very simple: Just define the same analytic function on both meshes and interpolate one of them to the other mesh and compute the difference.

We would like to point out that without unit tests it is often very hard to find certain errors: Assume for example that the weight of a quadrature rule is wrong. Then the iterative solver may not converge because the Galerkin matrix is singular. It's practically impossible to conclude from this, that the weight of the quadrature rule is wrong. A worse scenario is if the iterative solver does converge but the solution is slightly wrong. Then one will not find out about the error and can *make wrong conclusions*.

We also note that in most cases writing the unit test is much simpler than writing the actual implementation. Moreover, it is often possible to write an *abstract unit test* that works for all classes implementing a particular interface (e.g. for all approximation spaces). So writing a unit test will often not take much additional time but errors are found much earlier in the development process so that in the long run unit tests often

[2] In C++ an abstract unit test is often a function that accepts as an input any object that implements a particular interface and that performs the test on this object.

decrease the development time considerably. This is especially true for larger projects where multiple people are involved.

Unit tests have a few more advantages that are not all so obvious:

Refactoring, Maintainability As we have already pointed out in the previous section, unit tests simplify the refactoring of code considerably. That is one can change parts of the code and can then run the unit tests to check if it is still working as expected. In particular, there is no reason for the developer to be afraid to break something in the code that he is not aware of.

Compilation Time In C++ long compilation times are often an issue in bigger projects. Especially source files that include many header files can take a long time to compile. Assume that we want to implement a new kind of approximation space and use it in a simulation. If we don't want to use unit tests, we read a mesh from a file, setup the new approximation space, assemble the left-hand side and the right-hand side, solve the linear system of equations and visualize the result. In order to eliminate bugs in the code we will have recompile this code many times until the simulation looks right. One such compilation will clearly take a lot longer than compiling a simple unit test that checks if the derivatives of the basis functions are implemented correctly.

Debugging A similar argument is true for debugging: A debugger (such as gdb) has to load all the debug symbols that are present in an executable. So if the executable solves a BVP it will typically have much more debug symbols than a simple unit test that checks the derivatives of the shape functions (especially in the presence of templates). It's not surprising that the debugger is much slower in the first case.

Different compile environments Although C++ is supposed to be platform independent, this is in practice often not the case: Every implementation of the standard library is a bit different and every compiler makes different assumptions about the code (in particular this depends on the choice of the optimization flags). So unit tests become extremely handy when porting code from one compiler platform to another, especially across different operating systems. The same is of course true for external libraries whose version can also vary from one environment to another (and can contain bugs in some versions but not in others).

Although unit tests are not able to find every bug in a software, they enjoy great popularity in the software engineering community are used in all kinds of applications. However, in the view of the author there are not many other fields of programming where it is so easy to write unit tests and where unit tests are so effective as in the field of numerical algorithms.

6.3 Composite Grid

One central concept in HyDi is the so-called grid interface which is a *set of classes* in the `hydi::grid` namespace that represents the abstract concept of a (hierarchic) grid. A *grid manager* is a set of classes that implements this abstract concept.

The idea of using an abstract grid interface is borrowed from the Distributed and Unified Numeric Environment (DUNE) [16, 15] and turns out to be a very powerful one: First, it provides a consistent interface to deal with different types of meshes (non-conforming, hierarchic, hybrid, (un)structured) which allows developers to write grid managers that are optimized for specific purposes while the user always sees the same set of interface classes and can easily switch from one grid manager to another. I.e. the interface *encapsulates* the implementation details of the grid manager which makes life a lot easier for the user. Secondly, an interface makes it possible to use several well-established software design patterns [66].

One such design pattern is the *composite pattern* which, in this context, lets us combine multiple grid managers, that implement the grid interface, into one grid manager, that again implements the grid interface. The idea is of course that we can combine different grids/meshes $\{\mathcal{T}_{h,i}\}_i$ into one grid, $\mathcal{T}_h := \bigcup_i \mathcal{T}_{h,i}$. This is realized for hybrid 3D grids by the grid manager `hydi::grid::composite`.

Figure 6.1 illustrates this for the composite grid that was used in the simulation of the loop of wire moving in between the permanent magnets, cf. Section 4.2.4. We see that the grid shown in Figure 4.12 is composed of three sub-grids, which are represented by the three grid managers `top`, `middle` and `bottom` (which are all instances of the `hydi::grid::hybrid` grid manager). These three grid managers are merged to one grid by the grid manager `compositeGrid` (which is an instance of `hydi::grid::composite`) and which contains references to `top`, `middle` and `bottom`. We also see that all four grid managers implement the `hydi::grid` interface.

Gluing Let us now discuss *how* the `hydi::grid::composite` manager *glues* two (or more) grid managers together. It should be clear that the most difficult part is the detection of faces $F \in \mathcal{F}_h$ (in HyDi they are called intersections) that lie exactly in between two sub-grids. The composite grid manager offers three basic techniques for doing this, that is, it provides three types of *glues* that can be used to establish a relation between the boundary faces of the sub-grids, named henceforth sub-boundary-faces:

`ConformingGlue` is used to determine the common sub-boundary-faces that are conforming. This glue compares the coordinates of the nodes of the sub-grids and finds duplicates, its complexity is $O(N \log N)$ for N points.

`NonConformingGlue` is used to determine non-conforming faces which result from the intersection of two conforming, sub-boundary-faces. It uses a rather sophisticated algorithm that we describe below and has overall complexity $O(N \log N)$.

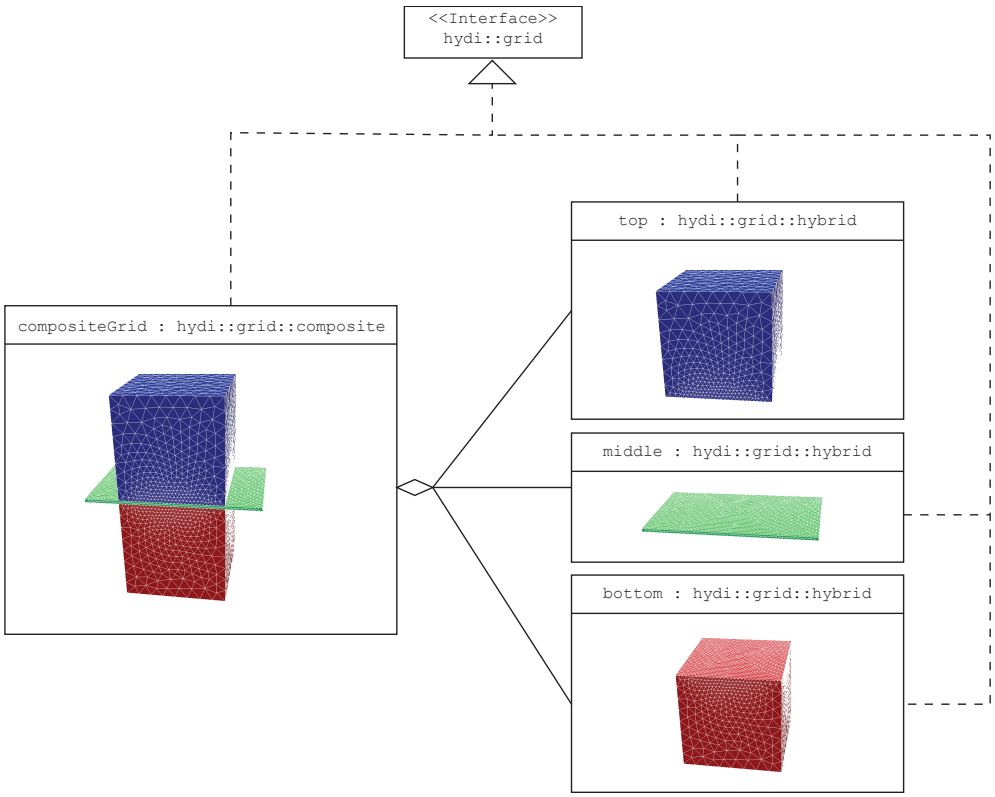

Figure 6.1: UML object diagram that represents the composite grid used for the simulation of the wire-loop example, cf. Section 4.2.4.

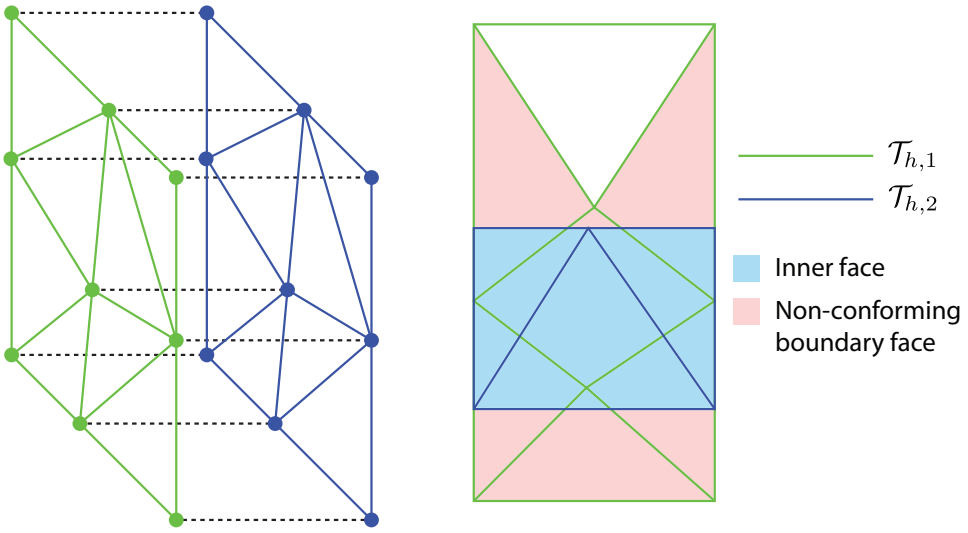

(a) Points matched by `ConformingGlue`

(b) Inner intersections determined by `NonConformingGlue` and non-conforming boundary intersections determined by `NonConformingBoundaryGlue`

Figure 6.2: Different types of glues can be used to "glue" sub-boundary-faces together.

`NonConformingBoundaryGlue` is applied after the inner, non-conforming faces have been detected by `NonConformingGlue` to detect the "left-overs", that is non-conforming boundary faces that result from subtracting one or more sub-boundary-faces from each other, cf. Figure 6.2b. This glue is essentially a wrapper around the General Polygon Clipper (GPC) library [103].

Each *glue* must be "applied" to some boundary faces of the sub-grids, i.e. the user must specify which sub-boundary-faces could possibly match with each other (respectively which sub-boundary-faces could be non-conforming).

6.3.1 The NonConformingGlue

In this section, we briefly explain how the `NonConformingGlue` computes the intersection between two sets of (flat) sub-boundary-faces which we denote by $\mathcal{F}^b_{h,1}$ and $\mathcal{F}^b_{h,2}$ (these are the sets of boundary faces to which the glue has been applied). The whole algorithm can be split into three stages:

1. Determine for each sub-boundary-face $F \in \mathcal{F}^b_{h,1} \cup \mathcal{F}^b_{h,2}$ the normal vector and round its components to a given precision (e.g. 2^{-16}). Now quick-sort the list of all normal vectors to find faces that lie in the same plane. The output are two lists of lists of faces $\{\mathcal{F}^{b,j}_{h,1}\}_{j=0}^{N_p-1}$, $\{\mathcal{F}^{b,j}_{h,2}\}_{j=0}^{N_p-1}$ that contain for each sub-grid the sub-boundary-faces that lie in the same plane (N_p is the number of planes).

2. For each plane $j \in \{0, \cdots, N_p - 1\}$ determine the faces $F_1 \in \mathcal{F}_{h,1}^{b,j}$ and $F_2 \in \mathcal{F}_{h,2}^{b,j}$ that could possibly intersect. For this we insert the bounding-box of all the faces $\mathcal{F}_{h,1}^{b,j}$ into an R^*-tree [68] and then query this tree with the bounding boxes of $\mathcal{F}_{h,2}^{b,j}$.
3. For each pair of sub-boundary-faces that could intersect, use a robust version of the *Sutherland-Hodgman algorithm* [143] to compute the intersection between two polygons (i.e. the faces). This algorithm is described below.

Remark 6.3.1 (Complexity). *Let $N = \#(\mathcal{F}_{h,1}^{b} \cup \mathcal{F}_{h,2}^{b})$ be the total number of faces to which the glue has been applied. It is easy to see that stage 1. of the above algorithm has complexity $O(N \log N)$. Moreover, since the insertion into the R^*-tree has total complexity $O(N \log N)$ and since one search operation has complexity $O(\log N)$, the total complexity of stage 2. is $O(N \log N)$. Stage 3. has constant complexity $O(1)$ for every pair since the two polygons can only be triangles or quadrilaterals. Therefore, the overall complexity of the* `NonConformingGlue` *is $O(N \log N)$. In practice the C++ implementation is* quite fast*, even though it is not parallelized: For example, the gluing of the meshes shown in Figure 6.1 takes* 0.4 *seconds ($N = 4048$). Even for the finest mesh of the wire-loop example from Section 4.2.4 the gluing takes less than* 5 *seconds ($N = 25460$).*

Stage 3. Robust Polygon Clipping

Computing the intersection of two polygons is also called *polygon clipping* in the computer graphics community. The goal is to clip the *subject polygon* with the *clip polygon*. Doing this in a numerically robust way turns out to be a very intricate task (see the remark below).

Remark 6.3.2 (Other software). *The author has tried to use various open-source polygon clipping libraries to do the task, including Clipper [82], Boost Geometry [68], General Polygon Clipper [103] and Boost Polygon [139]. Unfortunately, all of these software packages were* not *numerically robust as of July 2014, i.e. they suffered from one or more of the following problems:*

- *The clipping library claims that two polygons do not intersect but in fact they do and vice versa.*
- *The returned intersection polygon is non-convex, although the original clipping and subject polygon are both convex.*
- *The returned intersection polygon is completely wrong, e.g. the area of the returned polygon is bigger than the subject/clip polygon.*
- *The returned intersection polygon is self-intersecting.*

These problems occur only for very special inputs where the subject/clip polygons are extremely distorted.

In HyDi the intersection between two sub-boundary-faces is computed by a robust version of the Sutherland-Hodgman [143] algorithm which in turn relies on a robust version of the *gift-wrapping* algorithm [47, Section 33.3] to compute the convex hull of a set of points, cf. Algorithms 1, 3. It turns out that in both algorithms the crucial operation is the so-called *orientation test* which essentially computes the 2D cross product $(\boldsymbol{a} - \boldsymbol{c}) \times (\boldsymbol{b} - \boldsymbol{c})$:

1: **procedure** ORIENTATION(a, b, c)
2: **return** $(a_x - c_x)(b_y - c_y) - (a_y - c_y)(b_x - c_x)$
3: **end procedure**

We note that ORIENTATION(a, b, c) is positive if the points a, b, c are ordered anti-clockwise, negative if they are ordered clock-wise and zero if they all lie on a line. The important point is that the calculation of this cross product is numerically non-robust because of the minus sign that can lead to cancellation, in particular the sign of ORIENTATION(a, b, c) can be wrong if the computation is done in fixed-size arithmetic. Luckily Shewchuk [137] has implemented a robust and fast version of ORIENTATION which uses adaptive higher-order precision. Algorithm 1 shows the stabilized Sutherland-Hodgman algorithm that uses this stabilized ORIENTATION function for all floating point operations. This algorithm relies on two other robust algorithms, which also exclusively rely on the ORIENTATION algorithm: The CI algorithm 2 computes the intersection of two lines and Algorithm 3 computes the convex hull of a set of points using the gift-wrapping algorithm.

Bibliographical Remarks The paper of Gander and Japhet [67] presents an alternative to Algorithm 1 that is numerically robust. This paper gives also a good overview over different asymptotically linear methods to determine pairs of sub-boundary-faces that could potentially intersect.

6.4 Handling Changes in the Grid

This section presents how the *observer pattern* [66] is used in HyDi to deal with changes in the grid. By a change in the grid we mean the introduction/removal of mesh elements or changes in the connectivity of the grid. This happens for example when a part of the domain is moved or remeshed, cf. Remark 4.2.29. The presented approach is a bit unconventional at first sight but it has been very successful, especially for the simulation of electric arcs in circuit breakers where mesh changes are very frequent and complex.

It is important to note that in HyDi a partial differential equation is solved by constructing a set of objects that depend on each other, in fact these objects form a *directed acyclic graph* (DAC). Figure 6.3 shows a small part of the DAG that has been used to simulate the loop of wire passing through the magnetic field in Section 4.2.4. We see that only the `egv` object (instance of `hydi::grid::utils::EnhancedGridView`) depends directly

Algorithm 1 Robust Sutherland-Hodgman, cf. [143]

Require:
clip polygon must be convex

procedure ClipSH(*subject*,*clip*) ▷ Intersection between subject and clip polygon
  clipStart ← *clip.back*() ▷ Start point of clip-line
  result ← {}
  for *clipEnd* in *s* **do** ▷ Endpoint of clip-line
    subjectStart ← *subject.back*()
    for *subjectEnd* in *subject* **do**
      if Orientation(*clipStart*, *clipEnd*, *subjectEnd*) > 0 **then**
        ▷ End point of subject line lies inside clip polygon
        if Orientation(*clipStart*, *clipEnd*, *subjectStart*) < 0 **then**
          ▷ Start point of subject line lies outside clip-polygon
          result ← *result*∪{CI(*clipStart*, *clipEnd*, *subjectStart*, *subjectEnd*)}
        else
          result ← *result* ∪ {*subjectEnd*}
        end if
      else if Orientation(*clipStart*, *clipEnd*, *subjectEnd*) < 0 **then**
        if Orientation(*clipStart*, *clipEnd*, *subjectStart*) > 0 **then**
          result ← *result*∪{CI(*clipStart*, *clipEnd*, *subjectStart*, *subjectEnd*)}
        end if
      else ▷ *subjectEnd* lies exactly on *clipStart*, *clipEnd*
        result ← *result* ∪ {*subjectEnd*}
      end if
      subjectStart ← *subjectEnd*
    end for
    clipStart ← *clipEnd*
  end for
  return ConvexHull(*result*)
end procedure

Algorithm 2 Compute Intersection between two lines robustly

procedure CI(a, b, c, d) ▷ Intersection between $\overline{ab}$ and $\overline{cd}$
  $distC \leftarrow$ Orientation(a, b, c)
  $distD \leftarrow$ Orientation(a, b, d)
  $s = distC/(distC - distD)$
  return $s * d + (1 - s) * c$
end procedure

Algorithm 3 Robust Convex Hull Algorithm (gift-wrapping), cf. [47, Section 33.3]

```
1:  procedure ConvexHull(points)
2:      minPoint ← {arg min_i p[i]_x}                          ▷ Find left-most point
3:      result ← {}
4:      startPoint ← minPoint
5:      endPoint ← (startPoint + 1) modulo points.size()
6:                                          ▷ Find next point that is different
7:      while points[startPoint] == points[endPoint] and endPoint ≠ startPoint do
8:          endPoint ← (endPoint + 1) modulo points.size()
9:      end while
10:     repeat
11:         result ← result ∪ {points[startPoint]}
12:         for i in {0, ..., points.size() − 1} \ {startPoint, endPoint} do
13:             if Orientation(result.back(), points[endPoint], points[i]) < 0 then
14:                 endPoint ← i
15:             end if
16:         end for
17:         startPoint ← endPoint
18:         endPoint ← (startPoint + 1) modulo points.size()
19:     until points[startPoint] == points[minPoint]
20:     cleanResult ← {result[0]}
21:     for i in {1, ..., result.size() − 2} do                ▷ Remove colinear points
22:         if Orientation(cleanResult.back(), result[i], result[i + 1]) ≥ 0 then
23:             cleanResult ← cleanResult ∪ {result[i]}
24:         end if
25:     end for
26: end procedure
```

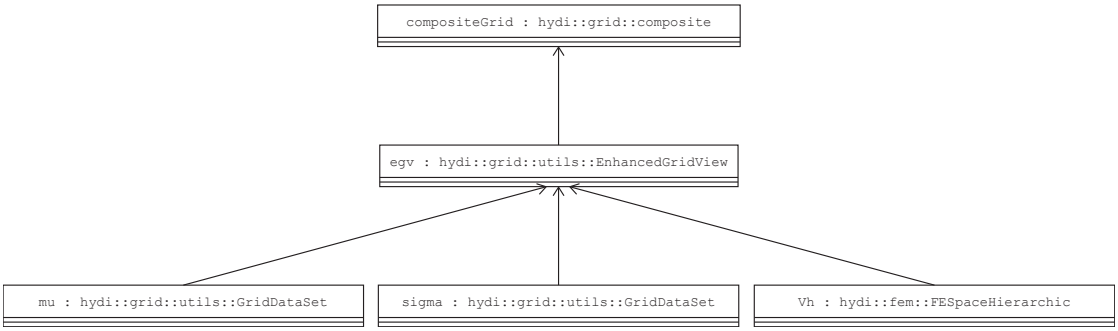

Figure 6.3: Small part of the object graph in HyDi that is used for the simulation of the wire-loop example in Section 4.2.4.

on the `compositeGrid` object (cf. Figure 6.1). The two `GridDataSets` `mu` and `sigma` store for every mesh element the magnetic permeability μ and the electric conductivity σ, respectively, and they both depend on the `egv` object. The approximation space `Vh` organizes basis functions that span the approximation space V_h. It depends also on the `egv` object.

If new elements are introduced into the mesh, the `GridDataSets` `mu` and `sigma` must be given a new value on these mesh elements and the approximation space `Vh` must introduce new unknowns that are linked to basis functions of the new mesh elements. Similarly, if elements are removed from the mesh, `Vh` must renumber its unknowns. More generally: *whenever a change in the underlying grid occurs, the components of the DAG must update their internal representation based on the new state of the objects that they depend on.*

Care must be taken that the objects of the DAG are updated in the correct order: the `egv` object should be updated before the `mu`, `sigma` and `Vh` objects because the update process of `mu`, `sigma` or `Vh` may rely on the updated information of the `egv` object. Because of this, the update process sweeps like a *wave* over the DAG of Figure 6.3: The wave starts on the `compositeGrid` object which passes it on to the `egv` object and from there it continues to the `mu`, `sigma` and `Vh` objects.

It is of course possible to trigger the update process of every component in the DAG manually, but this can be become a very tedious task if the DAG is large. Moreover, such an approach is not *maintainable* because every change to the DAG requires that the user understands the structure of the whole DAG (the order of the update process matters). To circumvent this problem in HyDi, the update procedure has been automated using the *observer pattern* [66]: Every member of the DAG registers itself with all the objects that it depends on, so that every object in the DAG has a list of other objects that depend on it. For example, the `egv` object knows that `mu`, `sigma` and `Vh` depend on it.

If a part of the grid is remeshed, the grid manager can trigger an *update wave* that travels through the DAG: it informs all dependent objects that a change has occurred.

Once all dependent objects have updated their internal representation, they forward the information to their dependent objects. In HyDi this update scheme is represented by the `hydi::base::IUpdateObserver` interface that must be implemented by every member of the DAG. It defines the precise communication protocol between the members of the DAG.

Remark 6.4.1 (Other changes). *In principle, the above pattern can also be used to handle a change in any other member of the DAG. For example, if the polynomial degree of the approximation space* `Vh` *is increased locally, this could trigger an automatic resize/reassembly of the Galerkin matrix (not shown in Figure 6.3).*

Remark 6.4.2 (Multiple dependencies). *If one object in the DAG depends on multiple objects, it is important that it only updates itself once all of its dependencies have updated themselves. Consider for example the following DAG:*

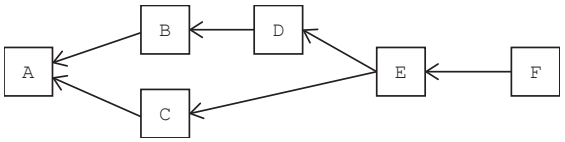

Here `E` *can only update itself and forward the update wave to* `F`*, once objects* `C` *and* `D` *have updated themselves.*

List of Symbols

Π_h $L^2(\Omega)$ projection operator into $\mathcal{P}_{k,h}(\mathcal{T}_h)$, page 70

$\{\!\{\cdot\}\!\}_\omega$ Weighted average operator, page 48

$\boldsymbol{\alpha}$ Multi-index, usually $\boldsymbol{\alpha} \in \mathbb{N}^d$, page 18

a_F Local length scale appearing in penalty term, page 51

$\boldsymbol{B}$ Magnetic induction, page 7

curl Vector valued weak curl operator, defined in 2D and 3D, page 24

curl Scalar valued weak curl operator, defined only in 2D, page 24

$C^k(\Omega)$ Set of k-times continuously differentiable functions, page 18

$C^k(\overline{\Omega})$ Set of functions that are continuosly differentiable up to the boundary or equivalently: The restriction of $C_0^k(\mathbb{R}^d)$ to Ω, page 18

$C_0^k(\Omega)$ Set of k-times continuously differentiable functions with compact support on Ω, page 18

$\mathbf{curl}_h$ Broken curl, page 47

$\tilde{D}(\Omega)$ Domain of definition of the Raviart-Thomas interpolation operator $\boldsymbol{w}_h$, page 70

$\boldsymbol{D}$ Electric Displacement Field, page 7

d Dimension of space in which Ω is embedded, $d = 2, 3$, page 16

$D_{k,h}(\Omega)$ Space of Raviart-Thomas elements, page 70

ϵ Electric Permittivity (linear materials), page 10

ϵ_0 Vacuum permittivity, page 9

$\boldsymbol{E}$ Electric field, page 7

$\mathbb{F}_T$ Set of all facets of mesh element T, page 45

$\mathcal{F}_h^b$ Set of all boundary faces, page 45

$\mathcal{F}_h^i$ Set of all inner faces, page 45

$\mathcal{F}_h$ Set of all faces of a mesh, page 45

$\mathcal{F}_K$ Set of all faces of mesh element K, page 45

γ Open subset of the boundary $\partial\Omega$, page 22

Γ_D Part of $\partial\Omega$ where Dirichlet boundary conditions are applied, page 30

γ_D Trace operator, $\gamma_D(f) \coloneqq f|_{\partial\Omega}$, page 20

Γ_i Connected components of $\partial\Omega_0$, $i \geq 0$, page 36

Γ_N Part of $\partial\Omega$ where Neumann boundary conditions are applied, page 30

γ_N Trace operator, $\Gamma_N(\boldsymbol{A}) \coloneqq \boldsymbol{n} \cdot \boldsymbol{A}|_{\partial\Omega}$, page 23

$\gamma_{\mu,F}$ μ dependent weight for the penalty term, page 51

$\mathbf{grad}_h$ Broken gradient, page 47

$\mathcal{H}$ The set of mesh-widths, page 46

$\boldsymbol{H}$ Magnetic field, page 7

$\boldsymbol{H}(\mathrm{div};\Omega) \coloneqq \left\{\boldsymbol{A} \in L^2(\Omega)^d \middle| \operatorname{div} \boldsymbol{A} \in L^2(\Omega)\right\}$, page 22

$\boldsymbol{H}_0(\mathrm{div};\Omega)$ Closure of $C_0^\infty(\Omega)^d$ w.r.t. $\|\cdot\|_{\boldsymbol{H}(\mathrm{div};\Omega)}$, page 22

h Mesh-width, page 44

$H(\mathbf{curl};\Omega)$ Subspace of $L^2(\Omega)$ $(d = 2)$ respectively $L^2(\Omega)^3$ $(d = 3)$, with square integrable vector curl, page 24

$H(\mathrm{curl};\Omega)$ For $d = 2$ the subspace of $L^2(\Omega)^2$ with square integrable scalar valued curl, page 24

$H^s(\Omega)$ Sobolev Space $W^{s,2}(\Omega)$, page 18

$H_0(\mathbf{curl};\Omega)$ Closure of $C_0^\infty(\Omega)^3$ $(d = 3)$, respectively $C_0^\infty(\Omega)$ $(d = 2)$ w.r.t. $\|\cdot\|_{H(\mathbf{curl};\Omega)}$, page 24

h_T Diameter of element $T \in \mathcal{T}_h$, page 46

$\boldsymbol{H}(\mathbf{curl};\mathcal{T}_h)$ Broken version of the Sobolev space $\boldsymbol{H}(\mathbf{curl};\Omega)$, page 47

$\boldsymbol{H}(\mathrm{div};\mathcal{T}_h)$ Broken version of the Sobolev space $\boldsymbol{H}(\mathrm{div};\Omega)$, page 47

$\hookrightarrow$ Continuous embedding, if $X \hookrightarrow Y$ then $X \subset Y$ and $\|x\|_Y \leq C\,\|x\|_X$, page 19

$(\cdot,\cdot)_{L^2_\kappa(\Omega)}$ Inner product, $(f,g)_{L^2_\kappa(\Omega)} \coloneqq (\kappa f, g)_{L^2(\Omega)}$, page 28

$[\![\cdot]\!]$ Jump operator, page 48

$[\![\cdot]\!]_\tau$ Tangential jump operator, page 48

$\boldsymbol{j}$ Total current density, page 7

$\boldsymbol{j}^i$ Externally impressed current density, page 10

$\mathrm{d}\ell$ Line element, page 8

$L^p(\Omega)$ Set of functions where the p-th power of the absolute value is Lebesque integrable, page 18

μ Magnetic Permeability (linear materials), page 10

$\boldsymbol{n}$ Surface unit normal defined on $\partial\Omega$ such that it points away from Ω, page 8

Ω Bounded open subset in $\mathbb{R}^3$ or $\mathbb{R}^2$

Ω_0 Open subset of Ω where $\sigma = 0$, page 36

Ω_σ Open subset of Ω where $\sigma \geq \sigma_{\min}$, page 36

$\oplus_\kappa$ Orthogonal sum w.r.t. to the inner product $(\cdot,\cdot)_{L^2_\kappa(\Omega)}$, page 28

$\mathbb{P}_k$ Space of polynomials of total degree $\leq k$, page 65

$\mathbb{P}_{k,h}$ Completely discontinuous approximation space with polynomials of total degree $\leq k$, page 77

$\mathcal{P}_k(\hat{T})$ A general polynomial space defined on a reference element $\hat{T}$ that contains $\mathbb{P}_k(\hat{T})$, page 67

$\mathcal{P}_{k,h}(\Omega)$ H^1 conforming, polynomial space of degree k, page 67

Φ_T Mapping from reference element to mesh element, page 44

π_h H^1 conforming projection operator, page 68

$\tilde{\mathbb{P}}$ Domain of definition of the H^1 conforming projection operator, page 68

$\tilde{P_\Omega}$ Any partition of Ω. Usually used to construct a piecewise conforming polynomial space, page 72

P_Ω Partition of Ω such that κ, μ are constant in every subdomain, page 49

$\mathbb{Q}_k$ Space of polynomials where the maximum monomial degree is k, page 65

ρ free Charge density, page 7

ρ_T Diameter of largest ball contained in a mesh element $\overline{T}$, page 46

$\tilde{R}(\Omega)$ Domain of definition of the Nédélec interpolation operator $\boldsymbol{r}_h$, page 69

$\tilde{r}_h$ Projection operator for the broken Nédélec approximation space, page 73

ϱ_1 Constant that gives a lower bound for a_F in terms of h_T, page 72

$R_{k,h}(\Omega)$ Nédélec/edge element approximation space, page 69

$R_{k,h}(\tilde{P}_\Omega)$ Broken version of the Nédélec approximation space $R_{k,h}(\Omega)$, page 72

ϱ_2 Constant that gives an upper bound for a_F in terms of h_T, page 51

$\mathrm{d}S$ Surface element, page 8

Σ A 2D Manifold embedded in $\mathbb{R}^3$ or 1D Manifold embedded in $\mathbb{R}^2$, page 8

σ Electric conductivity, page 10

$\sigma_{\mathcal{H}}$ Shape regularity constant for a mesh sequence $\mathcal{T}_{\mathcal{H}}$, page 46

$\mathcal{T}_{\mathcal{H}}$ Sequence of meshes, $\mathcal{T}_{\mathcal{H}} = \{\mathcal{T}_h\}_{h\in\mathcal{H}}$, page 46

$\mathcal{T}_h$ A mesh of the domain Ω, page 44

μ_0 Vacuum permeability, page 9

$\sqcup$ Disjoint union of two sets: $C = A \sqcup B \Leftrightarrow (C = A \cup B)$ and $A \cap B = \emptyset$, page 30

U_h Generic DG-approximation space for the 2D eddy current/Poisson problem, page 59

$\mathrm{d}V$ Volume element, page 8

V^* Space of extra regularity that makes sure that the traces of the solution $\boldsymbol{A}$ of the generic $\mathbf{curl}-\mathbf{curl}$ problem are well defined, page 50

V_h^* Completely broken space defined on mesh $\mathcal{T}_h$ with well-defined traces, page 50

V_h Discrete approximation space for the generic $\mathbf{curl}-\mathbf{curl}$ problem, page 50

ω Angular frequency in time-harmonic regime, page 12

$W^{s,p}(\mathcal{T}_h)$ Broken version of the Sobolev space $W^{s,p}(\Omega)$, page 47

$W^{s,p}(\Omega)$ Sobolev Space, page 18

References

[1] Mark Ainsworth and Joe Coyle. Hierarchic finite element bases on unstructured tetrahedral meshes. *International Journal for Numerical Methods in Engineering*, 58(14):2103–2130, 2003.

[2] Roger Alexander. Diagonally implicit Runge-Kutta methods for stiff O.D.E.s. *SIAM Journal on Numerical Analysis*, 14(6):1006–1021, 1977.

[3] Ana Alonso and Alberto Valli. Some remarks on the characterization of the space of tangential traces of $H(\mathrm{rot};\Omega)$ and the construction of an extension operator. *Manuscripta mathematica*, 89(1):159–178, 1996.

[4] Ana Alonso and Alberto Valli. A domain decomposition approach for heterogeneous time-harmonic Maxwell equations. *Computer methods in applied mechanics and engineering*, 143(1):97–112, 1997.

[5] Ana Alonso Rodríguez, Paolo Fernandes, and Alberto Valli. Weak and strong formulations for the time-harmonic eddy-current problem in general multi-connected domains. *European Journal of Applied Mathematics*, 14(04):387–406, 2003.

[6] Piergiorgio Alotto and Ilaria Perugia. Tree-cotree implicit condensation in magnetostatics. *IEEE transactions on magnetics*, 36(4):1523–1526, 2000.

[7] Piergiorgio Alotto, Andrea Bertoni, Ilaria Perugia, and Dominik Schötzau. Efficient use of the local discontinuous Galerkin method for meshes sliding on a circular boundary. *IEEE transactions on magnetics*, 38(2):405–408, 2002.

[8] Douglas N. Arnold. An interior penalty finite element method with discontinuous elements. *SIAM journal on numerical analysis*, 19(4):742–760, 1982.

[9] Douglas N. Arnold, Franco Brezzi, Bernardo Cockburn, and L. Donatella Marini. Unified analysis of discontinuous Galerkin methods for elliptic problems. *SIAM journal on numerical analysis*, 39(5):1749–1779, 2002.

[10] Ivo Babuška and Jens M. Melenk. The partition of unity method. *Internat. J. Numer. Methods Engrg.*, 40(4):727–758, 1997.

[11] Ivo Babuška and Hae-Soo Oh. The p-version of the finite element method for domains with corners and for infinite domains. *Numerical Methods for Partial Differential Equations*, 6(4):371–392, 1990.

[12] Ivo Babuška and Manil Suri. The *h-p* version of the finite element method with quasi-uniform meshes. *RAIRO Modél. Math. Anal. Numér.*, 21(2):199–238, 1987.

[13] Ivo Babuška and Manil Suri. The optimal convergence rate of the *p*-version of the finite element method. *SIAM J. Numer. Anal.*, 24(4):750–776, 1987.

[14] Florian Bachinger, Ulrich Langer, and Joachim Schöberl. Numerical analysis of nonlinear multiharmonic eddy current problems. Technical report, Johannes Kepler University Linz, 2004. SFB-Report No. 2004-01.

[15] Peter Bastian, Markus Blatt, Andreas Dedner, Christian Engwer, Robert Klöfkorn, Ralf Kornhuber, Markus Ohlberger, and Oliver Sander. A generic grid interface for parallel and adaptive scientific computing. part II: implementation and tests in dune. *Computing*, 82(2-3):121–138, 2008.

[16] Peter Bastian, Markus Blatt, Andreas Dedner, Christian Engwer, Robert Klöfkorn, Markus Ohlberger, and Oliver Sander. A generic grid interface for parallel and adaptive scientific computing. part I: abstract framework. *Computing*, 82(2-3): 103–119, 2008.

[17] Mario Bebendorf and Joerg Ostrowski. Parallel hierarchical matrix preconditioners for the curl-curl operator. *Journal of Computational Mathematics*, pages 624–641, 2009.

[18] Gary Bedrosian. Shape functions and integration formulas for three-dimensional finite element analysis. *International journal for numerical methods in engineering*, 35(1):95–108, 1992.

[19] Faker B. Belgacem. The mortar finite element method with Lagrange multipliers. *Numerische Mathematik*, 84(2):173–197, 1999.

[20] Morgane Bergot. *Éléments finis dordre élevé pour maillages hybrides*. PhD thesis, Thèse de doctorat, Université de Bordeaux, 2010.

[21] Morgane Bergot and Marc Duruflé. High-order optimal edge elements for pyramids, prisms and hexahedra. *Journal of Computational Physics*, 232(1):189–213, 2013.

[22] Christine Bernardi. Optimal finite-element interpolation on curved domains. *SIAM Journal on Numerical Analysis*, 26(5):1212–1240, 1989.

[23] Daniel Boffi. A note on the de Rham complex and a discrete compactness property. *Applied Mathematics Letters*, 14(1):33–38, 2001.

[24] Daniele Boffi, Franco Brezzi, and Michel Fortin. *Mixed finite element methods and applications*, volume 44 of *Springer Series in Computational Mathematics*. Springer, 2013.

[25] Matthias Bollhöfer and Yousef Saad. Multilevel preconditioners constructed from inverse-based ILU's. *SIAM Journal on Scientific Computing*, 27(5):1627–1650, 2006.

[26] Alain Bossavit. On the numerical analysis of eddy-current problems. *Computer methods in applied mechanics and engineering*, 27(3):303–318, 1981.

[27] Alain Bossavit. *Computational electromagnetism: variational formulations, complementarity, edge elements*. Academic Press, 1998.

[28] Franck Boyer and Pierre Fabrie. *Mathematical tools for the study of the incompressible Navier-Stokes equations and related models*, volume 183 of *Applied Mathematical Sciences*. Springer, 2012.

[29] Susanne C. Brenner. Poincaré–Friedrichs inequalities for piecewise H^1 functions. *SIAM Journal on Numerical Analysis*, 41(1):306–324, 2003.

[30] Susanne C. Brenner and L. Ridgway Scott. *The mathematical theory of finite element methods*, volume 15 of *Texts in Applied Mathematics*. Springer, New York, third edition, 2008.

[31] Haim Brezis. *Functional analysis, Sobolev spaces and partial differential equations*. Springer, 2010.

[32] Franco Brezzi and Michel Fortin. *Mixed and hybrid finite element methods*, volume 15 of *Springer Series in Computational Mathematics*. Springer-Verlag, New York, 1991.

[33] Annalisa Buffa and Patrick Ciarlet. On traces for functional spaces related to Maxwell's equations part I: An integration by parts formula in Lipschitz polyhedra. *Mathematical Methods in the Applied Sciences*, 24(1):9–30, 2001.

[34] Annalisa Buffa and Ilaria Perugia. Discontinuous Galerkin approximation of the Maxwell eigenproblem. *SIAM Journal on Numerical Analysis*, 44(5):2198–2226, 2006.

[35] Annalisa Buffa, Habib Ammari, and Jean-Claude Nédélec. A justification of eddy currents model for the Maxwell equations. *SIAM Journal on Applied Mathematics*, 60(5):1805–1823, 2000.

[36] Annalisa Buffa, Martin Costabel, and Dongwoo Sheen. On traces for $\mathrm{H}(\mathrm{curl}, \Omega)$ in Lipschitz domains. *Journal of Mathematical Analysis and Applications*, 276(2): 845–867, 2002.

[37] Annalisa Buffa, Yvon Maday, and Francesca Rapetti. Applications of the mortar element method to 3D electromagnetic moving structures. In *Computational electromagnetics*, pages 35–50. Springer, 2003.

[38] Annalisa Buffa, Paul Houston, and Ilaria Perugia. Discontinuous Galerkin computation of the Maxwell eigenvalues on simplicial meshes. *Journal of computational and applied mathematics*, 204(2):317–333, 2007.

[39] François Buret, Monique Dauge, Patrick Dular, Laurent Krahenbuhl, Victor Péron, Ronan Perrussel, Clair Poignard, and Damien Voyer. Eddy currents and corner singularities. *IEEE Transactions on Magnetics*, 48(2):679–682, 2012.

[40] Raffael Casagrande. Sliding interfaces for eddy current simulations. Master's thesis, ETH Zürich, 2013.

[41] Paul Castillo. Performance of discontinuous Galerkin methods for elliptic PDEs. *SIAM Journal on Scientific Computing*, 24(2):524–547, 2002.

[42] Philippe G. Ciarlet. *The finite element method for elliptic problems*. North-Holland Publishing Co., Amsterdam-New York-Oxford, 1978. Studies in Mathematics and its Applications, Vol. 4.

[43] Philippe Clément. Approximation by finite element functions using local regularization. *Revue française d'automatique, informatique, recherche opérationnelle. Analyse numérique*, 9(2):77–84, 1975.

[44] Bernardo Cockburn and Chi-Wang Shu. The local discontinuous Galerkin method for time-dependent convection-diffusion systems. *SIAM Journal on Numerical Analysis*, 35(6):2440–2463, 1998.

[45] Gary Cohen. *Higher-order numerical methods for transient wave equations*. Springer, 2013.

[46] Rodney Coleman. *Calculus on normed vector spaces*. Springer, New York, 2012.

[47] Thomas H. Cormen. *Introduction to algorithms*. MIT press, 2009.

[48] Martin Costabel and Monique Dauge. Weighted regularization of Maxwell equations in polyhedral domains. *Numerische Mathematik*, 93(2):239–277, 2002.

[49] Jean-Louis Coulomb, François-Xavier Zgainski, and Yves Maréchal. A pyramidal element to link hexahedral, prismatic and tetrahedral edge finite elements. *IEEE Transactions on Magnetics*, 33(2):1362–1365, 1997.

[50] Monique Dauge. private communication, 2016.

[51] Monique Dauge, Patrick Dular, Laurent Krähenbühl, Victor Péron, Ronan Perrussel, and Clair Poignard. Corner asymptotics of the magnetic potential in the eddy-current model. *Mathematical Methods in the Applied Sciences*, 37(13):1924–1955, 2014.

[52] Robert Dautray and Jacques-Louis Lions. *Mathematical analysis and numerical methods for science and technology. Vol. 3.* Springer-Verlag, Berlin, 1990. Spectral theory and applications, With the collaboration of Michel Artola and Michel Cessenat, Translated from the French by John C. Amson.

[53] Beman Dawes, David Abrahams, et al. The boost libraries. http://www.boost.org, 2016.

[54] Eleonora Di Nezza, Giampiero Palatucci, and Enrico Valdinoci. Hitchhiker's guide to the fractional Sobolev spaces. *ArXiv e-prints*, April 2011.

[55] Daniele Antonio Di Pietro and Alexandre Ern. *Mathematical aspects of discontinuous Galerkin methods*, volume 69. Springer, 2011.

[56] Heinz K. Dirks. Quasi-stationary fields for microelectronic applications. *Electrical Engineering (Archiv fur Elektrotechnik)*, 79(2):145–155, 1996.

[57] Maksymilian Dryja. On discontinuous Galerkin methods for elliptic problems with discontinuous coefficients. *Computational Methods in Applied Mathematics Comput. Methods Appl. Math.*, 3(1):76–85, 2003.

[58] Todd Dupont and Ridgway Scott. Polynomial approximation of functions in Sobolev spaces. *Mathematics of Computation*, 34(150):441–463, 1980.

[59] Albert Einstein. Zur Elektrodynamik bewegter Körper. *Annalen der Physik*, 322 (17):891–921, 1905.

[60] Alexandre Ern and Jean-Luc Guermond. *Theory and practice of finite elements*, volume 159 of *Applied Mathematical Sciences*. Springer-Verlag, New York, 2004.

[61] Alexandre Ern and Jean-Luc Guermond. Finite element quasi-interpolation and best approximation. *ArXiv e-prints*, May 2015.

[62] Lawrence C. Evans. *Partial differential equations*, volume 19 of *Graduate Studies in Mathematics*. American Mathematical Society, Providence, RI, second edition, 2010.

[63] Paolo Fernandes and Gianni Gilardi. Magnetostatic and electrostatic problems in inhomogeneous anisotropic media with irregular boundary and mixed boundary conditions. *Mathematical Models and Methods in Applied Sciences*, 7(07):957–991, 1997.

[64] George J. Fix, Sandeep Gulati, and Gary I. Wakoff. On the use of singular functions with finite element approximations. *Journal of Computational Physics*, 13(2):209–228, 1973.

[65] Bernd Flemisch, Yvon Maday, Francesca Rapetti, and Barbara I. Wohlmuth. Coupling scalar and vector potentials on nonmatching grids for eddy currents in a

moving conductor. *Journal of computational and applied mathematics*, 168(1): 191–205, 2004.

[66] Erich Gamma, Richard Helm, Ralph Johnson, and John Vlissides. *Design patterns. Elements of reusable object-oriented software*. Addison-Wesley, 1994.

[67] Martin J. Gander and Caroline Japhet. An algorithm for non-matching grid projections with linear complexity. In *Domain Decomposition Methods in Science and Engineering XVIII*, pages 185–192. Springer, 2009.

[68] Barend Gehrels, Bruno Lalande, Mateusz Loskot, and Adam Wulkiwicz. Boost geometry library. http://www.boost.org/libs/geometry, 2009.

[69] Vivette Girault and Pierre-Arnaud Raviart. *Finite element methods for Navier-Stokes equations*, volume 5 of *Springer Series in Computational Mathematics*. Springer-Verlag, Berlin, 1986.

[70] Vasile Gradinaru and Ralf Hiptmair. Whitney elements on pyramids. *Electronic Transactions on Numerical Analysis*, 8:154–168, 1999.

[71] Pierre Grisvard. *Elliptic problems in nonsmooth domains*, volume 69 of *Classics in Applied Mathematics*. Society for Industrial and Applied Mathematics (SIAM), Philadelphia, PA, 2011.

[72] Gaël Guennebaud, Benoît Jacob, et al. Eigen v3. http://eigen.tuxfamily.org, 2010.

[73] Jacques Hadamard. *Le problème de Cauchy et les équations aux dérivées partielles linéaires hyperboliques*. Hermann & Cie, 1932.

[74] Ralf Hiptmair. Finite elements in computational electromagnetism. *Acta Numerica*, 11:237–339, 2002.

[75] Ralf Hiptmair. Analysis of multilevel methods for eddy current problems. *Mathematics of computation*, 72(243):1281–1303, 2003.

[76] Ralf Hiptmair and Oliver Sterz. Current and voltage excitations for the eddy current model. *International Journal of Numerical Modelling: Electronic Networks, Devices and Fields*, 18(1):1–21, 2005.

[77] Karl Hollaus, Daniel Feldengut, Joachim Schöberl, Markus Wabro, and Dzevat Omeragic. Nitsche-type mortaring for Maxwells equations. In *Progress In Electromagnetics Research Symposium (PIERS 2010), Cambridge, Massachusetts, USA*, pages 1–5, 2010.

[78] Paul Houston, Ilaria Perugia, and Dominik Schotzau. Nonconforming mixed finite-element approximations to time-harmonic eddy current problems. *IEEE transactions on magnetics*, 40(2):1268–1273, 2004.

[79] Paul Houston, Ilaria Perugia, and Dominik Schötzau. Mixed discontinuous Galerkin approximation of the Maxwell operator: Non-stabilized formulation. *Journal of Scientific Computing*, 22(1-3):315–346, 2005.

[80] John David Jackson. *Classical electrodynamics*. Wiley, 1999.

[81] Frank Jochmann. A compactness result for vector fields with divergence and curl in $L^q(\omega)$ involving mixed boundary conditions. *Applicable Analysis*, 66(1-2):189–203, 1997.

[82] Angus Johnson. Clipper - an open source freeware library for clipping and offsetting lines and polygons. http://www.angusj.com/delphi/clipper.php, 2014.

[83] Nicolai M. Josuttis. *C++ templates: The complete guide*. Addison-Wesley Professional, 2003.

[84] Erik F. Kaasschieter. Preconditioned conjugate gradients for solving singular systems. *Journal of Computational and Applied mathematics*, 24(1):265–275, 1988.

[85] R. Bruce Kellogg. Higher order singularities for interface problems. In *The mathematical foundations of the finite element method with applications to partial differential equations (Proc. Sympos., Univ. Maryland, Baltimore, Md., 1972)*, pages 589–602. Academic Press, New York, 1972.

[86] Stefan Kurz, Joachim Fetzer, Günther Lehner, and Wolfgang M. Rucker. A novel formulation for 3D eddy current problems with moving bodies using a Lagrangian description and BEM-FEM coupling. *IEEE Transactions on Magnetics*, 34(5): 3068–3073, 1998.

[87] Lev Davidovich Landau and Evgeny M. Lifshitz. *Course of theoretical physics. Vol. 8*. Pergamon International Library of Science, Technology, Engineering and Social Studies. Pergamon Press, Oxford, 1984.

[88] Jonas Larsson. Electromagnetics from a quasistatic perspective. *American Journal of Physics*, 75(3):230–239, 2007.

[89] Paul D. Ledger and Sabine Zaglmayr. hp-finite element simulation of three-dimensional eddy current problems on multiply connected domains. *Computer Methods in Applied Mechanics and Engineering*, 199(49):3386–3401, 2010.

[90] R. Sherman Lehman. Developments at an analytic corner of solutions of elliptic partial differential equations. *Indiana Univ. Math. J.*, 8:727–760, 1959.

[91] Günther Lehner. *Elektromagnetische Feldtheorie: für Ingenieure und Physiker*. Springer-Verlag, 2010.

[92] Rolf Leis. *Initial boundary value problems in mathematical physics*. Courier Corporation, 2013.

[93] Mo Lenoir. Optimal isoparametric finite elements and error estimates for domains involving curved boundaries. *SIAM Journal on Numerical Analysis*, 23(3):562–580, 1986.

[94] Jacques-Louis Lions and Enrico Magenes. *Non-homogeneous boundary value problems and applications. Vol. I.* Springer-Verlag, New York-Heidelberg, 1972. Translated from the French by P. Kenneth, Die Grundlehren der mathematischen Wissenschaften, Band 181.

[95] James Clerk Maxwell. *A treatise on electricity and magnetism*, volume 1. Clarendon press, 1881.

[96] William Charles Hector McLean. *Strongly elliptic systems and boundary integral equations*. Cambridge University Press, Cambridge, 2000.

[97] Jens Markus Melenk. *On generalized finite element methods*. PhD thesis, The University of Maryland, 1995.

[98] Jens Markus Melenk and Ivo Babuška. The partition of unity finite element method: basic theory and applications. *Comput. Methods Appl. Mech. Engrg.*, 139(1-4):289–314, 1996.

[99] Norman G. Meyers and James Serrin. $H = W$. *Proc. Nat. Acad. Sci. U.S.A.*, 51: 1055–1056, 1964.

[100] Kennth M. Mitzner. An integral equation approach to scattering from a body of finite conductivity. *Radio Science*, 2(12):1459–1470, 1967.

[101] Peter J. Mohr, David B. Newell, and Barry N. Taylor. CODATA recommended values of the fundamental physical constants: 2014. *Rev. Mod. Phys.*, 88(3), 2016.

[102] Peter Monk. *Finite element methods for Maxwell's equations*. Oxford University Press, 2003.

[103] Alan Murta. GPC: General Polygon Clipper library. Astrophysics Source Code Library, December 2015.

[104] Jindřich Nečas. *Les méthodes directes en théorie des équations elliptiques*. Masson et Cie, Éditeurs, Paris; Academia, Éditeurs, Prague, 1967.

[105] Jean-Claude Nédélec. Mixed finite elements in $\mathbb{R}^3$. *Numerische Mathematik*, 35 (3):315–341, 1980.

[106] Jean-Claude Nédélec. *Acoustic and electromagnetic equations*, volume 144 of *Applied Mathematical Sciences*. Springer-Verlag, New York, 2001.

[107] Nilima Nigam and Joel Phillips. High-order conforming finite elements on pyramids. *IMA Journal of Numerical Analysis*, 2011.

[108] Joachim Nitsche. Über ein Variationsprinzip zur Lösung von Dirichlet-Problemen bei Verwendung von Teilräumen, die keinen Randbedingungen unterworfen sind. In *Abhandlungen aus dem mathematischen Seminar der Universität Hamburg*, volume 36, pages 9–15. Springer, 1971.

[109] Martin Nolte. *Efficient numerical approximation of the effective Hamiltonian*. PhD thesis, Universität Freiburg, 2011.

[110] J. Tinsley Oden, Ivo Babuŝka, and Carlos Erik Baumann. A discontinuous hp finite element method for diffusion problems. *Journal of computational physics*, 146(2):491–519, 1998.

[111] Roy Osherove. *The art of unit testing*. MITP-Verlags GmbH & Co. KG, 2015.

[112] Jörg Ostrowski. *Boundary element methods for inductive hardening*. PhD thesis, Universität Tübingen, 2002.

[113] Jörg Ostrowski, Romeo Bianchetti, Irena Erceg-Baros, Bernardo Galletti, Rudolf Gati, David Pusch, Michael Schwinne, and Benjamin Wüthrich. Computational magnetohydrodynamics in the simulation of gas circuit breakers. *International Journal of Computational Science and Engineering 2*, 9(5-6):433–444, 2014.

[114] Dirk Pauly. On Maxwell's and Poincaré's constants. *Discrete Contin. Dyn. Syst. Ser. S*, 8(3):607–618, 2015.

[115] Ilaria Perugia and Dominik Schötzau. On the coupling of local discontinuous Galerkin and conforming finite element methods. *Journal of Scientific Computing*, 16(4):411–433, 2001.

[116] Ilaria Perugia and Dominik Schötzau. The *hp*-local discontinuous Galerkin method for low-frequency time-harmonic Maxwell equations. *Mathematics of Computation*, 72(243):1179–1214, 2003.

[117] Alfio Quarteroni and Alberto Valli. *Numerical approximation of partial differential equations*, volume 23 of *Springer Series in Computational Mathematics*. Springer-Verlag, Berlin, 1994.

[118] Francesca Rapetti, Frédéric Bouillault, Laurent Santandrea, Annalisa Buffa, Yvon Maday, and Adel Razek. Calculation of eddy currents with edge elements on non-matching grids in moving structures. *IEEE transactions on magnetics*, 36(4): 1351–1355, 2000.

[119] Francesca Rapetti, Yvon Maday, Frédéric Bouillault, and Adel Razek. Eddy-current calculations in three-dimensional moving structures. *IEEE transactions on magnetics*, 38(2):613–616, 2002.

[120] Stefan Reitzinger and Joachim Schöberl. An algebraic multigrid method for finite element discretizations with edge elements. *Numerical linear algebra with applications*, 9(3):223–238, 2002.

[121] Michael Renardy and Robert C. Rogers. *An introduction to partial differential equations*, volume 13. Springer, 2006.

[122] Béatrice Rivière, Mary F. Wheeler, and Vivette Girault. Improved energy estimates for interior penalty, constrained and discontinuous Galerkin methods for elliptic problems. part i. *Computational Geosciences*, 3(3-4):337–360, 1999.

[123] Béatrice Rivière, Mary F. Wheeler, and Vivette Girault. A priori error estimates for finite element methods based on discontinuous approximation spaces for elliptic problems. *SIAM Journal on Numerical Analysis*, 39(3):902–931, 2001.

[124] Dave Rodger, Paul J. Leonard, and John F. Eastham. Modelling electromagnetic rail launchers at speed using 3D finite elements. *IEEE transactions on magnetics*, 27(1):314–317, 1991.

[125] Ana Alonso Rodríguez, Ralf Hiptmair, and Alberto Valli. A hybrid formulation of eddy current problems. *Numerical Methods for Partial Differential Equations*, 21 (4):742–763, 2005.

[126] Gennadiy Rozental and Raffi Enficiaud. Boost test library. http://www.boost.org/libs/test, 2001.

[127] Hanns Ruder and Margret Ruder. *Die Spezielle Relativitätstheorie*. Vieweg Braunschweig, Wiesbaden, 1993.

[128] Raymond A. Ryan. *Introduction to tensor products of Banach spaces*. Springer, 2013.

[129] Alfred H. Schatz and Lars B. Wahlbin. On the finite element method for singularly perturbed reaction-diffusion problems in two and one dimensions. *Mathematics of Computation*, 40(161):47–89, 1983.

[130] Olaf Schenk and Klaus Gärtner. Solving unsymmetric sparse systems of linear equations with PARDISO. *Future Generation Computer Systems*, 20(3):475–487, 2004.

[131] Kersten Schmidt, Oliver Sterz, and Ralf Hiptmair. Estimating the eddy-current modeling error. *IEEE Transactions on Magnetics*, 44(6):686–689, 2008.

[132] Anna Schneebeli. *Interior penalty discontinuous Galerkin methods for electromagnetic and acoustic wave equations*. PhD thesis, University of Basel, 2006.

[133] Joachim Schöberl and Sabine Zaglmayr. High order Nédélec elements with local complete sequence properties. *COMPEL-The international journal for computation and mathematics in electrical and electronic engineering*, 24(2):374–384, 2005.

[134] Ch. Schwab. *p- and hp-finite element methods*. Numerical Mathematics and Scientific Computation. The Clarendon Press, Oxford University Press, New York, 1998.

[135] Christoph Schwab. Variable order composite quadrature of singular and nearly singular integrals. *Computing*, 53(2):173–194, 1994.

[136] Christoph Schwab, Manil Suri, and Christos A. Xenophontos. Boundary layer approximation by spectral/hp methods. *Houston J. Math. Spec. Issue of ICOSAHOM*, 95:501–508, 1996.

[137] Jonathan Richard Shewchuk. Adaptive precision floating-point arithmetic and fast robust geometric predicates. *Discrete & Computational Geometry*, 18(3):305–363, October 1997.

[138] Jeremy Siek, Andrew Lumsdaine, and David Abrahams. Boost concept check library. `http://www.boost.org/libs/concept_check`, 2000.

[139] Lucanus Simonson and Andrii Sydorchuk. Boost Polygon Library. http://www.boost.org/libs/polygon, 2014.

[140] Rolf Stenberg. Mortaring by a method of JA Nitsche. *Computational mechanics*, 1998.

[141] Oliver Sterz. *Modellierung und Numerik zeitharmonischer Wirbelstromprobleme in 3D*. PhD thesis, Ruprecht-Karls-University Heidelberg, 2003.

[142] Gilbert Strang and George J. Fix. *An analysis of the finite element method*, volume 212. Prentice-hall Englewood Cliffs, NJ, 1973.

[143] Ivan E. Sutherland and Gary W. Hodgman. Reentrant polygon clipping. *Communications of the ACM*, 17(1):32–42, 1974.

[144] Luc Tartar. *An introduction to Sobolev spaces and interpolation spaces*, volume 3 of *Lecture Notes of the Unione Matematica Italiana*. Springer, Berlin; UMI, Bologna, 2007.

[145] Vidar Thomée. *Galerkin finite element methods for parabolic problems*, volume 25 of *Springer Series in Computational Mathematics*. Springer-Verlag, Berlin, second edition, 2006.

[146] Ursula van Rienen, Jürgen Flehr, Ute Schreiber, and Victor Motrescu. Modeling and simulation of electro-quasistatic fields. In *Modeling, Simulation, and Optimization of Integrated Circuits*, pages 17–31. Springer, 2003.

[147] Leon Vardapetyan and Leszek Demkowicz. hp-adaptive finite elements in electromagnetics. *Computer methods in applied mechanics and engineering*, 169(3): 331–344, 1999.

[148] Timothy Warburton and Jan S. Hesthaven. On the constants in hp-finite element trace inverse inequalities. *Computer methods in applied mechanics and engineering*, 192(25):2765–2773, 2003.

[149] Christian Weber. A local compactness theorem for Maxwell's equations. *Math. Methods Appl. Sci.*, 2(1):12–25, 1980.

[150] Mary Fanett Wheeler. A priori L_2 error estimates for Galerkin approximations to parabolic partial differential equations. *SIAM J. Numer. Anal.*, 10:723–759, 1973.

[151] Barbara I. Wohlmuth. *Discretization methods and iterative solvers based on domain decomposition*, volume 17. Springer Science & Business Media, 2001.

[152] Inc. Wolfram Research. Mathematica, 2015. Version 10.3.

[153] Christos Xenophontos. *The hp version of the finite element method for singularly perturbed problems in unsmooth domains.* PhD thesis, UMBC, 1996.

[154] Christos Xenophontos. The hp finite element method for singularly perturbed problems in nonsmooth domains. *Numerical Methods for Partial Differential Equations*, 15(1):63–90, 1999.

[155] Katsumi Yamazaki. Generalization of 3D eddy current analysis for moving conductors due to coordinate systems and gauge conditions. *IEEE Transactions on Magnetics*, 33(2):1259–1262, 1997.

[156] Sabine Zaglmayer. *High order finite element methods for electromagnetic field computation.* PhD thesis, Johannes Kepler University, 2006.